Contents

1 INTRODUCTION:

The emerging fields of nanoscience and nanoengineering are leading to unprecedented understanding and control over the fundamental building blocks of all physical matter. This is likely to change the way almost everything —from vaccines to computers to automobile tires to objects not yet imagined —is designed and made.

Some notes on Scale

$$\left.\begin{array}{l} 1A° = 10^{-10}\,m \\ 1nm = 10^{-9}\,m \end{array}\right\} \text{atomic/crystallographic}$$

$$1\mu m = 10^{-6}\,m \Big\} \text{microstructure}$$

$$\left.\begin{array}{l} 1mm = 10^{-3}\,m \\ 1cm = 10^{-2}\,m \end{array}\right\} \text{macrostructure}$$

The word "Nano" means dwarf in Greek language. Use it as a prefix for any unit like a second or a meter and it means a billionth of that unit. A nanosecond is one billionth of a second. And a nanometer is one billionth of a meter—about the length of a few atoms lined up shoulder to shoulder. A world of things is built up from the tiny scale of nanometers. The thousands of cellular proteins and enzymes that constitute eg. The human body are a few nanometers thick. Enzymes typically are constructions of thousands of atoms in precise molecular structures that span some tens of nanometers. That kind of natural nanotechnology is about ten times smaller than some of the smallest synthetic nanotechnology that has been prepared until now. The individual components of an Intel Pentium III microprocessor span about 200 nanometers. This is the reason that computing is so powerful and easy these days. Nanotechnology makes microelectronics to be mere hints of what will come from engineering that begins on the even smaller scales of nanostructures.

 (a)   (b)   (c)   (d)   (e)
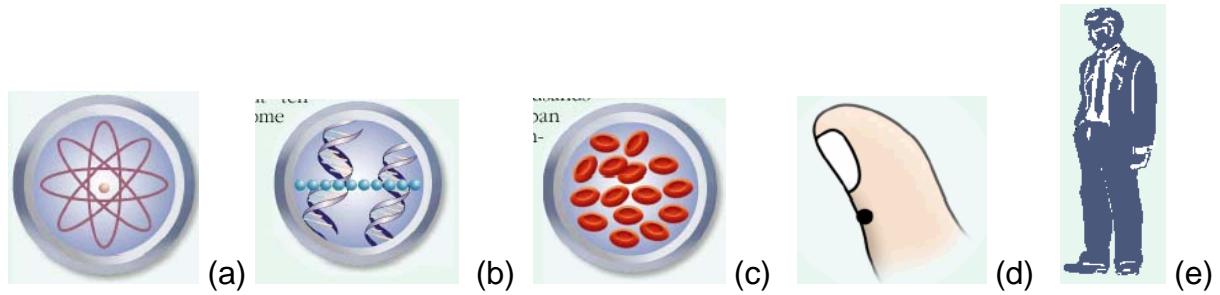
Figure 2.1: The whole size issue; (a**) Less than a nanometre**- individual atoms are up to a few angstroms, or upto a few tenths of a nanometer in diameter; (b) **Nanometer**- Ten shoulder-to-shoulder hydrogen atoms (blue balls) span 1 nm. DNA molecules are about 2.5 nm wide; (c) **Thousands of nanometers**- Biological cells, like these red blood cells, have diameters in the range of thousands of nm; (d) **a million nanometers**- A pinhead sized patch of this thumb (black point) is a million nanometers across; (e) **Billions of nanometers**- a two meter tall person is two billion nanometers tall.

LOGARITHMIC LENGTH
A matter of scale, and the levels of structure
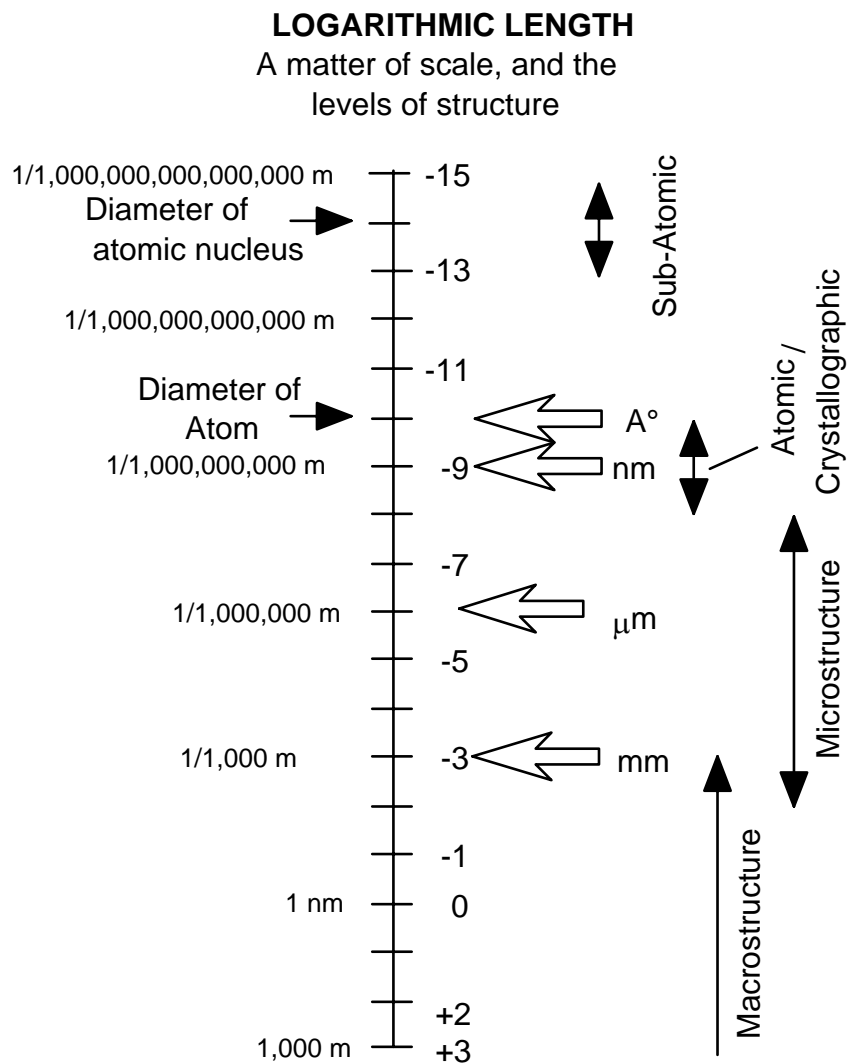
Nanostructure science and technology is a broad and interdisciplinary area of research and development activity that has been growing explosively worldwide in the past few years. It has the potential for revolutionizing the ways in which materials and products are created and the range and nature of functionalities that can be accessed. It is already having a significant commercial impact, which will assuredly increase in the future.
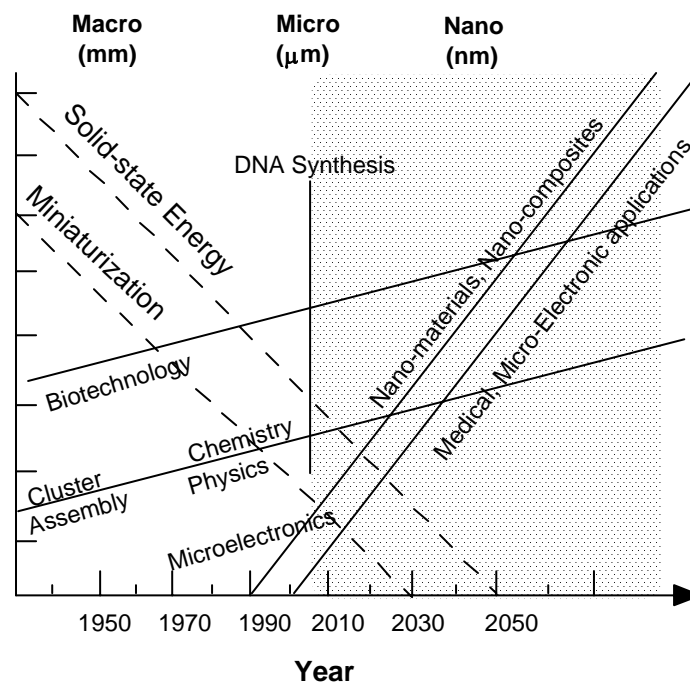
Figure 2.2: Evolution of science & technology and the future

1.1 What is nanotechnology?**:**

This is a term that has entered into the general and scientific vocabulary only recently but has been used at least as early as 1974 by Taniguchi.[1] Nanotechnology is defined as a technology where dimensions and tolerances are in the range of 0.1-100 nm (from size of the atom to about the wavelength of light) play a critical role. This definition is however too general to be of practical value because it could as well include, for example, topics as diverse as X-ray crystallography, atomic physics, microbial biology and include the whole of chemistry! The field covered down by nanotechnology is narrowed down to manipulation and machining within the defined dimensional range by technological means, as opposed to those used by craftsman,

and thus excludes, for example, traditional glass polishing or glass colouring techniques.

1.2 Mr. Feynman was not joking!:

One of the first to advocate a future for nanotechnology was Richard Feynman, a Physics Nobel laureate who died in 1988. In late 1959 at the California Institute of Technology, he presented what has become one of 20th century science's classic lectures entiitled "There is Plenty of Room at the Bottom". This classic lecture has become part of the nanotechnology community's founding liturgy. Feynman got his motivation from biology since biological systems can be exceedingly small. He said, "Many of the cells are very tiny, but they are active; they manufacture substances; they walk around; they wiggle; and they do all kind of marvellous things–all on a very small scale. Also, they store information. Consider the possibility that we too can make a thing very small which does what we want—that we can manufacture an object that manoeuvres at that level!"

Feynman talked about nanotechnology before the word existed. Feynman dreamed with a technological vision of extreme miniaturization in 1959, several years before the word "chip" became part of our every day life. Extrapolating from known physical laws, Feynman argued it was possible (with, say, an electron beam that could form lines in materials) to write all 25,000 pages of the 1959 edition of the Encyclopedia Britannica in an area the size of a pin head! He calculated that a million such pinheads would amount to an area of about a 35 page pamphlet. Feynman further added "All of the information which all of mankind has ever recorded in books can be carried in a pamphlet in your hand–and not written in code, but a simple reproduction of the original pictures, engravings and everything else on a small scale with-out loss of resolution."

And that's just how his talk began. He outlined how, with proper coding, all the world's books at the time actually could be stored in something the size of a dust speck, with each of the billions of bits in those books requiring a mere 100 atoms to store. How about building computers using wires, transistors, and other components that were that small? "They could make judgements," Feynman predicted. He discussed about using big tools to make smaller tools suitable for making yet smaller tools, and so on, until researchers had tools sized just right for directly manipulating atoms and molecules. Feynman further predicted that we will be able to literally place atoms one by one in

exactly the arrangement that we want. "Up to now," he added, "we have been content to dig in the ground to find minerals. We heat them and we do things on a large scale with them, and we hope to get a pure substance with just so much impurity, and so on. But we must always accept some atomic arrangement that nature gives us...I can hardly doubt that when we have some control of the arrangement of things on a small scale we will get an enormously greater range of possible properties that substances can have, and of different things that we can do."

Repeatedly, during this famous lecture, Feynman reminded his audience that he wasn't joking. "I am not inventing anti-gravity, which is possible someday only if the laws are not what we think," he said. "I am telling you what could be done if the laws are what we think; we are not doing it simply because we haven't yet gotten around to it."

1.3 History of nanomaterials**:**

The history of nanomaterials began immediately after the big bang when Nanostructures were formed in the early meteorites. Nature later evolved many other Nanostructures like seashells, skeletons etc. Nanoscaled smoke particles were formed during the use of fire by early humans.

STONE AGE	~2,000,000 BC
• Lower Paleolithic	1,500,000 BC
• Upper Paleolithic	40,000 BC
• Neolithic *(Aceramic)*	8,500 BC
• Neolithic *(Ceramic)*	7,000 BC
(End of Ice Age)	8,000 BC
CHALCOLITHIC	4,500 BC
BRONZE AGE	3,200 BC
IRON AGE	1,200 BC
• Cement Age	200 BC
• Steel Age	1,850 AD
SILICON AGE	1,950 AD
NEW - MATERIALS AGE	1990 AD….
• Nanomaterials	

The scientific story of nanomaterials however began much later. One of the first scientific report is the colloidal gold particles synthesised by Michael Faraday as early as 1857.[2] Nanostructured catalysts have also been investigated for over 70 years.[3] By the early 1940's, precipitated and fumed silica nanoparticles were being manufactured and sold in USA and Germany as substitutes for ultrafine carbon black for rubber reinforcements. Nanosized amorphous silica particles have found large-scale applications in many every-day consumer products, ranging from non-diary coffee creamer to automobile tires, optical fibers and catalyst supports. In the 1960s and 1970s metallic nanopowders for magnetic recording tapes were developed.[4] In 1976, for the first time, nanocrystals produced by the now popular inert- gas evaporation technique was published by Granqvist and Buhrman.[5] Recently it has been found that the Maya blue paint is a nanostructured hybrid material.[6] The origin of its color and its resistance to acids and biocorrosion are still not understood but studies of authentic samples from Jaina Island show that the material is made of needle-shaped

palygorskite (a clay) crystals that form a superlattice with a period of 1.4 nm, with intercalcates of amorphous silicate substrate containing inclusions of metal (Mg) nanoparticles. The beautiful tone of the blue color is obtained only when both these nanoparticles and the superlattice are present, as has been shown by the fabrication of synthetic samples.

Probably most celebrated historical comment on the advancement of nanomaterials was the public speculation by physicist Richard Feynman in 1959 at a meeting of the American Physical Society about the effects of manipulating minuscule bits of condensed matter in his famous talk "There's plenty of room at the bottom", that we have discussed in the preceding chapter.

Today nanophase engineering expands in a rapidly growing number of structural and functional materials, both inorganic and organic, allowing to manipulate mechanical, catalytic, electric, magnetic, optical and electronic functions. The production of nanophase or cluster-assembled materials, is usually based upon the creation of separated small clusters which then are fused into a bulk-like material or on their embedding into compact liquid or solid matrix materials. E.g. nanophase silicon, which differs from normal silicon in physical and electronic properties, could be applied to macroscopic semiconductor processes to create new devices. For instance, when ordinary glass is doped with quantized semiconductor "colloids," it becomes a high-performance optical medium with potential applications in optical computing.

1.4 What are nanomaterials?**:**

1.4.1 Classification of Nanostructured Materials:
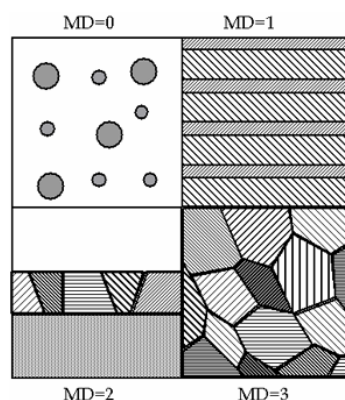
Figure 2.3: Definition of nanomaterials following Siegel[7]

Nanomaterials are materials which are characterised by an ultra fine grain size (< 50 nm) or by a dimensionality limited to 50 nm. Nanomaterials can be created with various modulation dimensionalities as defined by Richard W. Siegel: zero (atomic clusters, filaments and cluster assemblies), one (multilayers), two (ultrafine-grained overlayers or buried layers), and three (nanophase materials consisting of equiaxed nanometer sized grains) as shown in the above figure 2.3.

Nanomaterials consisting of nanometer sized crystallites or grains and interfaces may be classified according to their chemical composition and shape (dimensionality), as discussed above. According to the shape of the crystallites or grains we can broadly classify nanomaterials into four categories:

1. clusters or powders (MD=0)

2. Multilayers (MD=1)

3. ultrafine grained overyaers or buried layers (where the layer thickness or the rod-diameters are <50 nm) (MD=2)

4. nanomaterials composed of equiaxed nanomter-sized grains (MD=3)
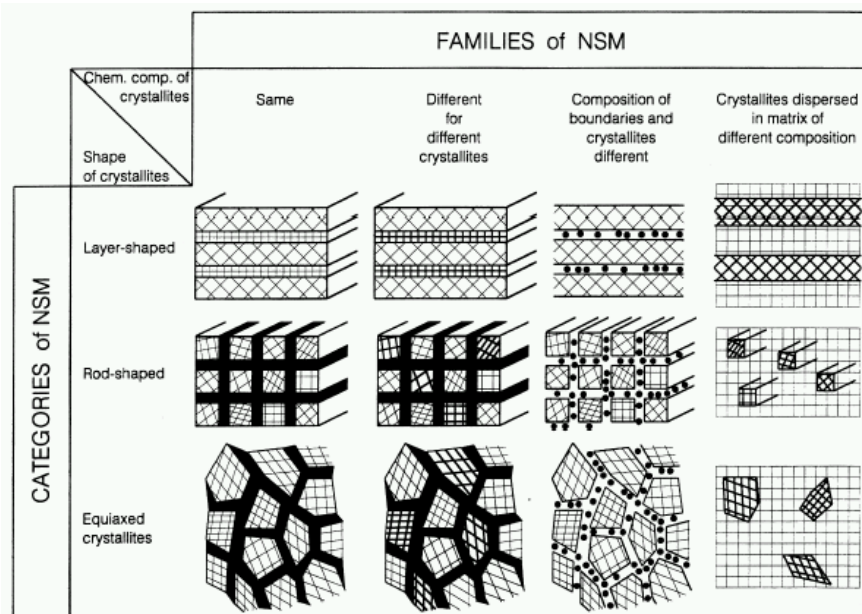
Figure 2.4: Classification schema for nanomaterials according to their chemical composition and the dimensionality (shape)of the crystallites (structural elements) forming the nanomaterial. The boundary regions of the first and second family of nanomaterials are indicated in black to emphasize the different atomic arrangements in

the crystallites and in the boundaries. The chemical composition of the (black) boundary regions and the crystallites is identical in the first family. In the second family, the (black) boundaries are the regions where two crystals of different chemical composition are joined together causing a steep concentration gradient.

The latter three categories can be further grouped into four families as shown in figure 2.4.

- In the most simple case (first family in the fig.2.4), all grains and interfacial regions have the same chemical composition. Eg. Semicrystalline polymers (consisting of stacked lamellae separated by non-crystalline region), multilayers of thin film crystallites separated by an amorphous layer (a-Si:N:H/nc-Si)[8]etc.

- As the second case, we classify materials with different chemical composition of grains. Possibly quantum well structures are the best example of this family.

- In the third family includes all materials that have a different chemical composition of its forming matter (including different interfaces) eg. Ceramic of alumina with Ga in its interface.[9]

- The fourth family includes all nanomaterials formed by nanometer sized grains (layers, rods or equiaxed crystallites)dispersed in a matrix of different chemical composition. Precipitation hardened alloys typically belong to this family. Eg. Nanometer sized Ni_3Al precipitates dispersed in a nickel matrix- generated by annealing a supersaturated Ni-Al solid solution- are an example of such alloys. Most high-temperature materials used in modern jet engines are based on precipitation-hardened Ni_3Al/Ni alloys.

A large part of this definition has been described in an article by Gleiter.[10,11]

1.4.2 Why so much interest in nanomaterials?:

These materials have created a high interest in recent years by virtue of their unusual mechanical, electrical, optical and magnetic properties. Some examples are given below:

- Nanophase *ceramics* are of particular interest because they are more ductile at elevated temperatures as compared to the coarse-grained ceramics.

- Nanostructured *semiconductors* are known to show various non-linear optical properties. Semiconductor Q-particles also show quantum confinement effects which may lead to special properties, like the luminescence in silicon powders and silicon germanium quantum dots as infrared optoelectronic devices. Nanostructured *semiconductors* are used as window layers in solar cells.

- Nanosized *metallic powders* have been used for the production of gas tight materials, dense parts and porous coatings. Cold welding properties combined with the ductility make them suitable for metal-metal bonding especially in the electronic industry.

- Single nanosized *magnetic particles* are mono-domains and one expects that also in magnetic nanophase materials the grains correspond with domains, while boundaries on the contrary to disordered walls. Very small particles have special atomic structures with discrete electronic states, which give rise to special properties in addition to the super-paramagnetism behaviour. Magnetic nano-composites have been used for mechanical force transfer (ferrofluids), for high density information storage and magnetic refrigeration.

- Nanostructured *metal clusters and colloids* of mono- or plurimetallic composition have a special impact in catalytic applications. They may serve as precursors for new type of heterogeneous catalysts (Cortex-catalysts) and have been shown to offer substantial advantages concerning activity, selectivity and lifetime in chemical transformations and electrocatalysis (fuel cells). Enantioselective catalysis were also achieved using chiral modifiers on the surface of nanoscale metal particles.

- Nanostructured *metal-oxide thin films* are receiving a growing attention for the realisation of gas sensors (NO_x, CO, CO_2, CH_4 and aromatic hydrocarbons) with enhanced sensitivity and selectivity. Nanostructured metal-oxide (MnO_2) find application for rechargeable batteries for cars or consumer goods. Nano-*crystalline silicon films* for highly transparent contacts in thin film solar cell and *nano-structured titanium oxide porous films* for its high transmission and significant surface area enhancement leading to strong absorption in dye sensitized solar cells.

- *Polymer based composites* with a high content of inorganic particles leading to a high dielectric constant are interesting materials for photonic band gap structure produced by the LIGA.

1.4.3 Influence on properties by "nano-structure induced effects":

For the synthesis of *nanosized particles* and for the fabrication of *nanostructured materials,* laser or plasma driven gas phase reactions, evaporation-condensation mechanisms, sol-gel-methods or other wet chemical routes like inverse micelle preparation of inorganic clusters have been used, that will be discussed later. Most of these methods result in very fine particles which are more or less agglomerated. The powders are amorphous, crystalline or show a metastable or an unexpected phase, the reasons for which is far from being clear. Due to the small sizes any surface coating of the nano-particles strongly influences the properties of the particles as a whole. Studies have shown that the crystallisation behaviour of nano-scaled silicon particles is quite different from micron-sized powders or thin films. It was observed that tiny polycrystallites are formed in every nano-particle, even at moderately high temperatures.

Roughly two kinds of "*nano-structure induced effects*" can be distinguished:

- First the *size effect*, in particular the *quantum size effects* where the normal bulk electronic structure is replaced by a series of discrete electronic levels,

- and second the *surface or interface induced effect*, which is important because of the enormously increased specific surface in particle systems.

While the *size effect* is mainly considered to describe physical properties, the *surface or interface induced effect*, plays an eminent role for chemical processing, in particular in connection with heterogeneous catalysis. Experimental evidence of the *quantum size effect* in small particles has been provided by different methods, while the *surface induced effect* could be evidenced by measurement of thermodynamic properties like vapour pressure, specific heat, thermal conductivity and melting point of small metallic particles. Both types of size effects have also been clearly separated in the optical properties of metal cluster composites. Very small semiconductor (<10 nm),

or metal particles in glass composites, and semiconductor/polymer composites show interesting quantum effects and non-linear electrical and optical properties.

The numerous examples, which are not complete, by far, indicate that these materials will most probably gain rapidly increasing importance in the near future. In general, properties, production and characterisation methods and their inter-relations are however not yet satisfactorily understood. Hence, efforts need to be made to enable the directed tailoring of nanophase, nanoscopic and nanocomposite materials needed for future technical and industrial applications.

1.5 Some present and future applications of nanomaterials

Here we list some of the present and future applications of nanomaterials that has been reported in recent literature:

1.5.1 In electronics & optoelectronics:

'nanophosphors' for affordable high-definition television and flat panel displays

electroluminescent nanocrystalline silicon, opening the way for optoelectronic chips and possibly new type of color displays

efficient light-emitting diodes based on quantum dots with a voltage-controlled, tunable output color

powder or plastic layers using nanoparticles as an active scattering medium

optical switches and fibers based on nonlinear behavior

transparent conducting layers

three-dimensional optical memories

1.5.2 Electronics:

materials for the next-generation computer chips

single-electron tunneling transistors using nanoparticles as quantum dots

efficient electrical contacts for semiconductor devices

electrically conducting nanoceramics

capacitive materials for, e.g., dynamic random access memories (DRAM)

1.5.3 Magnetic Applications:

magnetic memories based on materials with a high coercivity

magnetorestrictive materials, important for shielding components and devices

soft magnetic alloys such as Finemet

resistors and varistors (voltage-dependent resistors)

high-temperature superconductors using nanoparticles for flux pinning

1.5.4 In optics

graded refractive index (GRIN) optics: special plastic lenses

anti-fogging coating for spectacles and car windows

inexpensive colored glasses and optical filters

1.5.5 In energy storage:

novel solar cells, such as the Gratzel cell based on TiO_2 materials

window layers in classical solar cells utilizing the increased band gap due

high energy density (rechargeable) batteries

smart windows based on the photochrome effect or electrical magnetic orientation effects

better thermal or electrical insulation materials, again using the higher gap

nanocrystalline hydrogen storage materials

magnetic refrigerators from superparamagnetic materials

1.5.6 In Gas sensing devices:

gas sensors for No_x, So_x, CO, CO_2, CH_4 and aromatic hydrocarbons

UV sensors and robust optical sensors based on nanostructured silicon carbide (SiC)

smoke detectors

ice detectors

ice detectors on aircraft wings

1.5.7 Protection coatings:

cost-effective corrosion protection materials

elimination of pollutants in catalytic converters utilising the large surface area of nanomaterials

scratch-resistance top-coat using hybrid nanocomposite materials

1.5.8 Medical appplications:

longer-lasting medical implants of biocompatible nanostructured ceramic and carbides

bio-compatible coating for medical applications.

magnetic nanoparticles for hyperthermia

controlled drug release and drug delivery

1.5.9 Catalysis:

photocatalyst air and water purifiers

better activity, selectivity and lifetime in chemical transformations and fuel cells

precursors for a new type of catalyst (Cortex-catalysts)

stereoselective catalysis using chiral modifiers on the surface of metal nanoparticles

Table 1: **Some typical properties of nano-structured materials and possibilities of future applications**

Property	*Application*

Bulk

Single magnetic domain	Magnetic recording
Small mean free path of electrons in a solid	Special conductors
Size smaller than wavelength	Light or heat absorption, Scattering
High & selective optical absorption of metal particles	Colours, filters, solar absorbers, photovoltaics, photographic material, phototropic material
Formation of ultra fine pores due to superfine agglomeration of particles	Molecular Filters
Uniform mixture of different kinds of superfine particles	R&D of New Materials
Grain size too small for stable dislocation	High strength and hardness of metallic materials

Surface/ Interface

Large specific surface area	Catalysis, sensors
Large surface area, small heat capacity	Heat-exchange materials Combustion Catalysts
Lower sintering temperature	Sintering accelerators
Specific interface area, large boundary area	Nano-structured materials
Superplastic behaviour of ceramics	ductile ceramics
Cluster coating and metallization	Special resistors, temperature sensors
Multi-shell particles	Chemical activity of catalysts Tailored Optical elements

Table.2 Some examples of present and potential applications with significant technological impact:[12]

Technology	Present Impact	Potential Impact
Dispersions and Coatings	Thermal barriers	Enhanced thermal barriers
	Optical (visible and UV) barriers	Multifunctional nanocoatings
	Imaging enhancement	Fine particle structure
	Ink-jet materials	Super absorbant materials (Ilford paper)
	Coated abrasive slurries	Higher efficiency and lower contamination
	Information-recording layers	Higher density information storage
High Surface Area	Molecular sieves	Molecule-specific sensors
	Drug delivery	Particle induced delivery
	Tailored catalysts	Energy storage (fuel cells, batteries)
	Absorption/desorption materials	Grätzel-type solar cells, Gas sensors
Consolidated Materials	Low-loss soft magnetic materials	Superplastic forming of ceramics Materials
	High hardness, tough WC/Co cutting tools	Ultrahigh-strength, tough structural materials
	Nanocomposite cements	Magnetic refrigerants Nanofilled polymer composites Ductile cements
Bio-medical aspects	Functionalised nanoparticles	Cell labelling by fluorescent nanoparticles Local heating by magnetic nanoparticles
Nanodevices	GMR read heads	Terabit memory and microprocessing Single molecule DNA sizing and sequencing Biomedical sensors Low noise, low threshold lasers Nanotubes for high brightness displays

1.6 What about the industries in nanomaterials?

As we discussed in section 2.2, Nanoscale materials are at least a 100-year-old industry. Materials as mundane as the fillers in automotive tires are 10- to 500-nm particles of carbon black, graded by size. Large chemical companies like Cabot[13] and Degussa-Hüls[14] are the leading producers in this mature 6 million-ton-per-year global carbon black market for tires.

Plans for commercializing nanotechnology range from the development of nanoscale electronics and computing applications to the creation of molecular machines and manufacturing capabilities at the nanometer level. But most companies are busy preparing materials, producing organic, inorganic, and metal nanomaterials. At the present time, most of these companies have limited production capabilities for research-scale or development-scale quantities.

However, they are working with partners or alone to develop new applications for nanomaterials that will undoubtedly have an immense impact on our future life. These applications vary from use in polymers, batteries, electronics, cosmetics, sensors, fuel cells, and catalysis to coatings on metals and computer screens and other displays. Other companies are making nanoparticles for biological applications such as drug delivery, discovery, screening, diagnostics and even cure.

Polymers with nanosized reinforcing particles are in the verge of commercialisation. Compared with traditional fillers, nanocomposites generally offer enhanced physical features--such as increased stiffness, strength, barrier properties, and heat resistance, without loss of impact strength and with improved aesthetics--in a very broad range of common thermoplastics and thermosets. And because particle sizes are on the order of the wavelengths of visible light, they do not change optical properties such as transparency that is often required in these applications. Nanosized reinforcements will account for only 3 to 5% of this total, or tens of thousands of tons, since optimum benefits are achieved at this low level of incorporation. The most cost-effective nanomaterials available commercially today are layered, often chemically modified, clays consisting of nanometer-thick platelets of up to 1,000 nm in diameter.

By 2010, market research firm Bin & Associates,[15] estimates that global markets for nanoclays will be in the hundreds of millions of dollars, with nanocomposite markets valued 15 to 30 times higher. Two companies active in nanoclay development and

commercialization are Nanocor, Illinois (USA) based subsidiary of Amcol International,[16] and Southern Clay Products, Texas-based subsidiary of the U.K.'s Laporte.[17]

Most major polymer companies are exploring nanocomposite technologies. Plastics compounder RTP,[18] Minnesota (USA) has commercialized nylon nanocomposites for film and sheet applications, and Triton Systems, Massachusetts (USA) works in packaging. Dow Chemicals[19] and Magna International are developing production technology for automotive applications under the government's Advanced Technology Program. In Japan, Ube Industries[20] and Unitika[21] are commercial producers of nylon nanocomposites. Tetrapak (Switzerland) has developed and is producing commercially, improved silica coatings as diffusion barrier for their packaging products by nanostructuring the coatings.

Hybrid Plastics based in California (USA) has a technology for producing polyhedral oligomeric silsesquioxanes--essentially chemically modified nanoscale particles of silica--that can be incorporated into plastics. The company says it can manufacture bulk amounts and is collaborating with plastics producers and users, including the American Air Force.

The first 10 years of nanocomposite development were filled with frustrations: the demonstration of fantastic performance characteristics and yet inconsistent performance replication, high technical barriers, and exorbitant costs to achieve good deagglomeration and dispersion of the nanosized reinforcements. There are still some further technical barriers to rapid commercialisation can be achieved but there are reports that nanocomposite trials by several large technology companies have met full performance expectations. Few of these applications are close to commercialization, meaning they will be commercially available within the next few years. Hence in the next decade we shall be able to harness the fruits of the tremendous progress that have been achieved in material properties upon the utilisation of nanomaterials in practical scales.

1.6.1 Fullerenes and nanotubes

Carbon nanotube polymer composites are gaining interest as well. According to Principia Partners,[22] Pennsylvania (USA) the market for these composites will reach about 80,000 tons by 2009. The market research firm says interest in nanocomposites

is "keen, but uncertain," due to embryonic process and product development and other economic questions.

RTP (USA) offers nanotube-filled polymer compounds--based on nylon, polycarbonate, and other engineering polymers--that maintain the resins' key physical properties but have uniform surface conductivity. These materials avoid static charge buildup and are suitable for electronic wafer processing, disk drive components, and clean room applications. According to RTP these compounds are also being actively considered for automotive applications where static discharge is important.

Since 1990, Materials & Electrochemical Research (MER),[23] Tucson, has managed rights to fullerene production technology based on work by physics professor Donald R. Huffman at the University of Arizona and Wolfgang Krätschmer at Max Planck Institute for Nuclear Physics, in Heidelberg, Germany. MER has bulk production capabilities of up to 30 kg per day, a joint venture development effort with Mitsubishi (Japan), and has also licensed production technology to Honjo Chemicals in Japan.

Applications for fullerenes and nanotubes are emerging that look like they will reach commercialization and used in large quantities soon. An area that appears to have a great promise is in electrochemical electrodes, primarily in the battery industry. Another near-term application is using nanotubes in organic fibers, such as nylon and polyesters, where a very small amount of these nanotubes increases fiber strength and stiffness and also makes them conductive.

Hyperion Catalysis, in Massachusetts (USA) produces carbon nanotubes that it calls graphite fibrils. The fibrils can be used as a conductive filler in plastics and coatings and, after functionalization, as a catalyst support. GE Plastics (USA) has used Hyperion's technology to introduce a conductive resin for electrostatically painted molded parts, such as for cars, and for business equipment, such as computers, to avoid electrostatic charge buildup.

1.6.2 Biological applications

Companies are working with nanoparticles based on other materials as genetic or biological probes in drug discovery, screening, diagnostics and cure. Some others are looking at drug delivery.

One of the most straightforward approaches is nanocrystalline drugs. NanoSystems, owned by Irish drug company Elan,[24] uses its technology for drugs that have poor water solubility, stabilizing the drug nanoparticles with polymers on their surfaces. Nanosphere (USA) has a related technology--applicable, but not limited to, controlled-release drugs--that applies polymer, ceramic, metal, or biomaterial "nanosphere" coatings on particles.

Quantum Dot,[25] California (USA) makes semiconductor-based nanoparticles. The luminescent dots have hydrophillic surfaces so they can work in aqueous solution. They can be used with almost any optical detection method and will compete with traditional methods such as dyes. The quantum dots can be attached to DNA, to proteins, to various sorts of biological affinity molecules such as antibodies, or put within different sorts of microscopic carrier particles for colorimetric bar coding purposes.

Already on the market are 1.4-nm derivatized or silver-coated gold particles that are produced by Nanoprobes, New York (USA). Its nanoparticles can be used as chemically specific labeling reagents and immunoassay probes in light and electron microscopy, molecular biology, and cellular studies. Solaronix (Switzerland) has been producing and have commercialised TiO_2 nanoparticle based solar cells since a few years now.[26] And magnetic particles, such as those made of iron and activated carbon by San Diego-based FeRx,[27] can be carriers for targeted drug delivery. Metalor (Switzerland), as many other companies worldwide, supply wide ranging gold, silver, and other metal alloy colloidal formulations of different sizes.

Mach 1, based in Pennsylnavia (USA) plans to produce magnetic iron oxide for biological applications. The company has been making 3-nm iron oxide since 1992 and selling it for catalyst and solid rocket propellant applications. Volumes are still small if measured in tens of thousands of dollars and bordering between pilot and semi-commercial scale.

1.6.3 Metals and inorganics

Vapor-phase production is among the most commonly used processes, along with other combustion, sol-gel, and mechanochemical methods at different companies. Mach 1 uses a microwave plasma process that allows for making and coating inorganic nanoparticles for polymer, ceramic, and metal nanocomposites.

Nanophase Technologies,[28] Illinois uses vapor synthesis and has particle encapsulation technology as well. One of a very few public nanomaterials firms, it reported $1.7 million in revenues and a loss of $2.7 million for the first six months of 2000. Its largest volume product--at hundreds of tons per year--is zinc oxide, which it supplies to BASF,[29] Schering-Plough,[30] and others for use as a sunscreen and fungicide in cosmetics and personal care products. Nanophase anticipates becoming profitable by late 2001.

Nanophase also sells other inorganic nanomaterials for catalyst and coatings applications. In coatings, applications range from ophthalmic plastic lenses to vinyl flooring and applications where abrasion resistance is a particular interest. Nanophase has also developed thermal spray coatings, specifically metal oxide nanomaterials that is being used by the US Navy to repair worn or eroded metal parts.

Altair Technologies,[31] Nevada (USA) in collaboration with Nanopowder Enterprises,[32] New Jersey (USA) also is working on advanced ceramic coatings for the Office of US Naval Research. Altair's primary product is nanocrystalline titanium dioxide. Its plans are to produce up to 1,500 tons per year as markets develop.

The major markets for nanoscale titanium dioxide--as a pigment, UV protectant, or material in surface coatings--total about 4,000 tons a year at about $20,000 to $25,000 per ton, according to Michael Shonstrom, an analyst of Shonstrom Research Associates.[33] In addition to small nanotechnology companies, suppliers include the traditionally large chemical companies.

Over the next couple of years, the nanomaterials area will grow significantly. Once the markets for nanomaterials start to become significant in size, which justifies the investment in larger scale production, major companies will move very quickly into this space and drive the costs down. It's just a matter of time to see this revolution begin. Already today companies are producing a wide variety of nanomaterials ranging from metal and metal oxide powders, fullerines, carbon nanotubes, polymer nanofibers, clays for polymer composites, nanoparticles for drug delivery, nanocrystalline drugs, semiconductor Q dots, amongst others. A survey of the companies producing nanomaterials today is given in Appendix II.

1.7 What are the fundamental issues in nanomaterials?

The fundamental issues in this domain of nanomaterials are:

(1) ability to control the scale (size) of the system,

(2) ability to obtain the required composition -

not just the average composition - but details such as defects, concentration gradients, etc.,

(3) ability to control the modulation dimensionality,

(4) during the assembly of the nano-sized building blocks, one should be able to control the extent of the interaction between the building blocks as well as the architecture of the material itself.

More specifically the following issues have to be considered for the future development of nanomaterials:

- Development of synthesis and/or fabrication methods for raw materials (powders) as well as for the nanostructured materials.

- Better understanding of the influence of the size of building blocks in nano structured materials as well as the influence of microstructure on the physical, chemical and mechanical properties of this material.

- Better understanding of the influence of interfaces on the properties of nano-structured material.

- Development of concepts for nanostructured materials and in particular their elaboration.

- Investigation of catalytic applications of mono- and plurimetallic nanomaterials

- Transfer of developed technologies into industrial applications including the development of the industrial scale of synthesis methods of nanomaterials and nanostructured systems.

In the following chapters we will review the various developments that have been revolutionising the application of nanomaterials. We will attempt to correlate the improvements in the material properties that are achieved due to the fine microstructures arising from the size of the grains and/or dimensionality.

2 ATOMS, CLUSTERS AND NANOMATERIALS

| **atoms** | **molecules** | **cluster** | **nanocrystallites** |
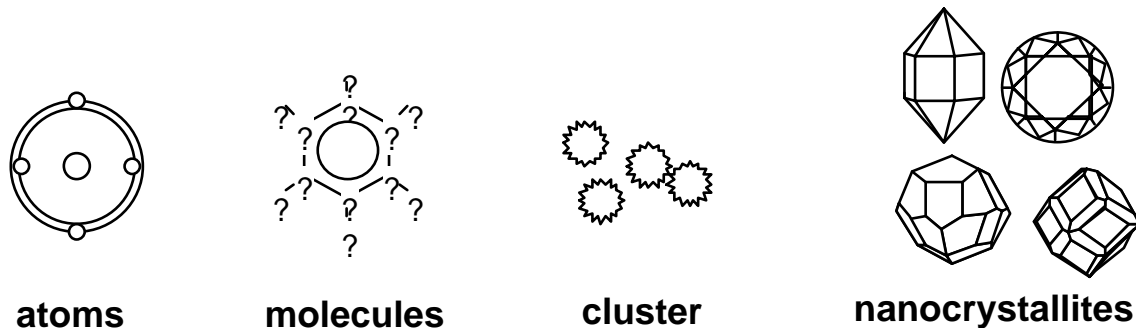
Figure : Schematic representation of various states of matter

2.1 Introduction

At the beginning of last century, increasing attention was focused on the physical chemistry of colloidal suspensions. By referring to them as "the world of neglected dimensions", Oswald was the first to realize that nanoscale particles should display novel and interesting properties largely dependant on their size and shape.[34] However, it is only in the last two decades that significant interest has been devoted to inorganic particles consisting of a few hundred or a few dozen atoms, called clusters. This interest has been extended to a large variety of metals and semiconductors and is due to the special properties exhibited by these nanometer-sized particles, which differ greatly from those of the corresponding macrocrystalline material.

Matter that is constituted of atoms and molecules as such, has been widely classified and satisfactorily explained. However, an ensemble of atoms, or molecules forming the so-called *'Clusters'* are far from being properly understood. Elemental clusters are held together by various forces depending on the nature of the constituting atoms:

- Inert gas clusters are weakly held together by van-der-waals interactions, eg. $(He)_n$

- Semiconductor clusters are held with strong directional covalent bonds, eg. $(Si)_n$

- Metallic clusters are fairly strongly held together by delocalised non-directional bonding, eg. $(Na)_n$
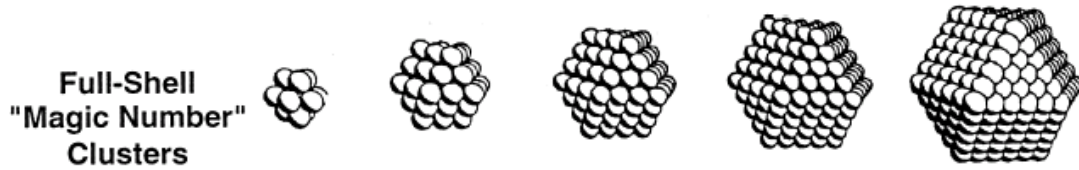
No. Of Shells	1	2	3	4	5
No. of atoms	M_{13}	M_{55}	M_{147}	M_{309}	M_{561}
Percentage of atoms	92%	76%	63%	52%	45%

Table: Idealized representation of hexagonal close packed full-shell 'magic number' clusters.[35] Note that as the number of atoms increases, the percentage of surface atoms decreases.
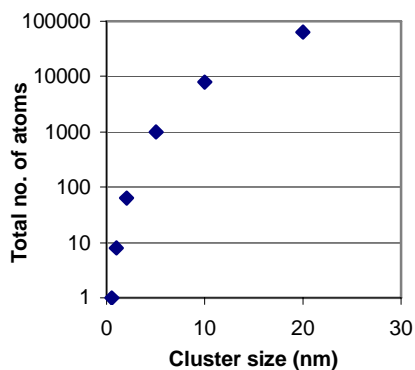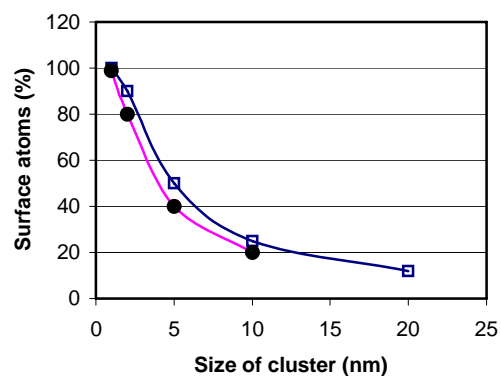
(1)   **(2)**

Figure: (1) Total Number of atoms with size of the cluster.

(2) Number of surface atoms for a hypothetical model sphere of diameter 0.5 nm and density 1000 Kgm^{-3} with a mass of 6.5×10^{-26} Kg occupying a volume of about 6.5×10^{-29} m^3 with a geometrical cross-section of 2×10^{-19} m^2 (in terms of atomic mass the sphere is considered to have a mass of 40 amu, where 1 amu = 1.67×10^{-27} Kg). Calculated by (a) considering dense structures (Square),[36] and (b) method suggested by Preining (dark circle).[37]

Either elemental clusters or a mixture of clusters of different elements constitute the vast expanding field of materials sciences called '**nanomaterials**'. One has to be clear right at this stage that clusters are not a fifth state of matter, as sometimes believed, but they are simply intermediate between atoms on one hand, and solid or liquid state of matter on the other, with widely varying physical and chemical properties.

Depending on the number of atoms forming the cluster determines the percentage of atoms that are exposed on the surface of the cluster. An example of such an ensemble of metal atoms show the decreasing number of surface atoms with increasing size of the cluster as shown in fig: . When an ensemble of atoms add up to form a few nanometer sized clusters, they form what we call '***nanoparticles***', since only a few atoms forming clusters are called '***molecular clusters***'. Agglomeration of a few atoms have been studied in great details by physicists working with molecular beams. Today, the mystery related to larger ensemble of atoms (in other words '***nanomaterial***') are getting clearer due to active research being carried over across the world over the last decade or two.

Size	Cross section	Mass	No. Of molecules	Fraction of molecules at surface (%)	
(nm)	(10^{-18} m^2)	(10^{-25} Kg)		a	b
0,5	0,2	0,65	1		
1	0,8	5,2	8	100	99
2	3,2	42	64	90	80
5	20	650	1000	50	40
10	80	5200	8000	25	20
20	320	42000	64000	12	

Table: Idealized representation of the variation of cross section, total mass, number of molecules and the effective surface atoms in clusters. Note (a) considering dense structures (Square),[36] and (b) method suggested by Preining (dark circle).[37]

In the table, we see that the smaller particles contain only a few atoms, practically all at the surface. As the particle size increases from 1-10 nm, cross-section increases by a factor of 100 and the mass number of molecules by a factor of 1000. Meanwhile, the proportion of molecules at the surface falls from 100% to just 25%. For particles of 20nm size, a little more than 10% of the atoms are on the surface!

Of course this is an idealized hypothetical case. If particles are formed by macro molecules (that are larger than the present example), number of molecules per particle will decrease and their surface fraction increase. The electronic properties of these ensemble of atoms or molecules will be the result of their mutual interactions so that the overall chemical behaviour of the particles will be entirely different from the individual atoms or molecules that they are constituted of. They will also be different from their

macroscopic bulk state of the substance in question under the same conditions of temperature and pressure.

Size (nm)	Surface area ($m^2\,mol^{-1}$)	Surface energy ($J\,mol^{-1}$)
1	1.11×10^9	2.55×10^4
2	5.07×10^8	1.17×10^4
5	2.21×10^8	5.09×10^3
10	1.11×10^8	2.55×10^3
20	5.07×10^7	1.17×10^3
10^2	1.11×10^7	2.55×10^2
10^3 (1 μm)	1.11×10^6	2.55×10

Table: Particle size, surface area and surface energy of CaCo$_3$.[38] (the surface energy of bulk CacO3 (calcite) is 0.23 Jm^{-2}.)

The idea of tailoring properly designed atoms into agglomerates has brought in new fundamental work in the search for novel materials with uncharacteristic properties. Among various types of nanomaterials, cluster assembled materials represent an original class of nanostructured solids with specific structures and properties. In terms of structure they could be classified in between amorphous and crystalline materials. In fact, in such materials the short-range order is controlled by the grain size and no long-range order exists due to the random stacking of nanograins characteristic of cluster assembled materials. In terms of properties, they are generally controlled by the intrinsic properties of the nanograins themselves and by the interactions between adjacent grains. Cluster assembled films are formed by the deposition of these clusters onto a solid substrate and are generally highly porous with densities as low as about one half of the corresponding bulk materials densities and both the characteristic nanostructured morphology and a possible memory effect of the original free cluster structures are at the origin of their specific properties.[39] From recent developments in the cluster source technologies (thermal, laser vaporisation and sputtering),[40,41] it is now possible to produce intense cluster beams of any materials, even the most refractory or complex systems (bimetallic,[42] oxides and so on), for a wide range of size from a few atoms to a few thousands of atoms.

2.1.1 Melting Point of Gold nanocrystal:

One particular phenomenon of interest is the size-dependent melting point depression in nanomaterials - small particles have a lower melting point than the bulk. The melting of small particles attracted interest long before the early days of modern cluster science.[43] The first attempts at theoretical understanding of the melting of small particles were made within a macroscopic frame-work,[44] using thermodynamic concepts such as surface energy. These analytical models predict a progressive depression of the melting point with decreasing particle size. While this approach is sound for mesoscopic particles with thousands of atoms, its applicability to much smaller clusters (where most if not all atoms are on the surface) is obviously tenuous. When computational resources became available, the melting of specific clusters was treated microscopically using molecular dynamics simulations. Most of this work was for noble gas clusters using a Lennard-Jones potential,[45] but lately metal clusters (sodium,[46] copper,[47] gold,[48] beryllium,[49] lead,[50] indium,[51] and nickel[52]) have been studied as well. These simulations revealed that some features of cluster melting are qualitatively different from bulk melting, such as a difference between the melting and freezing points and the coexistence of "solid" and "liquid" clusters.

The melting point depression is a direct consequence of the increase in the surface atoms with decreasing size, i.e. an increasing proportion of atoms occupy surface or interfacial sites. These atoms are more loosely bound than in the bulk, that facilitates the melting of the nanostructure. These changes in the melting temperature with decreasing size can roughly be described by thermodynamic models. Up to now, three main melting mechanisms have been considered to describe the relation between the melting temperature and the size of particles, resulting in different expressions for the parameter related to the interfacial tension between the solid phase and its environment:

- Homogeneous melting and growth model (HGM)[43]
- Liquid Shell model (LSM)[56,43]
- Liquid Nucleation and growth model (LNG)[53]

The homogeneous melting and growth model considers equilibrium between entirely solid and entirely melted particles, the liquid shell model differing from the HGM in the assumption of the presence of a liquid layer of a certain thickness in equilibrium at the surface of solid particle; while the liquid nucleation and growth model is based on the kinetic consideration that melting starts by the nucleation of liquid layer at the

surface and moves into the solid as a slow process with definite activation energy. Let us take the simple homogeneous melting model and calculate the melting point of a 8 nm gold particle.

Let us revisit the classical thermodynamic description of melting. A theory based on the Laplace equation of the surface and the Gibbs-Duhem equation[54] predicts a melting temperature depression of the form [55]

$$\Delta T = \frac{T_b - T_m}{T_m} \approx \frac{2.T_b}{H_b \rho_{sol} r_{sol}} \frac{\alpha}{r}$$

where T_b, H_b is the latent and ρ_{sol} are the bulk melting temperature, bulk latent heat of fusion and bulk density of the material, and r is the radius of the particle and α is a parameter related to the interfacial tension between the solid phase and its environment. As we discussed above, three main melting mechanisms have been considered to describe the relation between the melting temperature and the size of particles, resulting in different expressions for α.

1. Homogeneous melting:

α in this case is given by

$$\alpha_{HGM} = \gamma_{sv} - \gamma_{lv}(\rho_s/\rho_l)^{\frac{2}{3}}$$

2. Liquid shell model

$$\alpha_{LSM} = \frac{\sigma_{sl}}{1 - \frac{r_0}{r}} + \sigma_{lv}\left(1 - \frac{\rho_s}{\rho_l}\right)$$

where liquid layer thickness is given by r_0.

3. Liquid nucleation growth model

$$\sigma_{sl} < \alpha_{LNG} < \frac{3}{2}\left(\sigma_{sv} - \sigma_{lv}\frac{\rho_s}{\rho_l}\right)$$

σ represents the interfacial tension between solid, liquid, and vapour phases (indexes s, l and v, respectively) and ρ_l is the density of the liquid phase.

These models are related to the different proposed melting mechanisms of nanomaterials. Let us calculate the melting point of gold nanoparticles following the HGM model.

The changes in the melting temperature with decreasing size can roughly be estimated by:

$$\frac{T_b - T_m}{T_m} = \frac{2 \cdot \left[\gamma_{sol} - \gamma_{liq} (\rho_{sol}/\rho_{liq})^{2/3} \right]}{H_b \rho_{sol} r_{sol}}$$

where, T_b and T_m are the melting points of the bulk material and a particle of radius r, respectively, L is the enthalpy of melting, and γ and ρ are the surface tension and density respectively. For example, for a gold particle of diameter 8 nm, T_m is given by:

$$\frac{1336K - T_m}{T_m} = \frac{2 \left[1.38 N.m^{-1} - 1.135 Nm^{-1}(18.40/17.28) \right]}{\left(6.27 \times 10^4 NmKg^{-1} \right)(18400 Kgm^{-3})(\frac{1}{2} \times 8 \times 10^{-9} m)} = 0.0743$$

where all numerical values were taken from the work of Buffat & Borel. This yields a melting point of 1244 K, while the experimental value was approximately 1200 K.[56] A similar phenomenon has been observed for nanocrystals of CdS. The bulk melting point of CdS was reduced from 1678K to 1200K for nanocrystals with a 8 nm diameter.[57]

The fact that the melting points of nanoparticles are always lower than those of the corresponding bulk material is a paradigm supported by extensive experimental data for a large number of systems and by numerous calculations. However, there are some exceptions! Recently Shvartsburg and Jarrold,[58] has demonstrated that tin cluster ions with 10–30 atoms remain solid at 50K *above* the melting point of bulk tin. can change in the nanometer size regime. The cause of the abnormally high melting points of small tin clusters has been related to their heavily reconstructed geometries. The melting points of other reconstructed clusters, like small silicon and germanium species, are also expected to be above their bulk values, as calculated by Lu et. al.,[59] though yet to be proven experimentally. This will have an important technological implication especially in the field of microelectronics.

2.1.2 Vapour pressure of nanocrystals:

The vapor pressure increase in nanocrystals can be given by the following equation:[60]

$$p(r) = p_b \exp\left(\frac{2\gamma M}{r \rho RT} \right)$$

where, p, γ, M, ρ, r, R and T are vapour pressure, surface tension, molecular weight, density, radius, gas constant and temperature, respectively. The vapour pressure of bulk ZnS for example can be calculated by this equation to be[61]

$$p_b = \frac{10^{(10.29-13750/T)}}{760}\left(atm\right)$$

The surface tension of bulk ZnS is known: 1.672 N/m for the (100) spharelite face. Hence the increase in vapour pressure of ZnS crystal with a diameter of 8 nm at 700 °C can be estimated by:

$$\frac{p(r)}{p_b} = \exp\left[\frac{2\times1.672N/m\times97.39g/mol)}{(\frac{1}{2}\times8\times10^{-9}m)(4102000g/m^3)(973K)(8.314Nm/mol.K)}\right] = 11.6$$

Thus the vapour pressure of the 8 nm ZnS nanocrystal is:

$$p(r) = \frac{10^{(10.29-13750/973)}}{760}\times11.6 = 2.2\times10^{-6}atm$$

The surface tension of nanocrystals are much larger than the bulk, due to a weak dilation of the surface.[62] Yet another example can be given for CdS nanocrystals where the surface tension was determined to be 2.50 N/m, while the bulk value is just 0.750 N/m.[57]

3 NANOMATERIAL SYNTHESIS AND PROCESSING
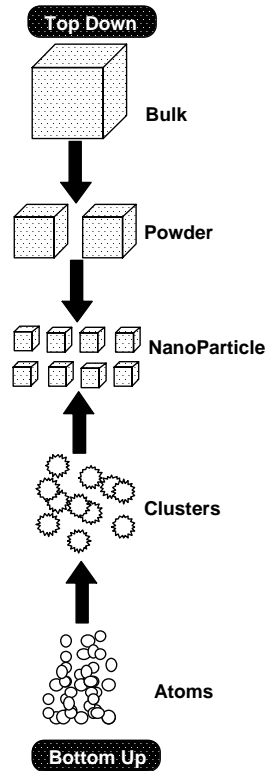
Figure: Schematic representation of the building up of Nanostructures.

Remember we are dealing with very fine structures: a nanometer is a billionth of a meter. This indeed allows us to think in both the 'bottom up' or the 'top down' approaches to synthesize nanomaterials,i.e. either to assemble atoms together or to dis-assemble (break, or dissociate) bulk solids into finer pieces until they are constituted of only a few atoms. This domain is a pure example of interdisciplinary work encompassing physics, chemistry, engineering upto medicine. Thus synthesis processes are as diverse as the application of nanomaterials and hence we will not be able to discuss each and every synthesis processes here. One basic aspect of the synthesis process to remember is that we have to make the material in an useful form or shape that we could process into any particular application. Lets take example of powdery nanomaterial, say gold nanoparticles. Simply these nanoparticles as a powder is practically useless for any application. We either have to consolidate the powder or put these nanoparticles in a composite material- be it glass, polymer, ceramics etc. or

find a way to make a film that could then be used for the desired application. Let's look into further details the methods that we can use for creating useful nanostructures.

3.1.1 Methods for creating nanostructures

There are many different ways of creating nanostructures: of course, macromolecules or nanoparticles or buckyballs or nanotubes and so on can be synthesized artificially for certain specific materials. They can also be arranged by methods based on equilibrium or near-equilibrium thermodynamics such as methods of self-organization and self-assembly (sometimes also called bio-mimetic processes). Using these methods, synthesized materials can be arranged into useful shapes so that finally the material can be applied to a certain application.

```
                    ┌─────────────────────┐
                    │ Methods for Creating │
                    │    nanostructures    │
                    └─────────────────────┘

    Kinetic        Reaction         Artificial      Biomimetic
    Limited        Controlled       Techniques      Techniques
                   Condition
```
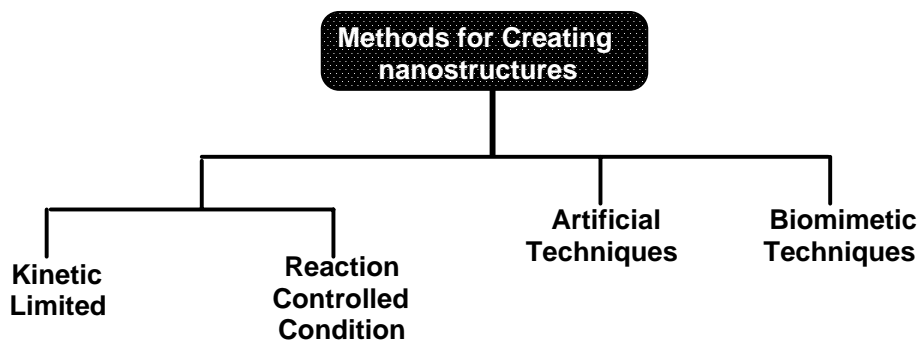
Methods based on non-equilibrium thermodynamics include growth under kinetic limited or reaction controlled conditions, and creation by artificial techniques. Nanotubes, nanoparticles, nanocolumn and some thin films are grown under reaction and kinetic limited conditions. Also lithography of all kinds, beam etching techniques of all kinds, probe microscope techniques, and combinations of these and other techniques form a part of this group. Some of the structures so grown can be thermally and chemically quite stable. Also a large number of them can be grown simultaneously.

For the artificial techniques used in microelectronics, photo-resist based techniques have already achieved better than 0.18 μm spatial resolution and some even predict that it can go down to 0.1 μm or less using special lenses or scanning optical microscope techniques. For even smaller sizes, beam techniques such as electron and ion beam lithography may be used, but they are limited by the beam energy and size, and do have difficulty of going down to subnanometer size. Using probe tip based techniques such as scanning tunnelling and scanning force

microscopes, single atoms and molecules can now be manipulated by the probing tip which can be made single atom sharpness, but the methods of manipulation are very slow and tedious at best.[63] Such methods are best used for making atomic size material structures for scientific studies and for making templates. In general, artificial non-equilibrium methods are relatively slow but can be accelerated by special synthesis techniques and/or by using parallel processing. Biomimetic techniques are being used to make hierarchical structures of nanoparticles.
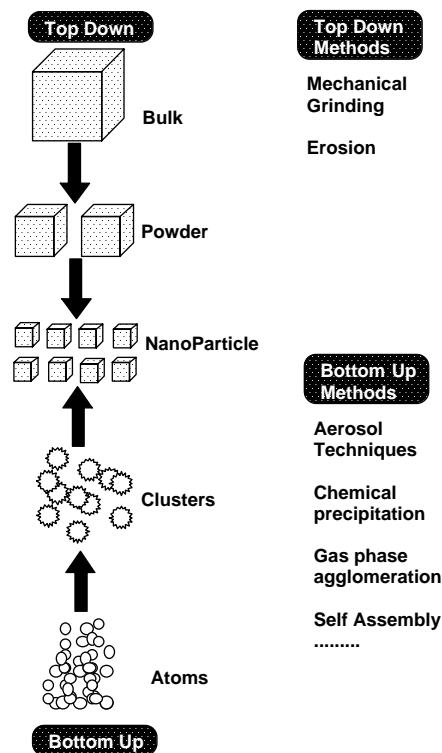
Figure: Schematic representation of the 'bottom up' and top down' synthesis processes of nanomaterials with the popular techniques that are used.

3.2 Processes for producing ultrafine powders

3.2.1 Mechanical grinding:

Mechanical attrition is a typical example of 'top down' method of synthesis of nanomaterials, where the material is prepared not by cluster assembly but by the structural decomposition of coarser-grained structures as the result of severe plastic deformation.[64] This has become a popular method to make nanocrystalline materials because of its simplicity, the relatively inexpensive equipment (on the laboratory scale)

needed, and the applicability to essentially the synthesis of all classes of materials. The major advantage often quoted is the possibility for easily scaling up to tonnage quantities of material for various applications. Similarly, the serious problems that are usually cited are

1) contamination from milling media and/or atmosphere, and
2) the need (for many applications) to consolidate the powder product without coarsening the nanocrystalline microstructure.

In fact, the contamination problem is often given as a reason to dismiss the method, at least for some materials.

Here we will review the mechanisms presently believed responsible for formation of nanocrystalline structures by mechanical attrition of single phase powders, mechanical alloying of dissimilar powders, and mechanical crystallisation of amorphous materials. The two important problems of contamination and powder consolidation will be briefly considered.
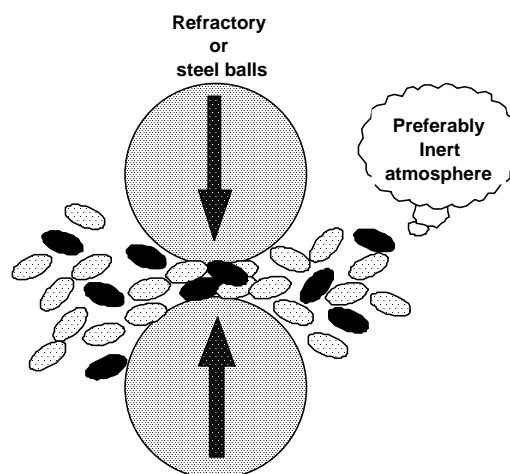
Figure 3.3.1: Schematic representation of the principle of mechanical milling.

Mechanical milling is typically achieved using SPEX (high energy shaker), planetary ball, or tumbler mills. The energy transferred to the powder from refractory or steel balls depends on the rotational (vibrational) speed, size and number of the balls, ratio of the ball to powder mass, the time of milling and the milling atmosphere. Nanoparticles are produced by the shear action during grinding as is obvious from figure below.
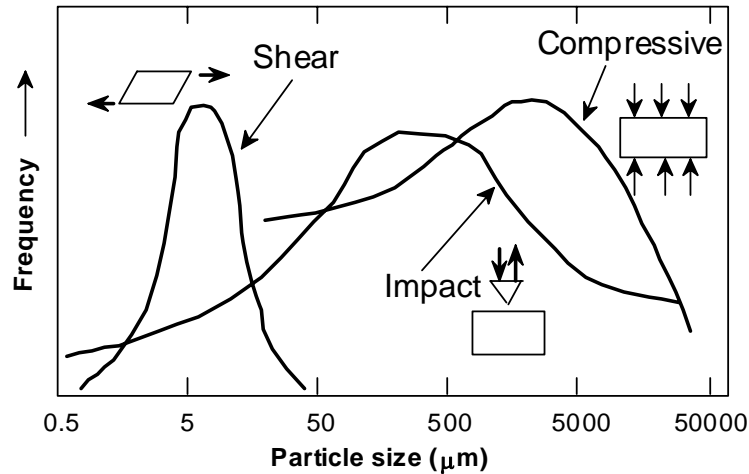
Fig. Size distribution of ground particles due to different grinding actions.

Milling in cryogenic liquids can greatly increase the brittleness of the powders influencing the fracture process. As with any process that produces fine particles, adequate steps to prevent oxidation is necessary. Hence this process is very restrictive for the production of non-oxide materials since then it requires that the milling take place in an inert atmosphere and that the powder particles be handled in an appropriate vacuum system or glove box. This method of synthesis is suitable for producing amorphous or nanocrystalline alloy particles, elemental or compound powders. If the mechanical milling imparts sufficient energy to the constituent powders a homogeneous alloy can be formed. Based on the energy of the milling process and thermodynamic properties of the constituents the alloy can be rendered amorphous by this processing. Generally materials that are harder than the material to be synthesized is used. As is shown below, α-alumina and zirconia are quite frequently used for milling due to their hardness.
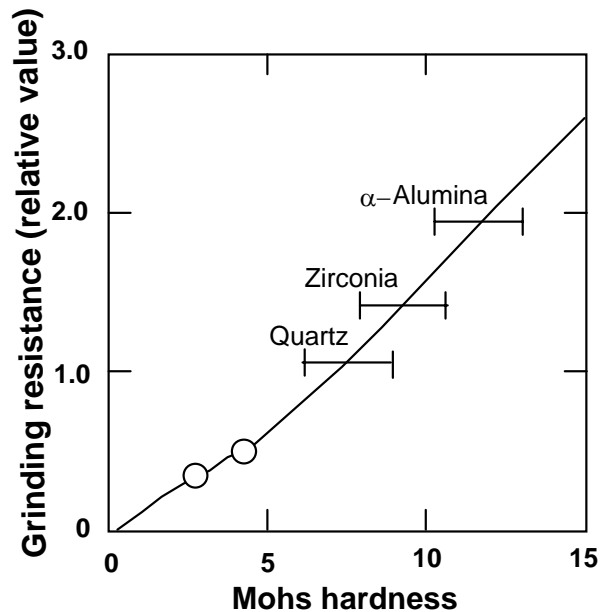
Figure: Grinding resistance Vs. Moh's hardness for typical materials used in mechanical attrition.

3.2.2 Wet Chemical Synthesis of nanomaterials

In principle we can classify the wet chemical synthesis of nanomaterials into two broad groups:

- The top down method: where single crystals are etched in an aqueous solution for producing nanomaterials, eg. The synthesis of porous silicon by electrochemical etching.[65]

- The bottom up method: consisting of sol-gel method, precipitation etc. where materials containing the desired precursors are mixed in a controlled fashion to form a colloidal solution.[66]

3.2.2.1 Sol/gel process:

The sol-gel process, as the name implies, involves the evolution of inorganic networks through the formation of a colloidal suspension (**sol**) and gelation of the sol to form a network in a continuous liquid phase (**gel**). The precursors for synthesizing these colloids consist usually of a metal or metalloid element surrounded by various reactive ligands. The starting material is processed to form a dispersible oxide and forms a sol in contact with water or dilute acid. Removal of the liquid from the sol yields the gel, and

the sol/gel transition controls the particle size and shape. Calcination of the gel produces the oxide.

There are two main ways to synthesize gels at room temperature. The first one consists of a common reaction which occurs in nature where silica chemical species diluted in aqueous solutions condense to lead to the formation of silica network. Such a condensation may occur in various aqueous solutions depending on pH and salt concentration. Different morphologies may be obtained and for silica the most known is the precious "opal" structure.

The other way to produce silica from solution corresponds to a chemical reaction implying metal alkoxides and water in an alcoholic solvent. The first reaction is an hydrolysis which induces the substitution of OR groups linked to silicon by silanol Si-OH groups. As previously, these chemical species may react together to form Si-O-Si (siloxane) bonds which lead to the silica network formation. This phase establishes a 3D network which invades the whole volume of the container. Of course, for these two syntheses the liquid used as solvent to perform the different chemical reactions remains within the pores of the solid network. A gel is thus obtained. This two phases material consists of shaped solid exhibiting specific properties. The typical steps that are involved in sol-gel processing is shown in the schematic diagram below.
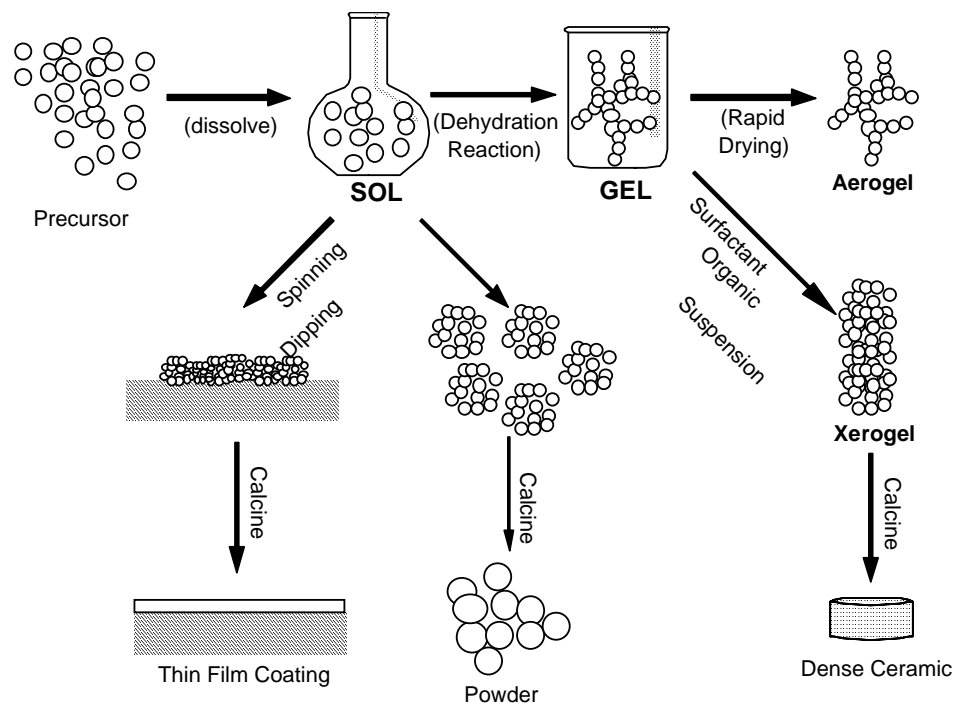
Figure 3.3.2.1: Schematic representation of sol-gel process of synthesis of nanomaterials.

The reactions involved in the sol-gel chemistry based on the hydrolysis and condensation of metal alkoxides $M(OR)_z$ can be described as follows:[67,68]

MOR + H_2O → MOH + ROH (hydrolysis)

MOH + ROM → M-O-M + ROH (condensation)

Sol-gel method of synthesizing nanomaterials is very popular amongst chemists and is widely employed to prepare oxide materials. Eg. The chemistry of a typical sol-gel process for synthesizing Yittria stabilised zirconia nanoparticles include the following steps:

Zr(OH)₄ (slurry) ──→ **Clear Zirconia SOL** ──→ **Yittria Zirconia SOL**
  HNO_3 + $Y(NO)_3$
  Heat +
  Water

Surfactant
(Span 80) +
Organic Liquid
(1,1,1,
trichloroethane)

Spherical YSZ Powder ◄── **Gelled Spheres** ◄── **Solid Spheres of SOL in an Organic Solution**
  Extract   Mixing
  Spheres &
  Calcine
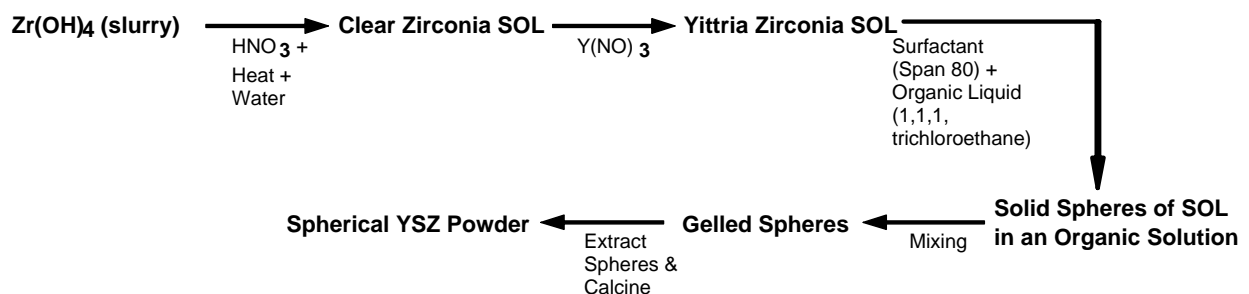
Figure 3.3.2.2: A typical scheme of steps that has to be carried out for the preparation of Yttria stabilized Zirconia nanomaterials by sol-gel process.

Usually the dehydration process of the gel of the oxide causes severe sintering and grain growth as also a damage to the pore structure and a considerable shrinkage of the gel network is generally observed. To preserve the texture of the wet gel, the vapour interface inside the pores are carefully eliminated during the drying process usually above its critical temperature and pressure in an autoclave. The resulting material so formed is called aerogel, which is a highly porous nanostructured material. The interest in this synthesis method arises due to the possibility of synthesizing non-metallic inorganic materials like glasses, glass ceramics or ceramic materials at very low temperatures compared to the high temperature process required by melting glass or firing ceramics. Another good example is the successful preparation of MgO by the aerogel method.[69] It has been found that MgO prepared by aerogel method as compared to the conventional technique (i.e. aqueous precipitation and dehydration) exhibited intrinsically different surface chemistry. The 4 nm crystallites prepared by the aerogel technique were individual spheroid particles compared to the 9 nm crystalline particles prepared by the conventional technique.

3.2.2.2 Liquid solid reactions:

Ultrafine particles are produced by precipitation from a solution, the process being dependent on the presence of the desired nuclei. For example, TiO_2 powders have been produced with particle sizes in the range 70-300 nm from titanium tetraisopropoxide.

The ZnS powders were produced by reaction of aqueous zinc salt solutions with thioacetamide (TAA).[70,71] Precursor zinc salts were chloride, nitric acid solutions, or zinc salts with noncommon associated ligands (i.e., acetylacetonate, trifluorocarbonsulfonate, and dithiocarbamate). The 0.05 M cation solutions were heated in a thermal bath maintained at 70° or 80 °C in batches of 100 or 250 ml. Acid was added dropwise to bring it to a pH of 2. The reaction was started by adding the TAA to the zinc salt solution, with the molar ratio of TAA and zinc ions being set to an initial value of either 4 or 8. In intervals, aliquots were collected from the reacting solution.[72]
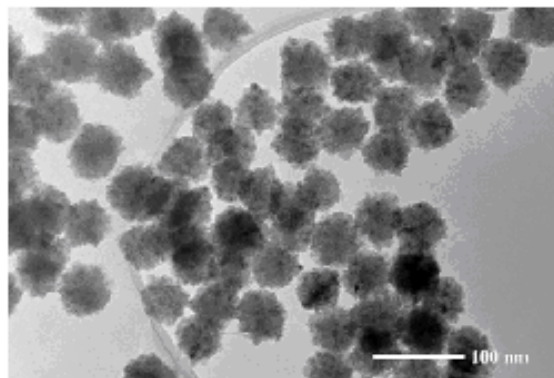
Figure 3.3.2.2: Typical nano sized Zinc sulphide particles prepared by the precipitation process

3.2.3 Gas Phase synthesis of nanomaterials:

This process includes all the gas phase reaction initiated synthesis. We will discuss some of the synthetic processes that have been developed. By no means this list is exhaustive but many of the 'so called' new methods of synthesis are at best simple variations of the known processes. The gas-phase synthesis methods are of increasing interest because they allow elegant way to control process parameters in order to be able to produce size, shape and chemical composition controlled nanostructures. Before we discuss a few selected pathways for gas-phase formation of nanomaterials, some general aspects of gas-phase synthesis needs to be discussed. In

conventional chemical vapour deposition (CVD) synthesis, gaseous products either are allowed to react homogeneously or heterogeneously depending on a particular application.

1) In homogeneous CVD, particles form in the gas phase and diffuse towards a cold surface due to thermophoretic forces, and can either be scrapped of from the cold surface to give nano-powders, or deposited onto a substrate to yield what is called *'particulate films'*.

2) In heterogeneous CVD, the solid is formed on the substrate surface, which catalyses the reaction and a dense film is formed.

In order to form nanomaterials several modified CVD methods have been developed. Gas phase processes have inherent advantages, some of which are noted here:

- An excellent control of size, shape, crystallinity and chemical composition
- Highly pure materials can be obtained
- Multicomonent systems are relatively easy to form
- Easy control of the reaction mechanisms

Most of the synthesis routes are based on the production of small clusters that can aggregate to form nano particles (condensation). Condensation occurs only when the vapour is supersaturated and in these processes homogeneous nucleation in the gas phase is utilised to form particles. This can be achieved both by physical and chemical methods.

3.2.3.1 Furnace:
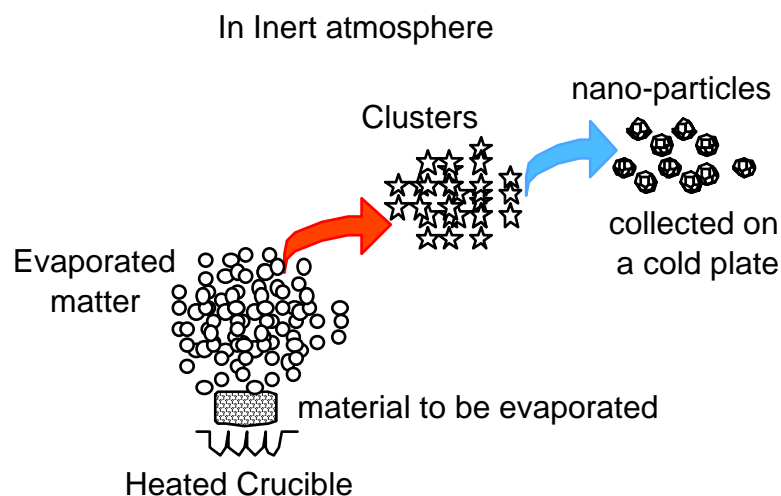
Figure 3.3.1: Schematic representation of gas phase process of synthesis of single phase nanomaterials from a heated crucible.

The simplest fashion to produce nanoparticles is by heating the desired material in a heat-resistant crucible containing the desired material. This method is appropriate only for materials that have a high vapour pressure at the heated temperatures that can be as high as 2000°C. Energy is normally introduced into the precursor by arc heating, electron-beam heating or Joule heating. The atoms are evaporated into an atmosphere, which is either inert (e.g. He) or reactive (so as to form a compound). To carry out reactive synthesis, materials with very low vapour pressure have to be fed into the furnace in the form of a suitable precursor such as organometallics, which decompose in the furnace to produce a condensable material. The hot atoms of the evaporated matter lose energy by collision with the atoms of the cold gas and undergo condensation into small clusters via homogeneous nucleation. In case a compound is being synthesized, these precursors react in the gas phase and form a compound with the material that is separately injected in the reaction chamber. The clusters would continue to grow if they remain in the supersaturated region. To control their size, they need to be rapidly removed from the supersaturated environment by a carrier gas. The cluster size and its distribution are controlled by only three parameters:

1) the rate of evaporation (energy input),
2) the rate of condensation (energy removal), and
3) the rate of gas flow (cluster removal).

Because of its inherent simplicity, it is possible to scale up this process from laboratory (mg/day) to industrial scales (tons/day).
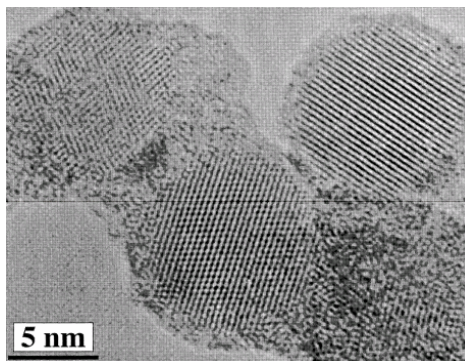
Figure 3.3.2: Defect-free Si particles synthesized by inert gas arc evaporation technique.[73]

3.2.3.2 Flame assisted ultrasonic spray pyrolysis:

In this process, precusrsors are nebulized and then unwanted components are burnt in a flame to get the required material, eg. ZrO_2 has been obtained by this method from a precursor of $Zr(CH_3\ CH_2\ CH_2O)_4$.[74] Flame hydrolysis that is a variant of this process is used for the manufacture of fused silica.[75,76] In the process, silicon tetrachloride is heated in an oxy-hydrogen flame to give a highly dispersed silica. The resulting white amorphous powder consists of spherical particles with sizes in the range 7-40 nm.
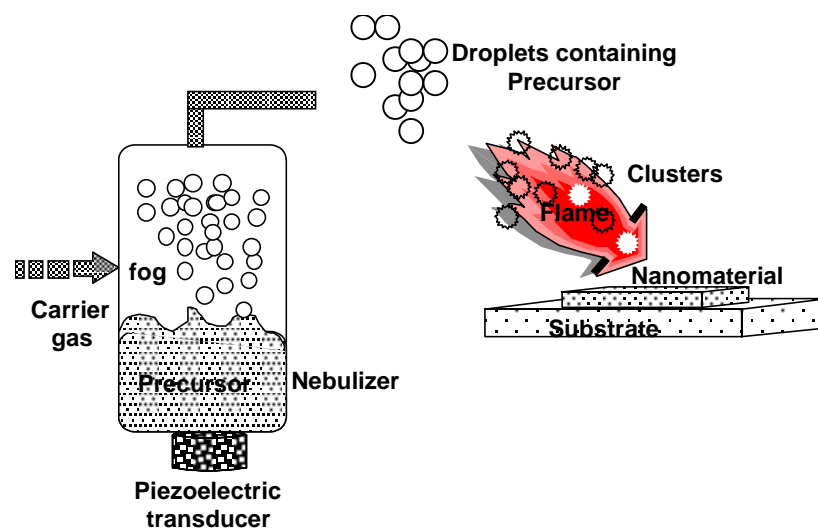
Figure 3.3.3.2: Flame assisted ultrasonic spray pyrolysis.[77]

The combustion flame synthesis,[78] in which the burning of a gas mixture, e.g. acetylene and oxygen or hydrogen and oxygen, supplies the energy to initiate the pyrolysis of precursor compounds, is widely used for the industrial production of powders in large quantities, such as carbon black, fumed silica and titanium dioxide. However, since the gas pressure during the reaction is high, highly agglomerated powders are produced which is disadvantageous for subsequent processing. The basic idea of low pressure combustion flame synthesis is to extend the pressure range to the pressures used in gas phase synthesis and thus to reduce or avoid the agglomeration. Low pressure flames have been extensively used by aerosol scientists to study particle formation in the flame. A key for the formation of nanoparticles with narrow size distributions is the exact control of the flame in order to obtain a flat flame front. Under these conditions the thermal history, i.e. time and temperature, of each particle formed

is identical and narrow distributions result. However, due to the oxidative atmosphere in the flame, this synthesis process is limited to the formation of oxides in the reactor zone.

3.2.4 Gas Condensation Processing (GPC)
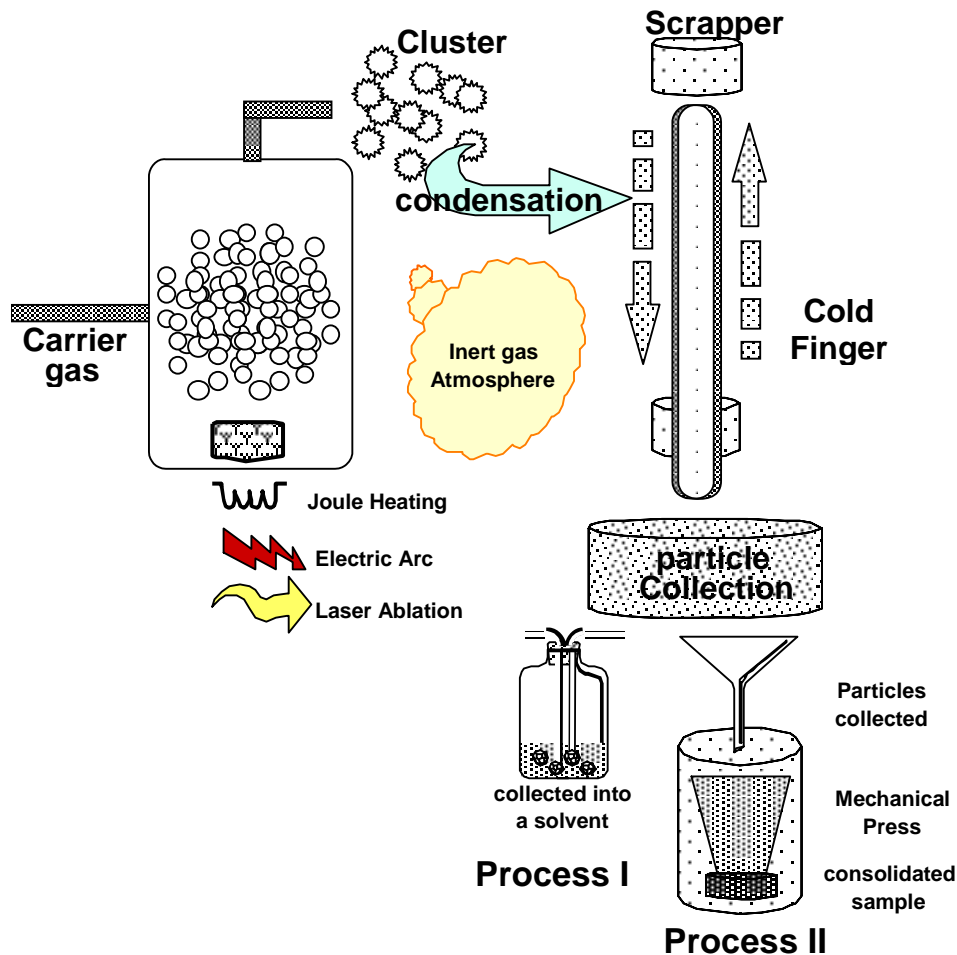
Figure 3.3.4: Schematic representation of typical set-up for gas condensation synthesis of nanomaterials followed by consolidation in a mechanical press or collection in an appropriate solvent media.

In this technique which was pioneered by Gleiter and co-workers[79] a metallic or inorganic material, e.g. a suboxide, is vaporised using thermal evaporation sources such as Joule heated refractory crucibles, electron beam evaporation devices or sputtering sources in an atmosphere of 1-50 mbar He (or another inert gas like Ar, Ne, Kr).[2,3] Cluster form in the vicinity of the source by homogenous nucleation in the gas phase and grow by coalescence and incorporation of atoms from the gas phase. The cluster or particle size depends critically on the residence time of the particles in the growth regime and can be influenced by the gas pressure, the kind of inert gas, i.e. He,

Ar or Kr, and on the evaporation rate/vapour pressure of the evaporating material.[4] With increasing gas pressure, vapour pressure and mass of the inert gas used the average particle size of the nanoparticles increases. Lognormal size distributions have been found experimentally and have been explained theoretically by the growth mechanisms of the particles. Even in more complex processes such as the low pressure combustion flame synthesis where a number of chemical reactions are involved the size distributions are determined to be lognormal.

Originally, a rotating cylindrical device cooled with a liquid nitrogen was employed for the particle collection: the nanoparticles in the size range from 2-50 nm are extracted from the gas flow by thermophoretic forces and deposited loosely on the surface of the collection device as a powder of low density and no agglomeration. Subsequenly, the nanoparticles are removed from the surface of the cylinder by means of a scraper in the form of a metallic plate. In addition to this cold finger device several techniques known from aerosol science have now been implemented for the use in gas condensation systems such as corona discharge, etc. These methods allow for the continuous operation of the collection device and are better suited for larger scale synthesis of nanopowders. However, these methods can only be used in a system designed for gas flow, i.e. a dynamic vacuum is generated by means of both continuous pumping and gas inlet via mass flow controller. A major advantage over convectional gas flow is the improved control of the particle sizes. It has been found that the particle size distributions in gas flow systems, which are also lognormal, are shifted towards smaller average values with an appreciable reduction of the standard deviation of the distribution. Depending on the flow rate of the He-gas, particle sizes are reduced by 80% and standard deviations by 18%.

The synthesis of nanocrystalline pure metals is relatively straightforward as long as evaporation can be done from refractory metal crucibles (W, Ta or Mo). If metals with high melting points or metals which react with the crucibles, are to be prepared, sputtering, i.e. for W and Zr, or laser or electron beam evaporation has to be used. Synthesis of alloys or intermetallic compounds by thermal evaporation can only be done in the exceptional cases that the vapour pressures of the constituents elements are similar. As an alternative, sputtering from an alloy or mixed target can be employed. Composite materials such as Cu/Bi or W/Ga have been synthesised by simultaneous evaporation from two separate crucibles onto a rotating collection device.[6] It has been found that excellent intermixing on the scale of the particle size can be obtained.

However, control of the composition of the elements has been difficult and reproducibility is poor. Nanocrystalline oxide powders are formed by controlled post-oxidation of primary nanoparticles of a pure metal (e.g. Ti to TiO_2) or a suboxide (e.g. ZrO to ZrO_2).[2]

Although the gas condensation method including the variations have been widely employed to prepared a variety of metallic and ceramic materials, quantities have so far been limited to a laboratory scale. The quantities of metals are below 1 g/day, while quantities of oxides can be as high as 20 g/day for simple oxides such as CeO_2 or ZrO_2. These quantities are sufficient for materials testing but not for industrial production. However, it should be mentioned that the scale-up of the gas condensation method for industrial production of nanocrystalline oxides by a company called nanophase technologies has been successful.[80]

3.2.5 Chemical Vapour Condensation (CVC)

As shown schematically in Figure, the evaporative source used in GPC is replaced by a hot wall reactor in the Chemical Vapour Condensation or the CVC-process. Depending on the processing parameters nucleation of nanoparticles is observed during chemical vapour deposition (CVC) of thin films and poses a major problem in obtaining good film qualities. The original idea of the novel CVC process which is schematically shown below where it was intended to adjust the parameter field during the synthesis in order to suppress film formation and enhance homogeneous nucleation of particles in the gas flow. It is readily found that the residence time of the precursor in the reactor determines if films or particles are formed. In a certain range of residence time both particle and film formation can be obtained. Adjusting the residence time of the precursor molecules by changing the gas flow rate, the pressure difference between the precursor delivery system and the main chamber and the temperature of the hot wall reactor results in the prolific production of nanosized particles of metals and ceramics instead of thin films as in CVD processing.

In the simplest form a metalorganic precursor is introduced into the hot zone of the reactor using mass flow controller. Besides the increased quantities in this continuous process compared to GPC it has been demonstrated that a wider range of ceramics including nitrides and carbides can be synthesised. Additionally, more complex oxides such as $BaTiO_3$ or composite structures can be formed as well. Appropriate precursor compounds can be readily found in the CVD literature. The

extension to production of nanoparticles requires the determination of a modified parameter field in order to promote particle formation instead of film formation. In addition to the formation of single phase nanoparticles by CVC of a single precursor the reactor allows the synthesis of

1. mixtures of nanoparticles of two phases or doped nanoparticles by supplying two precursors at the front end of the reactor, and

2. coated nanoparticles, i.e., n-ZrO_2 coated with n-Al_2O_3 or vice versa, by supplying a second precursor at a second stage of the reactor. In this case nanoparticles which have been formed by homogeneous nucleation are coated by heterogeneous nucleation in a second stage of the reactor.
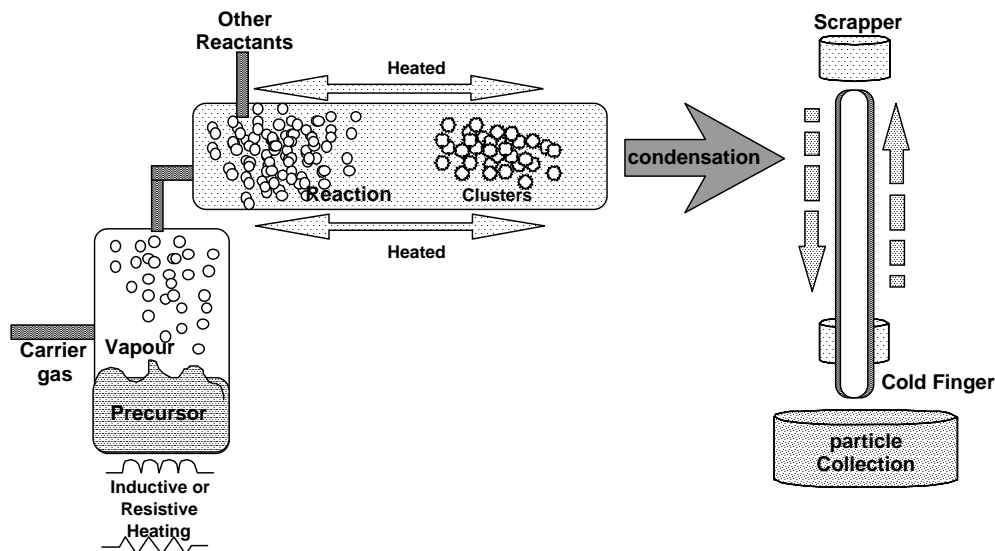
Figure 3.3.5: A schematic of a typical CVC reactor

Because CVC processing is continuous, the production capabilities are much larger than in GPC processing. Quantities in excess of 20 g/hr have been readily produced with a small scale laboratory reactor. A further expansion can be envisaged by simply enlarging the diameter of the hot wall reactor and the mass flow through the reactor. The microstructure of nanoparticles as well as the properties of materials obtained by CVC have been identical to GPC prepared powders.

3.2.5.1 Cold Plasma Methods:

3.2.5.1.1 Plasma CVD:
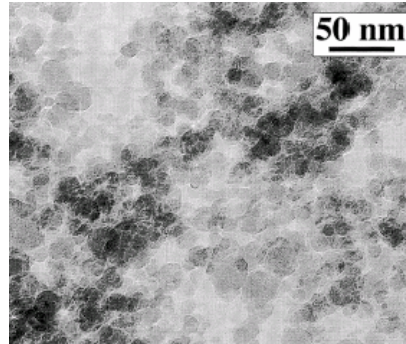
figure 3.3.5.1.1a: silicon nano-particles prepared by plasma CVD

Plasma CVD allows an additional control on the dissociation of precursors and the production of clusters that ultimately form nanoparticles as depicted in the figure below.
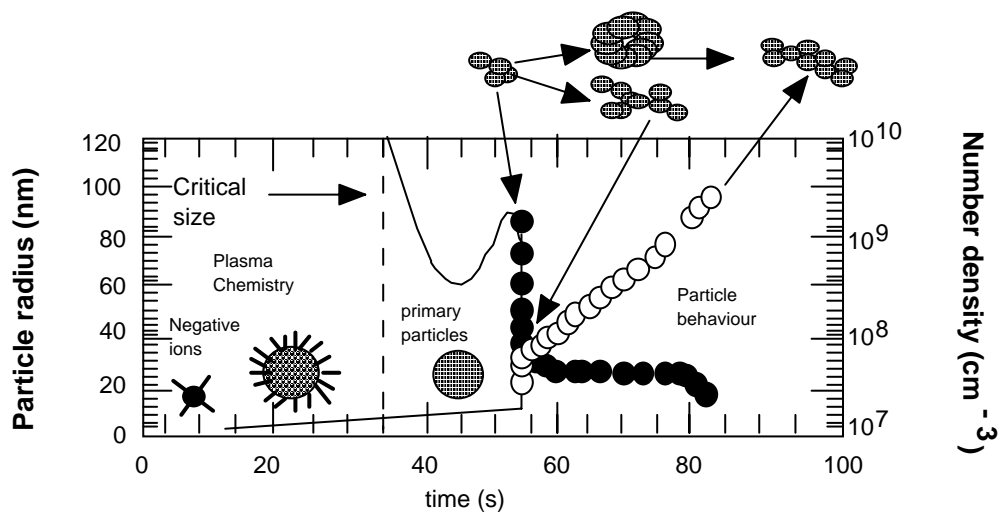
Figure 3.3.5.1.1b: Schematic representation of silicon particle growth in plasma CVD[81]

3.2.5.1.2 Sputtered Plasma Processing:

In this method is yet again a variation of the gas-condensation method excepting the fact that the source material is a sputtering target and this target is sputtered using rare gases and the constituents are allowed to agglomerate to produce nanomaterial. Both dc (direct current) and rf (radio-frequency) sputtering has been used to synthesize nanoparticles. Again reactive sputtering or multitarget sputtering has been used to make

alloys and/or oxides, carbides, nitrides of materials.[82,83] This method is specifically suitable for the preparation of ultrapure and non-agglomerated nanoparticles of metal.

3.2.5.1.3 Microwave Plasma Processing:

This technique is similar to the previously discussed CVC method but employs a plasma instead of high temperature for decomposition of the metalorganic precursors.[84] The method uses a microwave plasma in a 50 mm diameter reaction vessel made of quartz placed in a cavity connected to a microwave generator. A precursor such as a chloride compound is introduced into the front end of the reactor. Generally, the microwave cavity is designed as a single mode cavity using the TE10 mode in a WR975 waveguide with a frequency of 0.915 GHz. The major advantage of the plasma assisted pyrolysis in contrast to the thermal activation is the low temperature reaction which reduces the tendency for agglomeration of the primary particles. This is also true in the case of plasma-CVD processes. Additionally, it has been shown that by introducing another precursor into a second reaction zone of the tubular reactor, e.g. by splitting the microwave guide tubes, the primary particles can be coated with a second phase. For example, it has been demonstrated that ZrO_2 nanoparticles can be coated by Al_2O_3.[84] In this case the inner ZrO_2 core is crystalline, while the Al_2O_3 coating is amorphous. The reaction sequence can be reversed with the result that an amorphous Al_2O_3 core is coated with crystalline ZrO_2. While the formation of the primary particles occurs by homogeneous nucleation, it can be easily estimated using gas reaction kinetics that the coating on the primary particles grows heterogeneously and that homogeneous nucleation of nanoparticles originating from the second compound has a very low probability. A schematic representation of the particle growth in plasma's is given below:
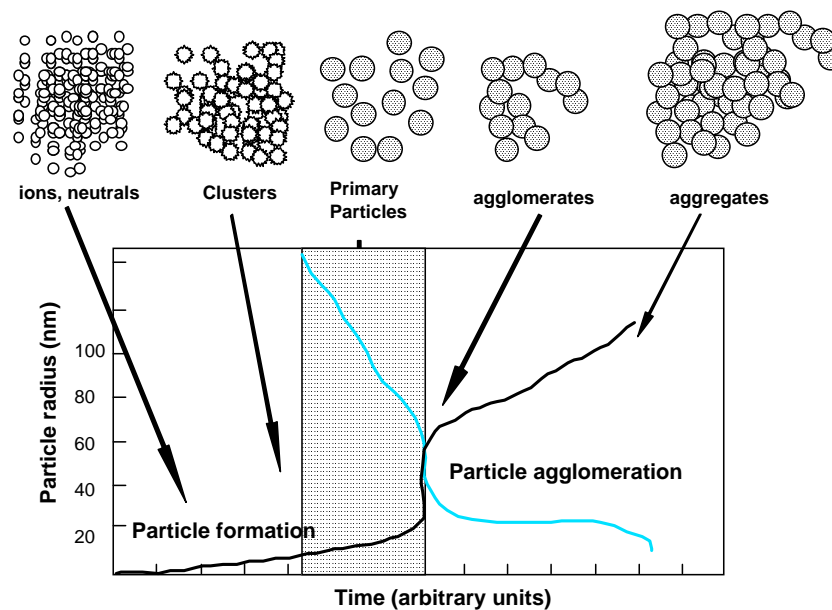
Figure: Cartoon representation of the growth of nanoparticles in a plasma
(PECVD, Microwave CVD, or sputtering).[85]

3.2.5.2 Laser ablation:

Laser ablation[86,87,88] have been extensively used for the preparation of nanoparticles and particulate films. In this process a laser beam is used as the primary excitation source of ablation for generating clusters directly from a solid sample in a wide variety of applications.[89] The possibility for preparing nanoparticulate web-like structures over large sample area is of particular interest in view of their novel properties that can be applied to new technological applications as shown by El-Shall and his collaborators.[90] In a recent investigation utilising a novel atomization system, (LINA-SPARK™), LSA, based on laser spark atomization of solids has been developed that seems to be very versatile for different materials.[91] Briefly, the LSA is capable of evaporating material at a rate of about 20 μg·s^{-1} from a solid target under argon atmosphere. The small dimensions of the particles and the possibility to form thick films make the LSA quite an efficient tool for the production of ceramic particles and coatings and also an ablation source for analytical applications such as the coupling to induced coupled plasma emission spectrometry, ICP,[92] the formation of the nanoparticles has been explained following a liquefaction process which generates an aerosol, followed by the cooling/solidification of the droplets which results in the formation of fog. The general dynamics of both the aerosol and the fog favours the aggregation process and micrometer-sized fractal-like particles are formed. The laser spark atomizer can be used to produce highly mesoporous thick films and the porosity can be modified by the carrier

gas flow rate thus enabling for a control of the microstructure of the coatings which make these nanoparticulate thick films suitable candidates for application in membrane technology, catalysis and lithium ion batteries. ZrO_2 and SnO_2 nanoparticulate thick films were also synthesized successfully using this process with quite identical microstructure. Synthesis of other materials such as lithium manganate, silicon and carbon has also been carried out by this technique.

3.2.5.3 Vapour-liquid-solid growth:

Classification with reference to size
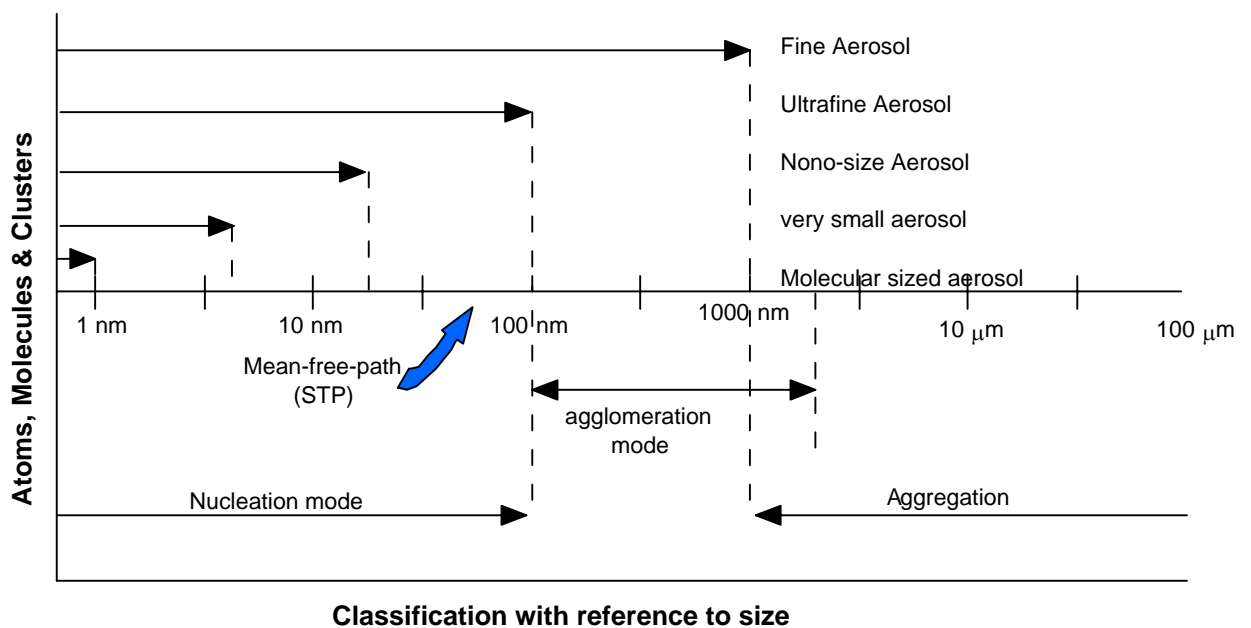
Figure: The classification of aerosol sizes: Coarse mode include particles larger than 1 mm that are formed by aggregation, fine aerosol includes particles smaller than 1 μm that mainly grow by nucleation, condensation & agglomeration; Ultrafine aerosol includes particles smaller than 100nm, while nanosize aerosol particles are smaller than 50 nm; very small aerosols include particles less than 5nm, while molecular size aerosol include particles smaller than 1nm (i.e. less than 10 molecules in each particle).

In this method, nanosized clusters are deposited onto a substrate where a heterogeneous reaction takes place. The activation of the substrate is usually achieved by dipping the substrate into a metal-ion-containing solution (if metals are being synthesized), followed by subsequent heating to activate surface diffusion processes. For example, the reactant could dissolve in the metal and crystallize when the solution gets to concentrated, leading to the formation of solid materials. These types of synthesis techniques include epitaxial growth of advanced semiconductor materials (like molecular beam epitaxy).

3.2.5.4 Particle precipitation aided CVD:

(1)

(2)
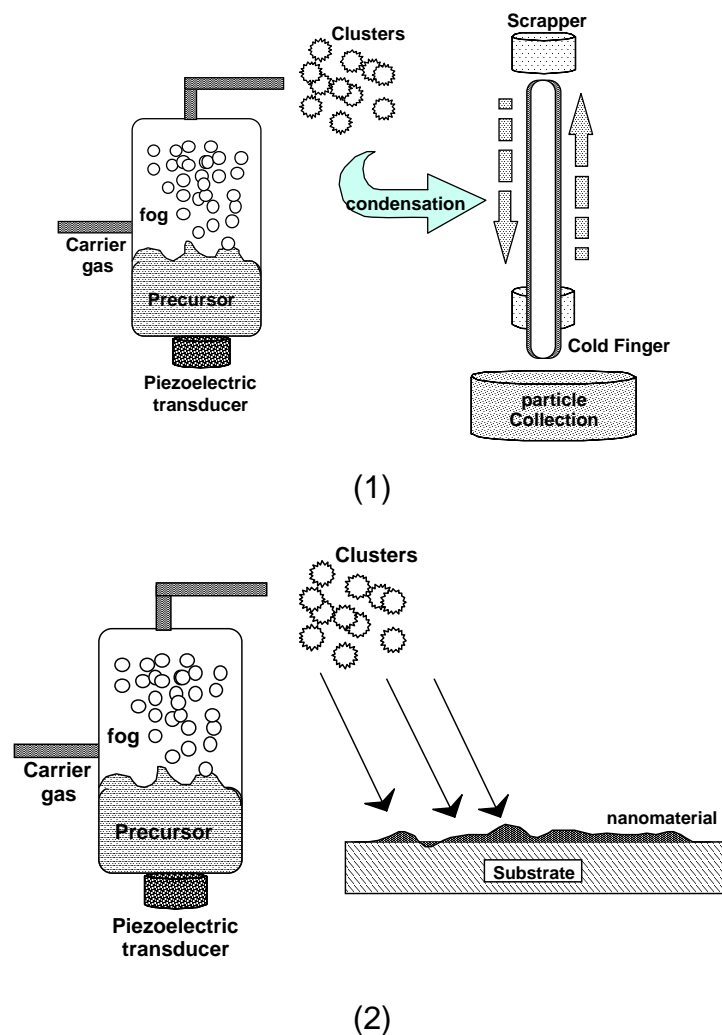
Figure: Schematic representation of (1) nanoparticle, and (2) particulate film formation.

In another variation of this process, colloidal clusters of materials are used to prepare nanoparticles. The CVD reaction conditions are so set that particles form by condensation in the gas phase and collect onto a substrate, that is kept under a different condition that allows heterogeneous nucleation. By this method both nanoparticles and particulate films can be prepared. An example of this method has been used to form nanomaterials eg. SnO_2,[93] by a method called pyrosol deposition process, where clusters of tin hydroxide are transformed into small aerosol droplets, following which they are reacted onto a heated glass substrate.[94]

3.2.6 Summary of Gas Phase Synthesis methods
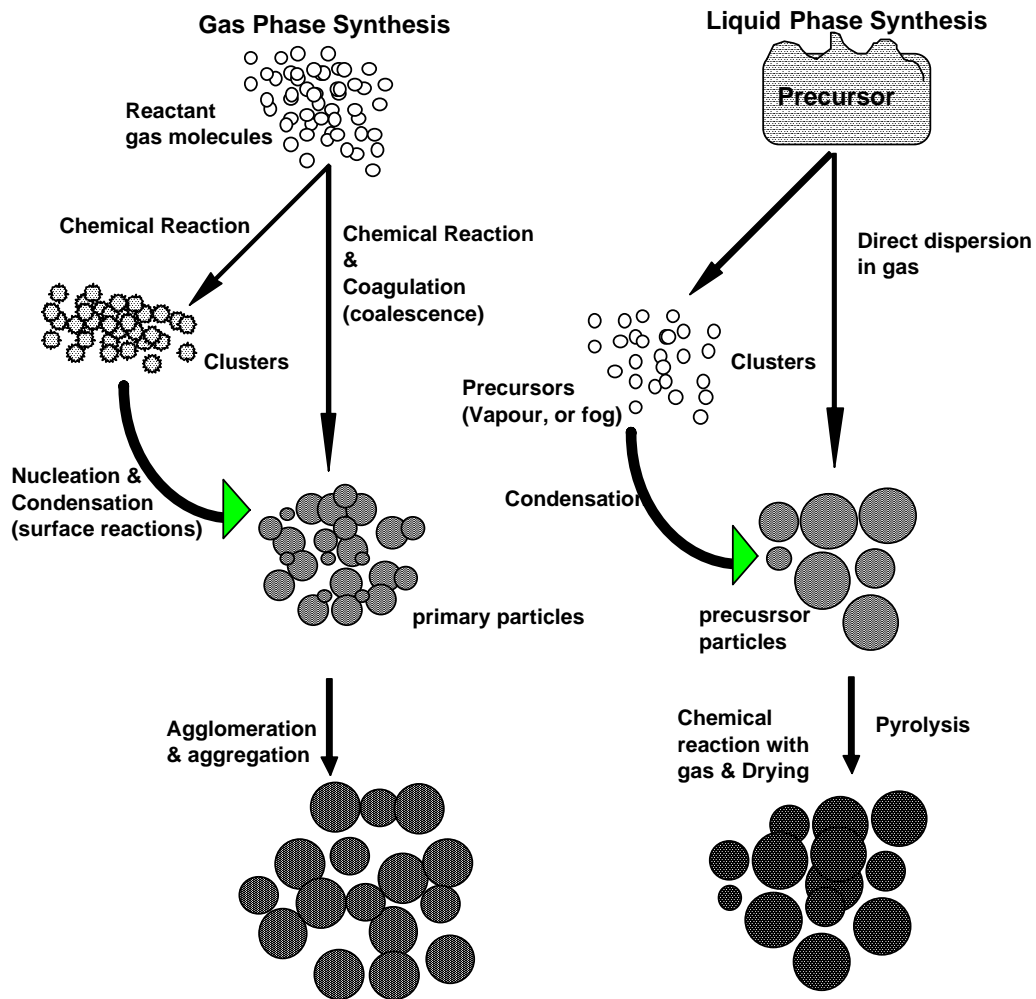
Figure: Schematic representation of various steps to the formation of nanoparticles in the gas phase synthesis methods.

It is evident that all materials can be prepared by means of gas phase synthesis in a nanocrystalline microstructure. In each case it has to be determined which technique is the most appropriate in terms of cleanliness of powder surfaces, degree of agglomeration, particle sizes and distribution, phases and quantities that can be synthesized. In addition to single phase materials some of the different techniques are capable of synthesising metal/metal, metal/ceramic and ceramic/ceramic composites as well as coated nanoparticles which might show interesting applications in the near future.

Gas Condensation		Chemical Vapour Condensation

Metals, Alloys, Intermetallics Fe, Au, Cu, Pd, W, Cu/Bi, TiAl etc.	Oxides SnO_2, TiO_2, ZrO_2, CeO_2, SiO_2, Al_2O_3,	Non-Oxides Si_3N_4, SiC, ZrN, TiN, GaAs, ZnS, CdS, ZnSe etc.

Plasma Processing	Aerosol processing
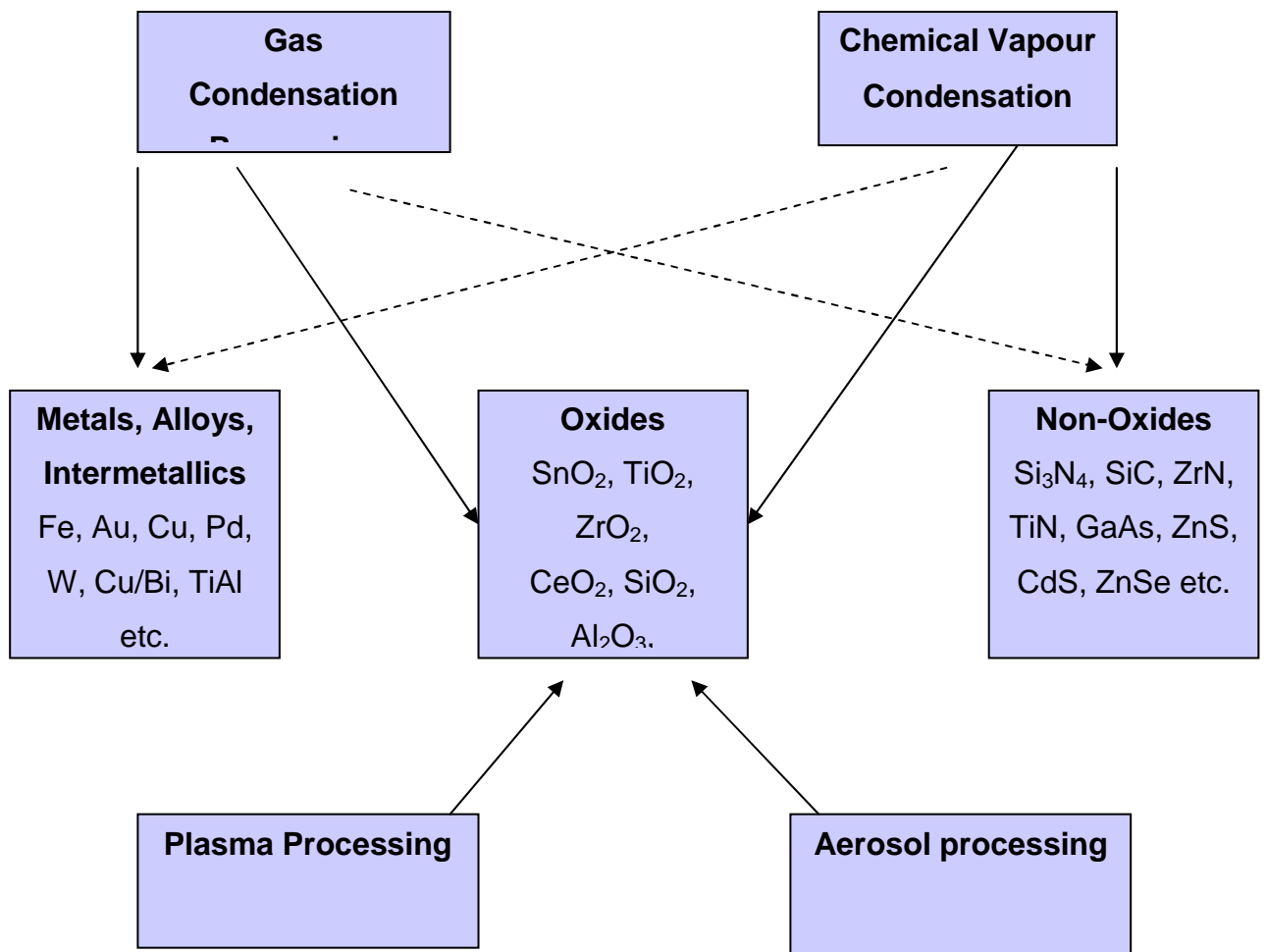
Figure: Schematic representation of the gas phase synthesis methods.

In the following table, the gas phase synthesis techniques generally used for the preparation of nanomaterials are schematically summarised. Both the gas phase and liquid phase precursors have been classified in this figure.

Table: Partial list of nanomaterials that can be synthesized by gas phase reaction, wet chemical methods and plasma chemical reaction processes.

Technology	Materials
Gas phase reactions	Metals, alloys, their oxides and carbides Ag, Cu, Au, Ti, Ni, W, Zr and others ZrO_2, Y_2O_3, Al_2O_3, $ZrO_2(Y_2O_3)Al_2O_3$, Si_3N_4, SiC, C_3N_4

Chemical precipitation	Metals, alloys, ceramics, metal-ceramics
	Au, Ag, Cu, Ni, Fe, ZnS, ZnSe, Fe-Cu, Fe-Ni-Cu, Al_2O_3, ZrO_2, Ti_2O_3, Ni- Al_2O_3
Plasma chemical reactions	Nanophase ceramics
	TiO_2, TiN, ZrO_2, Si, SiC, Si_3N_4, BN, NbTiCN

4 NANOCOMPOSITES SYNTHESIS AND PROCESSING

4.1 Introduction:

A major goal of material science is to produce hierarchical materials that are ordered on all length scales, from the molecular (1–100 Å) via the nano (10–100 nm) to the meso (1–100 mm) scale. In these materials, the larger-scale properties can be controlled by choosing the appropraite molecular characteristics.

"Nanocomposites" are a special class of materials originating from suitable combinations of two or more such nanoparticles or nanosized objects in some suitable technique, resulting in materials having unique physical properties and wide application potential in diverse areas that can be formed into a useful object which can be subsequently used. Novel properties of nanocomposites can be derived from the successful combination of the individual characteristics of parent constituents into a single material. To exploit the full potential of the technological applications of the nanomaterials, it is thus extremely important to endow them with good processability. Nanocomposites are either prepared in a host matrx of inorganic materials (glass, porous ceramics etc) or by using conventional polymers as one component of the nanocomposites. The second type of nanocomposites which are a special class of hybrid materials are termed "*polymeric nanocomposites*". These materials are intimate combinations (up to almost the molecular level) of one or more inorganic materials (nanparticles , eg.) with a polymer so that unique properties of the former can be mixed with the existing qualities of the polymer to result in a totally new material suitable for novel applications. In most of the cases such combinations require blending or mixing of the components, taking the polymer in solution or in melt form.[95] Resulting nanocomposites have found successful applications in versatile fields viz. battery cathodes,[96] microelectronics,[97] nonlinear optics,[98] sensors,[99] etc.

4.2 Historical perspective:

When nanocomposites are prepared in glassy or ceramic matrices, the particles are so produced, precipitated insitu or otherwise included into the matrix. Some of the synthesis and application of such nanocomposites are nothing new. For example, the synthesis and use of metallic nanoparticles in a glassy phase is a well known ancient

technique. During the study of a Roman mosaïc, the "Thomas Panel" found in Faiyum, 100 kms southwest of Cairo, R. H. Brill and D. Whitehouse[100] discovered that the romans embedded fine gold particles to colour some of their glass. The colours obtained ranged from bright red to purple. The finest example from this period however is the Lycurgus Cup (4th century AD), 165mm tall, with decorations in very intense red colour achieved by gold and silver nanoparticles contained in the glassy phase.

Since the XIIth century, copper and silver have been used to colour stained glass windows of cathedrals in red and yellow, respectively. The insertion of these nanoparticles were done either in the bulk or at the surface of the glass, depending on the desired luminosity. Later, during the XVIIIth century in China, under the reign of K'ang Hsi, the famous pink chinese porcelain where gold nanoparticles are embedded in enamel, were manufactured. These porcelains had great success and were widely used in Europe.

4.3 Different Synthesis methods of nanocomposites

4.3.1 Self Assembly or bio-mimetic processes:

When self assembly is used to organise nanomaterial into an useful form, irrespective of whether the structures so formed are points, lines, layers, composites, they are going to be periodic in arrangements, since such arrangements minimize the free energy of the systems. Methods developed to produce three-dimensional, bulk-like hierarchical structures include biomimetic methods, which use polypeptides as building blocks, and amphiphile and colloidal templating, which use amphiphilic or colloidal mesophases as templates for inorganic mesoporous materials. Designing finite mesostructures with a given geometry still remains a challenge.

One of the big advantages of using methods of self-organization and self-assembly is that very large number of identical structures can be formed simultaneously without having to make them one at a time. These structures are also thermally quite stable, at least stable up to the temperature at which they are formed. However one cannot synthesize non-periodic material structures using these methods.

Another difficulty is that the lack of mobility due to the existence of large activation barriers along the path to equilibrium may cause frustrations, thus can hinder some systems to make a perfect alignment. What we need to know for optimising these methods are atomic and molecular interactions of different materials, adatom-adatom

interactions at the surface, defect interactions such as vacancy-vacancy interactions and step-step interactions, line-line interactions and layer–layer interactions and so on for different combination of materials.

4.3.2 Film:

Another important area of research for nanomaterials is how to produce 'flat' macroscopic size surfaces and how to grow ultra-thin films of nearly perfect interfaces. Even for a perfectly cut surface, when it is annealed at high temperature to remove defects and impurities, from a thermodynamic consideration the surface will become wavy. Annealing at lower temperatures can reduce the height of these wavy structures. But at low temperature, surface diffusion becomes too slow to be able to remove defect structures. In growing a thin film, the ideal case is that the film can be grown layer by layer, and there are few defects in the film or at the interface. Unfortunately lattice mismatch can prevent growth behaviour from the ideal case and many defects will also form at the interface. Introduction of a surfactant may relieve some of these difficulties.[101,102] Finding appropriate surfactants which will promote the growth behaviour to near ideal conditions and which will not be incorporated inside the films or the substrates and which can also be easily removed after the films are grown will be an important subject for future research.

4.4 Processing of nanoparticles

4.4.1 Binding mechanisms in nanoparticles

If a dry powder is to be used for the preparation of a suspension for shaping them into useful form, an agglomeration of the primary particles usually has to be expected, depending on the material properties and the conditions during manufacture and storage. The following binding mechanisms can be imagined:

Binding adhesion forces between the particles. This involves mainly van der Waals' forces and electrostatic (Coulombian) forces (in the case of different charge signs). The type and value of these adhesion forces depend on the geometry of the contact surfaces (particle shape and surface roughness), plastic deformations due to external mechanical load and the complex effects of adsorption layers.

Binding by wetting liquids of low viscosity. Depending on the liquid saturation of the agglomerates, a boundary force is effective in the three-phase contact in addition to the capillary under pressure in the liquid bridges. Forces of this type are stronger than the adhesion forces and less influenced by surface roughness.

Binding by highly viscous liquids. Apart from the cohesive forces in such liquid, binding is mostly controlled by the adhesion between liquid and particles.

Binding by solid bridges. Force-transmitting solid bridges are generated by sintered processes, binder hardening or the crystallization of solved substances.

Positive bridges. Particles of extreme shape (fibres, plates) can form agglomerates with positive binding by entangling or felting.

4.4.2 Dispersion of nanoparticles

Dispersion requires counteracting these described forces by physicochemical and mechanical means to such a degree that the particles will eventually exist individually (i.e. agglomerate-free). For this, certain basic mechanisms can be followed, that can be described by the following three fundamental processes:

Wetting of the solid particles by the liquid.

Deglomeration of the particle agglomerates.

Stabilization of the suspension or prevention of renewed agglomeration.

The control of the wetting processes only allows modification of the adhesion forces between the particles and partially the binding forces produced by the liquids in the immediate capillaries. The methods of deglomeration should have an effect on all binding forces. Finally, stabilization is achieved mostly by modifying the interaction forces between the particles. In spite of their extraordinarily wide range, the methods used to influence and control these processes can be reduced to the following tasks:

Selection of a suitable liquid (suspending agent)

Selection of the type and concentration of a suitable (interface active) aid (dispersant).

Selection of the type and duration of mechanical preparation to dispersion.

In addition to its task of creating favourable condition for wetting, de-agglomeration and stabilization, the liquid medium has to meet several other requirements. In the case of sedimentation analysis, these are:

The solid must not dissolve or be chemically altered under the influence of the liquid; it must neither swell nor shrink.

Density and viscosity of the liquid have to be adapted to the solid density, maximum particle size and other parameters of the solid in such a way that measurement takes place at sedimentation velocities which are neither too high nor too low.

The liquid should have a vapour pressure as low as possible.

The liquid has to be non-toxic, inexpensive and easily available.

Table 4.2 Methods of dispersion control

Methods	Determination of:			
	Type of liquid	Type of dispersant	Concentration of dispersant	Type and duration of mechanical treatment
Wettability	+	+	(+)	-
Rheologic tests	+	+	(+)	-
Microscopic assessment	+	+	(+)	(+)
Sedimentation tests	(+)	+	+	+
Photometric measurement	+	+	+	+
Zeta potential measurement	(+)	+	+	+
Particle size analysis	+	+	(+)	(+)

+ = suitable; (+) = conditionally or hardly suitable; - = not suitable.

4.4.3 Stabilization of nanoparticles

Particles in the nanometer size range have a strong tendency to agglomerate owing to their relatively large specific surface area, which in turn accentuates their Van

der Waals interactions. Nanoclusters are only kinetically stable; they must be stabilized against aggregation into larger particles and, eventually, bulk material, their thermodynamic minimum. It is therefore important to utilise synthesis methods by which the particles can be stabilized, i. e., where repulsive forces between the particles can be provided to balance this attraction.[103]
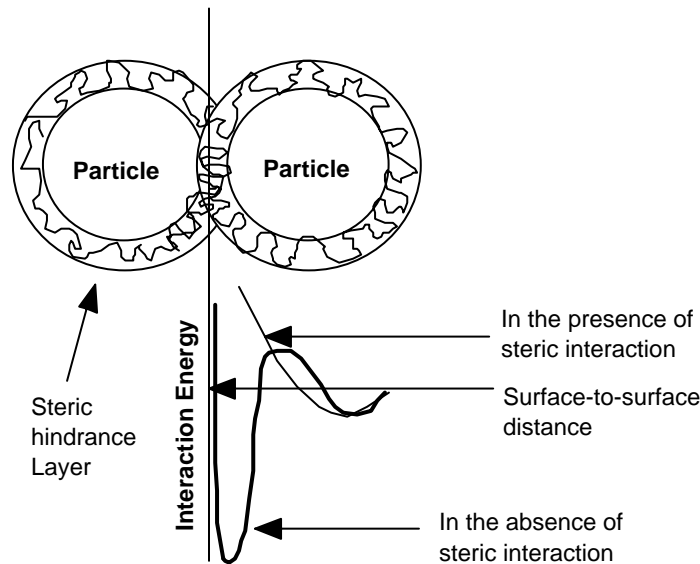
Figure : Schematic image of steric stabilization by adsorption of polymer chains onto a nanoparticle in solution. The steric layer created by the adsorbed polymers presents a large barrier against particle interaction, thus slowing aggregation.[104]
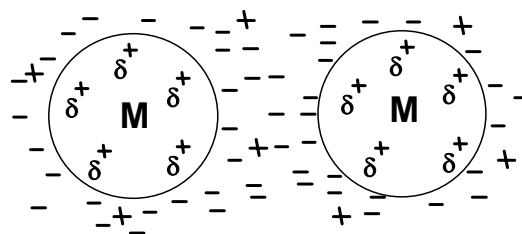
Figure: Schematic image of two electrostatically-stabilized nanoparticles. Ions adsorb onto the surface of the nanoparticles, creating an electrical double layer which provides Coulombic repulsion and thus stabilization against aggregation. The nature of the δ 'charge mirror' is discussed in detail in the literature.[105]

Stabilization can be accomplished in two precedented ways: electrostatic (charge, or 'inorganic') stabilization and steric (or 'organic') stabilization.[106] Electrostatic

stabilization occurs by the adsorption of ions to the often electrophilic metal surface.[107] Electrostatic stabilization involves the creation of an electrical double layer arising from ions adsorbed on the surface and associated counterions which surround the particle. Thus, if the electric potential associated with the double layer is sufficiently high, the Coulombic repulsion between the particles will prevent their agglomeration.[108,109]

Steric stabilization is achieved by surrounding the metal center by layers of material that are sterically bulky, such as polymers or surfactants. These large adsorbates provide a steric barrier that prevents close contact of the metal particle centers. The coil dimensions of polymers are usually larger than the range over which the attraction forces between colloidal particles are active. Two distinct effects describe this type of stabilization (ΔG_{el}, the volume restriction contribution and ΔG_m, the osmotic term), and they both contribute to the interaction free energy, ΔG_s,[110,111]

$$\Delta G_s = \Delta H - T\Delta S = \Delta G_m + \Delta G_{el}.$$
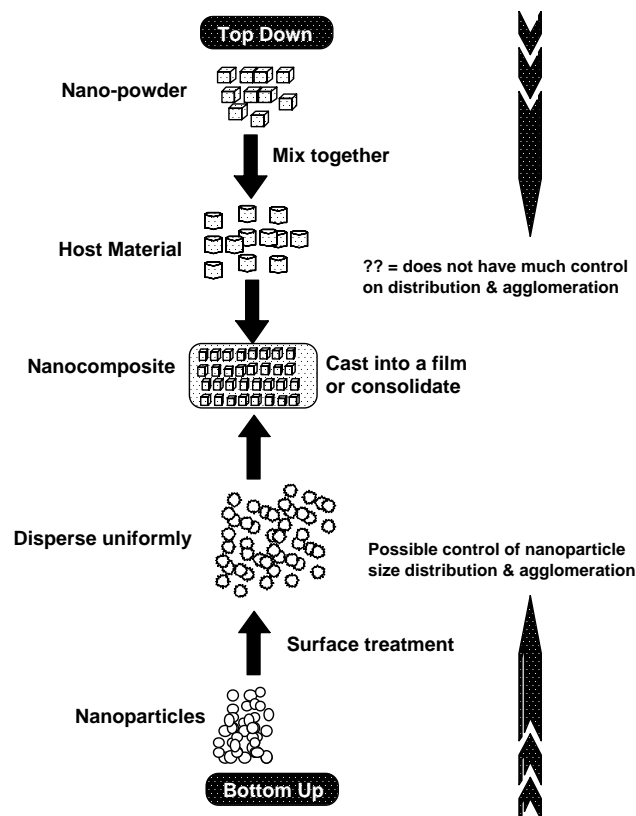
Figure: Schematic representation of the advantages of surface treatment for preparation of nanocomposites

First, the fact that the adsorbed molecules are restricted in motion causes a decrease in ΔG_{el}, the configurational entropic contribution to the free energy (Figure below). Second, the local increase in concentration of polymer chains between approaching particles results in an osmotic repulsion, since the solvent re-establishes equilibrium by diluting the polymer molecules and separating the particles. This is described by the energy of free mixing of polymer segments and solvent molecules, ΔG_m, calculated by the Flory-Krigbaum theory.[112]

(a)

(b)
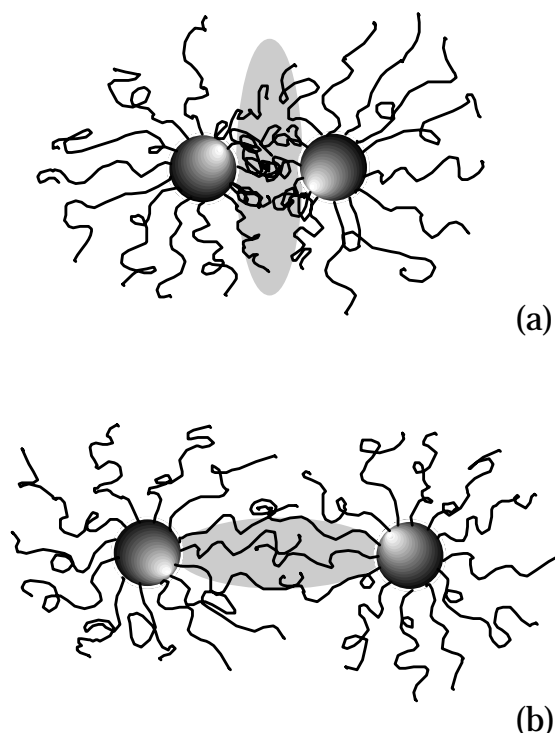
Figure 2.3 Steric stabilization of metal colloid particles by polymers: (a) entropic effect, (b) osmotic effect.

The conformation of adsorbed polymers on nanoparticles tend to be controlled by the strength of segment/surface interactions,[113,114] which may be described by the classical loop-train-tail model.[115,116] For an effective particle stabilization, it is important that the polymer form a complete, dense layer around the particle.[117] Then, the polymeric stabilizer must have sufficient tail length and adsorb sufficient amount of polymeric material to screen the attractive interaction between the particles.

The mode of adsorption is also dependant on molecular architecture. First, block or graft copolymers can be used to adsorb at the particle surface.[118] For instance, polyethylene oxide/polystyrene block copolymers lead to short-range interactions in the

physisorbing category which are responsible for adsorption and brush formation.[119,120,121] In this case, the copolymer part that has the lowest affinity with the solvent will adsorb on the surface. Secondly, chemisorption, where covalent bonds are formed between the particle and the protective organic layer: a short range and strong specific force. There has been intense interest in this type of interaction as a result of the ability of thiol-containing molecules to form spontaneously ordered monolayers (to "self-assemble") at metal surfaces.[122,123,124] Recently, this type of interaction has been extended to functionalized polymers that can be strongly and covalently bonded to gold.[125]

(a)   (b)
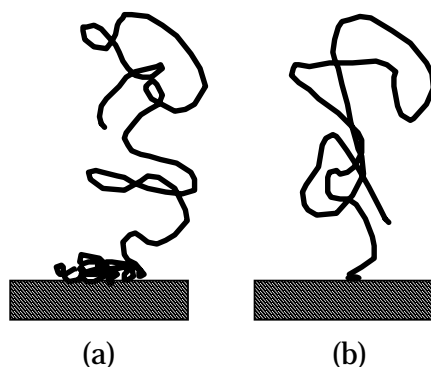
Figure 2.4 Schematic representation of the structure of a physisorbed block copolymer (a), and a chemisorbed end-functional polymer (b), to a surface.

Some nanocluster stabilizers combine both electrostatic *and* steric stabilization, as eg. the polyoxoanion-stabilized nanoclusters. Another requirement for a good particle stabilization is the use of appropriate solvents. The stabilizing polymer has to possess high affinity with the solvent in order to solvate the particles and form an extended layer for screening the Van der Waals attraction between the particles. It is however well known that adsorption is generally stronger when the affinity of the polymer to the solvent is low.[126,127] Therefore, block or graft copolymer micelles, in the presence of a selective solvent that solubilizes one of the blocks, lead to expanded chains which occupy more surface area. In the case of polymers with strong anchoring groups, spontaneous adsorption occurs from good solvent. de Gennes has discussed the density profile of polymers attached to the surface by one end and in contact with a good solvent. He predicts that "blobs" will form and fill space densely in a layer close to the surface.[128] Another important advantage of covalently attached polymers is that the

resulting interaction with the particle surface is stronger and desorption cannot occur by solvent effects or variations in temperature. [60,61]

2.5 Insitu synthesis of polymer nanocomposites

Polymers have often been used for preparation and stabilization of nanosized metal particles, i. e. gold, silver or palladium, or small semiconductor crystallites such as CdS and PbS. It is not the aim of this introductory chapter to review in detail all the work that has been done in this field, but to give a general survey of the evolution of this field using some relevant examples.

The first and most common procedure for preparing polymer-protected nanocrystal colloids is the reduction of a particular salt in the polymer solution[129] (Figure). The technique consists of mixing the metal salt with the polymer in solution, resulting in the formation of a complex between the salt and the functional polymer groups.[130,131,]132 Subsequently, the complex can be reduced and particles are formed. To permit the solubility of the salt precursor, polar solvents and polar polymers such as poly(ethylene glycol) (PEG) or poly(vinylalcohol) are generally chosen. Unfortunately, the reaction of gold complexes with PEG leads to fragmented and oxidized polymers.[133] More recently, the coalescence rate for gold particles in a poly(2-vinylpyridine) (P2VP) matrix has been shown to be lower than for gold particles in a polystyrene matrix, indicating that the polymer-metal interaction plays an important role in the particle stability.[134,135] The repulsive interaction between the colloidal gold particles is attributed to P2VP bridges between the particles.
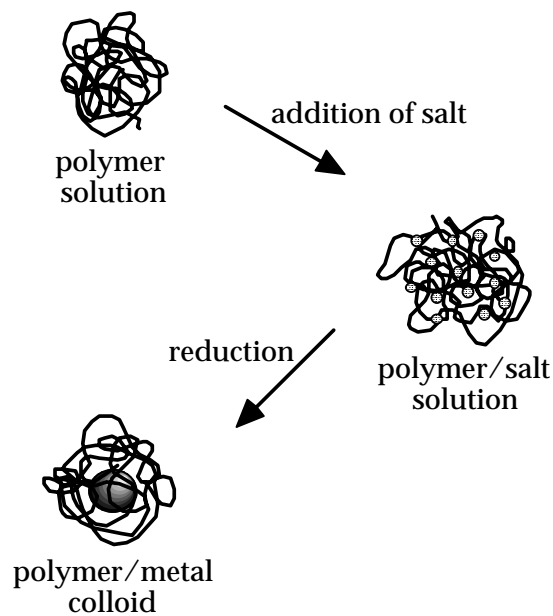
Figure 2.5: Reduction of metal salts in polymer solution.

Semiconductor nanoparticles have been synthesized in a matrix formed from a miscible polymer blend of poly(styrene phosphonate diethylate) and cellulose acetate.[136] The film is floated onto an aqueous $Cd(NO)_3$ solution so that cadmium ions can be incorporated into the homogeneous blend. By exposure to H_2S, it is possible to prepare thin polymer-CdS nanocomposites. CdS particles, trapped in a polymer, can also be prepared directly from the respective metallic elements, sulfur and N-methylimidazole that are added to a solution of poly(4-vinylpyridine) in methanol.[137] N-Methylimidazole acts as a coordinating ligand and increases the solubility of the primary metal particles. After casting films, CdS particles are formed at 160∘C in an inert atmosphere. Supercritical carbon dioxide solutions can also be used to load bulk polymer films with metal salts. Reduction of these salts to metal nanoclusters is then performed by chemical and thermal post-treatment.[138]

These methods are interesting since they permit the embedding of particles directly in a polymer matrix. However, as no real control of the particle size is achieved, it results in nanocomposites with a broad particle size distribution. Moreover, the spatial arrangement of particles is very heterogeneous and unstable leading to further growth of the nanocrystals due to the variation of temperature or pressure.

For the exploitation of the interesting size-dependent properties described earlier, a good control of the particle size as well as a regular spatial organisation is necessary. This can be achieved by utilising functional polymers with well-defined structure for the preparation of nanoclusters. Interactions can differ depending on the system used and are directly influenced by the degree of control in the syntheses, the effectiveness of the stabilization, and the final dispersion and organization of nanoparticles in the polymer matrix. There are two ways of achieving this: either by using "weak" interacting polymers which consist of amphiphilic block copolymers in a selective solvent that form micelles in which particles can be formed, or else by using polymers strongly that bind to particles, viz. by forming a covalent bond. It should be kept in mind however, that the terms "weak" or "strong" are only relative. They both represent adsorption on a particle surface and the "weak" interaction described here could also be very strong under certain conditions. The distinction made here only lies in the possibility of desorption, which can have a direct influence on the particle stabilization.

Some of the inorganic-in organic nanocomposites that have been prepared using different inorganic materials are listed below:[139]

- Nanocomposites with colloidal stability (SiO_2, SnO_2, $BaSO_4$, etc. as core materials)
- Nanocomposites with improved physical & mechanical properties (Fe_2O_3, ZrO_2, TiO_2, etc. as incorporated material
- Nanocomposites with magnetic susceptibility (using Fe_2O_3, γ -Fe_2O_3, etc. as magnetic particles)
- Nanocomposites with dielectric, charge storage, electrochromic activities, energy storage, piezoelectric and catalytic activities (using Pt, Pd, MnO_2, SnO_2, SiO_2, WO_3, CdS, ZnS, Si, TiO_2 etc.)

5 MECHANICAL PROPERTIES

5.1 Introduction

One of the very basic results of the physics and chemistry of solids is the insight that most properties of solids depend on the microstructure, i.e. the chemical composition, the arrangement of the atoms (the atomic structure) and the size of a solid in one, two or three dimensions. In other words, if one changes one or several of these parameters, the properties of a solid vary. The most well-known example of the correlation between the atomic structure and the properties of a bulk material is probably the spectacular variation in the hardness of carbon when it transforms from diamond to graphite. The important aspects related to structure are:

- atomic defects, dislocations and strains
- grain boundaries and interfaces
- porosity
- connectivity and percolation
- short range order

Defects are usually absent in either metallic or ceramic clusters of nanoparticles because dislocations are basically unstable or mobile. The stress field around a dislocation (or the electrostatic potential around charges and currents) have to satisfy the Laplace equation: $\nabla^2 \Phi = 0$. This sets up an image dislocation which pulls the defect out of the particle.

When these clusters are assembled under uniaxial pressure into a pellet, for example, it is found that the individual clusters are packed very tightly into a polycrystalline solid. Cluster-assembled materials often show close to 100% density. A fully consolidated nanophase material looks very much like a normal, dense polycrystalline aggregate, but at a far smaller scale.

5.2 Historical perspective

5.3 Property changes

5.3.1 Density

Nanocomposities with considerably improved mechanical properties have, to date, only been achieved in hot-pressed materials. The strength depends on relative density and decreased with increasing porosity. This might explain why Zhao *et al.*[140] found almost no strength increase in presureless sintered Al_2O_3/5vol% SiC nanocomposites with a density of 98.3% whereas in hot-pressed materials with a density of 99.9% considerable increase in strength was observed.

5.3.2 Fracture strength

Figure 1 shows a comparision of strength and fracture toughness of alumina-based nanocomposites at room temperature as a function of SiC content as reported by several groups. The strength of the monolithic alumina used as a reference varied from 350 to 560 Mpa! Therefore, a given relative improvement in strength of a ceramic nanocomposite can be misleading. Following Niihara's original work [141,142,143,144,145,146,147,148] the addition of only 5 vol% nanosize SiC increased the strength to 1050Mpa. A further increase of SiC content lowers the strength to a constant value of approximately 800 Mpa. However, Niihara explains the decrease of strength value for higher SiC contents due to agglomeration problems.
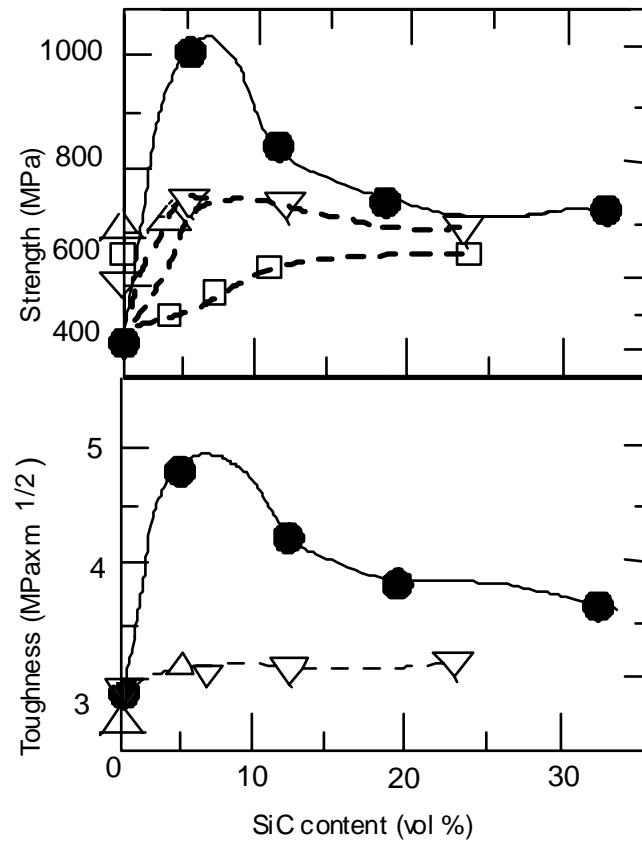
Fig. 5. Strength and toughness of Al_2O_3/SiC nanocomposites as a function of SiC content (adapted from various works): (●) Niihara & Nakahira[145] measured by three-point bend test and Vickers indentation; (□) Borsa *et al.*[149] by four-point bend test; (Δ) Zhao *et al.*[140] by four-point bend test and indentation-strength method; (V) Davidge *et al.* [150] [58] by three-point bend test and notched beams.

Figure 10 shows strength and fracture toughness for various Si_3N_4/SiC nanocomposites as a function of SiC volume fraction. All data were obtained from different publications of Niihara and his co-workers. Nanocomposites derived from the classical powder route are represented by solid symbols and nanocomposites fabricated from an amorphous Si-C-N powder by open symbols. With few exceptions, all data point follows a defined trend. The toughness increased from approximately 5MPa√m for mopnolithic Si_3N_4 to 6 MPa√m for manocomposites with ≥ 10 vol% SiC. This increase is accompanied by a modest increase in strength from 900 Mpa to 1100 Mpa.
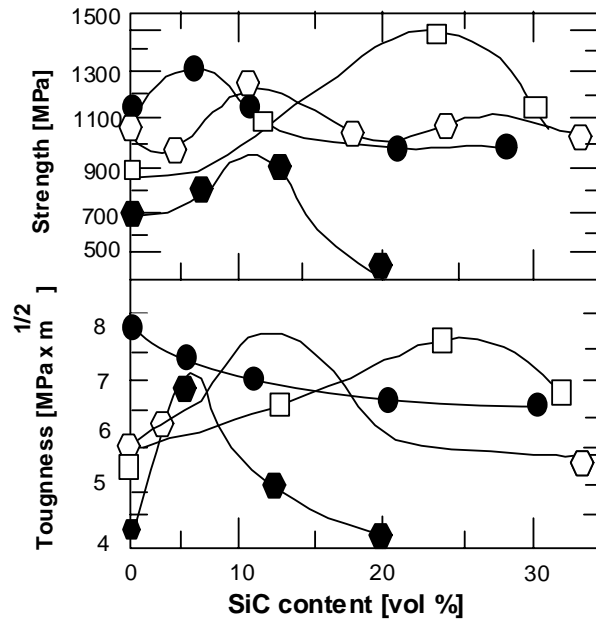
Fig. 10. Strength and toughness of Si $_3$N$_4$/SiC nanocomposites as a function of SiC content: (●) Ref 66; (⬢) Ref. 65; (□) Ref. 79; (⬡) Ref. 84.

5.4 Strengthening and Toughening Mechanisms

The evidence is that Ai$_2$O$_3$/SiC nanocomposites show an explicit increase in strength accompanied by a modest increase in toughness. Furthermore, grain boundaries are strengthened in nanocomposites as manifested by the transcrystalline fracture mode as well as by the increased resistance to wear and creep.

5.4.1 Critical flaw size reduction (c-mechanism)

5.4.1.1 Zener grain size boundary pinning

One of the main features of nanocomposites is that matrix becomes refined on adding nanosize SiC. Following the Hall-Petch relation a refinement of the grain size leads to higher strength. Furthermost, abnormal grain growth is reduced in nanocomposites, thus leading to a narrower grain size distribution. The effect of grain boundary pinning by small inclusions is described by Smith[151 107] after a semi quantitative approach by Zener:

$$\overline{R} \cong \frac{3}{4}\frac{r}{V_f} \text{ -------------------(3)}$$

where R is the average matrix grain boundary radius of curvature, depending on the radius (r) and the volume fraction (V_f) of spherical inclusions. Equation (3) is often given in the form

$$D \propto r/V_f$$

Where D is the average matrix grain diameter.
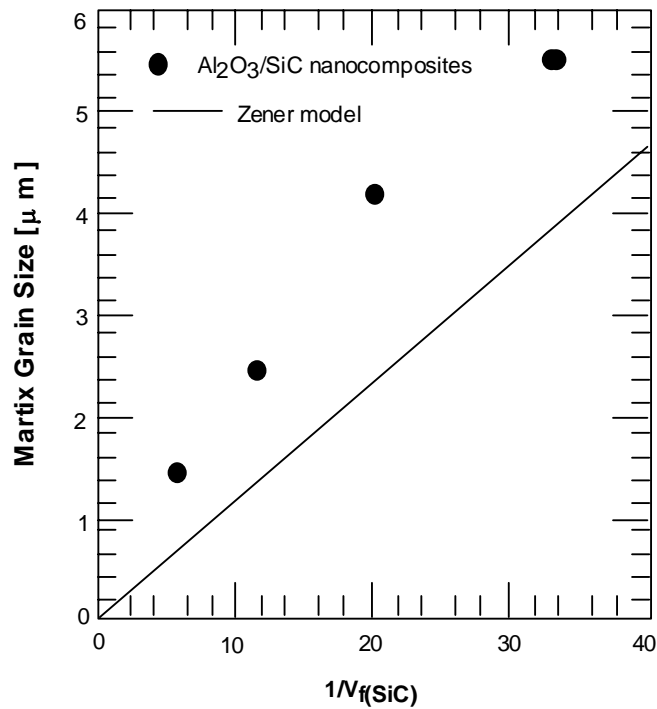
Fig. 12. Matrix size as a function of the inverse of the SiC volume fraction for Al $_2$O$_3$/SiC nanocomposites: (●) experimental data after Ref. 34; (-) prediction after eqn (3).

In Fig. 12 the Zener model (eqn (3)) is compared with experimental data where R is plotted as a function of $1/V_f$. the radius of SiC nanoparticles used in the calculation was taken to be 150 nm, which is typical for the materials studied. The model agrees well with the experimental data but large SiC volume fractions. However, one has to consider that SiC particles are not completely inert during sintering.

It has been found that α-SiC particles change their morphology from as received irregular fragments to spherical after sintering. Furthermore, for high SiC volume fractions SiC particles can form agglomerations or sinter together forming large particles. This has to be taken in account if better agreement is to be obtained between the model and experimental results at high SiC volume fraction because eqn (3) predicts larger matrix grains for larger SiC particle sizes.

However, the reduction of the matrix grain size is obvious when taken into account that monolithic alumina sintered under the same conditions possess a much larger grain size of about 20 μm.

5.5 Reduction in processing flaw size

A further explanation for the increased strength of the nanocomposites is a reduction in the size of processing flaws. Fractographical studies on broken four-point bend test beams have shown that the strength-determining processing flaws change in size and in morphology from large-volume pores in alumina to crack-like flaws due to SiC agglomerations in Al_2O_3/SiC nanocomposites.[152][36] The different processing flaw type results from the specific nanocomposite processing rather than from an intrinsic nanocomposite effect. In Al_2O_3/SiC nanocomposite powder mixtures, hard SiC agglomerates. The latter commonly cause large processing flaws such as voids in alumina ceramics.

5.6 Crack healing (annealing treatment)

Zhao et al.[140][55] suggest that SiC particles only indirectly influence the strength by enabling the compressive stress induced by the grinding process to be retained in the surface region of the test specimens. Another theory is that cracks in nanocomposites can heal during annealing. Alumina and Al_2O_3/SiC nanocomposites are indented with a Vicker's piramid to generate radial cracks. After annealing at 1300 $^\circ$ C in Ar for 2 h the material behave completely differently.[153][110] Whereas cracks in alumina grow, cracks in nanocomposites close, thus explaining the strength increase of annealing nanocomposites.

Possible reasons for the crack healing have not yet found and more systematic work is needed. However, by taking into account internal stresses, one has to distinguish between the stresses introduced by the Vicker's indentation (comparable to machining-introduced stresses), stresses introduced by the thermal expansion mismatch of Al_2O_3 and SiC and, finally, stresses due to the thermal anisotropy of alumina grains. Fang et al.[153][110] observed that residual stresses introduced by Vicker's indentation fully relax in alumina after an annealing procedure whereas compressive stresses are still present in nanocomposites.

5.7 Toughening (*K*-mechanisms)

5.7.1 R-curve effects

Concerning R – curve effects one has to distinguish between mechanisms acting on the crack wedge behind the crack tip and mechanism acting directly at or in front of the crack tip. It is well known that manolithic alumina ceramics exhibits R – curve behaviour due to crack bridging mechanisms. The fracture mode is intercrystalline with partially connected grains acting as ligaments.[154][111] In nanocomposites any toughening effects acting on the crack wedge behind the crack tip are unlikely because of the lack of bridging elements. This is supported by the transgranular fracture mode. Therefore, only mechanisms acting directly at or in front of the crack tip can be assumed to be applicable to nanocomposites. Such micro-toughening mechanisms do not necessarily lead to an increase in the toughness plateau value but they can result in a steep rise of the R – curve for very short crack lengths. This would explain a higher strength, as schematically shown in Fig. 16 where the crack resistance is plotted as a function of crack length. The slope of the tangents on the R – curves represents the strength. [154][111] By assuming the same initial flaw sizes and plateau toughness values, a higher strength can be achieved for a sharply rising R-curve.
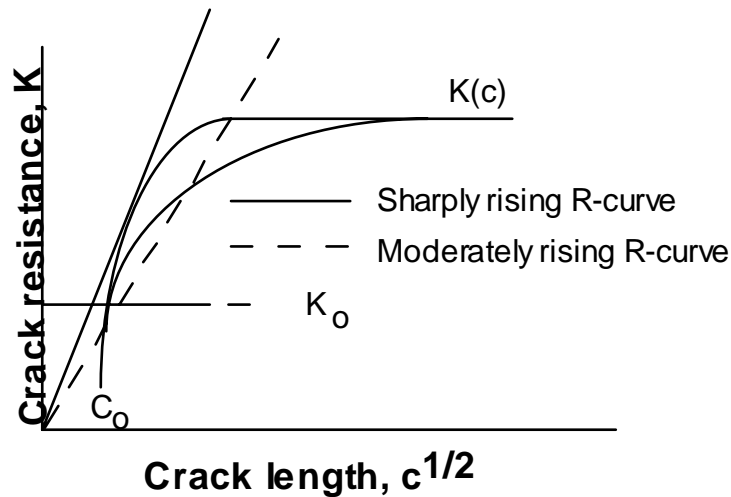
Fig. 16. Schematical dependence of the tougnness as a function of crack length by assuming a step and a flat rise for short crack lengths.

5.7.2 Crack Deflection

The interactions of a crack front with second-phase inclusions, such as spherical particles in nanocomposites, depend on the differences in the thermoelastic properties of the matrix and inclusions. If there are no differences, the planar crack front will not be influenced.[155][112] Following Faber and Evans,[156][113] in the case of such differences, the crack front will be deflected from planarity by a single particle or twisted between two neighbouring particles. The toughening of the composite is a result of diminishing the stress intensity directly at the tip of the deflected crack. The extend of toughening increase can be obtained by calculating the local stress intensities at the crack front. The toughness increase depends on the shape, volume fraction and interparticle spacing of the reinforcement. As discussed later, crack deflection can also explain the change in fracture mode.

Niihara has proposed a toughening effect due to crack deflection caused by compressive residual stresses around the SiC particles.[141] One requirement of the crack deflection theory is strong interface between the SiC particles and the matrix. Investigations of SiC/Al_2O_3 interfaces, as presented in Fig. 17, revealed that the boundary is free of second phases. 114.28 An alignment of the SiC particles with the Al_2O_3 matrix can be observed in some cases.[157][114] These examinations suggest strong adhesion between the SiC particles and the matrix. Concerning SiC/Al_2O_3 interfaces at SiC particles located at Al_2O_3/Al_2O_3 grain boundaries, Jiao et al.[157] [114] have estimated

that the interfacial fracture energy between SiC and alumina is twice that of the alumina grain boundary fracture energy.

5.8 Grain boundary strengthening mechanisms

Several authors[158] [35, 55, 59] have found that grain pullout is significantly reduced in Al_2O_3/SiC nanocomposites during polishing, machining or abrasive wear. Furthermore, the fracture mode changes to transcrystalline. All these observations indicate that matrix grain boundaries are strengthened in nanocomposites. This effect is probably the most important difference between nanocomposites and the pure matrix. Conceivable reasons for the grain boundary strengthening are: (1) deflection of a crack running along a grain boundary at an SiC particle into the grain (2) strengthening of the grain boundaries due to local internal stresses. Therefore, internal stresses are discussed in detail in the following sections.

5.9 Thermal expansion mismatch (Selsing model)

Since the microstructures of nanocomposite ceramics are formed during sintering at high temperatures, differences in the thermal expansion coefficient of the matrix (α_{matrix}) and of the nano-particles ($\alpha_{particle}$) cause strains during cooling. These thermal expansion misfit strains, $\langle \alpha * \rangle$, can be calculate by an integration over temperature. The upper limit is taken as the temperature below which plastic deformation is insignificant ($T_{plastic}$) and the lower limit is the room temperature.

$$\left\langle \alpha^* \right\rangle = \int_{T_0}^{T_{plastic}} \left(\alpha_{particle} - \alpha_{matrix} \right) dT \text{ ---------(4)}$$

The thermal expansion misfit stress, σ_T, inside a single spherical inclusion in infinite matrix can be described by the following expression after Selsing:[159] [118]

$$\sigma_T = \frac{\left\langle \alpha^* \right\rangle}{\dfrac{1+v_m}{2E_m} + \dfrac{1-2v_p}{E_p}} \text{ ----------------(5)}$$

E and v are Young's modulus and Poisson's ratio of the matrix (m) and the particles (p). The tangential, σ_T, and the radial, σ_T, stress distributions in the matrix around the particle are given by:

$$\sigma_T = -\frac{\sigma_T}{2}\left[\frac{r}{x}\right]^3 \quad \sigma_{Tr} = \sigma_T\left[\frac{r}{x}\right]^3 \text{-------------(6)}$$

where r denotes the radius of the inclusion and x is the radial distance from the inclusion surface. Assuming T $_{plastic}$ as 1500°C and the room temperature thermoelastic data given in Table 5, eqn (5) leads to a compressive hydrostatic stress inside the SiC particle of 2.0 Gpa for the Al_2O_3/SiC and 4.3 Gpa for the MgO/SiC system. Tensile hydrostatic stresses of 500Mpa and 600Mpa can be calculated for the Si_3N_4/SiC and the Al_2O_3/TiN systems, respectively. Evidently, a change in fracture mode occurs only in systems with high compressive stresses within the nano-particles such as Al_2O_3/SiC and MgO/SiC.

Table 5. ***Thermoelastical data for matrix and nanophase***

	E[Mpa]	*v*	$\alpha[10^{-6} K^{-1}]$
Al_2O_3	*400*	*0.23*	*8.3*
Si_3N_4	*300*	*0.27*	*3.2*
MgO	*300*	*0.18*	*14*
TiN	*~470*	*~0.25*	*9.4*
SiC	*480*	*0.17*	*4.4*

5.10 Average internal stresses

A model developed by Taya et al.[160][119] incorporates the influence of the particle volume fraction on the average residual microstress in the matrix for a composite material with spherical inclusions showing a thermal expansion mismatch. Their model is based on Eshelby's equivalent inclusions approach referring to the inelastic eigenstrains. The average residual microstresses inside the matrix and the particles, $\langle\sigma_m\rangle$ and $\langle\sigma_p\rangle$, are given by the following expressions:

$$\frac{\langle\sigma_p\rangle}{E_m} = \frac{-2(1-V_f)\beta\langle\alpha^*\rangle}{(1-V_f)(\beta+2)(1+v_m)+3\beta V_f(1-v_m)}$$

$$\frac{\langle\sigma_m\rangle}{E_m} = \frac{2V_f\beta\langle\alpha^*\rangle}{(1-V_f)(\beta+2)(1+v_m)+3\beta V_f(1-v_m)} \quad\text{-----------(7)}$$

where $\quad \beta = \dfrac{1+v_m}{1-2v_p}\cdot\dfrac{E_p}{E_m}$

In the case of $\alpha_m > \alpha_p$, the average thermal stresses are compressive inside the particles and tensile in the matrix. For $V_f=0$, eqn (7) provides the same value for the stresses inside the particles as the Selsing model.[159][118] Another boundary condition is givenby mechanical equilibrium with $\langle\sigma_m\rangle(1-V_f)+\langle\sigma_p\rangle V_f=0$.

Figure 18 shows experimental results together with a prediction using eqn (7). A stress-free temperature of 1500°C, below which plastic deformation is insignificant, is assumed. (By considering that internal stresses at the surface of a nanocomposite are not relieved after annealing at 1300°C, as observed by Fang et al.,[153][110] the stress-free temperature must be somewhere between 1300 and 1550°C which is the minimum hot-pressing temperature to get fully dense nanocomposites).
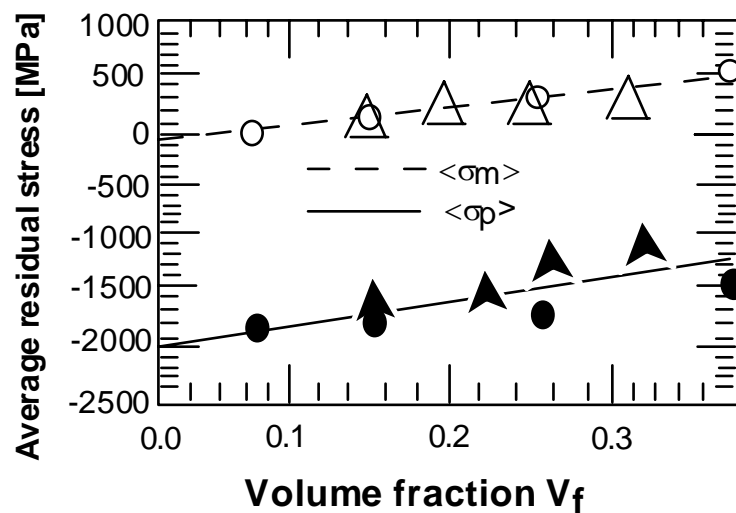
Fig. 18. **Average residual microstresses in the matrix** $\langle\sigma_m\rangle$ **and nano inclusions** $\langle\sigma_p\rangle$**for Al₂P₃/SiC nanocomposites. (△,▲) adapted from Todd et. al; (○, ●) Ref. 120)**

It has to be emphasised that all theoritical calculations concerning internal stresses depend strongly on value used for the thermoelastic properties of the matrix and inclusions.

Levin et al.[161] [123] have presented a model for the influence of the SiC particles on the fracture toughness of nanocomposites. The average tensile stress field in the matrix due to the thermal expansion mismatch of Al_3O_2 and SiC reduces the fracture toughness. As shown in Fig. 18, the average microstress in the matrix is approximately 100 Mpa for an Al_2O_3/5 vol% SiC nanocomposites. SiC submicron particles within the grains strengthen the grain boundaries because of compressive radial stress components, thus increasing the fracture toughness via a change in the fracture mode. It has been claimed that a net increase in toughness can only be achieved for small SiC volume fractions because the strengthening effect of grain boundaries is high and only in the case are the average internal stresses small. The maximum increase of fracture toughness at 5 vol% SiC as shown by Niihara[141] [4] agrees with the model proposed by Levin et al.[161] [123] and is plausible when taking into account the two opposite effects of grain boundary strengthening and average tensile internal stresses.

5.11 Local stress distribution

For discussion of the grain boundary strengthening effect due to internal stresses it is helpful to review the stress fields around the SiC particles. For the model presented in this review, a superposition of stresses in an arrangement of several boundaries including a grain boundary is assumed. Figure 19 shows the configuration assuming nine particles in a cubic-body-centred arrangement with an average nearest particle spacing equivalent to a SiC volume fraction of 2.5%. One particle is located in the plane. The remaining particles are the same distance from that plane. Each particles causes a stress field which can be calculated using the Selsing equation (eqn (3) and (4)). The total stress at each point in the x-y-plane highlighted in Fig. 19 can easily be calculated assuming a simple superposition. For simplicity, only the superimposed stresses normal to the plane are plotted in Fig. 20. Obviously, the particle at the grain boundary generates high tensile stresses immediately around it and the other eight particles nearby to the plane generate compressive stresses up to 120 Mpa. Figure 20 makes evident that SiC particles within the Al_2O_3 grain boundaries strengthen the grain boundaries due to radial compressive stresses. The influence of SiC particles within grain boundaries is still unclear, but could be expected to generate countervailing tensions across the boundary.
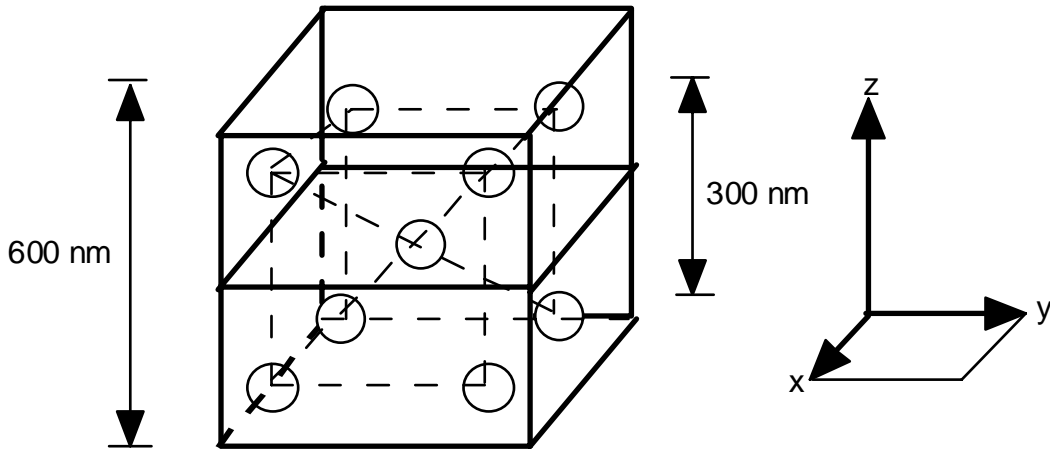
Fig. 19. Configuration for the stress distribution model
in Fig. 20.

5.12 Final remarks on strengthening and toughening mechanisms

Table 6 summarises all the mechanisms discussed in the modeling chapter. The strength increase observed in nanocomposites can be explained by a decrease in critical flaw size. As shown above, not only in the size of processing flaws decreased but also their morphology changes completely. Furthermore, the matrix grain size is reduced with a narrow size distribution due to the grain boundary pinning by inert SiC particles. Dislocation network plays only a minor role.

A clear identifications of the toughening mechanism in nanocomposites remains difficult because, first, the toughness increase is small or even absent and, second, there is no single persuasive mechanism (Table 6). A balance exists between mechanisms decreasing toughness, i.e. crack deflection or grain boundary strengthening. All these mechanisms depend highly on specific processing and microstructural details. However, it appears that grain boundary strengthening due to local radial compressive stress components around SiC particles or due to a riveting effect is the most likely nanocomposite effect. The mechanism explains the transition in fracture mode as well as the improved resistance to wear and machining damage.

Table 6: Summary of strengthening and toughening mechanisms

Mechanism	Comment	Ref.

Zener grain boundary pinning mechanism (c-mechanism)	Matrix grain sizes are drastically reduced (typical for nanocomposites)	141,142,**Erreur ! Signet non défini.**
Reduction in processing flaw size (c-mechanism)	Strength increase can be fully explained by observed change in processing flaw type (careful processing is very important)	152
R-curve effects (K-mechanism)	Steep rising R-curve behaviour is proposed (no experimental evidence)	150
Crack Deflection (K-mechanism)	Cracks seem to be reflected at SiC particles (importance for toughening is unclear)	156
Thermal expansion mismatch (grain boundary strengthening)	Fracture mode is changed to transcrystalline if $\alpha_{particle} < \alpha_{matrix}$ (eg. For Al_2O_3/SiC)	**Erreur ! Signet non défini.,**
Average internal stresses (grain boundary strengthening)	Average tensile stresses in matrix if $\alpha_{particle} < \alpha_{matrix}$ (toughness is reduced)	160,161, **Erreur ! Signet non défini.,Erreur ! Signet non défini.**

Local stress distribution (grain boundary strengthening)	Local compressive stresses in matrix grain boundaries if $\alpha_{particle} < \alpha_{matrix}$ (can explain change in fracture mode)	161

5.13 Inhomogeneous State of Nanoparticles and Nanocrystallities

Contrary to massive solids the lattice structure of nanoparticles may be non-uniformaly distorted (translational invariance of the crystal lattice is absent). Multicomponent nanoparticles may exhibit concentrational and phase inhomogeneities as well. To a certain extent, nanocrystals also posses these features.

5.14 Crystal-lattice inhomogeneous state

In nanoparticles and nanocrystallities the fraction of 'surface' (or 'interface') atoms is large. Then, appreciable distinctions between nano-objects and massive bodies in lattice parameters and the types of atomic structures are plausible. These difference manifest themselves in normal and tangential relaxations of nanoparticles.[54] An atom on the surface has fewer neighbours than one in the volume, all the neighbours of the former being located on one side only. This breaks the equilibrium of the interatomic forces and gives rise to both the change of interatomic spacing (normal relaxation) and tensile deformations which 'smooth' verticles and edges (tangential relaxation).

A rough estimate of the average distortion of the interatomic distances *a* in nanoparticles caused by surface tension is shown below: [55]

$$\Delta a / a = \theta_2 . \kappa . \frac{\overline{\gamma}}{l'} ....(7)$$

where θ_2 is the numerical coefficient of the order of 1 (in the case of isotopic spherical particles it may be estimated as $^2/_3$), κ is the volume compressibility coefficient. According to the estimate the lattice construction is about several tenths of a percent at typical values of parameters $\kappa \sim 10^{-11}$ m^3/J, $\gamma \sim 1$ J/m^2 for nanoparticles with radius $l \sim 10$ nm.

Here it should be mentioned that parameters entering this formula are, in turn, size-dependent. The surface energy of nanoparticles, for example, depends on *l* as follows: [56]*

$$\bar{\gamma}' = \bar{\gamma}.\left(1 - \theta_3 \frac{a}{r} + \theta_4 \left(\frac{a}{r}\right)^2 + ...\right),................(8)$$

where numerical coefficient $\kappa \sim 10^{-11} m^3/J$, $\gamma \sim 1\ J/m^2$. According to this estimate the surface energy of nanoparticles decreases as *r* decreases which is intuitively clear, since both the number of bonds formed by the surface atoms and their bond energy are reduced as size decreases. Size-dependent corrections are, in a general case, functions of temperature.[59] The difference in the lattice parameters of contacting nanoparticles may seriously influence the process of interparticle sliding (see Section 5.2.2).

For several decades contradictory experimental results were calling into question eq. (7) for the contraction of interatomic spacing (see references in Ref. (45)). Some of these ambigious results are caused by experimental artifacts and difficulties, while others are associated with the complicated spatial distribution of lattice parameter distortions. In the absence of oxide layers,[60] absorbed impurities, etc., there is an average overall contraction in the lattice parameter of a nanoparticle. However, interatomic spacing in the outer part of nanoparticles may be expanded despite the contracted interior.[61] Moreover, the degree of distortion varies with crystallographic as a result of the anisotropy of the volume compressibility coefficient.[62,63] In summary, the experimental and theoretical results show that the average contraction of the lattice parameter in the nanoparticles is inversely proportional to nanoparticles radius *r*.

5.15 2.3.2 Concentrational inhomogeneity

The spatial distribution of a second component over the bulk of heterogeneous nanoparticles and nanocrystallities ma contrast with that for analogous macrocrystals. A non-uniform distortion of the crystal lattice in nanovolumes (see the previous section) and the comparability of the width of segregated layers Δ_s, with the radius r may both bring about an inhomogeneous distribution of the second component.

One may estimate the characteristic of a nano-object when the segregated layer occupies half its volume. A simple geometrical consideration gives the following relationship:[65]

$$r_s^* = \theta_5 . \Delta_s , \text{..................................(9)}$$

where the numerical coefficient θ_5 is of the order of unity. For spherical nanoparticles (nanocrystallites) it is close to 5. Using $\Delta_s \approx 3a$ as typical width of the segregated layers the corresponding diameter of nanoparticles (nanocrystallites) is ~10nm. Thus, under some conditions the multicomponent nanocrystals with grains of the size may be considered 'massive' segregated layers.

If the main contribution of driving force for segregation is the mismatch in atomic radii of the matrix and foreign atoms, Δ_s and r_s^* may be estimated for a heterophase nanocrystal. The mismatch may be described by the relative difference $\delta_s = (a_f / a - 1)$ where a_f is the effective radius of a foreign atom. If the nanocrystallites in a nanocomposite the components of which have shear moduli G and G are elastically isotropic and possess non-slipping boundaries (see terminology in Section 3.1.2), the characteristic length l_{sl}^* is as follows:[65]

$$r_{sI}^* = \theta_6 a. \left(\frac{\delta_s^2 a^3 (G - G)}{kT} \right)^{1/3} \text{.............................(10)}$$

where the numerical coefficient $\theta_6 \approx 3.5$, k is the Boltzman constant, and T is temperature. This estimate was obtained by equation kT to the energy of the elastic interaction of the foreign atom with the non-slipping interface. Provided that other driving forces for segregation (heat of mixing, the difference between surface energies of the component) are negligible or cancel each other, when a nanocrystallite has a shear modulus G less than that G of the neighbouring crystallites segregation in that nanocrystallite becomes impossible. So, the concentration of foreign atoms in the vicinity of interfaces diminishes in elastically softer nanocrystallites.

Segregation effects change the composition of the interior of nanoparticles. It can be shown [66] that the average concentration c of the second

component for a two-component nanoparticle varies with its size, following the relationship:

$$\bar{c} = c_b + \theta_8 . (c_s - c_b) \frac{\Delta_s}{r} \dots\dots\dots\dots\dots\dots\dots\dots\dots\dots (12)$$

where the numerical coefficient $\theta_8 \approx 3$, c_s and c_b are concentrations in the surface layer of width Δ_s and in bulk of nanoparticles, respectively. If concentrations c_s and c_b were independent of r over the whole range of sizes, this relationship would be of a general character. When size r is not too small, one may estimate the change in the concentration of foreign atoms in the smaller the size r, the stronger the concentrational inhomogeneity which may reach as much as 10%. This conclusion agrees with the numerical simulations of small-atomic clusters [67] and experiments [68] with CuNi nanoparticles.

Certain conclusions about the character of the independence of surface concentration c^s on nanoparticle (nanocrystallite) radius r can be drawn on the basis of simple mass balance considerations. In the limit of small nanoparticles, when all the atoms belong to the surface, the surface composition in an ensemble of nanoparticles would be identical to the average composition in the massive alloy. [69] Such a decrease of the surface segregation has been observed experimentally. [70] In the opposite of very large particles they will behave like semi-infinite crystals, and the surface composition would be similar to that obtained in microscopic samples. In the in the intermediate range of sizes, where the number of surface sites is not a negligibly small fraction of the total number of sites available in the particle volume, there exists a regime where segregation to the surface tends to decrease the bulk concentration of the segregant.

The depletion of the segregated atoms, which would follow from elementary mass-balance considerations, may be impossible if the physical and/or chemical properties are size-dependent. For instance, the change in the surface energy (see eq. (8)) may modify the segregation effect. The lattice contraction (eq. (7)) and the external pressure also effects segregation phenomena.

In their effects on segregation, applying external pressure and contracting the crystal lattice of nano-objects are to a certain degree equivalent to the difference in the atomic radii of the segregant and matrix atoms, [71] which is

described by the relative size mismatch δ_s . In fact, external pressure P is connected with the change in the relative size mismatch δ_s by the simple relationship (cf. eq. (7)):

$$\Delta \delta_s = \frac{P}{3}.\left(\kappa_1 - \kappa_2 \right), \ldots\ldots\ldots\ldots(13)$$

where κ_1 and κ_2 are the volume compressibility of the segregant and the solvent, respectively. The hydrostatic stress include by surface tension, approximated as $2\gamma/l$, may, thus, change the relative size mismatch by $\Delta\delta_s$. According to the well-known Hume-Rothery rule (if the relative size mismatch exceeds the 15% limit, solid solubility will be restricted [72]) a critical size l^*_{sol} should exist, above which the solid solubility remains qualitatively the same:

$$\Delta^*_{sol} = \left| \theta_2 . \frac{\overline{\gamma}.(\kappa_1 - \kappa_2)}{0.15 - \delta_s} \right| \ldots\ldots\ldots\ldots\ldots\ldots\ldots(14)$$

Similarly to thin films and needle-like crystals, the thermodynamic condition of phase equilibrium in nanoparticles alter due to the significant contribution of the surface to the energetic balance and new faces unusual in a massive state may appear. Therefore the phase diagrams of nanoparticles (and to a lesser extent for nanocrystals) and the parameters of structural transformations may be very different from those expected for macrocrystals.

The free energy of two-component nanoparticles may be decreased by the formation of phase inhomogeneities within their volume. Considering the free energy of a two-component system A-B with fractions (f_0; 1-f_0) of constituent atoms which is at equilibrium within a certain temperature interval: both the change in the volume contribution due to the redistribution of component, i.e. the formation of a new phase (e.g. a chemical compound) in the surface layer of width $l - r$ (Fig. 2) and the change in the term brought about by the formation of an interface (of area S_2) between the phases correspond to an energy loss. The decomposition is energetically favourable when the gain caused by the change in the surface (of area S_1) energy exceeds this loss. This situation may be described by the following equation [74]

$$F_{v1.f1} + F_{v2.f2} + \frac{\overline{\gamma}_1 S_1}{V_1} + \frac{\overline{\gamma}_{1.2} S2}{V} < F_{v.f_0} + \frac{\overline{\gamma}_i S_1}{V'} \quad .....(15)$$
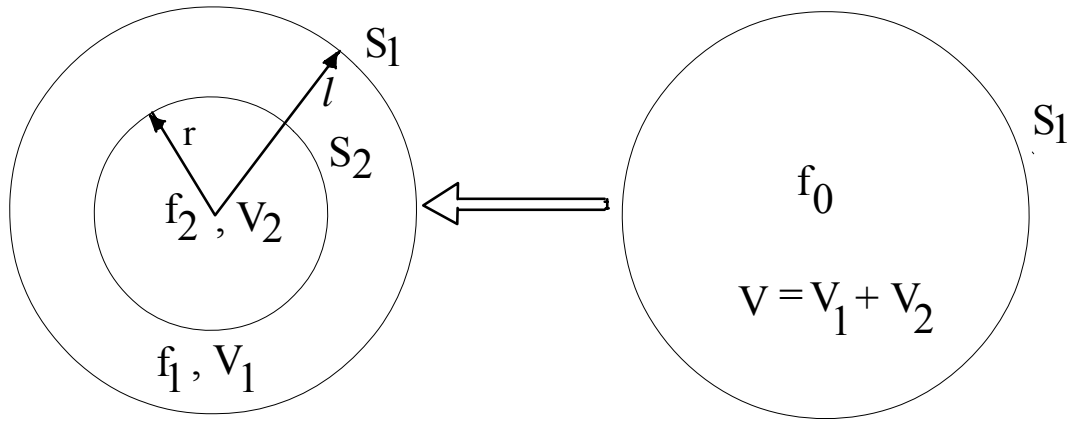
Fig. 2. Schematic transformation of two-element nanoparticle with initially hamogeneous structure into the heterogeneous phase.

where f_1 and $f_2 = 1-f_1$ are the concentrations of component A in nanoparticles formed after decomposition, the subscript $_i$ denoting the initial state of the surface.

Manifestations of these effects have been detected in alumina nanoparticles (Fig. 3). [75] The phase composition of nanoparticles can depend on both their dimensions and the synthesis route. Spatially inhomogeneous structures have been observed in alumina nanoparticles. Both electron and X-ray diffraction have revealed similar in zirconia nanoparticles.

Generalizing the experimental observations of multiphase nanoparticles one can conclude:

- all the nanoparticles with the exception of the smallest ones appear to be multiphase, the phase composition varying with nanoparticle size;

- surface layers are enriched with high temperature modifications (having higher symmetry and lower density). This indicates that the decrease in the entropic and surface contributions to free energy outweighs the increase in the nanoparticle's internal energy due to stabilization of high-temperature modifications;

- a nanoparticle's structure depends on the particular methods of synthesis, so the particle size cannot be used ambiguously for characterizing the nanoparticle structure and its structure-sensitive properties.

5.16   2.4.1. Thermodynamic aspects of size effects

It's a natural to begin with a discussion of the differences between the equilibrium state of nanoparticles and that of conventional macrosystems. The conventional definition of thermodynamic functions must be modified to take account of the large contribution of the surface energy, which is comparable with that of the nanoparticle volume energy *F* of any elementary system containing N atoms may be represented as follows: [76]

$$F = f_1(P,T).N + f_2(P,T).N^{2/3} + f_3(P,T).N^{1/3} + f^4(P,T) + f^5(P,T).N.\log N,......(16)$$

b)
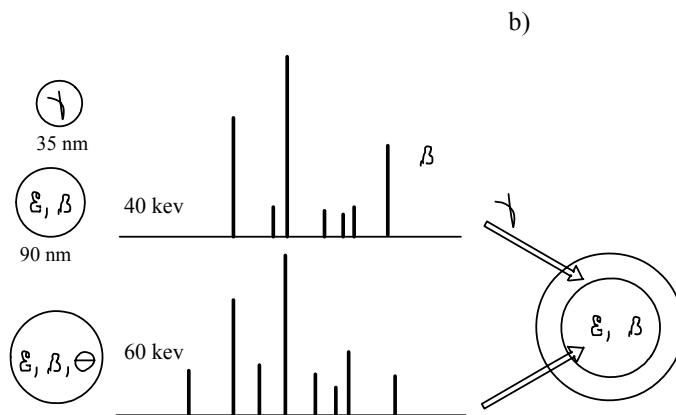
Fig. 3. Phase in alumina nanoparticles of different size. (a) X-ray diffraction patterns. (b) Electron diffraction paterns. The phase composition of the nanoparticles is shown schematically.

where the first four terms refer to volume, surface, edge and vertex contributions into nanoparticle free energy, respectively, the last term corresponding to the entropy contribution.*

It is very important to note that the characteristic size l_{th} associated with the qualitative modification of thermodynamic parameters in nanoparticles follows from the comparison of the first two terms in the previous equation: [14]

$$l_{th}^* \sim \frac{\overline{\gamma} a^3}{\Delta\mu'} \dots\dots\dots\dots\dots\dots\dots(17)$$

Where $\Delta\mu/a^3$ is of the order of the energy density, or in the case of multicomponent nanoparticles, is comparable with the heat of mixing per unit cell (cf. eqs (1) and (84)).

Using typical values for the crystal lattice parameter $a \sim 3 \times 10^{-10}$ m, surface energy $\gamma \sim 1 J/m^2$ and $\Delta\mu \sim kT$ one may obtain $l_{th} \sim 10$ nm.

It is noteworthy that ordinary thermodynamic relationships are not valid for small systems. In the case of macrosystems they have the following form:

$$\mu = \left(\frac{\partial F}{\partial N}\right)_{P.T} = \frac{F}{N}; S = -\left(\frac{\partial F}{\partial T}\right)_{N.P} = -N.\left(\frac{\partial F}{\partial T}\right)_{P}; \left(\frac{\partial \mu}{\partial T}\right)_{N.P} = -\frac{S}{N} \dots\dots(18)$$

where μ is the chemical potential; S, the entropy. To obtain the correct thermodynamic relationships for small-atomic systems two different chemical potentials

$$\mu = \frac{F}{N}$$

and

$$\mu = \left(\frac{\partial F}{\partial N}\right)_{P.T}$$

should be used then: [76]

$$\left(\frac{\partial \overline{\mu}}{\partial N}\right)_{P.T} = \frac{\mu - \overline{\mu}}{N}; \left(\frac{\partial \overline{\mu}}{\partial T}\right)_{N.P} = -\frac{S}{N}; \left(\frac{\partial \mu}{\partial T}\right)_{N.P} = \left(\frac{\partial S}{\partial N}\right)_{P.T} . ----(19)$$

Naturally, these two chemical potentials become identical in macrosystems as N→∞. The relationships are valid when nanoparticles and a macrosystem are in equilibrium and the ergodic hypothesis holds (equivalance of averagings over time and over coordinates). This allows one to average thermodynamic parameters over a large number of corresponding ensembles of small systems and to establish thermodynamic relations for each small system. The essential result of averaging is that: intensive parameters (for instance, *P, T,* etc.) may depend on the number of atoms in these systems, i.e. on the size of particles. This statement means that small systems possess an additional degree of freedom compared to the analogous macrosystems.

There are a number of effects caused by fluctuations in the thermodynamics parameters in nanovolumes. In general, in the case of ordinary systems thermodynamic relations are valid for the average magnitudes of extensive parameters (volume, entropy, etc.). they hold only owing to the smallest of fluctuations in small systems are significant and comparable with the average values [77] so that, for example, phase transitions in small systems are noticeably smeared.

5.17   2.4.2 Structural transformations

The temperature of phase transitions or structural transformations, their width (due to fluctuations; see the previous section) [77, 78] depend on nanoparticle size. The condition for phase 1 to be stable in a massive specimen at a certain temperature is that : $F_1 < F_2$. When the contribution of surface terms to the free energy cannot be neglected, phase 2 may become the equilibrium phase (cf. eq. (15)) [48]

$$F_{v_2,f_2} + \frac{\overline{\gamma_2}S_2}{V_2} < F_{v_1,f_1} + \frac{\overline{\gamma_1}S_1}{V_1} \dots\dots\dots\dots\dots\dots\dots(20)$$

The simplest expression for the relative difference of phase transition temperature T_t between nanoparticles and massive bodies may be derived from this condition for the phase equilibrium and the Clasusius-Clapeyron relationship: [79, 80]

$$\Delta T_{t=} \frac{T_t}{\lambda} \cdot \left(\frac{\overline{\gamma}_2 S_2}{V_2} - \frac{\overline{\gamma}_1 S_1}{V_1} \right),..(21)$$

where λ is the heat of phase transition per unit volume. Thus, one can see that the change in the temperature of phase transitions ΔT_1 may be roughly estimated as $T_t\gamma/\lambda l$.

The last formula implies that with decreasing nanoparticle size the phase with lower surface energy (packed more tightly) become energetically favoured. For example, in the case of the common body-centered cubic (BCC) and face-centered cubic (FCC) crystal lattice the latter may become energetically more favourable, since its specific volume and surface energies are less than those of the BCC lattice. Thus, if a FCC phase is stable in the massive state, it will exist with nanoparticles sizes decreasing until nanoparticles begin to melt. If a relatively loosely packed BCC-structure is stable in a massive body within a certain temperature range, a structural transition to a denser structure becomes possible. Experiment s have shown that nanoparticles of Nb, Mo, W, Ta – with mean sizes of 5 – 10 nm have hexagonal close – packed (HCP)- or FCC – lattice instead of the BCC – structure observed in a massive state, and that nanoparticles of less-common metals Y, Gd, Td, Dy, Ho, Er, Tm have FCC- rather than HCP-lattice. [48]

Viewpoint may turn out to be useful in analyzing phase transitions, the dynamic characteristics of nanoparticle structure and similar feature. Nanoparticles may be described as having an enhanced mobility of the crystal lattice. It has been observed that nanoparticles of radius less than the characteristic scale $l*_{1,2}$ (see section 3.3.1) often gradually change shape. The mean-square displacement of atoms in nanoparticles are greater than those in the massive state under the same temperature conditions.[48] This effect may also occur in nanocrystals and measurements of their thermal expansion indirectly support this suggestion. [82]

5.18 Metastable phase diagrams

Metastable phase diagrams with one of the constituent phases being a nanophase are quite new. Simplest estimates of phase equilibrium may be obtained by taking into account the contribution of surface energy to the free

energy. [83]
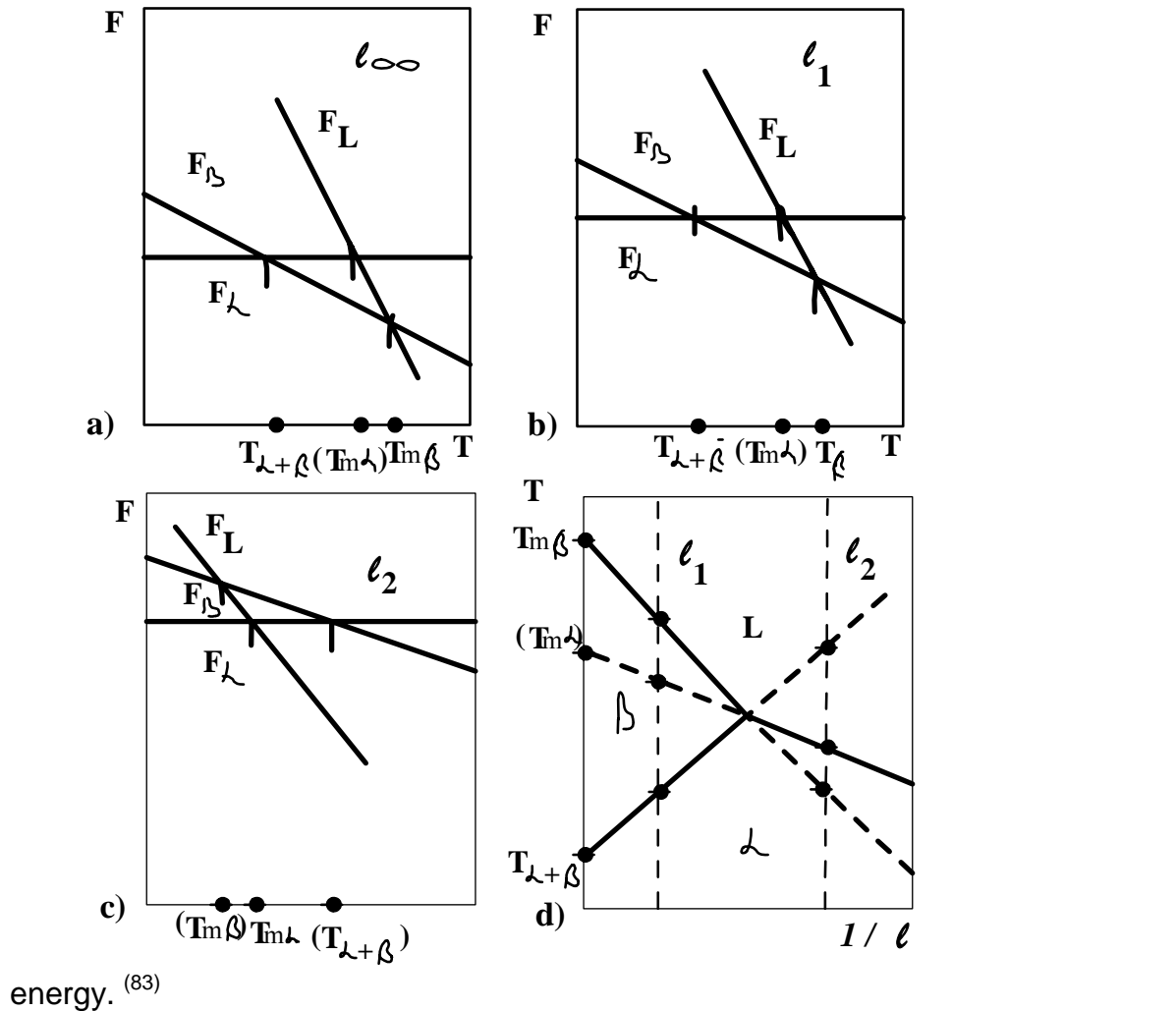
Fig. 4. Polymorphism in nanoparticles of material that also shows polymorphism in the massive state. (4) Phase diagram of infinite body. (b) Phase diagram for nanoparticles of size l_1. (c) Phase diagram for nanoparticles os size l_2 ($l_1 > l_2$). (d) T corresponding diagram in coordinates $T - 1/l$. here T_{m2} and T_{mB} are the melting temperatures of α and β - phases, respectively. L denotes the liquid phase.

As one would expect, binary nanophase systems show more diverse phase diagrams than elementary nanophase systems. Melting temperature, temperatures of polymorphous transformations (see the previous section) and other characteristics of phase diagrams depend on the nanophase size. Thus, the phase diagram of nanophase materials become three-dimensional, the third coordinate being the nanophase size *l*.

On the basis of eq. (21) one may obtain the binary phase diagrams of nanophase materials. Figure 4 schematically presents a part of the phase diagrams of a material which is polymorphous in the massive state of different nanoparticles sizes. [79] (The surface energy γ was assumed to be only slightly dependent on temperature and concentration.) From which one of the phase transitions does not exist.

Another situation arises if the material in the massive state does not show polymorphism (see fig. 5). For example, if the β - phase is stable over the whole
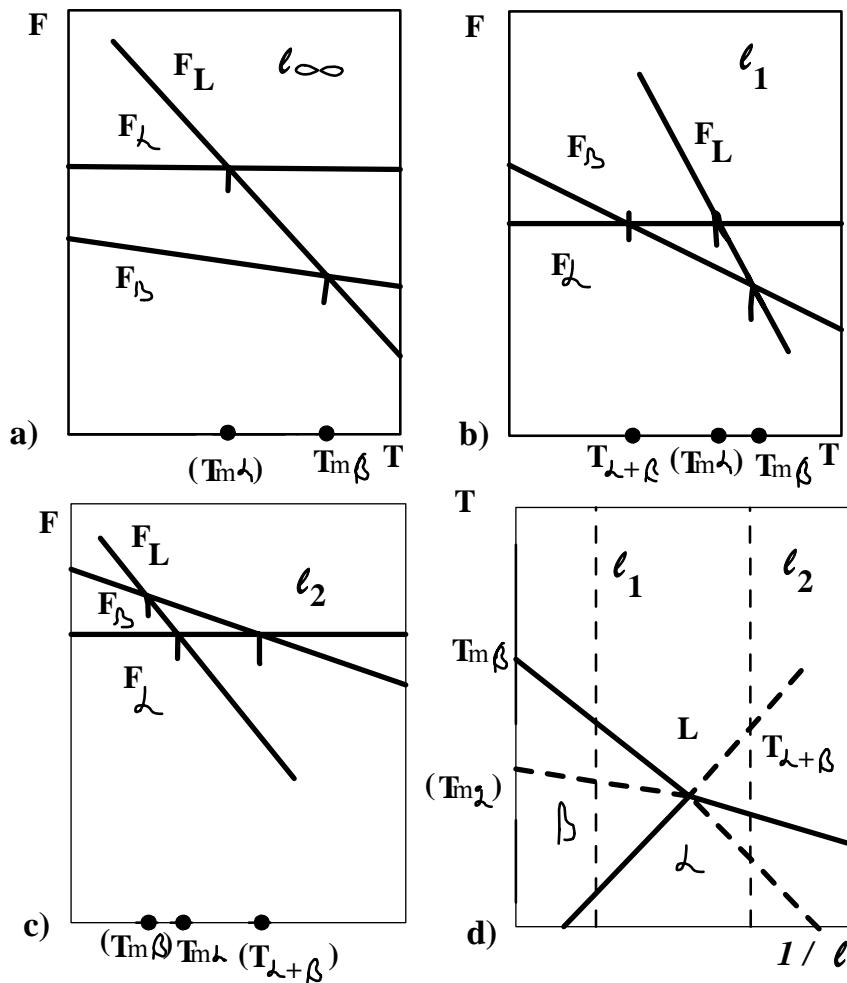
range of temperature in massive bodies, decreasing the sample dimensions may give rise to the formation of the $\propto$ -phase.

2.2.1 *Hall-Petch effects.* Strengthening of polycrystalline materials by grain size refinement in technologically attractive because it generally does not adversely affect ductility and toughness. The classical effect of grain size on yield stress [19, 20] can, among other possibilities, be explained by a model invoking a pile-up of dislocations against grain boundaries, which results in a dependence of the hardening increment on the square root of the grain size *D*:

$$\tau = \frac{k_{HP}}{\sqrt{D}} \dots\dots\dots\dots\dots\dots\dots\dots\dots\dots\dots(12)$$

Where k_{HP} is a constant. This is the classical Hall-Petch effect.

5.19   2.2.2 Limits to Hall-Petch behavior: dislocation curvature vs. grain size.

Whereas many metallic materials obey such a relationship over several orders of magnitude in grain size, it is inevitable that the reasoning behind equation (12) must break down for very small grains. A clear limit for the occurrence of dislocation plasticity in a poly-crystal is given by the condition that *at least one dislocation loop must fit into average grain* [Fig 8(a) and (b)]. The characteristic length, i.e. the loop diameter [equation (1)], must now be compared with the grain size *D* as the relevant size parameter:

$$d(\tau) = D \dots\dots\dots\dots\dots\dots\dots\dots(13a)$$

or

$$\tau = \frac{2T_d}{bD} \approx \frac{Gb}{D} \dots\dots\dots\dots\dots\dots(13b)$$

Figure 8(c) illustrates schematically this limit on Hall-Petch behavior: "conventional" grain size strengthening can be expected only to the right of the heavy line which signifies the limiting condition (13a) – (b). for Cu, as am example, the critical grain size estimated in this way is about 50nm; this value is in reasonable agreement with experimental results by Chokshi *et al.* [23], as shown I fig. 9.

The plastic behavior of nanocrystalline materials with grain sizes below the critical value is not fully clear. Some authors (e.g. Refs [25-27]) also report an "inverse" Hall-Petch effect, others find an insensitivity to grain size or a reduced Hall-Petch constant k_{HP} in this range. It has been argued that because of the viscous behaviour of amorphous materials (which can be considered the

limiting case for grain refinement) the grain size strengthening effect will have to be reversed once the grain size *D* starts to approach the grain-boundary thickness δ_b. One possible explanation for such a softening effect comes from a re-consideration of the line tension T_d in equation (13b). the more refined expression

$$T_d = \frac{Gb^2}{4\pi} In \frac{r_1}{r_0} \quad ....(14)$$

contains a lower (r_0) and an upper (r_1) cut-off distance for the stress field of the dislocation. In conventional materials r_1 generally lies in the micrometer range and therfore significantly exceeds r_0 (for which values between 2 and 10b are commonly assumed); this justifies replacing the logarithmic term by a constant. However, in nanocrystalline materials it is reasonable to equate r_1 to the grain size, which now gives $r_1 \approx r_0$ and makes *T* sensitive to the value of the grain size *D*. Therefore, we now have a case in which the characteristic length (d) is a function of the size parameter (*D*). The resulting strength increment is given by

$$\tau = \frac{Gb}{2\pi D} In \frac{D}{r_0} ....(15)$$

This expression vanishes rapidly as the grain size *D* approaches the lower cut-off distance r_0. An even more refined expression has been obtained by Scattergood and Koch [22].

They draw upon Li's model [29] for the generation of dislocations from grain-boundary sources: as the dislocation density ρ scales inversely with grain size *D*, the obstacle spacing is $L \sim 1/\sqrt{p} \sim \sqrt{D}$, which yields

$$\tau \approx \frac{Gb}{\sqrt{D}} In \frac{D}{r_0} ....(16)$$

This expression, which is schematically shown as dotted line in Fig. 8(c), reduces correctly to Hall-Petch behavior for $D \gg r_0$. It gives a possible interpretation of grain-boundary softening behavior in nanocrystalline Cu and Pd[22].
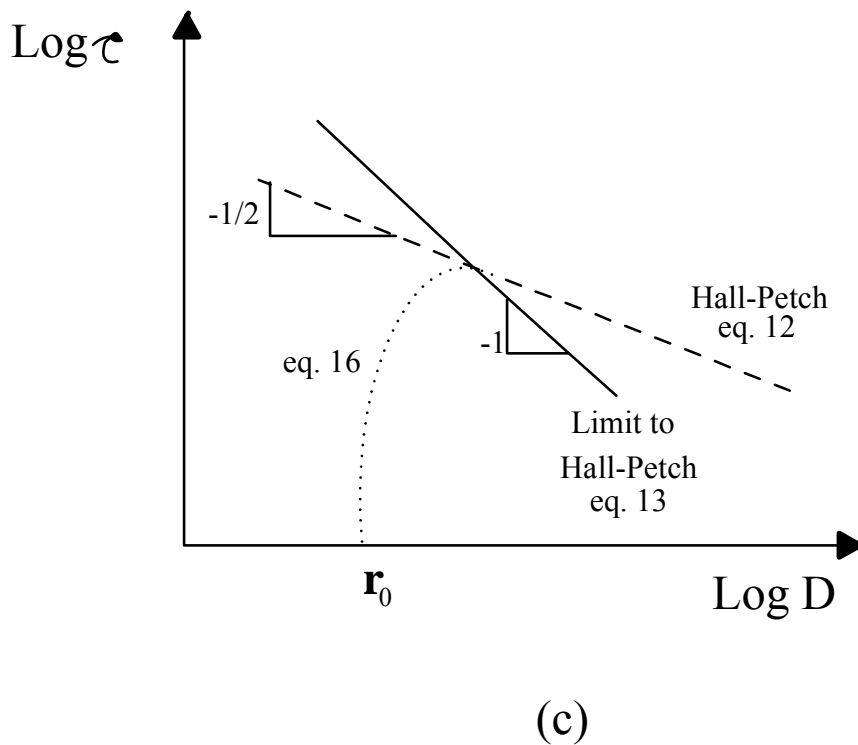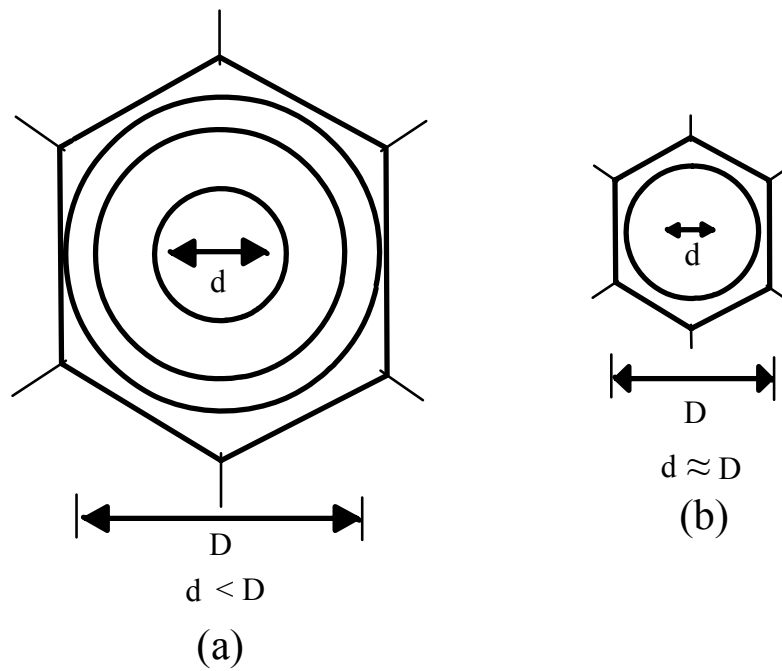
Fig. 8. Grain size strengthening, as explained by pile-ups of dislocation loops against grain boundaries (a). this mechanism must break down when the diameter *d* of the smallest loop no longer fits into a grain of size *D* (b). The limiting condition is shown as the heavy line in (c) where the shear strength τ is plotted schemetically as a function of grain size *D*. Hall-Petch behavior can only be found

to the right of this line; abnormal or inverse behavior may result otherwise. The dotted line reflects schematically the Scattergood-koch [22] equation [equation (16)].
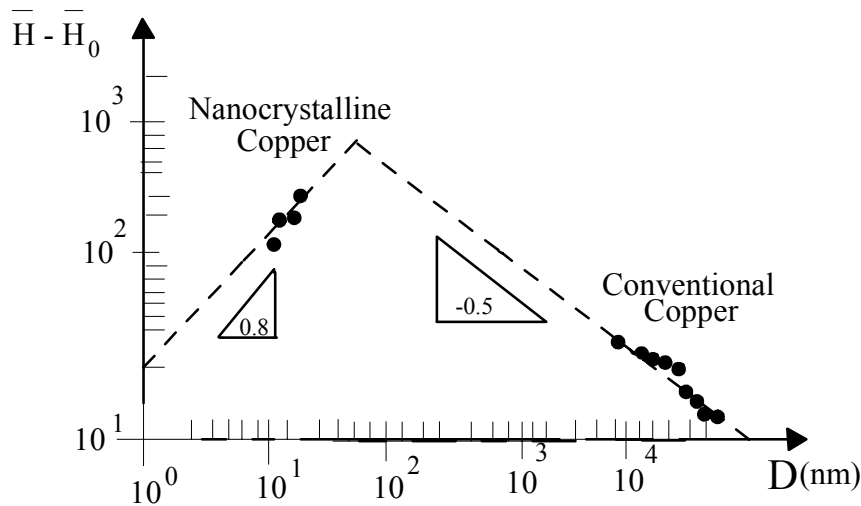
Fig. 9. Inverse Hall-Petch behavior in nanocrystalline Cu (H-H_0) denotes the hardness increment, D the grain size): the classical behavior breaks down at a grain size of about 50 nm, in agreement with an estimate based on the loop diameter [equations (13a) – (b)]. Replotted after Chokshi *et al.* [23].

6 OPTICAL PROPERTIES

6.1 Introduction:

Optical properties of nanomaterials are much important for several optical applications. It is an important field of study as the optical properties of nano-composites differs largely from their constituents. These constituents are to be chosen in such a way that the typical grain dimensions and spacing must be much smaller than an optical wavelength. The greater part of optical studies of nanocomposites is to prepare composites having a desired effective dielectric constant. In several theoretical & practical approach have been taken to find out this dielectric constant from those of the constituents and this controls the basic idea of practical application also.

6.2 Classical optics:
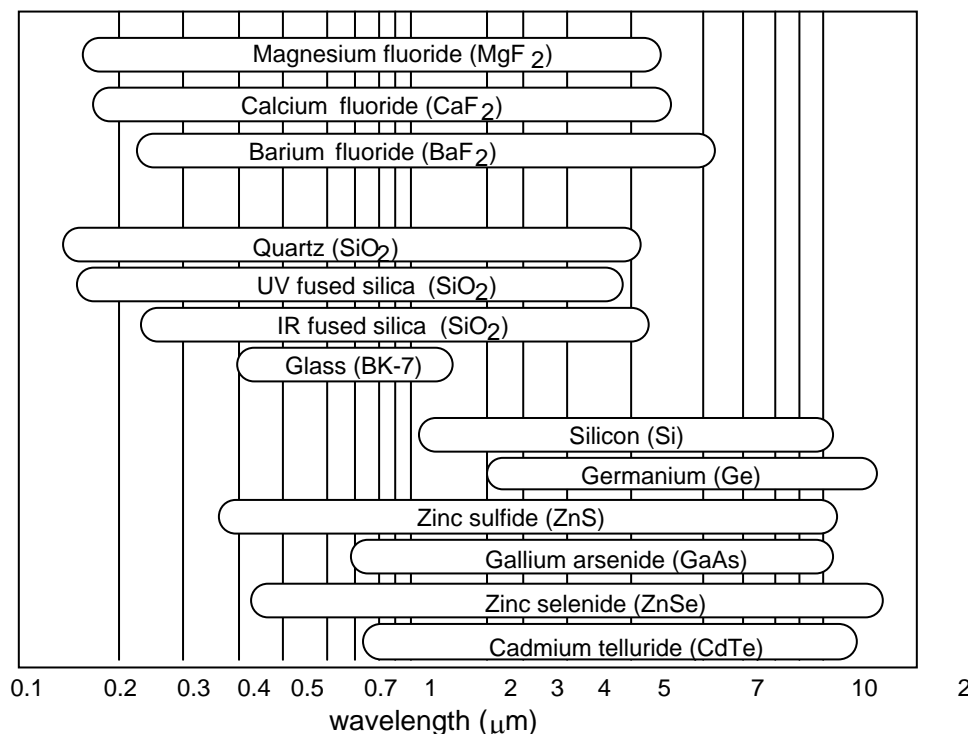
Figure: Spectral band widths within which selected classical optical materials transmit light

From the electromagnetic point of view light is just the transverse undulation of electric & magnetic fields that are perpendicular to each other. Now, if in the path of light propagation the medium shows some discontinuity in its dielectric constant some part of it is reflected and the rest part begins to transmit and in a more involved situation absorption takes place. Reflection occurs due to change of phase of phase of the incident wave and has nothing to do with the material on which light is incident. The phenomena of refraction depends upon the refractive index – a properly that origin from the molecular or atomic polarization developed due to the electromagnetic perturbation (light). In an isotropic dielectric (so named as light propagates with same velocity in all direction) the refractive index is accounted by the fact of induced vibration of bound electron in atomic orbit. When the frequency of incident matches with the naturally frequency of bound electron, absorption takes place. In conducting material (metal) the undulating wave just gets damped & the energy is absorbed by the metal. For an anisotropic medium the direction of light propagation & that of energy flux are not same unlike an isotropic medium.

6.3 Absorption of light in semiconductor materials

Two processes are fundamental to the operation of all semiconductor opto-electronic devices:

Electron hole pair (EHP) generation by the absorption of a photon. This leads to certain important phenomenon like photoconductivity, which is responsible for the operation of semiconductor photodetectors.

Recombination of a electron and a hole can lead to a phonon or photon emission. One utilizes this radiative recombination process for the emission of light in a useful wave length for different applications. Spontaneous radioactive electron hole recombination is the underlying concept of the working of light emitting diodes (LED'S), while stimulated electron-hole recombination is employed in semiconductor lasers.
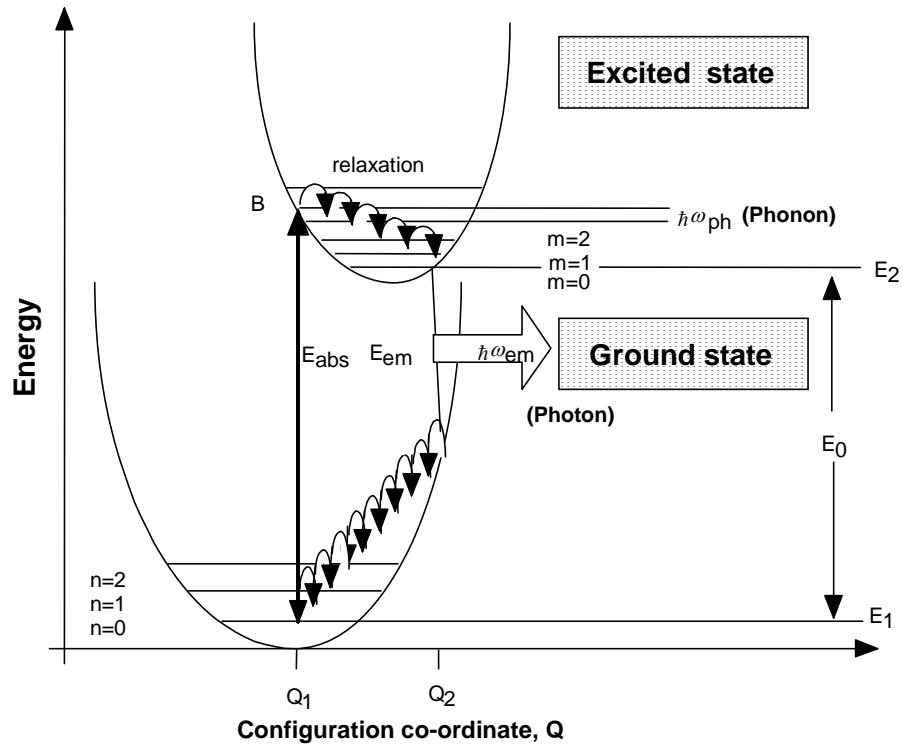
Figure: Configurational coordinate diagram following Ridley (1998), showing optical absorption and emmision energies as well as the vibrational levels.

6.3.1 Energy – momentum relations

In free space the energy E and momentum p (only magnitude) of an electron are related by

$$E = \frac{p^2}{2m_0} = \frac{\hbar^2 k^2}{2m_0}$$

where k is the magnitude of the wave vector-associated with the wave function for the electron and M_0 is its rest mass. The E-K relation is a simple parabola. The motion of electrons in the conduction band and holes in the value band is governed by the Schrodinger equation and the periodicity of the lattice concerned.

6.3.2 Effective Mass

Near the bottom of the conduction band, the E-k relation may be given by

$$E = E_c + \frac{\hbar^2 k^2}{2m_c}$$

where E_c is the energy at the bottom of the conduction band and m_c is the effective mass of the electron in the conduction band (Fig. 10). Similarly, near the top of the valence band,

$$E=E_v - \frac{\hbar^2 k^2}{2m_v}$$

where E_v is the energy at the top of the valence band and m_v is the effective mass of the hole in the volume band. (fig. 10)

$$E_v = E_c - E_g$$

where E_g is the band gap.

(a)

(b)
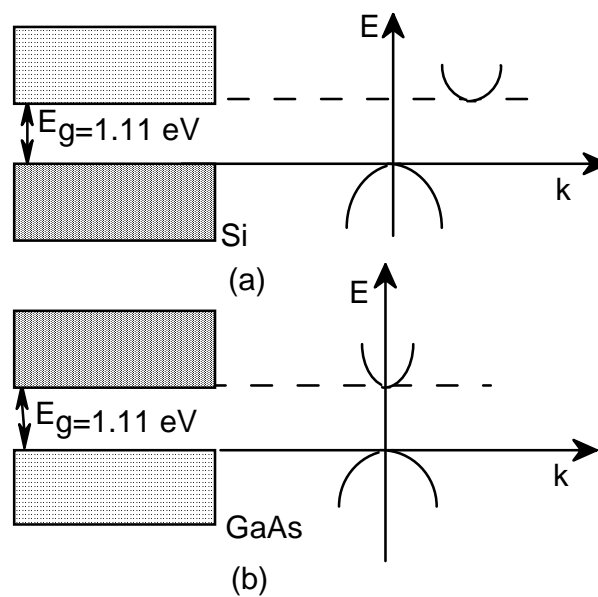
Figure: Approximately the E-k diagram at the bottom of the conductance band and at the top of the valence band of Si and GaAs by parabolas.

6.3.3 Direct and indirect – gap semiconductors

The band gap is the difference in energy between the lowest point of conduction band (conduction band edge) and the highest point of the valence band (valence band edge).

In the direct absorption process, a photon is absorbed by the crystal with the creation of an electron hole pair. Semiconductors using the phenomena have their valence band maxima and their conduction band manima corresponding to the same momentum and are called direct-gap materials (Fig 10 (b)). For such materials, $E_g = \hbar\omega_g$ where ω_g is the absorption frequency.

In the indirect absorption process, the band gap involves electron and holes separated by a wave vector k_c i.e. the maximum of valence band and minimum of conduction band do not correspond to the same momentum. Such materials are called indirect gap materials (Fig. 10(a)). If a photon of wave vector K and frequency Ω is created in the process, then

$$\vec{k}(\text{photon}) = \vec{k}_c + \vec{k} \cong 0\, ; \ \hbar\omega = E_g + \hbar\Omega$$

The photon energy $\hbar\Omega$ is, in general, much less than E_g.
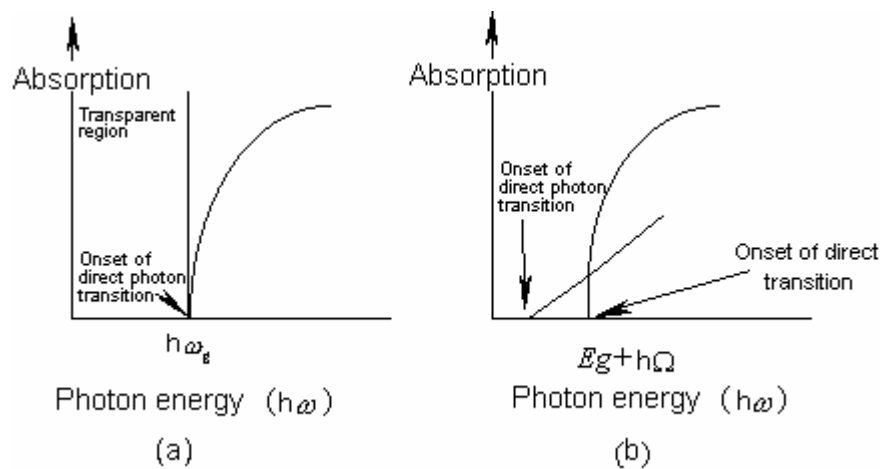
Figure: (a) Optical absorption in a crystal with direct gap (b) Optical absorption in a crystal with indirect gap.

6.3.4 Radiative & Non – radiative recombination

A molecule in its excited state must eventually return to the ground state, unless it gets involved in some photochemical reaction.

After the initial absorption process,

$$A + h\upsilon \rightarrow A^{'*}$$
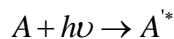
where $A^{'*}$ is either electronically excited molecule with excess vibrational energy is S_1 (first excited singlet) state or a molecule excited to higher singlet states S_2, S_3 etc, the various possible photophysical are as follows:

$A^{'*} \rightarrow A + heat$	Internal conversion (IC)	$S_n \Rightarrow S_1$
$A^{*} \rightarrow A + heat$	Internal conversion (IC)	$S_1 \Rightarrow S_0$
$A^{*} \rightarrow A + h\upsilon_f$	Fluorescence emission	$S_1 \Rightarrow S_0$

$A^* \rightarrow {}^3A + heat$	Intersystem crossing(ISC)	$S_1 \Rightarrow T_1$
${}^3A \rightarrow A + h\nu_p$	Phosphorence emission	$T_1 \Rightarrow S_0$
${}^3A \rightarrow A + heat$	Reverse intersystem crossing(ISC)	$T_1 \Rightarrow S_0$
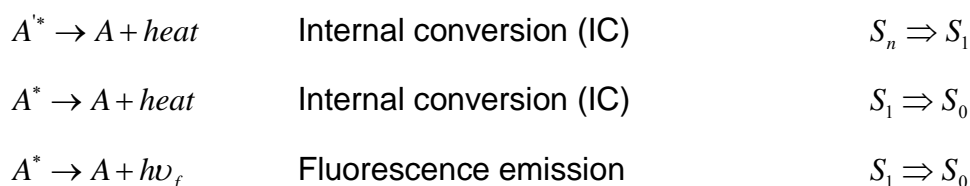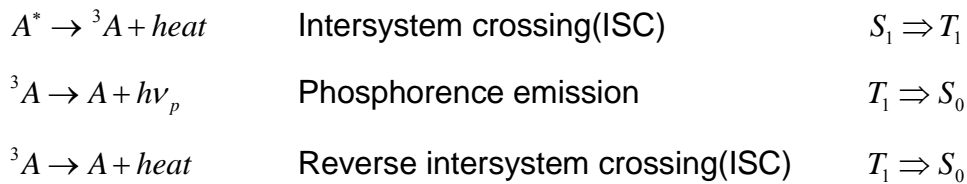
Here, A*, ^{3}A and A refer to molecule in first excited singlet state, molecules in triplet state and in the ground state respectively. Radiative transitions are denoted by straight arrows, while non – radiative processes are denoted by wavy arrows. In radiation less processes such as internal conversion and intersystem crossing, the excess energy is lost to the surroundings as thermal energy. Radiation less transition occurs at the point of intersection of potential energy surfaces.
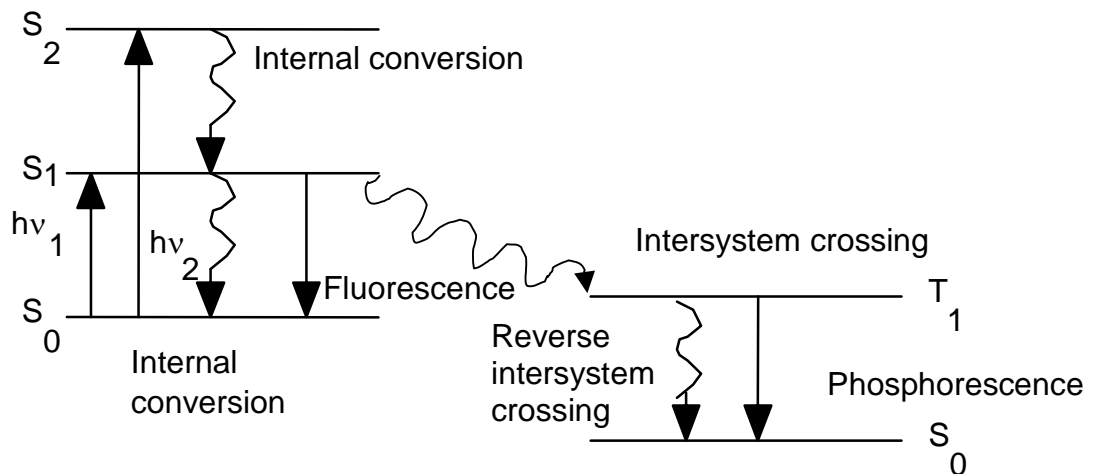
Figure: Possible optical recombination processes in a material

Initially, the molecule may be raised to higher electronic energy states S_2, S_3 etc. or to higher vibrational levels of the S_1 state by absorption of electromagnetic radiation in a time period 10^{-15} (rate constant, K = 10^{15} s^{-1}) obeying Frank-Condon principle. The electronic energy of S_2, S_3 states or the excess vibrational energy os S_1 state is quickly lost to the surroundings by a mechanism known as internal conversion (IC) (k ~ 10^{13}-10^{12}s^{-1}). Once the molecule has reached the zero vibrational level of S_1, it may return to ground states by:

radiative fluorence emission $S_1 \Rightarrow S_0$,

non – radiative internal conversion $S_1 \Rightarrow S_0$,

non – radiative intersystem crossing (ISC) from S_1 to T_1 ($S_1 \Rightarrow T_1$) followed by radiative phosphorence emission $T_1 \Rightarrow S_0$ or non – radiative reverse intersystem crossing $T_1 \Rightarrow S_0$. (Fig.)

The internal conversion process is so called because it occurs between electronic states of same multiplicity (i.e. same spin type), whereas intersystem crossing involves states of two different spin manifolds). Also, since a radiative transition from triplet to singlet state is forbidden by selection rules, phosphorence emission may occur minutes or even hours after the initial absorption while fluorescence is a short lived emission process of the order of 10^{-8} sec.

6.3.5 Laser

The term 'laser' stands for 'light amplification by stimulated emission of radiation'. Many atoms have one or more excited energy levels with lifetime of the order of 10^{-3} sec. Such long-lived states (called metastable states) play a key role in laser transitions. The laser is a device which produces a light beam with some amazing properties:

- o The light is coherent i.e., the waves are all exactly in phase with one another.
- o The light is very nearly monochromatic and the beam hardly diverges.
- o The light is extreme intense.

Consider two energy levels E_0 & E_1, in an atom. Then the possible transitions involving electromagnetic radiation which can occur between them are:

Induced absorption- The atom is E_0 state is raised to E_1 state by absorption of a photon of energy $E_1 - E_0 = h\nu$.

Spontaneous emission- The atom in E_1 state may return to the ground state E_0, by emitting a photon of energy $h\nu$.

Induced (or stimulated) emission- in the case, an incident photon of energy $h\nu$ causes a transition from E_1 to E_0. The emitted light waves are exactly in phase with the incident waves, hence, an enhanced beam of coherent light is obtained.
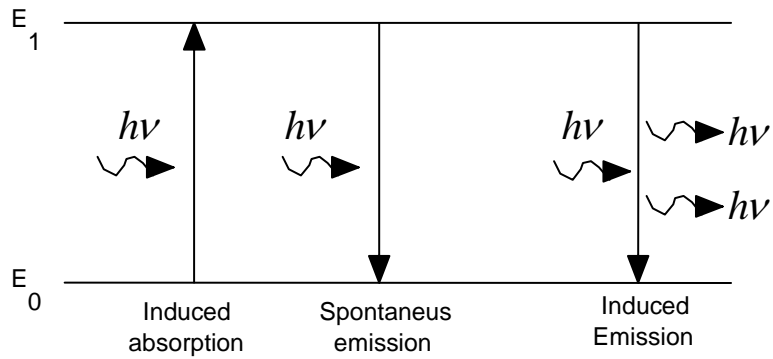
Figure: Schematic representation of induced absorption, spontaneous emission and induced emission processes.

Consider an assembly of atoms having metastable state of energy E_1. If by some means, a majority of atoms are raised to the metastable level and then this assembly is irradiated by light of frequency v_1 there will be more induced emission from the metastable level than induced absorption by the lower level. Hence the original light will be amplified considerably. This is the basic concept behind the operation of a laser. The process of raising majority of the atoms from the ground state to the metastable is called population inversion. It can be achieved in a number of ways, one of them being optical pumping (Fig.). This method is used in a ruby laser, the first successful laser. Other examples of lasers are the helium – neon laser and the solid state lasers used in compact-disc player.
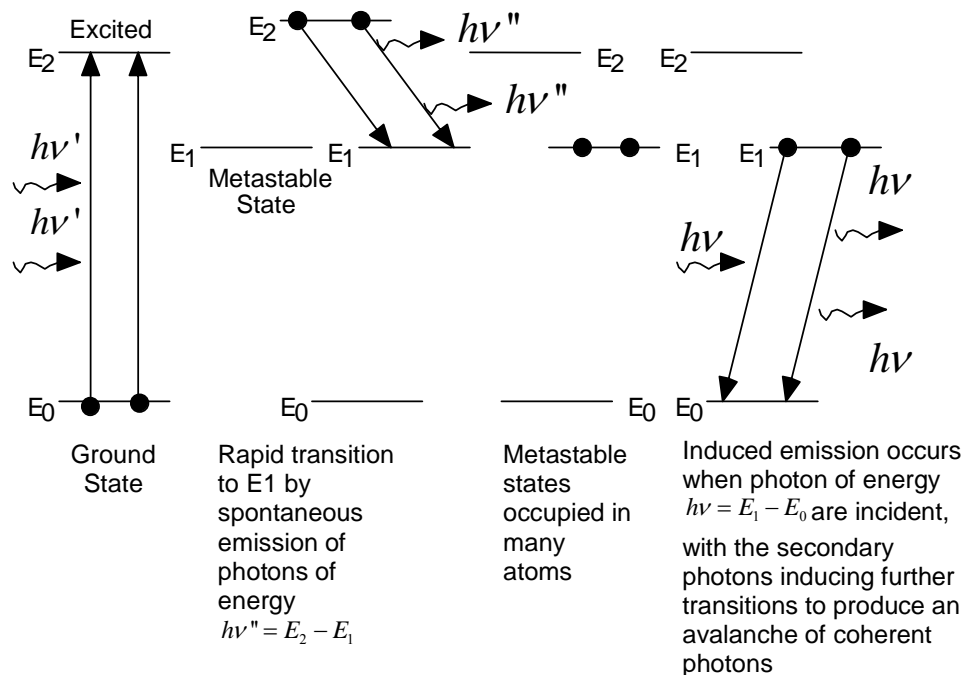
Fig. The principle of laser

6.4 Optical properties of a translucid object

6.4.1 Model of an ideal translucid object

If we define a translucid object that is subjected to an incident light as shown in the figure. The incident light upon reaching the object will go through several dispersion modes, i.e. reflection, scattering and absorption. Reflection of light can be either by specular or diffuse reflection processes.

Incident
beam I_0

Specular
reflection R

θ θ diffuse
reflection R

Absorption

R R

Transmitted light
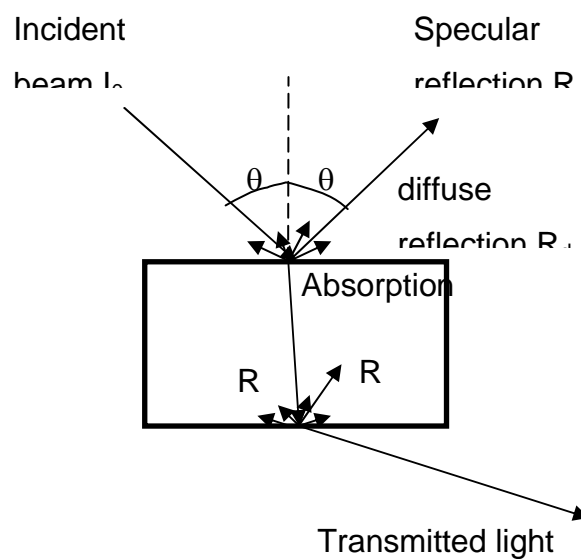
Figure 2.1 : interaction of light with an ideal translucid material

The specular reflection arises from the interface where there is a change in the refractive index. The reflected light is always at an angle θ_2 with the normal that is equal to the angle of incidence, θ_1. The diffuse reflection however depend on the surface properties of the material. The diffused light is scattered in all directions including some part that is 'back scattered' i.e. rays are opposite to the direction of the incident beam of light.
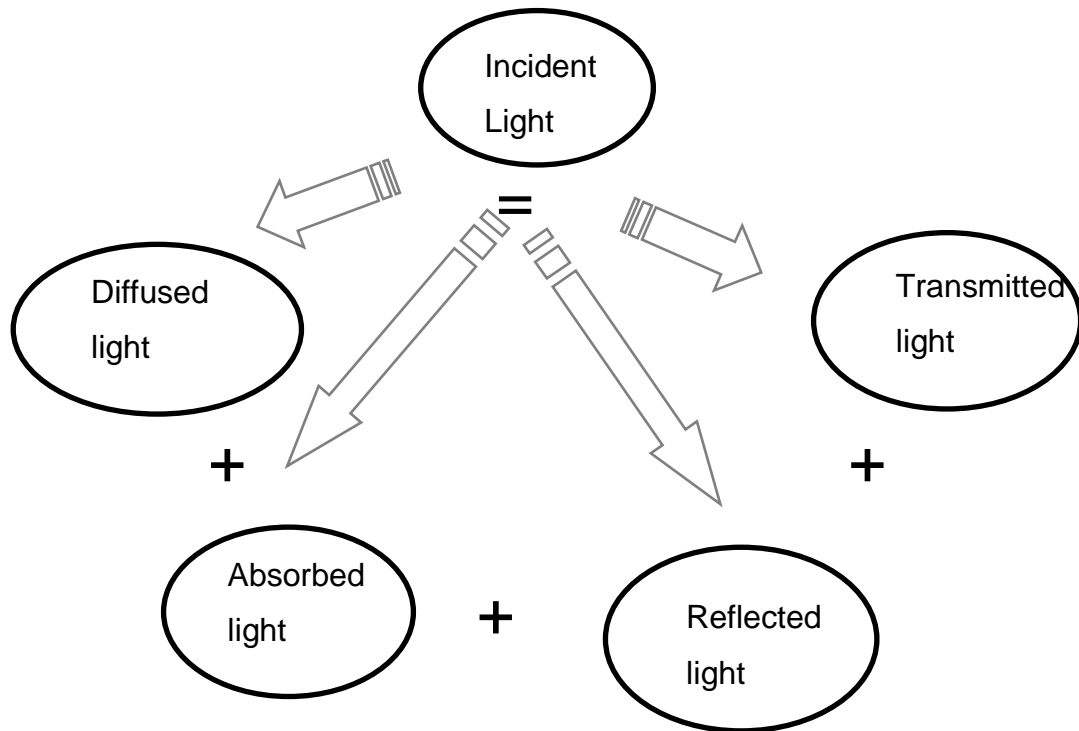
Figure 2.2 : Representation of different dispersion modes of an incident beam on a material.

Absorption of light in the material leads to several processes of excitation in the material. Absorption depends on the dielectric property of materials. Rays that are not reflected, scattered or absorbed are the ones that are transmitted.

6.4.2 Doped translucid material

With respect to the previous case, the model used for metal-doped translucid materials is different. The dispersion modes are the same but the intensity of each mode is different with respect to the ideal case. For example, the intensity of absorption increases due to the metallic nanoparticles that have been included in matrix. The scattering shows a non-negligible increase if the size of the nanoparticles are sufficiently large. In the last case, the scattering occurs in a non-geometric fashion in virtually all directions. This scattering arises due to the presence of surface plasmons that will be discussed later. The transmitted light however is reduced in intensity since the metallic nanoparticles block (absorb/reflect/scatter) some part of the incident beam of light.

Incident
Ray I_0

Specular
reflection R_s

θ | θ

Diffuse reflection
R_d

Scattering

Absorption

Metallic nanoparticle

R_d | R_s

Transmitted beam
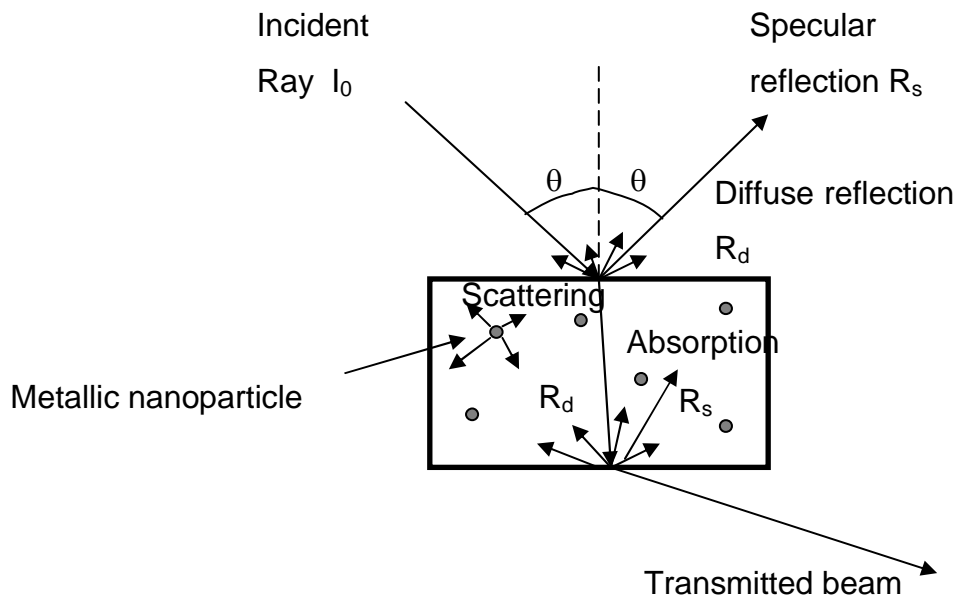
Figure 2.3 : translucid material with metallic nanoparticle inclusion

6.4.2.1 Model of real case of a metal doped translucid material

This model can be used in most of the practical cases of metal doped translucid materials, like metal inclusions in glass, ceramic, polymers etc. The major assumption necessary to apply the model is to consider that atleast a certain depth of the dielectric material is translucid. With respect to the bulk translucid material properties the size of metal inclusions effect the optical propertis of the composite. Generally one has to consider the absorption, scattering in the host material and the multipolar excitations in the nanometric metallic particles

6.4.2.1.1 Refractive index n and absorption coefficient k

The propagation of electromagnetic radiation in a material can be characterised by the refractive index of the material which is the ratio of velocity of the propagation of light in vacuum to the velocity in the material, $n = C_{vacuum}/C_{material}$., while the absorption coefficient k, describes the loss of the intensity of the incident light in the material. It is possible to relate the refractive index to the coefficient of absorption through the consideration of the dielectric constants of the material. If we consider an incident beam of electromagnetic radiation E with an angular frequency ω propagating in the Z-axis in

a non-magnetic media with a conductivity of $\sigma(\omega)$ with a dielectric constant $\varepsilon(\omega)$, then we can express as :

$$\varepsilon\varepsilon_0\mu_0\frac{\partial^2 E_x}{\partial t^2} + \sigma\mu_0\frac{\partial E_x}{\partial t} = \frac{\partial^2 E_x}{\partial z^2} \quad \ldots\ldots\ldots\ldots(2.1)$$

where, ε_0 et μ_0 are respectively the permittivity and permeability in vacuum. In case of a magnetic material, we have to replace μ_0 by $\mu\mu_0$, where μ is the magnetic susceptibility of the material.

The solution of the above equation is of the type :

$$E_{x_1} = E_0 e^{i\omega(t-\frac{z\tilde{n}}{c})} \quad \ldots\ldots\ldots\ldots(2.2)$$

where, $c = \dfrac{1}{\sqrt{\varepsilon_0\mu_0}}$, $\tilde{n}$ represents the complex refractive index of the material. $\tilde{n}$ can be related to the real refractive index ,n, and the absorption coefficient, k, by substituting equation (2) in the equation (1).

$$\tilde{n}^2 = \varepsilon + \frac{i\sigma}{\varepsilon_0\omega^2} = (n-ik)^2 = n^2 - k^2 - 2ik \quad \ldots\ldots\ldots\ldots(2.3)$$

By definition, $\tilde{n}$ can be correlated to the dielectric function of the material by the following equation:

$$\tilde{n}^2 = \tilde{\varepsilon} = \varepsilon_1 - i\varepsilon_2 \quad \ldots\ldots\ldots\ldots(2.4)$$

This complex dielectric function describes the response of electrons in an oscillating field of frequency ω. The equations (2.4) and (2.5) allows the correlation of the complex refractive index ñ and the absorption coefficient k to the real ε_1 and imaginary part ε_2 of the dielectric constant of the material.

$$n^2(\omega) - k^2(\omega) = \tilde{\varepsilon}_1(\omega)$$
$$2k(\omega) = \tilde{\varepsilon}_2(\omega) \quad \ldots\ldots\ldots\ldots\ldots\ldots\ldots\ldots (2.5)$$

6.4.2.1.2 Reflectance R

The total reflectance consists of the specular reflectance, that can easily be determined, and the diffuse reflectance. The diffuse reflectance can be determined by simply subtracting the specular reflectance from the total reflectance.

$$R_{total} = R_S + R_{diffuse} \qquad (2.6)$$

The specular reflectance R_S is defined as :

$$R_s = \frac{I_{R_s}}{I_0}$$

$$(2.7)$$

where, I_{R_s} is the intensity of reflected light at the interface where the refractive indices are different, and I_0 is the intensity of incident light at the interface where the refractive indices are different. For a wave incident perpendicular to the surface of the sample, R_s, can be calculated from the following equation :

$$R_s = \left|\frac{\tilde{n}-1}{\tilde{n}+1}\right|^2 = \frac{(n-1)^2 + k^2}{(n+1)^2 + k^2} \quad \dots\dots\dots\dots\dots\dots 2.8$$

6.4.2.2 Absorbance (or extinction) A

Following Beer-Lambert' law, the absorption is defined as :

$$A = -\log_{10}(\frac{I_T}{I_0}) \quad \dots\dots\dots\dots(2.9)$$

where, I_T is the intensity of the transmitted light across the material and I_0 is the incident intensity of light. The absorbance can be defined with respect to the refractive index and the absorption coefficient by the relation:

$$A = -\log_{10}\left\{(1 - \frac{(n-1)^2 + k^2}{(n+1)^2 + k^2})^2 \cdot \exp(\frac{-4\pi k D}{\lambda})\right\} \quad \dots\dots\dots\dots(2.10)$$

where D is the thickness of the sample and λ is the wavelength of the incident beam of light.

6.4.2.3 Surface Plasmon mode & linear optical properties:

Since clusters are an ensemble of atoms, we can consider two types of effects that are related to the size of these clusters: the intrinsic effects that are related to the changes in the volume and surface of the cluster, and extrinsic effect that is related to the size of the cluster which varies according to the external constraints that are generated due to the applied field. The interface between the cluster and the surrounding media plays an extremely important role in the electrical and optical properties. Numerous theories have been developed to explain the properties of clusters as a function of their nature, size, shape and the surrounding matrix. No single theory however can explain all the effects in entirety.

One of the notions that needs to be developed is the definition of the surface plasmons. Since a large number of atoms of the metallic nanoparticle are actually on the surface, the neighbouring electrons form sort of an electron gas since they are in continuous interaction with their neighbours.[162] The surface plasmons are thus collective excitation of free electrons on the surface of the clusters. In other words, plasma oscillation in metal is a collective longitudinal excitation of the conduction electron gas and a plasmon is a quantum of a plasma oscillation – an excitation that occurs when an electron passes through a cluster, nanoparticle, film where surface atoms are considerably large.

Incident light on any material creates an electric field that excites the electrons leading to a movement in the electrons in the atoms. These electronic movements will induce electrical dipoles that will oscillate between the centre and the surface of each atom, as shown in the figure.
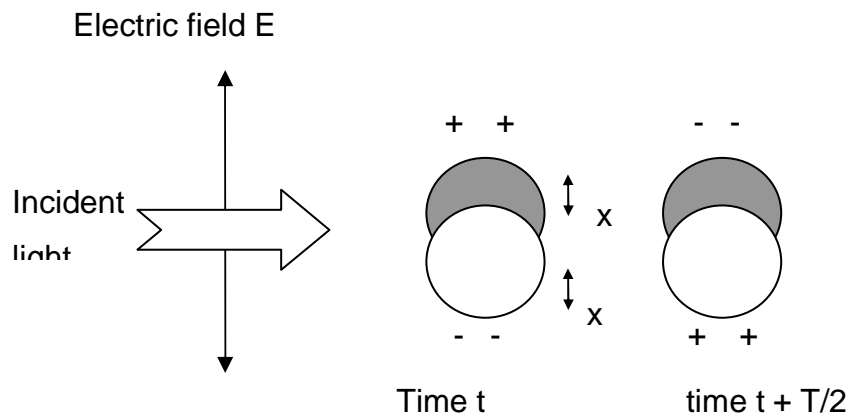
Figure2.4 : excitation of surface plasmons in nanoparticles upon the application of an electric field

The equation describing the movement of one free electron under an applied external electric field is given by

$$E = E_0 \cdot e^{-i\omega t}$$

When this field is created by an incident electromagnetic wave of frequency ω, then the field experienced by the electrons can be expressed as :

$$m_e \cdot \frac{\partial^2 (x)}{\partial (t)^2} + m_e \cdot \gamma \frac{\partial (x)}{\partial (t)} = e \cdot E_0 e^{-i\omega t} \quad \dots\dots\dots\dots\dots\dots(2.11)$$

where, m_e is the electron mass, γ an absorption factor that takes into account the forces arising from friction induced by the free electrons with the matrix. The dipolic oscillation between the centre and the surface of a nanoparticle x_0 creates a dipolar moment that can be expressed as :

$$p = e.x_0$$

This moment allows us to introduce the notion of polarisation with respect to the total number of electrons per unit volume :

$$P = n.p$$

The polarisation can also be defined with respect to the electric field E as follows :

$$P = n.\alpha.E$$

where α represents the polarisibility. The dielectric function $\varepsilon(\omega)$ can also be defined as:

$$\varepsilon = 1 + P/(\varepsilon_0 E)$$

$\varepsilon(\omega)$ is further related to the complex refractive index of the material by the following relationship:

$$n + ik = \varepsilon^{1/2}$$

The complex dielectric function of a system with n free electrons per unit volume can be expressed as :

$$\tilde{\varepsilon}(\omega) = \varepsilon_1(\omega) + i\varepsilon_2(\omega)$$

i.e.

$$\tilde{\varepsilon}(\omega) = 1 - \frac{\omega_p^2}{\omega^2 + i\gamma\omega} \quad \dots\dots\dots\dots\dots\dots\dots(2.12)$$

where, ω_p is the Drude plasma frequency or simply plasmon frequency.

Simplifying the above equations of the classical Drude theory under the effect of plasma oscillation, the dielectric function of a metal is given by

$$\varepsilon = 1 - \frac{\omega_p^2}{\omega^2}; \qquad \omega_p = \left(4\pi n e^2 \middle/ m\right)^{\frac{1}{2}}$$

where, ω_p, is the plasma frequency, n – the electronic concentration is the main factor here in controlling plasma oscillation in metal especially for alkali metals.

In the case of the electrons that are not free, the equation relating to the movement of the electrons are modified and can be expressed as :

$$m_e \cdot \frac{\partial^2(x)}{\partial(t)^2} + m_e \cdot \gamma' \frac{\partial(x)}{\partial(t)} + Kx = e \cdot E_0 e^{-i\omega t} \quad \dots\dots\dots\dots(2.13)$$

where K is a constant.

From this equation we can determine the Lorentz's formula that corresponds to the complex dielectric function in the case where the electrons are not free:

$$\tilde{\varepsilon}(\omega) = 1 + \frac{4\pi \cdot e^2 m N_a (\omega_0^2 - \omega^2)}{m^2 (\omega_0^2 - \omega^2)^2 + \gamma'^2 \omega^2} - i \frac{4\pi \cdot e^2 N_a \gamma' \omega}{m^2 (\omega_0^2 - \omega^2)^2 + \gamma' \omega^2} \quad ....(2.14)$$

where ω is the frequency of oscillation of the electric field, ω_0 the resonant frequency of the oscillators, and N_a the number of such oscillators.

Colloidal dispersions of metals behaves differently and here the term surface plasmon mode is frequently spoken of. If we consider a single representative spherical particle of diameter d with complex dielectric constant[163] embedded in a medium of dielectric constant ε_m, in an oscillating electric field a density oscillation is built up. This is known as surface plasma mode. The dielectric function under this mode is found proportional to $1/\tau^2$ where τ is the average size-limited scattering time, which is the main factor for the optical properties for small particles. A new effect i.e. quantum size effect plays considerable role for tiny particles where classical scattering concept breaks down. In this case surface plasmon mode is treated quantum mechanically. The resonance peak of surface plasmon get shifted for quantum calculation than that for classical one. Considering all such effect silver is found to be most effective metal with sharp response to surface plasmon resonance. Subsequent research in this field reveals the fact that plasmon peak shift sensitivity depends on the interaction of the cluster with surrounding atoms or molecules. The more electron that are spilled out of the geometrical surface of the metal cluster the more a red shift is favored. On the other hand the more electrons that are injected into the metal cluster through the surface, the more a blue shift is observed.

6.4.3 Effective medium theory

The optical and dielectric properties of materials are generally described by the effective medium theory. The purpose of this theory is to predict the optical and dielectric properties of a composite material as a function of the constituting matter, the volume fraction and the shape of the each of the inclusions in the matrix. Thus this theory can describe an imaginary material that is completely homogeneous only defined by its effective dielectric function ε_{eff} that takes care of the response of the sample under

an external electric field. This material would then have the same macroscopic optical properties as the composite (figure 2.5).

Matrix, ε_m

Effective medium, ε_{eff}

Metallic particles, ε
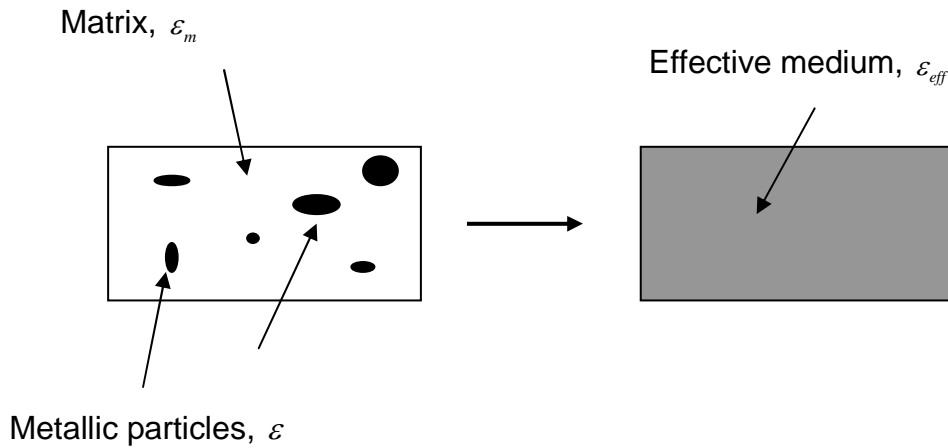
Figure 2.5 : Concept of the effective medium approach applied to a composite material

The Clausius-Mossoti equation valid only for static fields is the basis of all the effective medium theories. This equation is only valid in describing the optical properties for inclusions that are very small and dispersed so that scattering and interactions between the particles are negligible. This is the quasi-static approximation condition. In this circumstance the particle size should be sufficiently small so the following condition is satisfied:

$$\mathrm{d}/\lambda < 0.1$$

where λ is the wavelength of the incident beam of light.

6.4.4 Clausius-Mossoti equation

Let us consider a composite material consisting of a dielectric matrix with polarisable metallic inclusions. The immediate surrounding of the particles are homogeneous only when a large scale is considered. We thus have two regions: the region in the immediate neighbourhood of the particles are not homogeneous, however the region away from the spherical inclusions are homogeneous. This spherical region is called Lorentz's sphere (figure 2.6). The electric field in the particle can be expressed as:

$$E_{local} = E_M + \Delta E + \Delta E'$$

where, E_M is the macroscopic field in the neighbourhood of the Lorentz's sphere, ΔE the correction factor due to the polarisation of the surface of the Lorentz's sphere and $\Delta E'$ represents the contribution of other polarisable particles located in the Lorentz's sphere.
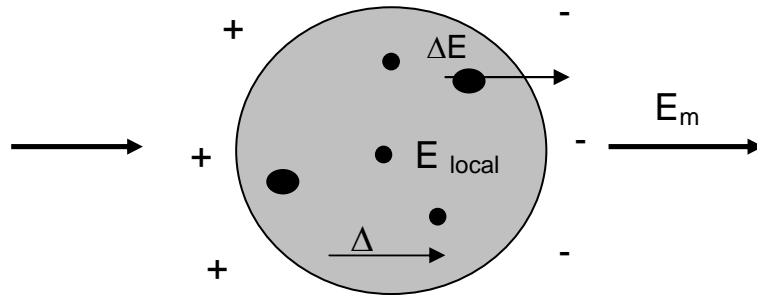
Figure 2.6 : definition of Lorentz's sphere

If the particles are distributed in and around the Lorentz's sphere, then $\Delta E'=0$. In this quasi-static condition, we have:

$$\Delta E = \frac{P}{3\varepsilon_0 \tilde{\varepsilon}_m} \quad \dots\dots\dots\dots\dots\dots\dots(2.15)$$

where, P is the polarisation of charges on the surface of Lorentz's sphere, ε_0 is the permittivity of free space and $\tilde{\varepsilon}_m$ is the dielectric constant of the matrix. P can also be expressed as the sum of all the particles that are present in the Lorentz's sphere:

$$P = E_{local} \sum n_j \cdot \alpha_j = \varepsilon_0 (\tilde{\varepsilon}_{eff} - \tilde{\varepsilon}_m) E_m \quad \dots\dots\dots\dots(2.16)$$

where, n_j and α_j represent the number of particles per unit volume and the polarisation of the jth type of particle, respectively.

Combining equation 2.15 and 2.16 we deduce the equation of Clausius-Mosotti:

$$\tilde{\varepsilon}_{eff}(\omega) = \tilde{\varepsilon}_m \frac{1 + \dfrac{2}{3\varepsilon_0 \tilde{\varepsilon}_m} \sum n_j \cdot \alpha_j}{1 - \dfrac{1}{3\varepsilon_0 \tilde{\varepsilon}_m} \sum n_j \cdot \alpha_j} \quad\text{..................................(2.17)}$$

that can also be expressed as :

$$\frac{\sum n_j \cdot \alpha_j}{3\varepsilon_0 \tilde{\varepsilon}_m} = \frac{\tilde{\varepsilon}_{eff} - \tilde{\varepsilon}_m}{\tilde{\varepsilon}_{eff} + 2\tilde{\varepsilon}_m} \quad\text{...................................(2.18)}$$

6.4.5 Maxwell Garnett theory:

According to Maxwell Garnett theory it is assumed that inclusion of particles in dielectric medium are randomly dispersed. The model is successful for linear optical response of metal-doped glasses. Taking the particles to be spherical in shape & the inclusion radius was much smaller than the typical spacing between inclusions which in turn was much smaller than an optical wave length. The dielectric constant of the composites is determined. In this models the spheres are displaced by model atom emitting electro-magnetic radiation.

The Clausius-Mosotti equation can be modified to describe speherical metallic nanoparticles that are influenced by each other in a host matrix i.e. the distance between the particles are very small. The two constituting matter of the composite can be expressed by:

$$\frac{\alpha_a N_a}{3\varepsilon_0 \tilde{\varepsilon}_m V} + \frac{\alpha_b N_b}{3\varepsilon_0 \tilde{\varepsilon}_m V} = \frac{\tilde{\varepsilon}_{eff} - \tilde{\varepsilon}_m}{\tilde{\varepsilon}_{eff} + 2\tilde{\varepsilon}_m} \quad\text{..................(2.19)}$$

where $n_j = N_j / V$ with N_j representing the number of particles of type j in a volume of V. Considering each of these constituting matter in the matrix, we obtain :

$$\frac{\alpha_a N_a}{3\varepsilon_0 \tilde{\varepsilon}_m V_a} = \frac{\tilde{\varepsilon}_a - \tilde{\varepsilon}_m}{\tilde{\varepsilon}_a + 2\tilde{\varepsilon}_m}$$

$$\frac{\alpha_b N_b}{3\varepsilon_0 \tilde{\varepsilon}_m V_b} = \frac{\tilde{\varepsilon}_b - \tilde{\varepsilon}_m}{\tilde{\varepsilon}_b + 2\tilde{\varepsilon}_m} \quad\text{...............................(2.20)}$$

whereV_a et V_b are the respective volume of species a and b.

Replacing V_a and V_b by the total volume V we obtain :

$$\frac{\alpha_a N_a}{3\varepsilon_0 \tilde{\varepsilon}_m V} = f_a \frac{\tilde{\varepsilon}_a - \tilde{\varepsilon}_m}{\tilde{\varepsilon}_a + 2\tilde{\varepsilon}_m}$$

$$\frac{\alpha_b N_b}{3\varepsilon_0 \tilde{\varepsilon}_m V} = f_b \frac{\tilde{\varepsilon}_b - \tilde{\varepsilon}_m}{\tilde{\varepsilon}_b + 2\tilde{\varepsilon}_m} \quad \dots\dots\dots\dots\dots\dots\dots\dots\dots(2.21)$$

where f_a et f_b represent the volume fraction of the components a et b respectively.

The equation 2.19 becomes :

$$f_a \frac{\tilde{\varepsilon}_a - \tilde{\varepsilon}_m}{\tilde{\varepsilon}_a + 2\tilde{\varepsilon}_m} + f_b \frac{\tilde{\varepsilon}_b - \tilde{\varepsilon}_m}{\tilde{\varepsilon}_b + 2\tilde{\varepsilon}_m} = \frac{\tilde{\varepsilon}_{eff} - \tilde{\varepsilon}_m}{\tilde{\varepsilon}_{eff} + 2\tilde{\varepsilon}_m} \quad \dots\dots\dots\dots\dots\dots (2.22)$$

The Maxell-Garnett approximation consist of assuming $\widetilde{\varepsilon}_m = \widetilde{\varepsilon}_b$ when $f_a << f_b$. Following equation 2.11, we then obtain :

$$f_a \frac{\tilde{\varepsilon}_a - \tilde{\varepsilon}_b}{\tilde{\varepsilon}_a + 2\tilde{\varepsilon}_b} = \frac{\tilde{\varepsilon}_{eff} - \tilde{\varepsilon}_b}{\tilde{\varepsilon}_{eff} + 2\tilde{\varepsilon}_b} \quad \dots\dots\dots\dots\dots\dots\dots\dots. (2.23)$$

By simple algebra, we are led to,

$$\frac{\tilde{\varepsilon}_{eff} - \tilde{\varepsilon}_b}{\tilde{\varepsilon}_{eff} + 2\tilde{\varepsilon}_b} = \beta f_a$$

where,

$$\beta = \frac{\tilde{\varepsilon}_a - \tilde{\varepsilon}_b}{\tilde{\varepsilon}_a + 2\tilde{\varepsilon}_b}$$

Here f_a represents the volume fill fraction of the inclusion particles.
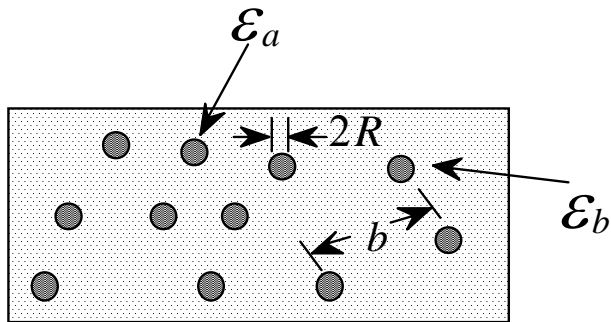
figure: Maxwell-Garnet composite geometry

The salient feature of this model are :

For metal inclusion particles, which have a negative real part of the dielectric constant, the real part of the denominator of β may go to zero, implying the existence of the resonance.

This theory indicates that effective medium theory can yield accurate predictions for composites materials.

The local field driving the polarization of the inclusion particles is not the same as the macroscopic electric field appearing in Maxwell's eqn.

Maxwell Garnett theory can be generalized for non-spherical geometry also.

6.4.5.1 Maxwell-Garnett equation for non-spherical nanoparticles

If we generalise the equation 2.23 by including a screening factor, κ :

$$ f_a \frac{\tilde{\varepsilon}_a - \tilde{\varepsilon}_b}{\tilde{\varepsilon}_a + \kappa\tilde{\varepsilon}_b} = \frac{\tilde{\varepsilon}_{eff} - \tilde{\varepsilon}_b}{\tilde{\varepsilon}_{eff} + \kappa\tilde{\varepsilon}_b} \quad \dots\dots\dots\dots\dots\dots\dots(2.24) $$

This new parameter κ depends on the shape of the particles and their orientation to the electric field. The screening factor κ is related to the depolaristaion factor of Lorentz by the following relation :

$$ \kappa = \frac{1-q}{q} \quad \dots\dots\dots\dots(2.25) $$
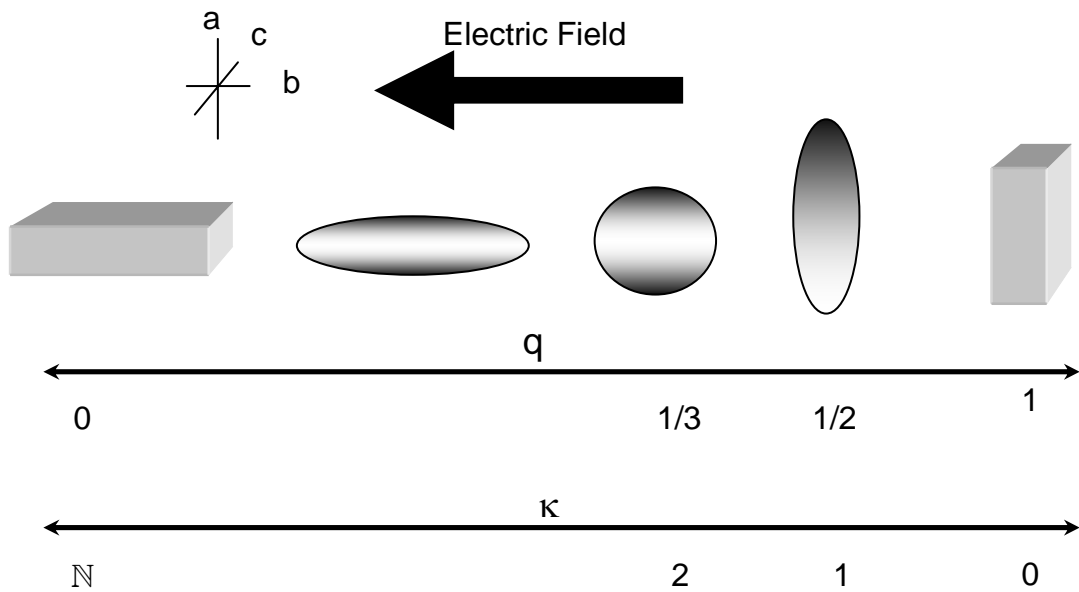
Figure 2.7 : Values of q & κ as a function of the geometrical shape of the particles

If we consider ellipsoidal particles with major and minor axes measuring a and b respectively, with the incident electric field parallel to the minor axis, the relationship that interlinks q and the geometric parameters a & b of the particles is as follows (figure 2.7) :

$$q = \frac{1/b}{\dfrac{1}{a} + \dfrac{2}{b}}$$ .... (2.26)

6.4.6 Bruggeman theory:

This theory treats the constituent symmetrical. The model assumes that grain of two or more materials are randomly interspersed. To analyze such a composite[164] one considers a single grain within the whole. This grain will be surrounded by grains of each type of constituent material including its own type. It is also assumed that the grain will be surrounded by a material of uniform dielectric constant given by that of the effective medium.

Just as in the case of Maxwell Garnetts equation, Bruggeman's equation can be applied to quasi-static(very small particles) condition of metallic nanoparticles in a matrix. In addition to this, the density of particles present in the matrix is so high that the

phenomena of percolation needs to be taken into consideration. In these conditions(figure 2.8):

$f_a \sim f_b$ and $f_b = 1 - f_a$

The Bruggman approximation considers the dielectric constant of the matrix to be equal to the effective dielectric constant of the nanocomposite, $\tilde{\varepsilon}_m = \tilde{\varepsilon}_{eff}$.

A   B
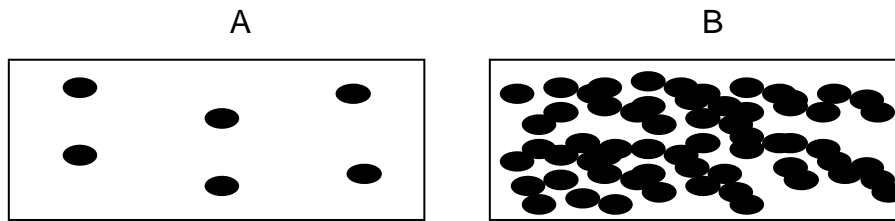
Figure 2.8 : Nanocomposite used in approximation of Maxwell-Garnett with $f_a \ll f_b$ (A) and the approximation of Bruggeman with $f_a \sim f_b$ (B)

The Bruggeman equation is also derived from the Clausius-Mossotti equation:

$$f_a \frac{\tilde{\varepsilon}_a - \tilde{\varepsilon}_m}{\tilde{\varepsilon}_a + 2\tilde{\varepsilon}_m} + f_b \frac{\tilde{\varepsilon}_b - \tilde{\varepsilon}_m}{\tilde{\varepsilon}_b + 2\tilde{\varepsilon}_m} = \frac{\tilde{\varepsilon}_{eff} - \tilde{\varepsilon}_m}{\tilde{\varepsilon}_{eff} + 2\tilde{\varepsilon}_m} \quad \ldots\ldots\ldots\ldots\ldots(2.27)$$

With, $\tilde{\varepsilon}_m = \tilde{\varepsilon}_{eff}$:

$$f_a \frac{\tilde{\varepsilon}_a - \tilde{\varepsilon}_{eff}}{\tilde{\varepsilon}_a + 2\tilde{\varepsilon}_{eff}} + f_b \frac{\tilde{\varepsilon}_b - \tilde{\varepsilon}_{eff}}{\tilde{\varepsilon}_b + 2\tilde{\varepsilon}_{eff}} = 0 \quad \ldots\ldots\ldots\ldots\ldots\ldots\ldots\ldots(2.28)$$

The salient features of this model is

With the increase of the volume fraction of one constituent there will come a point at which the grains begin to join & form continuous threads throughout the composite, properties like conductivity etc. may change significantly due to this percolation, the composites behaves as metal not as insulators.

With the increase of volume fraction, resonance peak due to surface plasmon as predicted by Bruggeman theory should be broadened.

It presents a successful description of non – linear optical theory.

6.4.6.1 Dynamic Maxwell-Garnett equation

When the particle size is not sufficiently small, the quasi-static approximation that considers only the dipolar excitations neglecting all the multipolar excitations are no longer valid. The Maxwell-Garnett's approximation remains useful only when we consider the screening factor κ dynamic.

$$\kappa = \frac{1}{q_{eff}} - 1 \qquad \dots\dots\dots\dots(2.29)$$

where, q_{eff} is the effective depolarisation factor that takes into account the effect of the particle size:

$$q_{eff} = q_b - \frac{1}{3}(\frac{2\pi \cdot n_o}{\lambda})^2 b^2 + i\frac{2}{9}(\frac{2\pi \cdot n_o}{\lambda})^3 b^3 \qquad \dots\dots\dots\dots(2.30)$$

where b represents the minor axis of the ellipsoid, and n_o is the refractive index of the matrix of dielectric constant q_b :

$$q_b = \frac{1 - q_a}{2} \qquad \dots\dots\dots\dots(2.31)$$

$$q_a = \frac{1 - E^2}{E^2}\left[\frac{1}{2E}\ln(\frac{1+E}{1-E}) - 1\right] \qquad \dots\dots\dots\dots(2.32)$$

$$E = \sqrt{1 - \frac{b^2}{a^2}} \qquad \dots\dots\dots\dots(2.33)$$

6.4.6.2 Condition of resonance

When a metallic nanoparticle is embedded in a matrix, we have observed that the surface plasmons play an important role in the way the material interacts with the electric field E_0 due to the incident electromagnetic field of wavelength λ. Thus, for nanoparticles of radius R (where $R \ll \lambda$, the quasi-static condition), the internal electric field E_i can be expressed as :

$$E_i = E_0 \frac{3\tilde{\varepsilon}_m}{\tilde{\varepsilon} + 2\tilde{\varepsilon}_m} \quad \text{............................(2.34)}$$

where $\tilde{\varepsilon}$ and $\tilde{\varepsilon}_m$ are the dielectric functions of metal and the matrix respectively. The resonant condition can be verified when the internal field E_i is maximum, which in other words mean that the denominator in equation 2.34 approaches zero.

6.4.7 Linear optical properties:

6.4.7.1 Theoretical analysis of the optical spectra of a Au- SiO$_2$ nanocomposite :

What we require as basic information is simply the refractive indices and the absorption coefficient as a function of the incident wavelength λ of each of the constituting materials, i.e. the metal nanoparticles and the dielectric matrix. These can be obtained from the literature. [165-166]
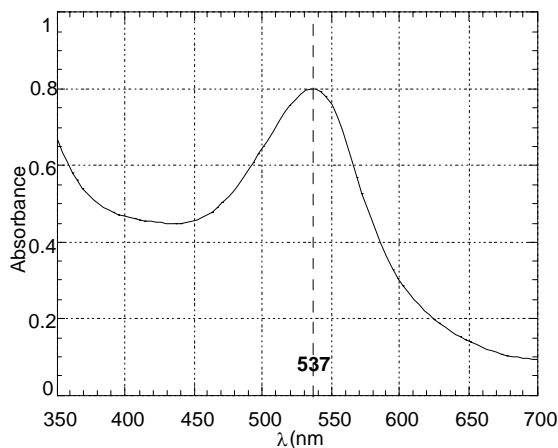
Figure: Absorbtion spectra of a commercially available red glass (doped with 430 ppm of gold) used in jeweleries (Manufactured by the company Baccara, France)[167]
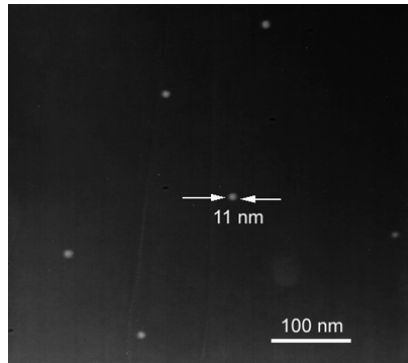
Figure: darkSTEM of the glass obtained from Baccara doped with 430ppm gold.[167]

This allows us to calculate the dielectric constant of each of the constituent materials and also the nanocomposite, following Maxwell Garnetts equation 2.2.3. The absorption spectra as a function of wavelength is determined from the equation 2.10 once we have determined the refractive index of the nanocomposite $\tilde{n}_{eff}$ from the following equations:

$$\tilde{n}^2_{eff} = (n_{eff} - ik_{eff})^2 \ldots\ldots\ldots\ldots\ldots\ldots\ldots\ldots(2.36)$$

$$n_{eff} = \left. \begin{array}{l} n_{eff} = \sqrt{\dfrac{\varepsilon_1^{eff} + \sqrt{(\varepsilon_1^{eff})^2 + (\varepsilon_2^{eff})^2}}{2}} \\[3ex] k_{eff} = \dfrac{\varepsilon_2^{eff}}{2} \end{array} \right\} \ldots\ldots\ldots\ldots\ldots\ldots..(2.37)$$

If we consider the nanoparticles to be perfect spheres, then in this case κ =2. In the following figure the simulated spectra of nanocomposites with a constant volume fraction of metallic inclusion as fv=0.001%, with respect to several particle sizes varying from 10 nm to 60 nm is shown. We can observe that for particle sizes of 10-20nm, $\lambda_{max} = 537 nm$. As the particles are larger than 20 nm, the absorption peak shifts to the red (λ_{max} = 587 nm for particle size ~40 nm, and λ_{max} >700 nm for particle size ~60nm). Also we can observe that with increasing particle size, the total absorption increases. The absorption is just 20 % for particles 10nm in size, while it is nearly 50% for 40 nm particle inclusions. The theoretical spectra is quite similar to the experimental spectra. The slight anomaly that one can observe can be reduced if the refractive indices are more precisely measured.
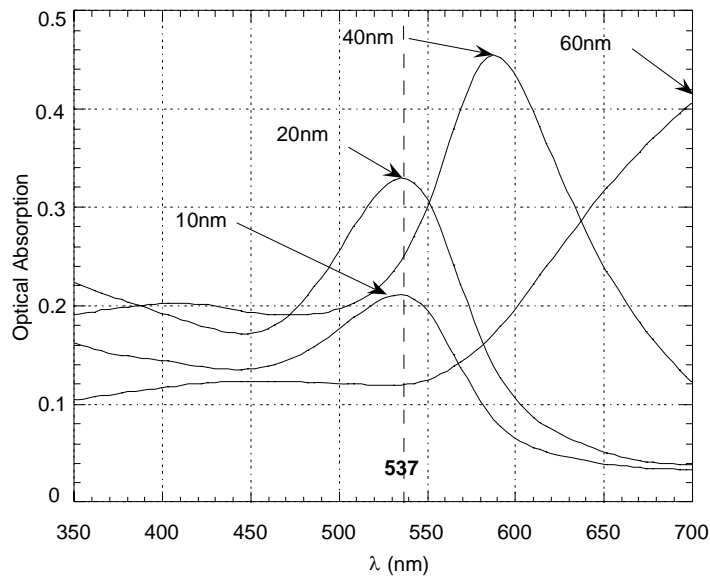
Figure 2.11 : Simulated absorption spectra of a SiO_2-Au nanocomposite (f_v=0.001%).
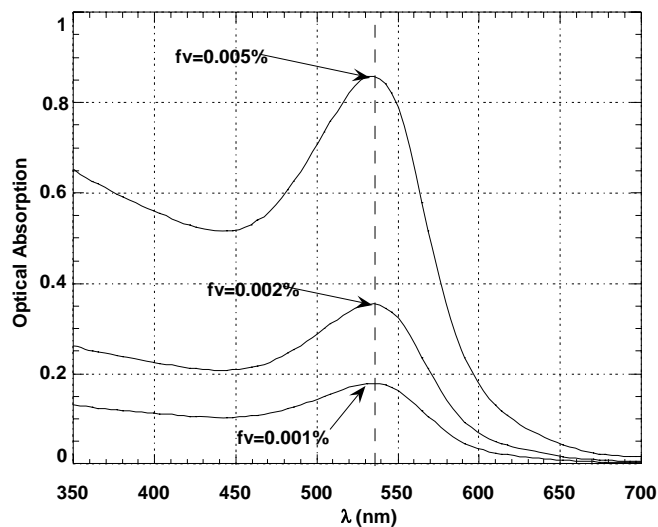
Figure 2.12 : Influence of the volume fraction of gold on the absorption spectra of a SiO_2-Au nanocomposite

In the figure 2.12, the influence of the volume fraction of metallic nanoparticles in the nanocomposite is plotted. We can see that the absorption peak remains constant but the intensity of absorption increases with increase ion the volume fraction of the particles in the nanocomposite.

6.4.8 Nonlinear optical properties :

Semiconductor and metal nanocrystals are also of interest as third order nonlinear optical (NLO) materials.[168] Light has an electromagnetic field which interacts

with charge carriers in materials. Nonlinear optical properties develop due to the square, cubic or higher order dependence of dielectric polarization on electric field given by:

$$\vec{P} = \chi^{(1)}\vec{E} + \chi^{(2)}\vec{E}^2 + \chi^{(3)}\vec{E}^3$$

All interactions with light are to some extent nonlinear. However, in most cases the nonlinearities are too small to be detected. Typical materials with high $\chi^{(2)}$ are those consisting of molecules with electron-donor and electron-acceptor groups. In such molecules, the electron will be drawn to the electron-acceptor group, but they will resist being pushed towards the electron-donor. These additional positive and negative contributions to polarization are responsible for the production of light at twice the frequency of the incoming light.

When light is transmitted through a third-order NLO material, it will not only create a electrical field component at the third harmonic (light at a frequency three times higher than the frequency of the incoming light), but also induce a change in the refractive index which depends on the intensity of light. A transparent small-particle semiconductor can be made to become suddenly opaque by changing the intensity of light shining on it. This behaviour can be the basis for an optical switch that will work 100-1000 times faster than electronic switches.[169]

Finally, it is important to point out that the surface of nanometer particles of both semiconductors and metals can be changed chemically. This has a direct influence on their electronic behaviour, and hence on their optical properties. As mentioned before, a substantial percentage of crystallite atoms are surface atoms, and these largely account for the chemical and physical properties of the nanoparticles. Surface atoms, if they are not coordinated to any organic stabilizers, interact only with atoms inside the particles and have free valences outside. Their electronic contribution to the behaviour of the particle is therefore different from that of the inner atoms which are fully coordinated. In semiconductor nanoclusters, charge trapping can occur in the electronic surface states, thereby diminishing the electro-optical effect associated with spatial confinement. Therefore, in order to prevent higher wavelength emission, surface states must be eradicated. This can be achieved by chemically binding the particles to a suitable material with a higher band gap.[170]

It is well known that nonlinearity exists in metallic clusters and it is reported to arise due to quantum size effect.[171] Due to surface plasmon resonance the local field

increases in the particle and from "effective medium theory" consequent polarization shows complicated dependence of electric field. Here a third order nonlinearity arises where susceptibility depends on I/r^3 (r= radius of the metallic sphere).

Another possible mechanism attributed to non-linear response is based on fermi smearing or non-equilibrium electron heating. By pump-probe technique electrons are energized resulting in a high electron temperature while the lattice remains cool. It is observed that χ is size independent.

It is observed recently that non-linearities of metallic clusters could be further increased if the composites consist of a core shell structure such as metallic core and non-linear shell or vice–versa. This recent model predicts that a limited range of resonance tunability can be achieved by adjustment of shell thickness

6.5 Optical Applications

NANOPHOTONICS
Nanoscale optical science and technology

Nanoscale confinement of matter	**Nanoscale confinement of radiation**	**Nanoscale photoprocesses**
- **Nanoparticles** - **Nanomers** - **Nanodomains** - **Nanocomposites**	- **Near field optical microscopy** - **Photon scanning tunneling microscopy** - **Photon localization in photonic crystals** - **nanocavities**	- **Nanofabrication** - **Nanosensors and actuator** - **Nanoscale optical memory**
Control of optical resonance,local interactions, excitation dynamics and energy transfer	**Control of propagation properties of radiation and its interaction with matter**	**Control of spatial confinement of photochemical and photophysical processes**

Optical application, in other words nano-photonics is widely promising as far as scientific and technological application is concerned. To name a few, nanophotonics is used in the study of matter radiation interaction, description of photochemical process, preparation of Quantum – well lasers Quantum cascade laser and even for simple consumer products (sunscreen lotion as preventive to UV radiation hazards).

6.5.1 Laser crystals:

Stimulated emission has been observed in polymer thin films and in some organic crystals. The requirements for laser action in the latter are :

Use of strongly fluorescent molecules with an appropriate life time.

Crystals must have, suitable dimension being a good resonator & it should have smooth end faces.

To withstand high input pumb energy thermal stability is necessary.

6.5.2 Electro optic crystals:

Non-linear optical phenomena discussed earlier results in a redistribution of electron in dielectrics which manifest this redistribution in terms of polarizabilities. The effect co – efficient of polarizabilities has to be maximized in crystal to obtain large NLO response. On the other hand 2nd harmonic generation (SHG) – the doubling of frequency of an incident laser beam – linear electro optic effect – the electric field induced change in refractive index are some of the widely used application of nanomaterials. Sometimes inclusion formation with channel type organic host comes out to be a successful approach to produce polar crystal.

6.5.3 I – D photo – conduction:

I – D photo – conduction is released with the help of polarisable, closed-packed channel type porous materials. Moreover is the molecules have large β_{max} values & are aligned in a polar fashion the materials may exhibit. Photo – refraction – an alteration of the refractive index of a material when exposed to a spatially inhomogeneous light source. Crystalline organic photorefractive materials have potential application in the field of high density optical storage and image processing techniques.

6.5.4 Electrical rectification:

When a photocurrent is generated by illumination of a suitable material, a difference in the current should occur with respect to the polarity the applied electrical potential for measuring the current.

6.5.5 Electroluminescent nanotubes:

So far polymeric LEDS are concerned nano – materials have managed a large space in the technology. Usual polymeric material shows randomness in e – h recombination and other related processes. By using porous-channel type materials containing light emitting & electronically interacting guests a greater degree of order can be achieved.

6.5.6 POWDER LASER :

This topic primarily deals with microlaser made of disordered media. Microlaser has important application to integrated photonic circuits. The key issue of the microlaser is to confine tight in a small volume with dimensions on the order of optical wavelength. In vertical cavity surface emitting laser light is confined by two distributed Bragg-reflectors. The phenomena of total internal reflection is used in microdisk laser. Recently two dimensional photonic band-gap defect-mode laser the lateral confinement of light is achieved by Bragg. Scattering in a 2-D periodic structure. Very recent work on laser is related to disordered media. Here the optical confinement is based on Anderson localization of light in a micrometer scale random medium. The fabrication of such laser is easier and cheaper than most microlaser.[172]

Fig. 1 shows the emission intensity as function of the incident pump pulse energy. A threshold behaviour is clearly seen.

The bright spots are related to the laser light.

For highly disordered structure of the cluster strong light scattering takes place. Here the scattering mean free path is characterized in macroscopic scale film made of ZnO powder with coherent back-s cottering measurement. For a parfticular configuration of scatterers in a cluster photon localization occurs only at a certain warelengths. Because

of the finite size of the random medium poton localization is not complete, some photons escape through the surface of a cluster. This gives rise to the loss of localization cavities. When optical gain exceeds the loss of a localization cavity laser oscillation occurs at localization frequency. The spatial distribution of laser light intensity exhibits the spatial profile of the localization mode.

Ref.

1.   J.L. Jewell, J.P. Harbison, A. Scherer, Y.H. Lee, and L.T. Florez, IEEE J. Quantum Electron (1991) 27, 1332.

2.   Painter, R.K. Lee, A Scherer, A. Yaviv, J.D. O'Brien, P.D. Dapkins and I. Kim, Science (1999) 284, 1819.

7   MAGNETISM

7.1 Introduction:

The phenomenon of magnetism, that is, the mutual attraction of two pieces of iron or iron ore, was surely known to the antique world. The ancient Greeks have been reported to experiment with this mysterious force. The name magnetism is said to be derived from a region in Turkey which was known by the name of Magnesia and which had plenty of iron ore.

A piece of magnetic material such as iron ore does not immediately attract other pieces of the same material. For this, at least one of the elements need to be magnetised. In simple terms, its internal elementary magnets need alignment in order for it to become a permanent magnet! Today, magnetising is a pretty elementary job: one merely places a piece of iron into an electric coil through which a direct current is passed for a short time. (This was discovered by Oersted in the last century).

Magnetic materials made an important contribution to the development of the consciousness of mankind because they paved the way to discoveries of new continents once the compass had been invented. The British coined the world lodestone for the iron ore **Fe$_3$O$_4$** which meant to say that this mineral points the way. Our modern technology would be unthinkable without magnetic materials and magnetic properties. Magnetic tapes, television, motors, generators, telephones, and transformers are only a few examples of their applications.

Thus far, we have used the word magnetism very loosely when implying the mutual magnetic attraction of pieces of iron. There are, however, several other classes of magnetic materials that differ in kind and degree in their mutual interaction. We shall distinguish in the following between ferromagnetism(which term we restrict to the classical magnetism in iron and a few other metals and alloys) and para-, dia-, antiferro- and ferrimagnetism. The oldest known magnetic ore, the magnetite, or lodestone, Fe_3O_4 is actually a ferrimagnet (FeO) (Fe_2O_3 called iron ferrite).

Over the past several decades, amorphous and more recently nanocrystalline materials have been investigated for applications in magnetic devices requiring magnetically soft materials such as transformers, inductive devices, etc. Most recently, research interest in nanocrystalline soft magnetic alloys has dramatically increased.

This is due, in part, to the properties common to both amorphous and crystalline materials and the ability of these alloys to compete with their amorphous and crystalline counterparts. The benefits found in the nanocrystalline alloys stem from their chemical and structural variations on a nanoscale which are important for developing optimal magnetic properties. In the following sections, we will first revisit the magnetic properties of matter and then pass on to discuss about the magnetic nanomaterials.

7.2 Basic Concepts in Magnetism

At least five different types of magnetic materials exist as mentioned in the Introduction. A qualitative, as well as a quantitative distinction between these different types, can be achieved in a relatively simple way following a method proposed by Faraday. The magnetic material to be investigated is suspended from one of the arms of a sensitive balance and is allowed to reach into an inhomogeneous magnetic field.
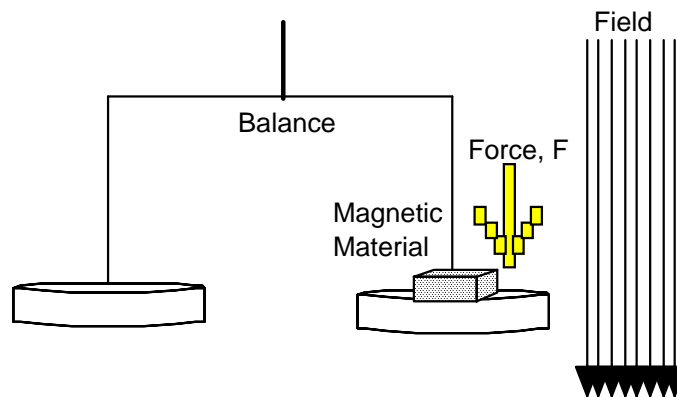
Diamagnetic materials are expelled from this field, whereas para-, ferro-, antiferro-, and ferrimagnetic materials are attracted in different degrees. It has been empirically found that the apparent loss or gain in mass, that is, the force F on the sample exerted by the magnetic field is.

$$F = V \chi H \, dH/dx$$

Where dH/dx is the change of the magnetic field strength $|\mathbf{H}|$ in the direction of the field and V is the volume of the sample. The magnetic material can be characterised by a material constant, χ, called the susceptibility which expresses how responsive this

material is to an applied magnetic field. Frequently, a second material constant, the permeability μ, is used. This constant is related to the susceptibility by the definition

$$\mu = 1+4\pi\chi$$

For empty space, and for all practical purposes, also for air, χ is zero and thus $\mu = 1$. For diamagnetic materials one finds χ to be small and negative and thus μ slightly less than 1. For para- and antiferromagnetic materials χ is again small, but positive. Thus, μ is slightly larger than one. Finally, χ and μ, are large and positive for ferro- and ferri-magnetic materials. The magnetic constants are temperature dependent, except for diamagnetic materials.

The magnetic field parameters at a given point in space are defined to be the magnetic field strength **H**, which we introduced above, and the magnetic flux density or magnetic induction **B**. In free space **B** and **H** are identical. Inside a magnetic material, the induction **B** consists of the free-space component (**H**), plus a contribution to the magnetic field which is due to the presence of matter.

$$\mathbf{B= H+}\ 4\pi\mathbf{M}$$

where **M** is called the magnetisation of the material. For a material in which the magnetisation is thought to be proportional to the applied field strength we define

$$\mathbf{M} = \chi\mathbf{H}$$

Combining the above two equations we get:

$$B = H(1+4\pi\chi) = \mu H$$

Finally, we need to define the magnetic moment, μ_m, through the following equation:

$$M = \mu_{m/V}$$

that is the magnetisation is the magnetic moment per unit volume.

It needs to be noted that in magnetic theory several unit systems are commonly in use. The scientific and technical literature on magnetism is still widely written in electromagnetic cgs (emu) units. The magnetic field strength in cgs units is measured in Oersted and the magnetic induction in Gauss.

7.2.1 Magnetic Phenomena & their classical interpretation:

We stated earlier that different types of magnetism exist and that they are characterized by the magnitude and the sign of the susceptibility. Since various materials respond so differently in a magnetic field, we suspect that several

fundamentally different mechanisms must be responsible for the magnetic properties. In the first part of this chapter we shall attempt to unfold the multiplicity of the magnetic behaviour of materials by describing some pertinent experimental findings and giving some brief interpretations.

(a)   Paramagnetic
Disordered spin (2D)

(b) Ferromagnetic
Ordered (align)spin (2D)

(c) Antiferromagnet

(d) Ferrimagnet

Ordered (opposed) spins (2D)

(e) Canted antiferromagnets or weak ferromagnet (2D)
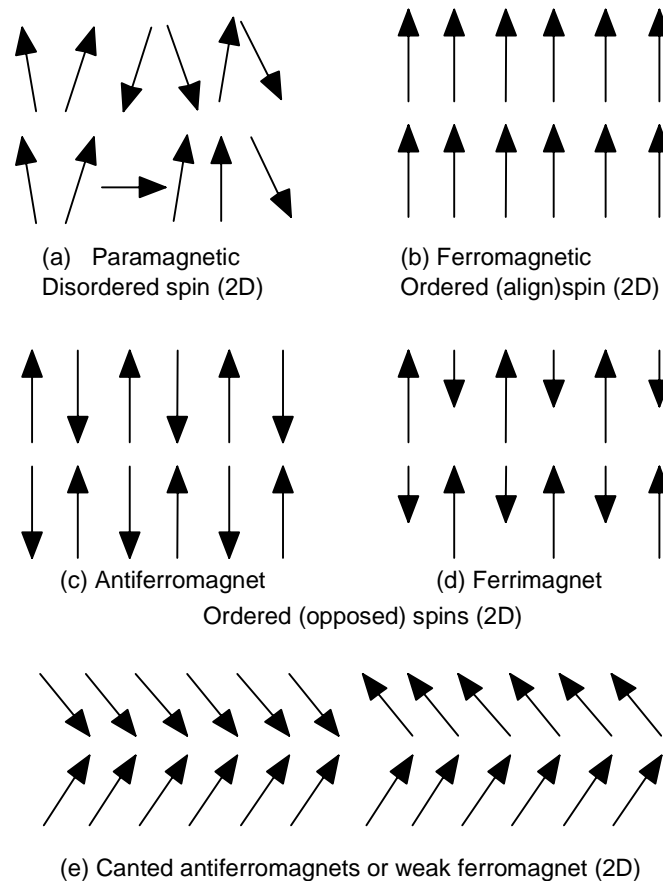
Figure: Schematic illustration of spin-coupling behaviours, including (a) paramagnetic disordered spins (2D), (b) ferromagnetic ordered (aligned) spins (2D), antiferromagnetic ordered (opposed) spins (2D), (d) ferrimagnetic ordered (opposed) spins (2D), and (e) canted antiferromagnets or weak ferro magnets (2D).

7.2.2 Diamagnetism

Ampere postulated more than one hundred years ago that molecular currents are responsible for the magnetism in a solid. He compared the molecular currents to an electric current in a loop-shaped piece of wire which is known to cause a magnetic moment. Today, we replace Ampere's molecular currents by orbiting valence electrons.

For the understanding of diamagnetism, a second aspect needs to be considered. It was found by Lenz that a current is induced in a wire loop whenever a bar magnet is moved towards (or from) this loop. The current thus induced causes in turn a magnetic moment which is opposite to the one of the bar magnet . (This has to be so in order for mechanical work to be expended in producing the current; otherwise, a perpetual motion would be created) Diamagnetism may then be explained by postulating that the external magnetic field induces a change in the magnitude of inner-atomic currents, that is, the external field accelerates or decelerates the orbiting electrons, in order that their magnetic moment is in the opposite direction from the external magnetic field. In other words, the response of the orbiting valence electrons counteract the external field and thus shield the inner electrons from an external magnetic field. A more accurate and quantitative explanation of diamagnetism replaces the induced currents by precessions of the electron orbits about the magnetic field direction (Larmor precession).

Here, we have only considered electrons which are bound to their respective nuclei. In metals the free electrons are forced to move in a magnetic field in a circular path. This leads to a second contribution to the diamagnetic moment; specially, the circulating free electrons cause a magnetic moment, similarly as described above.

7.2.3 Paramagnetism

Paramagnetism in solids is attributed to a large extent to a magnetic moment that results from electrons which spin around their own axis. We already know that because of the Pauli principle no two electrons can have the same value and sign for the spin moment. In other words, each electron state can be occupied by two electrons only; one with positive and the other with negative spin. An external magnetic field tries to turn the unfavourably oriented spin moments in the direction of the external field. Spin paramagnetism is slightly temperature dependent. It is generally very weak and is observed in some metals and in salts of the transition elements.

Free atoms (dilute gases) as well as rare-earth elements and their salts and oxides possess an additional source of paramagnetism, which arise due to the magnetic moment of the orbiting electrons. Without an external magnetic field, these magnetic moments are randomly oriented and thus they mutually cancel one another. As a result, the net magnetization is zero. However, when an external field is applied the individual magnetic vectors tend to turn into the field direction, that is counteracted by

thermal agitation alignment. Thus, electron-orbit paramagnetism is temperature dependent.

The temperature dependence of many paramagnetic materials is governed by the experimentally found Curie law which states that the susceptibility χ is inversely proportional to the absolute temperature

$$\chi = C/T$$

where C is called the Curie constant. For many other substances, a more general relationship is observed, which is known as the Curie-Weiss law:

$$\chi = C/(T-\theta)$$

where θ is another constant which has the same unit as the temperature and may have positive as well as negative values.

Metals, with a few exceptions, do not obey the Curie-Weiss law. However, Ni, the rare earth elements, and salts of the transition elements (for example, the carbonates, chlorides, or sulfates of Fe, Co, Cr, Mn) obey the Curie-Weiss law quite well.

In most solids, only spin paramagnetism is observed. This is believed to be due to the fact that in crystals, the electron orbits are essentially coupled to the lattice which prevents the orbital magnetic moments from turning into the field direction. One says in this case that the orbital moments are "quenched." Exceptions are the rare earth elements and their derivatives, which have "deep lying" 4f-electrons. The latter ones are shielded by the outer electrons from the crystalline field of the neighboring ions. Thus, the orbital magnetic moments of the f-electrons may turn into the external field direction and contribute to electron-orbit paramagnetism. The fraction of the total magnetic moment contributed by orbital motion versus by spin is defined as the "g-factor."

It is now possible to make some general statements about whether para- or diamagnetism might by expected in certain materials. For paramagnetic materials, the magnetic moment of the electrons is thought to point in the direction of the external field, that is, the magnetic moment enhances the external field. Diamagnetism counteracts an external field, as we have seen earlier. Thus, para- and diamagnetism oppose each other. Solids, which have both orbital as well as spin paramagnetism, are clearly paramagnetic. Rare earth metals with unfilled 4f-electron-bands are an example for this. In most other solids, however, the orbital paramagnetism is "quenched", as we said above. Yet, they still might have spin paramagnetism. The presence of a net spin-paramagnetic moment depends upon whether or not the

magnetic moments of the individual spins cancel each other. More specifically, if a solid has completely filled electron bands, we anticipate (because of the Pauli principle) the same number of electrons with spins up as well as with spins down. For example, a completely filled d-band contains 5N electrons with spins up and 5N electrons with spins down. This results in a cancellation of the spin moments and net spin paramagnetism is expected. These materials are thus diamagnetic (no orbital and no spin paramagnetic moment). We mention as examples for filled bands, intrinsic semiconductors, insulators, and ionic crystals such as NaCl. (In the latter case, an electron transfer occurs between cations and anions which causes closed electron shells, that is, filled bands.)

In materials with partially filled bands, the electron spins are arranged, according to "Hund's rule" in such a manner that the total spin moment is maximized. This condition is energetically more favorable, as quantum mechanics shows. For examples, in an atom with eight valence d-electrons, five of the spins align, say, up, and three spins point down which results in a net total of 2 spins up. The atom is then expected to have two units of magnetism.

The smallest unit (or quantum) of the magnetic moment is called one Bohr magneton, μ_B,

$$\mu_B = eh/4\pi m = 0.927 \times 10^{-20} \text{ (erg/Oe)}$$

 (The symbols have the usual meaning). In the above example, the metal is said to have 2 Bohr magnetons per atom.

One word of caution should be added about applying the above general principles too rigidly. Some important exceptions do exist. They must be explained by considering additional information. For example, copper which has one s-electron in its valence band should be paramagnetic according to our considerations brought forward so far. In reality, copper is diamagnetic. Other examples are superconductors which are perfect diamagnetics below a transition temperature; they repel the magnetic flux lines from their interior.

7.2.4 Feromagnetism

We return now to ferromagnetics and commence with the experimentally found magnetization curve for these materials. *Ferromagnetism* occurs in rather few elements, Fe, Co, Ni, Gd and a few rare earths with low Curie temperatures (many fewer than superconductors!).A newly cast piece of iron (often called virgin iron) is inserted into a ring-shaped solenoid (The ring shape is used to contain the magnetic field within the

coil). If the external field strength is increased (by increasing the current in the primary winding), then the magnetization (measured in a secondary winding with a flux meter) rises at first slowly and then more rapidly. Finally, M levels off and reaches a constant value, called the saturation magnetization M_s.   When H is reduced to zero, the magnetization retains a positive value, called the remanent magnetization or remnance M.   It is this retained magnetization which is utilized in permanent magnets. The remanent magnetization can be removed by reversing the magnetic field strength to a value H_c, called the coercive field. Solids having a large combination of M_s and H_c are called hard magnetic materials.   A complete cycle through positive and negative H-values, as shown in Figure, is called a hysteresis loop. It should be noted that a second type of hysteresis curve is often used, in which B (instead of M) is plotted versus H. No saturation value for B is observed. (The residual induction B at H = 0 is called the retentivity). Removal of B requires a field which is called coercivity. However, remance and retentivity, as well as coercive field, coercive force, and coercivity are often used interchangeably).
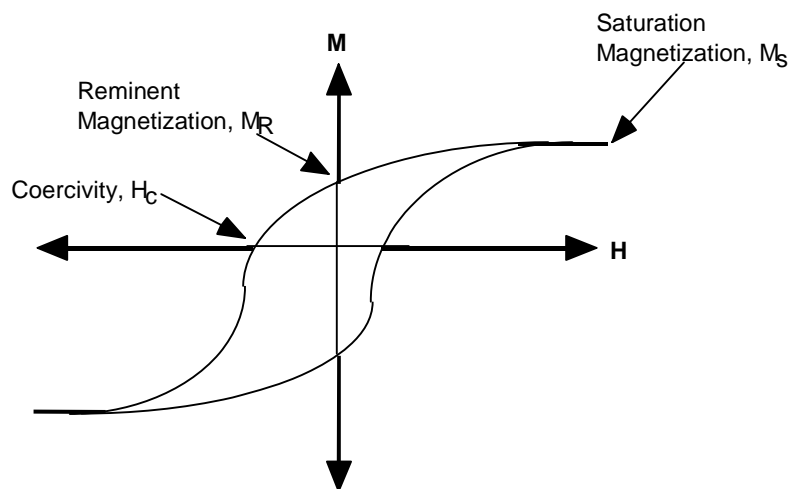
figure: Important parameters obtained from a magnetic hysteresis loop. The saturation magnetization, M_S, remanent magnetization, M_R, and coorcivity, H_C, are Shown.

The saturation magnetization is temperature dependent. Above the Curie temperature, T_c ferromagnetics become paramagnetic. Table below lists saturation magnetizations and Curie temperatures of some elements.

Table: Saturation magnetization of some ferromagnetic materials

Metal	$4\pi M_S$	T_c(K)
	(Maxwells/cm^2)	
Fe	2.2×10^4	1043
Co	1082×10^4	1404
Gd	7.11×10^4	289
Ni	0.64×10^4	631

A few words should be said to explain the above mentioned observations. In ferromagnetic materials, the spins of unfilled d-bands spontaneously align parallel below T_c, that is, they align within small domains without the presence of an external magnetic field (Figure). Specifically, the individual domains are magnetized to saturation. The spin direction in each domain is however different (see Figure) so that the individual magnetic moments for the material as a whole cancel each other and the net magnetization is zero. An external magnetic field causes those domains whose spins are parallel or nearly parallel to the external field to grow at the expense of the unfavorably aligned domains (figure). An increase in temperature progressively destroys the spontaneous alignment. The gradual transition from ferromagnetism to paramagnetism is believed to be due to the fact that slighly above T_c, small clusters of spins are still aligned parallel to each other, a phenomenon which is called magnetic short-range order.

7.2.5 Antiferromagnetism

Antiferromagnetic materials exhibit, just as ferromagnetics a spontaneous alignment of moments below a critical temperature. However, the responsible neighboring atoms in antiferromagnetics are aligned in an antiparallel fashion (Figure). Actually, one may consider an antiferromagnetic crystal to be divided into two interpenetrating sublattices A and B, each of which has a spontaneous parallel alignment of spins.

Antiferromagnetic materials are paramagnetic above the Neel temperature T_N, that is, they obey there a linear $T = f(1/\chi)$ law. Below T_N, however, the inverse susceptibility may rise with decreasing temperature. The extrapolation of the paramagnetic line to $1/\chi = 0$ yields a negative θ. Thus, the Curie-Weiss law needs to be modified for antiferromagnetics to read

$$\chi = C/T-(-\theta) = C/T+\theta$$

The Neel temperature is often below room temperature. Most antiferromagnetics are found among ionic compounds. They are insulators or semiconductors. No practical application for antiferromagnetism is known at this time.

7.2.6 Ferrimagnetism

Ferrimagnetic materials are of great technical importance because they exhibit a spontaneous magnetic moment below a Curie temperature just as iron, cobalt, or nickel and they are poor electrical conductors. A large resistivity is often desired for high frequency applications (e.g., to prevent eddy currents in cores of coils). To explain the spontaneous magnetization in ferrimagnetics. Neel proposed that two sublattics should exist in these materials (just as in antiferromagnetics) each of which contains ions.

Table: Calculated and measured number of Bohr Magnetons for some ferrites

Ferrite	Mn	Fe	Co	Ni	Cu
Calculated μ_B	5	4	3	2	1
Measured μ_B	4.6	4.1	3.7	2.3	1.3

whose spins are aligned parallel to each other. The crucial point is that each of the sublattices contain a different amount of magnetic ions. This causes some of the magnetic moments to remain un-cancelled. As a consequence, a net magnetic moment results. Ferrimagnetic materials can thus be described as imperfect antiferromagnetics. The crystallography of ferrites is rather complex. We defer its discussion until later. For the time being it suffices to know that there are two types of lattice sites which are available to be occupied by the metal ions They are called A sites and B sites. (As before, oxygen ions do not contribute to the magnetic moments).

The temperature dependence of most ferrimagnetics is very similar to ferromagnetics. The saturation magnetization decreases with increasing

temperature until it vanishes at a Curie temperature T_c. Above T_c, ferrimagnetics behave paramagnetically, having a nonlinear 1/x versus T relationship.

7.3 Magnetic Properties of small atomic clusters

7.3.1 Introduction :

Metal clusters are composed of a few atoms to hundreds of atoms which demonstrate properties different from the bulk due to the large surface to volume ratio compared to its bulk state.[173] e.g. for a cluster of thousand atoms, one quarter of the atoms lie on the surface. Even in the very compact icosahedral configuration, a nickel cluster of 55 atoms has 32 atoms on the surface. This provides an unique opportunity to study the evolution of the physical properties of bulk solid with the variation of the number of atoms in the system under investigation. Hence, the understanding of the properties of the clusters in isolation has become a subject of considerable interest from the stand point of fundamental research.

Another important aspect of the cluster research is that since the physical properties of the clusters are size specific, there is possibility that materials with desired properties can be custom made by changing the size and composition of the cluster aggregates. e.g. thin films with controlled nanostructure characteristics can be obtained by low energy cluster beam deposition technique.[174] It is however essential to understand the intrinsic cluster properties in order to control the final material properties.

Molecular beam technique is ideal for measuring the properties of clusters in isolation as the clusters are free from any external influences. Metal clusters can be produced by making a supersonic beam of metal vapour from an oven, typically known as cluster-source. In the molecular beam experiment a cluster source and one cluster detector is required. With the development of the pulsed laser vaporization of metal substrates inside a high pressure pulsed nozzle, it is possible to synthesize clusters of almost any metal. Cluster detectors are typical ion detectors specially designed for the particular mode of experiment.**Erreur ! Signet non défini.**

One of the areas of cluster research currently being pursued is the investigation of the magnetic properties of small atomic clusters. Since large number of atoms of the clusters are on the surface, one expects the clusters of these elements to exhibit larger magnetic moments. Being small particles, it is possible to measure the magnetic

moment directly by measuring the interaction with a magnetic field in terms of their deflection from the original trajectories.

7.3.2 Magnetic measurements and results:

Following Stern and Gerlach's historical experiment on Silver atoms, non-resonant magnetic deflection experiments have been performed for many atoms. In the direct measurement of moments by deflection methods, it is necessary that the sample have reasonable number of particles with a narrow size distribution. In analogy with the Stern-Gerlach experiment, the deflection for clusters is ;

$$d_N = K \mu \frac{dB / dz}{Nmv_N^2} \qquad (1)$$

where K is the geometrical factor related to magnet length and detector position, dB/dz is the magnetic field gradient transverse to the field, m is the mass of the atom, N is the number of atoms in the cluster, v_N is the velocity of the cluster and μ is the total magnetic moment of the cluster, equal to μ_B for N=1. The deflections are scaled in terms of the deflection of atoms in a fixed field gradient.[175] The experiment essentially consists of the following steps :

i) Production of clusters and selection of a narrow mass and velocity distribution ,

ii) passage of the selected clusters through a magnetic field gradient or a quadrupole magnet,

iii) the final detection of the clusters along with a measurement of the amount of deflection from their original trajectories.

The cluster beam from the source is chopped by employing a mechanical chopper to form tiny packets of clusters (few centimeter long) which are subjected to deflection in the gradient magnetic field. The chopper also acts as a clock to the whole time sequence of the measurement and the velocity of the clusters can hence be determined from a known distance of travel through the experimental setup by employing an electronic time-synchronization technique. The deflected neutral clusters are ionized by an ionizing laser and detected usually by a time of flight (TOF) mass spectrometer. The deflections are measured applying mass-integrated or position-sensitive techniques. Clusters having same mass but ionized at different positions in the ion volume get to the detector in the mass-integrated detection mode,[176] whereas the voltages are optimized in the position-sensitive mode so that the flight time of clusters with the same mass depends on the initial positions in the ion volume. The ionizing

laser pulse is shifted in a linear scale to record the transverse profile of the beam at a particularly deflected position from its original trajectory.

7.3.3 Deflection profile:

The Stern-Gerlach deflection profiles for clusters show a single peak and are unlike those for atoms and molecules. The deflections are in one direction only, corresponding to the direction of increasing magnetic fields. With the increase of the magnetic fields, the profiles shift towards the strong field and finally forms a ramp that increases from zero near the beam axis to a maximum value at a strong field before dropping off abruptly. The effect of the gradient magnet is manifested as a shift of the spatial profile for each cluster size towards the direction of strong magnetic field. The single peak in the profile shows that the cluster magnetic moments are polarized during the passage through the magnetic field. This situation is unlike the quantization behaviour of magnetic moments in atoms and molecules but similar to the situation of a bulk ferromagnet with an applied magnetic field.**Erreur ! Signet non défini.,Erreur ! Signet non défini.**

From the average deflections of the size selected clusters, the magnetization can be determined using equation (1). The μ in equation (1) gives the total effective magnetic moment of the cluster which can be used to determine the average magnetic moment per atom from the knowledge of number of atoms in a cluster. Since there is no interaction between the clusters formed in a molecular beam, and the size of even a typical thousand atom cluster is much less than the critical size of a single domain, it can be assumed that the clusters posses superparamagnetic relaxation where the atomic moments of clusters are ferromagnetically aligned and the magnetic anisotropy energy is much smaller compared to thermal energy. The net magnetization in any given direction is zero without the magnetic field but as the field is applied, the clusters develop magnetic moment on time scales depending on the relaxation time. The magnetic moment per atom in the cluster can then be calculated by simply applying the Langevin relation for paramagnetism.
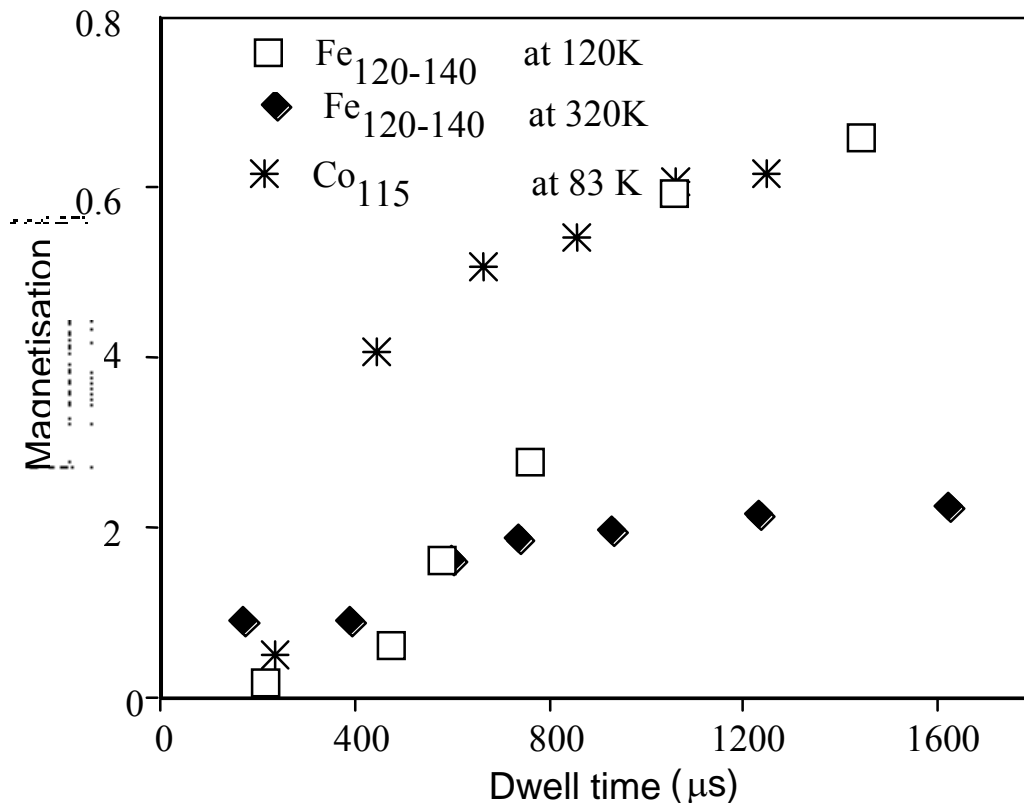
Figure 1: Cluster magnetization in units of Bohr magneton as a function of dwell (residence) time. The data for the iron clusters are after W.A. de Heer et al[177,Erreur ! Signet non défini.] The data for the cobalt clusters are from Douglass et. al.[Erreur ! Signet non défini.]

Obviously from the assumptions, this can be applied only when there is good linearity in the magnetization. The moment remains fairly linear with the applied magnetic field in a low gas pressure in the source chamber with fairly long dwell time for clusters within the chamber. In this quasi-effusive process the cluster vibrational-temperature is essentially equal to the nozzle temperature.[Erreur ! Signet non défini.] It has been observed that the cluster vibrational temperature at fairly long residence(dwell) time becomes equal to the source temperature (Fig1).[178] Allowing a longer dwell time to the clusters actually helps attaining thermal equilibrium with the source condition. Attempts have been made to explain the low value of magnetization at small dwell times in terms of spin resonance-type phenomenon where spin resonantly couples to the cluster rotations through the cluster lattice anisotropy field, similar to what happens in an ESR experiment, considering the clusters to be classical particles having a rotational frequency.[Erreur ! Signet non défini.] Due to lower mass flow rate in the molecular beam the cluster moments saturate at comparatively lower dwell times at higher temperatures (Fig.1). But the growth period to a finite total moment should also depend on attaining a particular geometrical arrangement of atoms in a cluster.

7.3.4 Size dependence:
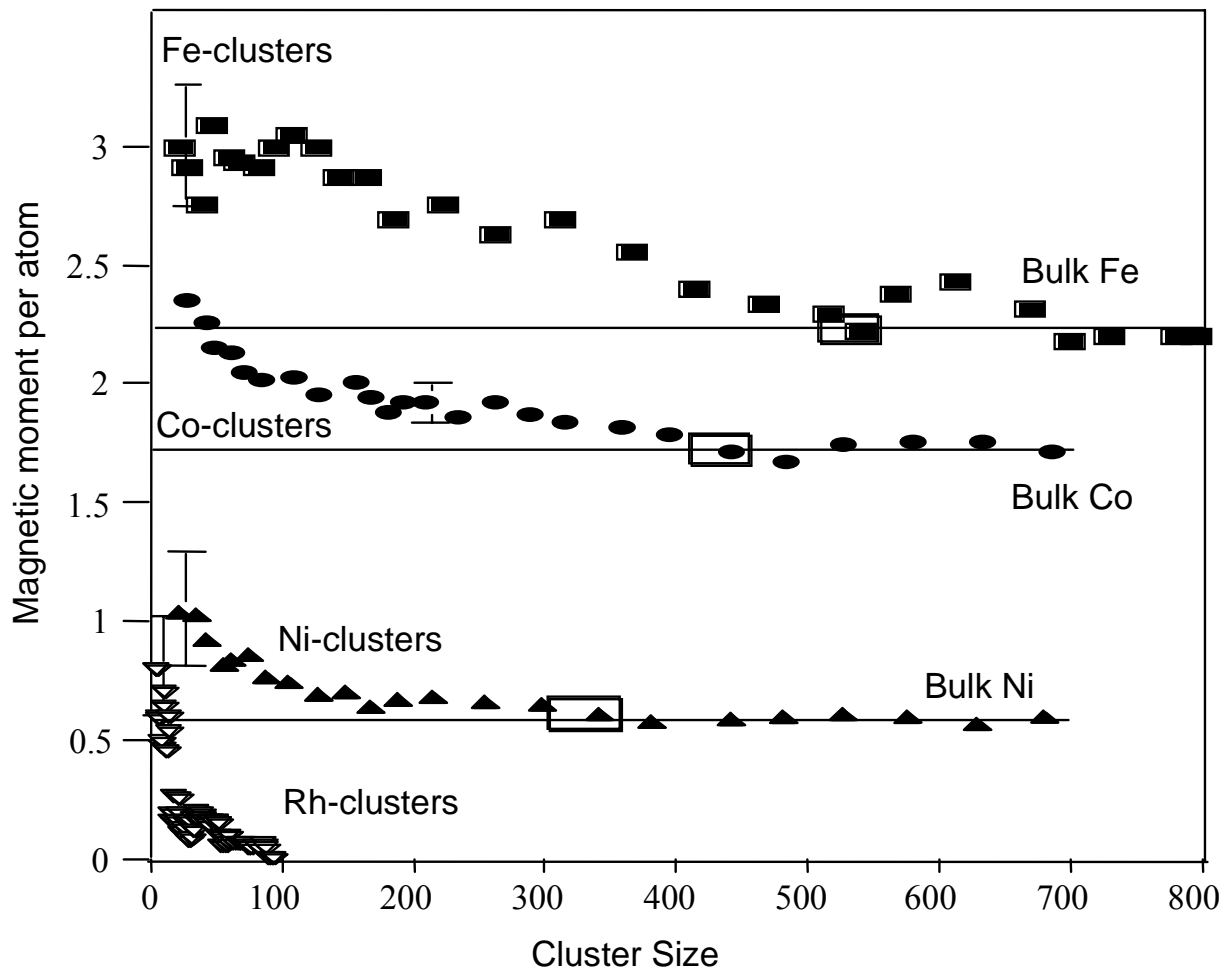
Fig.2 Magnetic moment per atom in units of Bohr magnetron for iron, cobalt, nickel and rodium clusters as a function of cluster size. The enclosed data points show the sizes of the respective clusters at which they attain bulk moments. Only the maximum error in the data for each clusters are shown. Iron, cobalt and nickel data are from W. A. de Heer et al.[179] and Billas.**Erreur ! Signet non défini.** The rodhium data is from Cox et. al.**Erreur ! Signet non défini.**

The magnetic moment of transition metals decreases in general with the increase of number of atoms(size) in the clusters. However, the moment of different transition metal clusters are found to depend differently on the size of clusters. Among the ferromagnetic 3d transition metals, Nickel clusters attain the bulk moment at N=150, whereas Cobalt and Iron clusters reach at the corresponding bulk limit at N=450 and N=550 respectively (Fig.2). In icosahedral configuration these numbers correspond to 3, 4 and 5 shells respectively.[180] However one needs to confirm the bulk like behavior only

after measuring the temperature dependence of magnetic moment for clusters. The spin imbalance at 3d-orbital has been correlated to the measured moment as :

$$n(+) - n(-) = \frac{2}{g_x} \mu_x(N)$$

(2)

where g_x is the bulk g-factor for the respective metal. The results show that in the lower size limit the clusters have high spin majority configuration and the behaviour is more like an atom, but with the increase of size an overlap of the 3d-band with the Fermi level occurs, which reduces the moment towards that of the bulk with slow oscillations.**Erreur ! Signet non défini.** In analogy with the layer-by-layer magnetic moments in the studies of surface magnetism, the clusters are assumed to be composed of spherical layers of atoms forming shells and the value of moment of an atom in a particular shell is considered to be independent of the size of cluster. The magnetic moment values of the different shells are optimized to fit with the total moment per atom maintaining the overall trend of observed decrease with size. It is generally observed that the per atom moment for the surface atoms in the 1st layer are close to that of an atom and deep layers correspond the bulk. The intermediate layers show an overall decreasing trend. For both nickel and cobalt there are oscillations in the values at least upto the 5th shell. For nickel, the second layer is found to have a negative coupling with the surface atoms and the 3rd-4th layers in iron are magnetically dead. The model gives more or less close agreement with the experimental results for cobalt and nickel. But in a more realistic model one has to account for both the geometric shell closing as well as the electronic structure. However this model provides a good first order picture to understand the magnetic behavior of 3d transition metal clusters.

Though the 4d transition metals are non-magnetic, the small clusters of rhodium are found to be magnetic following the calculations.[181] Within the size range N=10-20, the moment varies between 0.8 to $0.1\mu_B$ per atom but the clusters become non-magnetic within N=100. Due to reduced size, the individual moments on the atoms in clusters are aligned. First principal calculations show that the ground state of Rh_6 is non-ferromagnetic, while Rh_9 , Rh_{13} and Rh_{19} clusters have non-zero magnetic moments. Rh_{43} is found to be non-magnetic as the bulk. Ruthenium, palladium, Chromium, Vanadium and Aluminium clusters are found to be non-magnetic.**Erreur ! Signet non défini.**

7.3.5 Thermal behaviour:

Since ferromagnetic state requires the moments to remain mutually aligned even at relatively high temperatures, it is important to study the thermal behaviour of the magnetic clusters. Temperature dependent studies show that upto 300K the moment remains constant for nickel clusters and then it decreases at higher temperatures resembling closely the bulk behaviour. This indicates that the interactions affecting the mutual alignment of moments with temperature are in the same order of magnitude as in the bulk. $Ni_{550-600}$ is almost bulk-like. Cobalt clusters also follow the same trend but the moment increases slightly between 300K to 500K which might be due to a structural phase transition corresponding to the hcp-fcc phase transition in bulk at 670K, where the moment increases by 1.5%. Clusters of different size ranges of iron behave differently; Fe_{50-60} shows a gradual reduction of moments from $3\mu_B$ at 120K to $1.53\mu_B$ at 800K. Upto 400K, $Fe_{120-140}$ remains with a constant moment of $3\mu_B$ and then decreases to finally level off at 700K to $0.7\mu_B$. The size range N=82-92 behaves like $Fe_{120-140}$ below 400K and like Fe_{50-60} above 400K. The moment for the higher size ranges decreases steadily with the increase of temperature but $Fe_{250-290}$ levels off at 700K whereas $Fe_{500-600}$ levels off between 500-600K to $0.4\mu_B$. Comparing with the thermal behavior of bulk iron, the level-off temperature can be termed as the *critical temperature* (T_C) for clusters of a particular size and it decreases with the increase of size of the clusters. But, since the bulk Curie temperature is 1043K, one realizes clearly that this trend must reverse at higher sizes to reach the bulk. It is also interesting to note that for $Fe_{120-140}$ the moment decreases more rapidly within 600-700K. The specific heat measurement for both $Fe_{120-140}$ and $Fe_{250-290}$ also show a peak at 650K. This might be because iron clusters undergo a structural phase transition in this temperature range similar to the bulk iron which undergo bcc-fcc-bcc phase transition, but only beyond the Curie temperature. Since the structure of clusters cannot be detected in a molecular beam, this remains an unsettled question. However, there is a competition between the different structures for iron clusters,**Erreur ! Signet non défini.** and it is more probable that a structural transition occurs at low temperature for increasing cluster size but revealing it needs a better characterization.

7.3.6 Rare earth clusters:

The magnetic interaction in rare earth solids are RKKY type which is mediated by the conduction electrons. Since in clusters, structure and filling up of the conduction band differs from that in the bulk, rare-earth clusters are expected to exhibit an altogether different magnetism compared to the bulk. Magnetic properties of gadolinium, terbium and dysprosium clusters show a very size-specific behavior.^{Erreur ! Signet non défini.} Gd_{22} behaves super-paramagnetically but Gd_{23} shows a behavior like a rigid magnetic rotor as if the moment is locked to the cluster lattice. Gd_{17} shows super-paramagnetism near room temperature but at low temperatures it shows locked-moment behaviour. It indicates that there are at least two groups of clusters sharing the same number of atoms which might correspond to two different isomers, either magnetic or structural. But it is not clear whether the two isomers co-exist in the beam or there occurs a phase transition of any kind. The behaviour of other clusters from N=11-30, is like Gd_{22} or Gd_{23} or Gd_{17} . Similar is the case for Tb and Dy clusters. Tb_{17} , Tb_{22} , Tb_{27} , Dy_{22} , Dy_{27} , show super-paramagnetic behavior but Tb_{23} and Tb_{26} show locked-moment behavior. In fact Tb_{26} is temperature dependent like Gd_{17} . Assuming the clusters to be spherical with a moment of inertia and a body fixed moment which rotates with the cluster, calculations show a very complex precession and nutation when the rotational kinetic energy becomes comparable to the magnetic potential energy. With two parameters viz. the rotational temperature and the magnetic moment, a fit of the experimental data for Gd with several initial conditions and a rotational temperature of 5K, shows an agreement at least for sizes lower than N=30.

7.4 Why interest in nano-scale magnetic materials?

There is a dramatic change in magnetic properties when the critical length governing some phenomenon (magnetic, structural, etc.) is comparable to the nanoparticle or nanocrystal size. Since a large amount of surface is exposed, effects due to surfaces or interfaces are stronger.

Changes in magnetization of a material occur via activation over an energy barrier. Each physical mechanism responsible for an energy barrier has an associated length scale. The fundamental magnetic lengths are the crystalline anisotropy length, l_k , the applied field length, l_H , and the magnetostatic length, l_S , which are defined as follows:

$$l_k = \sqrt{J/k}$$

$$l_H = \sqrt{2J/HM_S}$$

$$l_S = \sqrt{J/2\pi M_S^2}$$

Here, k is an anisotropy constant of the bulk material due to the dominant anisotropy and J is the exchange within a grain. If more than one type of barrier is present, then magnetic properties are dominated by the shortest characteristic length. For most common magnetic materials, these lengths are of the order of 1 – 100 nm. For example, nickel at 1000 Oe and room temperature has lengths $l_S \cong 8$ nm, $l_k \cong 45$ nm, and $l_H \cong 19$ nm.

When a sufficiently large magnetic field is applied the spines within the material align with the field. The maximum value of magnetization achieved in this state is called the saturation magnetization, M_S. As the magnitude of the field decreases, spines cease to be aligned with the field and the total magnetization decreases. In ferromagnets, a residual magnetic moment remains at zero field. The value of the magnetization at zero field is called the remanent magnetization, M_R. The ratio of the remanence magnetization to the saturation magnetization, M_R/M_S, is called the remanence ratio and varies from 0 to 1. The magnitude of the field that must be applied in the negative direction to bring the magnetization of the sample back to zero is called the coercive field, H_C magnetic recording applications require a large remanent magnetization, moderate coercivity, and (ideally) a square hysterisis loop.
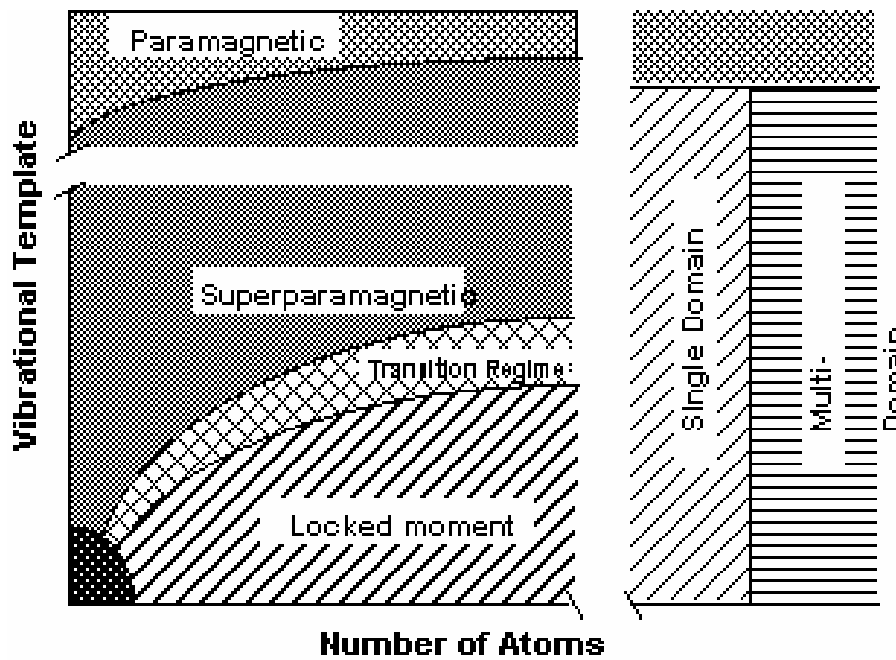
Figure: Different regimes of magnetism with respect to the number of atoms in the material.

7.4.1 Anisotropy:

Most materials contain some type of anisotropy effecting the behavior of the magnetization. The most common forms of anisotropy are:

Crystal anisotropy,

Shape anisotropy,

Stress anisotropy,

Externally induced anisotropy, and

Exchange anisotropy.

The two most common anisotropies in nanostructure materials are crystalline and shape anisotropy. The anisotropy can often be modeled as uniaxial in character and represented by (in the simplest form)

$$E = kV \sin^2\theta$$

where k is the effective uniaxial anisotropy energy per unit volume, θ is the angle between the moment and the easy axis, and V is the particle volume.

Magnetocrystalline anisotropy arises from spin-orbit coupling and energetically favors alignment of the magnetization along a specific crystallographic direction. The direction favored by the magnetocrystalline anisotropy is called the easy axis of the material. The magnetocrystalline anisotropy is specific to a given material and

independent of particle shape. In hcp cobalt, magnetocrystalline anisotropy causes the magnetization to point along the C axis. In cubic system (such Fe and Ni) symmetry creates multiple easy axes. In nickel, the <111> axes are easy axes, while in iron, the <100> axes are the easy axes. The magnitude of the magnetocrystalline anisotropy at room temperature is 7×10^6 erg/cm^3 in Co, 8×10^5 erg/cm^3 in Fe, and 5×10^4 erg/cm^3 in Ni. The coercivity is proportional to the anisotropy constant, so high-anisotropy materials are attractive candidates for high coercivity applications.

A polycrystalline sample with no preferred grain orientation has no net crystal anisotropy due to averaging over all orientations. A nonspherical polycrystalline specimen can, however, posses shape anisotropy. A cylindrical sample, for example, is easier to magnetize along the long direction than along the short directions. Shape anisotropy is predicted to produce the largest coercive forces.

Stress anisotropy result from internal or external stresses that occur due to rapid cooling, application of external pressure etc. Anisotropy may also be induced by annealing in a magnetic field, plastic deformation, or by ion beam irradiation.

Exchange anisotropy occurs when a ferromagnet is in close proximity to an antiferromagnet or ferromagnet. Magnetic coupling at the interface of the two materials can create a preferential direction in the ferromagnetic phase, which takes the form of a unidirectional anisotropy. This type of anisotropy is most commonly observed in type – B particles, when an antiferromagnetic or ferromagnetic oxide forms around a ferromagnetic core.

7.5 Classifications of magnetic nanomaterial:

The magnetic behavior of most experimental realizable systems of is result of contributions from both interaction and size effects. The correlation between nanostructure and magnetic properties suggests a classification of nanostructure morphologies. The following classification is designed to emphasize the physical mechanisms responsible for the magnetic behavior. Fig.1. schematically represents the classification. At one extreme are systems of isolated particles with nanoscale diameters, which are denoted by type A. These non interacting systems derive their unique magnetic properties strictly from the reduced size from the components, with no contribution from interparticle interactions. At the other extreme are bulk materials with nanoscale structure denoted by type D, in which a significant fraction (upto 50%) of the sample volume is composed of grain boundaries and interfaces. In contrast to type A

systems, magnetic properties here are dominated by interactions. The length of the interactions can span many grains and is critically dependent on the character of interface. Due to this dominance of interaction and grain boundaries, the magnetic behavior of type D nanostructures cannot be predicted simply by applying theories of polycrystalline materials with reduced length scale. In type B particles, the presence of a shell can help prevent particle interactions, but often at the cost of interaction between the core and the shell. In many cases the shells are formed via oxidation and may themselves be magnetic. In type C materials, the magnetic interaction are determined by the volume fraction of the magnetic particles and the character of the matrix they are embedded in.
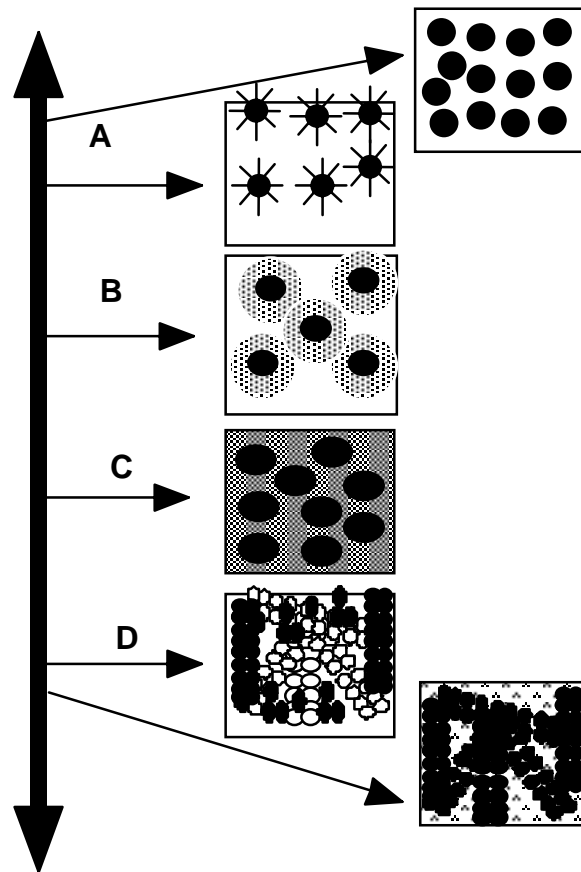
Figure 1. Schematic representation of the different types of magnetic nanostructures. Type-A materials include the ideal ultrafine particle system, with interparticle spacing large enough to approximate the particles as noninteracting. Ferrofluids, in which magnetic particles are surrounded by a surfactant preventing interactions, are a subgroup of Type-A materials. Type-B materials are ultrafine particles with a core-shell morphology. Type-C nanocomposites are composed of small magnetic particles embedded in a chemically dissimilar matrix. The matrix may or may not be magnetoactive. Type-D materials consists of small crystallites dispersed in a

noncrystalline matrix. The nanostructure may be two-phase, in which nanocrystallites are a distinct phase from the matrix, or the ideal case in which both the crystallites and the matrix are made of the same material.

7.5.1 Ferrofluid:

A ferrofluid is a synthetic liquid that holds small magnetic particles in a colloidal suspension, with particles held aloft their thermal energy. The particles are sufficiently small that the ferrofluid retains its liquid characteristics even in the pressure of a magnetic field, and substantial magnetic forces can be induced which results in fluid motion.

A ferrofluid has three primary components. The carrier is the liquid element in which the magnetic particles are suspended. Most ferrofluids are either water based or oil based. The suspended materials are small ferromagnetic particles such as iron oxide, on the order of 10 – 20 nm in diameter. The small size is necessary to maintain stability of the colloidal suspension, as particles significantly larger than this well precipitate. A surfactant coats the ferrofluid particles to help maintain the consistency of the colloidal suspension.

The magnetic properties of the ferrofluid is strongly dependent on particle concentration and on the properties of the applied magnetic field. With an applied field, the particles align in the direction of the field, magnetizing the fluid. The tendency for the particles to agglomerate due to magnetic interaction between particles is opposed by the thermal energy of the particles. Although, particles vary in shape and size distribution, insight into fluid dynamics can be gained by considering a simple spherical model of the suspended particles.
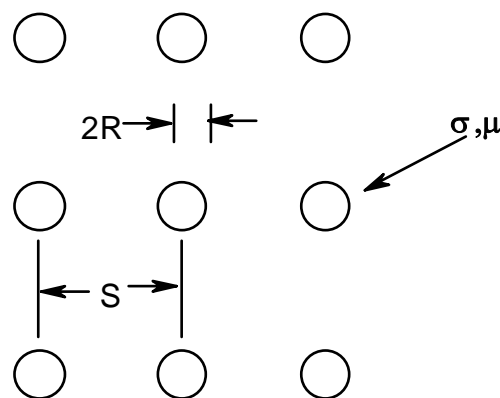

figure: Representative model of a typical ferrofluid.

The particles are free to move in the carrier fluid under the influence of an applied magnetic field, but on average the particles maintain a spacing S to nearest neighbor. In a low density fluid, the spacing s is much larger than the mean particle radius 2R, and magnetic dipole – dipole interactions are minimal.

Applications for ferrofluids exploit the ability to position and shape the fluid magnetically. Some applications are:

- rotary shaft seals

- magnetic liquid seals, to form a seal between region of different pressures

- cooling and resonance damping for loudspeaker coils

- printing with magnetic inks

- inertial damping, by adjusting the mixture of the ferrofluid, the fluid viscosity may be change to critically damp resonances accelerometers,

- level and attribute sensors

- electromagnetically triggered drug delivery

Table: Material Parameters of a typical ferrofluid:[182]

Sample Volume	$1.7 \times 10^{-6}\, m^3$
Electrical conductivity of particles	$\sigma_f = 3 \times 10^6 (\Omega m)^{-1}$
Electrical conductivity of ferrofluid	$\sigma_{fluid} < 10^{-7} (\Omega m)^{-1}$
Volume percentage of particles	$\approx 3\%$ by volume
Initial magnetic permeability of particles	$\mu \approx 100 \mu_0$
Particle mean radius	$R \approx 10^{-8}$ m
Density of magnetic particles	ρ_{FE} = 7.8 g/cm^3
Fluid density	ρ_f = 1 g/cm^3
Fluid viscosity of carrier fluid	η =1 cp = 0.01 g/cm. sec

7.5.2 Single Domain Particles

Domains – groups of spins all pointing in the same direction and acting cooperatively -– are separated by domain walls, which have a characteristic width and energy

associated with their formation and existence. The motion of domain wall is a primary means of reversing magnetization. The dependence of coercivity on particle size is similar to that schematically illustrated in Fig. 3.
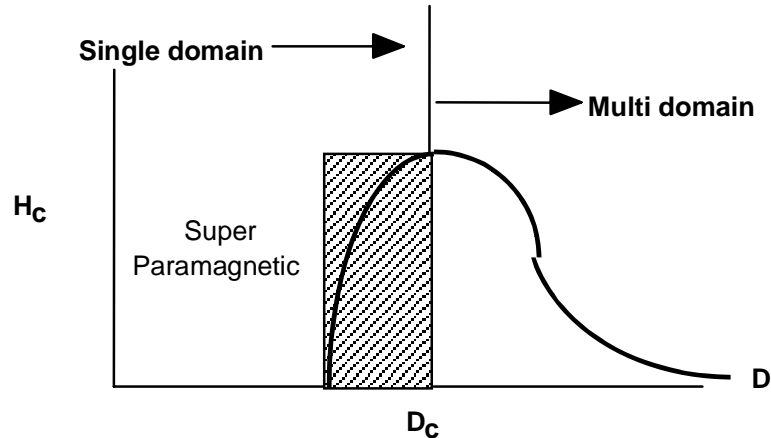

Figure 3. Qualitative illustration of the behaviour of the coercivity in ultrafine particle systems are the particles size changes.

In large particles, energetic considerations favor the formation of domain walls. Magnetization reversal thus occurs through the nucleation and motion of these walls. As the particle size decreases towards some critical particle diameter, D_c, the formation of domain walls becomes energetically unfavorable and the particles are called single domain. Changes in the magnetization can no longer occur through domain wall motion and instead require the coherent rotation of spins, resulting in larger coercivity. As the particles size continues to decrease below the single domain value, the spins get increasing affected by thermal fluctuations and the system becomes superparamagnetic. Particles with sufficient shape anisotropy can remain single domain to much larger dimensions than their spherical counterparts.

7.5.2.1 Single-Domain Characteristics:

In a granular magnetic solid with a low volume fraction, one has a collection of single domain particles each with a magnetic axis along which all the moments are aligned. In the absence of a magnetic field, parallel and anti parallel orientations along the magnetic axis are energetically equivalent but separated by an energy barrier of CV, where C is the total anisotropy per volume, and V is the particle volume. Since the size of each single domain remains fixed, under an external field, only the magnetic axes rotate. Thus the measured magnetization (M) of a granular magnetic field solid with a collection of single domain particles is the global magnetization

$$M = \frac{\left\langle \vec{M} . \vec{H} \right\rangle}{H} = M_s \left\langle \cos \theta \right\rangle$$

where θ is the angle between the magnetic axis of a particle. M_s, is the saturation magnetization, $\vec{H}$ is the external field, and the average <cos θ> is taken over many ferromagnetic particles. The hysterisis loop of a granular solid is thus a signature of the rotation of the magnetic area of the single-domain particles. This should be contrasted with the hysterisis loop of a bulk ferromagnet, in which the sizes and the direction of the domains are altered drastically under an external field.
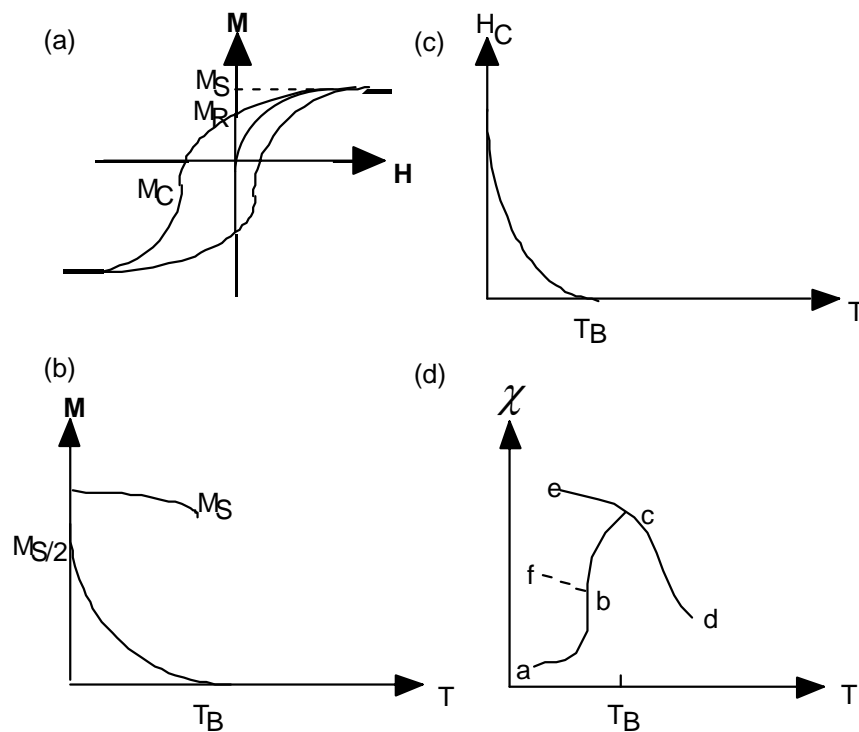
Figure 4. (a) Hysterisis loop at 5K; (b) temperature dependence of saturation magnetization (M_S) and remnant magnetization (M_R); (c) temperature dependence of field cooled (FC) and zero-field cooled (ZFC) susceptibility. At the blocking temperature (T_B), M_R and H_C vanish, whereas the ZFC susceptibility shows a cusp like feature.

An example of a hysterisis loop of a granular magnetic solid at low temperature is shown in Fig. 4a. In the initial unmagnetized state with M = 0 at H = 0, the magnetic axes of the particles are randomly oriented, each along its own magnetic axis, which is determine by the total magnetic anisotropy of the particles. The directions of the giant moments are random and static at low temperatures. A saturation magnetization (M = M_S) is realized under a large field when all the magnetic axes are aligned. In the

remnant state when H is reduced to H = 0, one observes the remnant magnetization (M_R), whose values at low temperature is $M_R = M_{S/2}$. This is because the magnetic axes are oriented only in one hemisphere due to the uniaxial anisotropy of the single-domain particle.

It should be noted that the initial M=0 state and the initial magnetization curve if in fig. 4a does not reappear, whereas the field cycle part does. The simples way to recover the initial M=0 state is to heat the sample above the blocking temperature and cool the sample in zero field back to low temperatures.

Because of the single domain nature of the magnetic entities, the coercivity (H_C) of the ultra fine particles is much higher than that in bulk material.

7.5.3 Superparamagnetic relaxation:-

At sufficient high temperatures, the energy barrier (CV) is overcome by the thermal energy. Consequently, the magnetic moments within a particle rotate rapidly in unison, exhibiting the superparamagnetic relaxation phenomenon. The simplest form of the relaxation time can be described by the Arrhenius relation,

$$\tau = \tau_0 . exp(CV/_{k_B T})$$

where τ is the relaxation time, τ_0 is the characteristic time, and CV is the total anisotropy energy. The behavior of τ is dominated by the exponential argument. Assuming representative valves ($\tau_0 = 10^{-9}$s, $K_B = 10^6$erg/cm^3, and T=300K), a particle of diameter 11 – 4 nm will have a relaxation time of 0.1 s. Increasing the particle diameter to 14.6 nm increases τ to 10^8s. For an instrument that can measure certain magnetic characteristics (e.g. magnetometry, AC susceptibility, Mössbauer spectroscopy) with a measurement time of τ_i, one can define a blocking temperature.

$$T_B = \frac{CV}{k_B \ln(\tau_i/\tau_0)}$$

At T<T_B, τ_i is less than τ and the instrument detects the ferromagnetic nature (e.g. a hysterisis loop) of the system. However, at T>T_B, because τ_i is longer than τ, the time averaged value of the ferromagnetic characteristics (e.g. magnetization and coercivity) vanish within the measuring time of τ_i. then the system is in an apparent paramagnetic or superparamagnetic state, even though within each particle the magnetic moments remain ferromagnetically aligned. Because of the superparamagnetic relaxation, the

value of remnant magnetization (M_R) and coercivity (H_c) decrease with increasing temperature and vanish at the blocking temperature (T_B). Above T_B, all apparent ferromagnetic characteristics disappear. These aspects are shown in Fig. 4b and c. The blocking temperature in a superparamagnetic system decreases with increasing measuring fields, being proportional to $H^{2/3}$ at large magnetic fields and proportional to H^2 at lower fields.

Another useful technique for the measurement of superparamagnetic relaxation is low-field susceptibility measurements in both zero field cooled (ZFC) and field – cooled (FC) modes. As shown in Fig. 4d, the FC and ZFC data are the same and hence reversible. Below T_B, however, the FC and ZFC data are totally different and irreversible. In particular, the ZFC data shows a readily detectable cusp-like feature at T_B.

7.5.4 Giant Magnetoresistance (GMR)

The discovery in 1988 of the giant magnetoresistance (GMR) effects in magnetic multilayers with nanometer-scale layer thickness[183] and subsequent research leading to materials showing the effect in very small magnetic fields has opened options for the applications of GMR materials in read heads for high density digital disk & tape recording.[184]

7.5.4.1 Structure and functioning of exchange-biased spin valve GMR

According to the structure given in the following figure two ferromagnetic (F) layers are separated by a non-magnetic (NM) spacer layer. A third magnetic layer of a properly chosen composition and structure [usually antiferromagnetic (AF)] is in contact with F layers. This is called a simple exchange biased spin valve structure.[185]
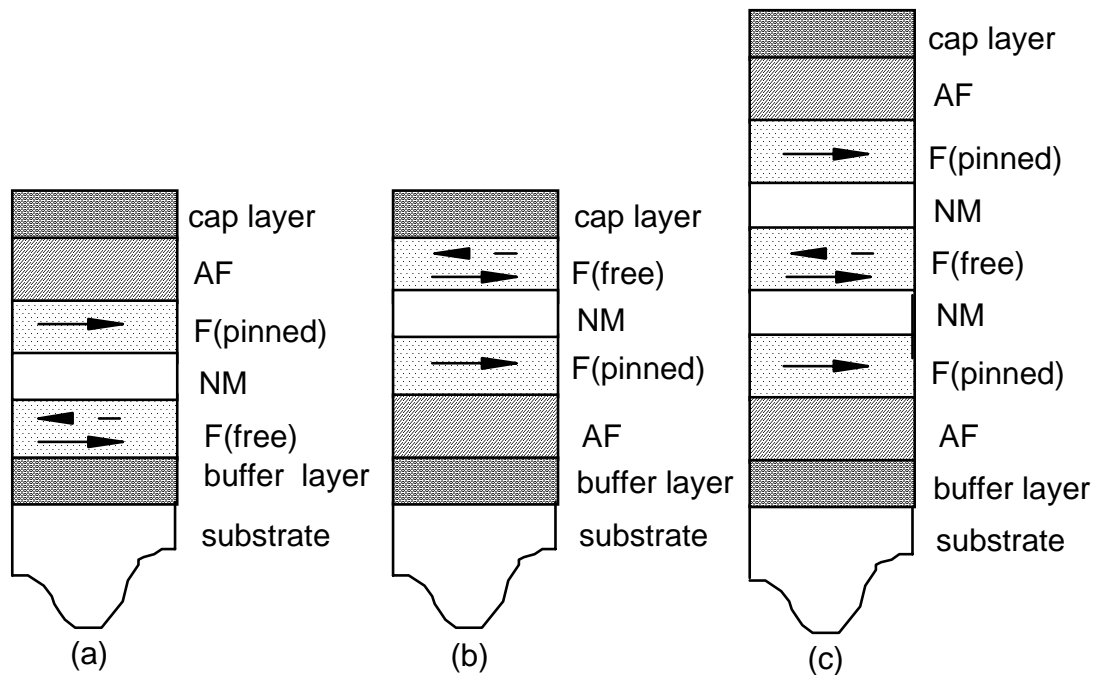
Figure: Fig. 1. Schematic cross-section of a top (a), bottom (b) and a symmetric (c) exchange-biased spin-valve structure.

The thickness of F layers in 3 to 10 nm & that of spacer layer is 2 to 3 nm. Under a suitable preparation condition (Growth in a magnetic field) part of the layer which is in contact with AF layer undergoes pinning of the magnetization due to exchange interaction across the interface (known as exchange biasing). The unpinned (free) F layer is usually magnetically very soft while the NM spacer layer is sufficiently thick as to almost eliminate the magnetic coupling between F layer. Moreover, the presence of only a few monolayers of second ferromagnetic metal at the F/NM interface can lead to a strong enhancement of the "magnetoresistance ratio". The interaction energy E between the pinned 'F' layer and antiferromagnetic layer is given by $E=-K_{eb} Cos\theta$ and the exchange biasing field varies inversely with layer-thickness.

In a small field interval (H=O) the magnetization of free F layers reverses while that for pinned F layer remains fixed. To overcome the exchange biasing interaction a large negative field (equal to the exchanging biasing field) which switches the pinned layer. In general magnetic layer thickness can be different leading to a nonzero magnetization in the antiparallel state. The GMR effect is the increase of resistance upon the exchange of the angle between neighboring magnetic layers from a parallel to an antiparallel alignment. The observed angular variation of the resistance is given by the following phenomenological equation:

R (θ)=R (θ=0) + ΔR_{GMR}(1-cosθ)/2

Where θ= angle between the magnetization direction of the free and pinned layers.[186]

The ratio ΔR_{GMR}/ R (θ=0) is called the GMR ratio.

7.5.4.2 Origin of the GMR effect

For a macroscopic electrical conductor the resistance R is given by R=P 1/A, which is independent of shape, cross section and above all the scattering process involved therein. Especially, electron-electron and electron-proton scattering process bring the out-of-equilibrium distribution of accelerated electrons back to the equilibrium distribution thereby contribution to resistance. This usual picture loses its validity when the dimension of the material becomes of the order of relevant collision-mean-free path (λ). now for an elastic scattering process the conductivity due to spin up and spin down electron is given by

$\sigma = \sigma_1 + \sigma_2$ (for an elastic scattering process)[187]

For the occurrence of the GMR effect it is crucial that

the angles between the magnetization directions of the ferromagnetic layer can be modified by the application of an applied magnetic field,

the electron scattering probability at the interfaces or within the bulk of the layers is spin-dependent, and

in the case of parallel magnetizations, the layer averaged electron mean-free path for (at least) one spin direction is larger than the thickness of the non-magnetic spacer layer.

Now, each layer in a GMR- structure acts as a spin selective valve. In case of parallel-alignment-layer the contribution towards conductance due to spin up electron is highly leading to higher valve of total conductance. However, for antiparallel alignments the magnetic layers results in appreciable scattering for electrons in both spin direction and hence a lower total conductance. If the F layers are much thinner than $\lambda\uparrow$ the spin up conductance in the parallel magnetization state is limited by strong spin-dependent scattering in the buffer layer and in the AF layer. The contrast with spindown conductance can then be enhanced by increasing the F-layer thickness. It is to be noted that only a part of F-layer which is of the order of $\lambda_\uparrow/2$ from the interface responds to the above situation.
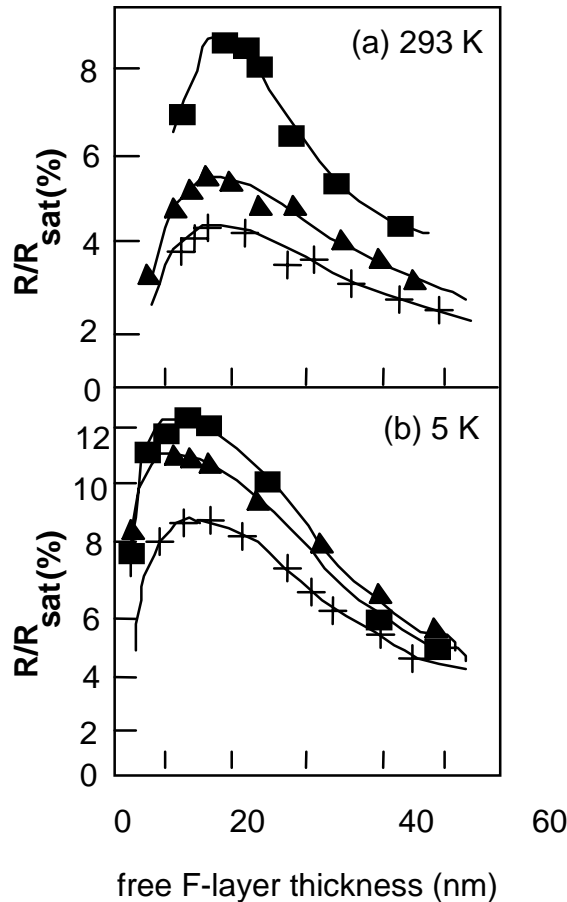
Fig. 7. Dependence of the MR ratio on the free magnetic layer thickness, measured at 293 K (a) and at 5K (b), for $(X/Cu/X/Fe_{50}Mn_{50})$ spin valves, grown on 3nm Ta buffer layer on Si(100) substracts, with X=Co (squares), $X=Ni_{66}Fe_{16}Co_{18}$ (traingles) and $(X= Ni_{80}Fe_{20})$ (+), measured at 5K. Layer thickness: t_{Cu} = 3nm (but 2.5 for F=(X= $Ni_{80}Fe_{20}$); t_F(pinned layer)=5nm (but 6nm for F= $Ni_{66}Fe_{16}Co_{18}$)[188].

Requirements for F/NM combinations with a high GMR ratio are:

the F and NM materials possess, for one spin direction, very similar electronic structures, whereas for the other spin direction the electronic structures are very dissimilar, the electron transmission probability (transmission without diffusive scattering) through the F/NM interfaces is large for the type of electrons for which the electronic structure in the F and NM layers are very similar, and the crystal structures of theF and NM materials match very well.

7.5.4.3 Thermal stability

A number of factors control the use and processing of exchange-biased spin-valve layered structures at elevated temperatures.

Exchanging biasing field decreases with increasing temperature. For some exchange biasing materials this effect determines the temperature range within which sensors can be applied.

The induced magnetocrystalline anisotropy of the free layer may be affected by heating the material.

As multilayers are thermodynamically metastable system the enhanced diffusion rates during annealing will inversibly degrade the layered structure.

Diffusion may also affect the effective coupling between the layers. There are three contributions in interlayer coupling-

Coupling via ferromagnetic bridges between the ferromagnetic layers.

The mangetostatic Neel-type coupling.

Interlayer exchange coupling.

7.5.4.4 Factors determining the switching field interval.

7.5.4.4.1 Induced magnetic anisotropy:

This is believed to be due to the result of a very small degree of divertional pair order of atom a in the otherwise random solid solution. The anisotropy field depends upon the composition, the layer thickness, and the material between which the layers are sandwiched. In case of a GMR spin valve the anisotropy effect is relevant for the thickness below 15 nm. The effect is most likely due to a region with a decreased degree of pair order situated in the ferromagnetic layer close to the interface with the buffer layer. The result shows that addition of Co to permalloy is unfavourable as far as switching field interval is concerned. But one of the advantages is that the range of linear operation of GMR sensor elements are improved. Annealing the sample can affect the anisotropy field. It is often necessary to anneal the sample after decomposition in a magnetic field that is directly perpendicular to field direction during growth, in order to rotate the exchange direction over an angle of 90°. this leads to cross anisotropy configuration. Therefore it is suggestive to anneal with the field parallel to the induced anisotropy before annealing briefly with perpendicular field. On the other hand strain results in an additional magnetocrystalline anisotropy due to magnetostriction. So for sensor element coefficient of magnetostriction should be small. $Ni_{66}Co_{18}Fe_{16}$ alloy is a good candidate for application in GMR sensor elements.

7.5.4.4.2 **Superimposed AMR effect:**[189]

If the current direction is parallel to the easy axis of the free F layer, the magnetoresistance is given by

$$\Delta R(H) = \frac{\Delta R(GMR)(1-\cos\theta)}{2} + \Delta R(AMR)\sin_2\theta$$

The AMR-term represents the resistance change due to the change of angle $(\frac{\pi}{2}-\theta)$ between the magnetization of the free layer and the current direction. The presence of AMR effect increases the sensitivity $\frac{\partial R}{R}\Big/\partial H$ if an operating point between H=0 to H=+H$_a$ is chosen. Experiment shows that due to AMR effects the sensitivity of the spin valve is almost 50% higher then expected from GMR effect. It is suggestive for practical purpose to operate a material around the field H=0, where the element is magnetically most stable.

7.5.4.4.3 Coupling between the magnetic layer:

If we make NM layer very thin the free F layer is found to be magnetically coupled. This coupling leads to an offset of the field around which the free layer switches to a field H= - H$_{couple}$. The coupling field is due to[190]

Ferromagnetic coupling via pinhole.

Ferromagnetic Neel-type coupling.

An oscillatory indirect exchange coupling.

All three contributions are influenced by the microstructure of the material and hence control of the coupling field requires very good control of the deposition condition. This issue is very relevant for sensor application. Most of the cases the coupling field is equal or greater than the anisotropy field. Fortunately, in a sensor element the resulting shift of the switching field is balanced by

Application of a bias magnetic field from a current though an integrated bias conductor.

The magnetostatic coupling between the pinned and the free layer which arises as a result of the stray magnetic field origination from the magnetization of a pinned layer, which is directly along the long axis of the stripe.

Interlayer coupling influences the switching field interval due to the following two effects

The magnetization of the pinned layer is not quite fixed upon the rotation of the free layer. This increases the switching field interval. This effect increases upon an increases of the ratio between the coupling field and the exchange biasing field.

Lateral fluctuations in the coupling field increase the switching field interval.

7.5.4.4.4 Exchange biasing

The interaction energy E between the pinned F layer and the antiferromagnetic layer is given by,

$E = -K_{cb} Cos\theta$.

Where θ be the angle between the biasing direction and the magnetization of the pinned F layer. The exchange biasing field varies inversely with the thickness of the pinned layer

To obtain exchange biasing the AF layer thickness should generally exceed critical valve.

In conclusion, we must say that exchange-biased spin valve layered structures show a combination of properties that are attractive for the application in low field sensors, such as read head in hard disk and tape recording. For a yoke-type GMR head an output gain of a factor 10 has been obtained compared with a barbar-pole biased AMR head. The following factors contribute to operational gain,

Larger MR ratio.

Larger sheet resistance.

Larger flux efficiency of the head, due to the small thickness of the magnetic layer.

Future developments are expected to focus on exchange-biased spin valve materials with an high thermal stability, on the improvement of the effective softness, of the free magnetic layer while remaining a high GMR ratio, and on relation between micromagnetic aspects such as domain wall nucleation and propagation and sensor noise.

7.6 Storage Devices

The design and fabricatrion of nonstructured film are playing an increasing important role in modern science and technology. In the case of non-scale magnetic films, a large part of the interest in driven by information storage and magneto electronic devices.

7.6.1 Magnetic data storage :

Magnetic non-structure are starting to pay a role in technology, particularly in "non-volatile magnetic data storage". New combination with semi-conductor technology are developing such as magnetic random access memories (MRAMS) where the storage capacitor of a traditional semiconductor in replaced by a non-volatile magnetic dot. The storage media to today's magnetic hard disc drives may be viewed as an array of magnetic nanoparticles. The magnetic coating of the disk consists of a ternary Co-Pt-Cr. Mixture which segregates into magnetic Co-Pt grains. These grains are magnetically separated by Cr at the grain boundaries. Typical grain sizes are 10-20 NM using about 10^3 grains/bit at a recording density of 1 Gbit/inch^2 for commercial devices. The grains segregate randomly, which introduces statistical noise into the read out signal due to the variation in grain size, coercivity and domain structure. This explains the large number of grains that are required to reduce these fluctuation in a device.

There is a fundamental limit or the improvement of magnetic storage density. The limit is controlled by

      i)   Thermal flipping of the bits as the grains become smaller;

      ii)   Energy barrier at between the two stable magnetizations along the easy axis becomes comparable with kT. Eventually superparamagnetic limit is reached where individual grains stay matnetized, but their orientation fluctuates thermally.

For typical magnetic storage media, the superparmagnetic limit imposes a minimum particle size of about 10 nm, that is a maximum recording density of several terabits per square inch. This is almost four order of magnitude higher than the density of 1 Gbit/inch^2 found in top-of-the-line disc drives today. While the current particle size is already close to the superparamagnetic limit the number of particle / bits is still more

than 10^3. There are many signal to noise issues on the way towards reducing this number and reaching the theoretical limit. Inconsistent switching of different particles and an irregular domain structure require averaging over many particles. Controlling coercivity, size, orientation and position of magnetic non-particles will be essential for reducing the number of particles needed to store a bit. For example a large crystalline anisotropy can produce a higher switching barrier than the shape anisotropy above. Single domain nanoparticle with high saturation magnetization and coercivity are being optimized for this purpose. The orientation of segregated grains can be controlled using multilayered structures where the first layer acts as seed for small grains and subsequent layers shape the crystalline orientation for the desired anisotropy. A further improvement would be the more from longitudinal to perpendicular recording where demagnetizing field does not destabilize the written domains.

The ultimate goal in magnetic storage in single-particle-per-bit on quantized recording. It is aimed at producing single domain particles close to the superparamagnetic limit with uniform switching properties. Lithography is currently the method of choice for producing regular arrays of uniform magnetic dots. Dot arrays with a density of 65 – 250 Gbit/inch^2 have been produced by electron beam lithography.

7.6.2 Sensors:

Nanostructured material has also been used in the development of some reading head devices. The traditional inductive pick up of the magnetic signal is replaced by a magnetoresistive sensor in state-of-the-art devices.

Permalloy / (Cu/Co) multilayers are utilized in reading heads. Currently, reading heads in high-end disc drives are based on the 2% AMR of permalloy. The resistance is highest for the current parallel to the magnetization and lowest perpendicular to it, producing a sinusoidal orientational dependence. The magnetic stray field between adjacent bits with opposite orientation rotates the magnetization in the permalloy film with respect to the current and thus induces a resistance change. That is directly connectible into a read-out voltage.

Present activities with GMR are directed towards, lowering the switching field while keeping a large magneto-resistance. To obtain the best of both characteristics one obtains soft permalloy layer for easy switching with a high-spin co-layer that enhances the magnetoresistance.

Another type of non-volatile magnetic storage device avoid moving parts altogether at the expense of having to pattern the storage medium. This is a combination of magnetic memory elements with semi-conductor circuits that sense and amplify the magnetic state (MRAM).

Further into the future are logic devices based on magnetic nanostructures. A bipolar spin switch has been demonstrated that acts like a transistor.

8 ELECTRONIC PROPERTIES OF NANOMATERIALS

8.1 Introduction:

New types of elementary devices based on different physics[191] may become available before atomic dimensional limits are encountered. The exploitation of quantum resonances in one dimension has already found its way into practice through the HEMT or modulation-doped field-effect transistors (MODFETs) and single and multiple quantum well (SQW and MQW) semiconductor lasers. Precise control of thin-layer deposition to dimensions as small as 5 or 10 nm has been common in semiconductor manufacturing for years. The resulting one-dimensional resonances result in quantum confinement in the vertical dimension, leading to two-dimensional electron gases with a number of useful attributes, such as energy level splitting with restricted energy transfer between levels and a constant density of states.

With the ability to fabricate horizontal structures lithographically with dimensions of 50 to 100 nm, it becomes possible to provide quantum confinement in any or all three dimensions, leading to a variety of ***quantum plane, wire, and dot*** configurations. Because of the quantum effects, the number of electrons in the well of a quantum dot is quantized to an integer number of electrons, and even if the number is as large as tens to hundreds, single-electron changes can be observed.[192] Combining quantum dots with very thin insulating layers, single-electron tunneling transistors have been implemented, and the possibility of single-electron logic is on the horizon. Although ingenious designs are being proposed, the less-than-unity voltage gain that characterizes the devices tested to date remains a fundamental unsolved engineering problem.

Research in this promising discipline has been active since its formulation in the mid-1980s. Even quantum molecules—i.e., several closely spaced quantum dots interacting via quantum mechanical tunneling-have been explored. All these single-electron semiconductor concepts apply equally well to superconductor implementations with a single Cooper pair replacing the single electron. The work to date has provided a sound theoretical and experimental basis for the underlying physics. The challenge remaining is to come up with practical, working, manufacturable devices in time to keep up with the exponential growth of digital electronics projected for the time frame beyond 2020. It seems likely that the transition from microelectronics to nanoelectronics and its

future high-speed devices will depend on single-charge tunneling effects and the single-electron transistor.

Lasers and similar devices will increasingly be built to exploit quantum effects--the peculiar, discrete behavior of subatomic particles, especially electrons, that have been confined to ultraminute realms in fewer than three dimensions (in clusters). The theory behind quantum devices has been known for decades. But in recent years the technologies that make such confinement possible by building infinitesimal structures out of individual atomic layers or molecules have been advancing at a remarkable pace. By controlling precisely the structure and composition of layers of materials tens of atoms or even just a few atoms thick (nanomaterials), scientists are proving they can program the electronic characteristics they want into a compound.
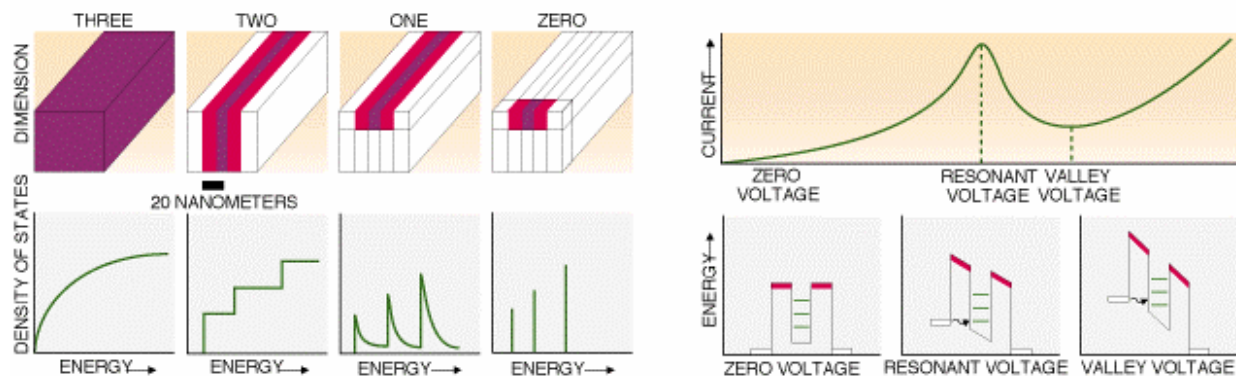

Fig.: The dimensionality of a material can be reduced by sandwiching it between two layers of another material that has higher-energy electrons. This confinement changes the density of electron states, or specific energy levels, that will be filled by incoming electrons (left). The current conducted by a quantum-well device, shown by the green energy levels (right), peaks when the energy level of the incoming electrons matches, or is in resonance with, an energy level of the quantum well. At higher or lower voltages, little current leaks through the device.

Confined within such a thin sheet of material, an electron takes on peculiar properties. On an atomic scale, the energy of an electron orbiting, say, a proton in a hydrogen atom can be at only one of a number of well-defined, discrete levels. The electron need not be part of an atom to exhibit this quantum- effect; it is necessary only for the electron to be confined to a region whose dimensions measure anywhere from a few to a few hundred atoms. This characteristic size, known as the electron wavelength, approximates the hypothetical, indistinct electron cloud representing the probability of

the electron occupying that position. Thus, it makes sense to speak of an electron's wavelength in a ***semiconductor material--which is about 10 nanometers***. Consider Lucent's quantum-cascade laser: electrons are free to occupy the slices of gallium indium arsenide. Partially confined to these semiconductor planes of only a few nanometers thick, the electrons begin to exhibit quantum behavior, such as having discrete energy levels. Through clever materials design, these electrons can be induced to jump from one energy level to another in an organized fashion, causing them to perform another useful trick--typically, emitting or detecting photons of light.

8.2 Review of Atomic Physics

8.2.1 Pauli Exclusion Principle

Let us revisit basic atomic physics to review how electrons "stack up" in an atom. Each electron in an atom must have a unique state,i.e. each electron must have a different set of quantum numbers

$$(n, l, m, s)$$

We can find an analogy with students sitting in a classroom

- no two students are in the same seat
- each seat may be indexed by row and "column" *(like it is done in a theater hall, cinema etc.)*

The energy is primarily determined by the prinicipal quantum number n = **1**, **2**, **3**, ...Then follows the so-called orbital angular momentum values l,m ......, followed by spin s, either spin-up, s = +1/2, or spin-down, s = -1/2. A particular atomic orbital has fixed values of n, l, and m and can thus contain a maximum of **TWO** electrons (one of each spin).

8.2.2 Building Elements

Each additional electron gives the electron "cloud" of the atom a much different behavior -- That is why **each element is different.** Only two electrons may go into the lowest energy state, known as the **1**s state, with (n,l,m)=(1,0,0). Two more may go into the **2**s state, with (n,l,m)=(2,0,0). Six may go into the **2**p state, since there are 3 different angular momentum values: (2,1,-1), (2,1,0), (2,1,1).

Some other examples are given in the following table:

hydrogen:	**1**s1
helium:	**1**s2
lithium:	**1**s2, **2**s1
beryllium:	**1**s2, **2**s2
boron:	**1**s2, **2**s2, **2**p1
carbon:	**1**s2, **2**s2, **2**p2
nitrogen:	**1**s2, **2**s2, **2**p3
oxygen:	**1**s2, **2**s2, **2**p4
flourine:	**1**s2, **2**s2, **2**p5
neon:	**1**s2, **2**s2, **2**p6
sodium:	[Ne] **3**s1

8.3 Origin of energy band in solids:

The properties of any solid material depend upon both the ratio of the constituent atoms and the crystal structure of the solid. Electrons can exist in stable orbit near the nucleus only for the certain allowed value of energy called energy levels of the atoms.

When atoms come across together to form a solid crystal, electrons in the upper levels of adjacent atoms interact to bind the atoms together. Because of strong interaction between these outer or valence electrons, the upper levels are altered drastically (Fig. 1)

Consider two isolated atoms, initially, each with an energy level diagram for the outer electrons as shown in fig. 1(a). When the two atoms are brought close together, the valence electrons in both atoms are attracted by both nucleus. The result is that the energy required to remove an electron from one nucleus and to place it on the other is reduced i.e. an outer electron is equally likely to be located near either nucleus. The approximate energy level diagram for this combination has two energy levels near each atom core.
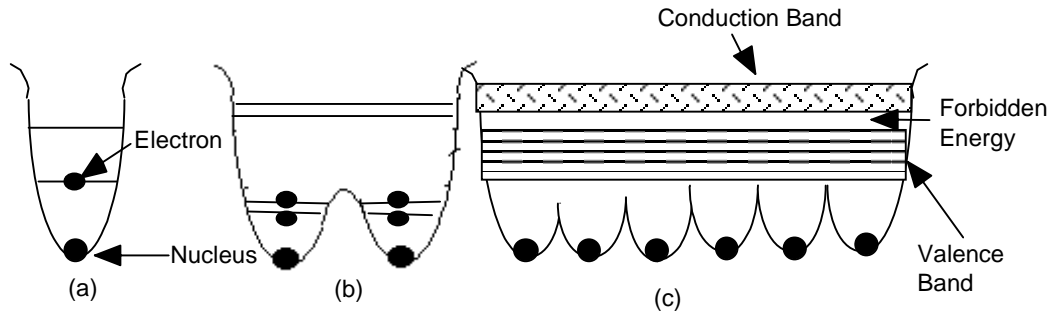
Figure: Energy level diagram for (a) isolated atom, (b) two atoms close together and (c) solid crystal.

The higher unoccupied levels similarly split indicating that these levels can contain two electrons as well. When three atoms are brought together, three energy levels are available. Since there are millions of atoms in a crystal and hence millions of energy levels close together, the energy level diagram appropriate for the crystal has a band of levels. The lowest band, called the valence band (VB) is completely filled i.e. all its permissible energy levels are occupied by electrons. No electron in filled band has any space to move and hence such electrons cannot contribute to electric current. The conduction band (CB) represents the next larger group of permissible energy levels which are not completely filled or is empty. There is an energy gap, E_g between the valence band and the conduction band, called the forbidden energy gap because no permissible energy levels exist in this gap. The gap corresponds to the energy region between energy levels in the isolated atoms as can be seen from Fig. 1. An electron in a conduction band does not belong to any particular atom. Rather, it moves through out the crystal. Such electrons are thus called free electrons. These electrons are not completely free as they are still bound to the crystal.

8.4 Conductor, insulator and semiconductor:

Conduction
Band

$E_g \simeq 5eV$

or more

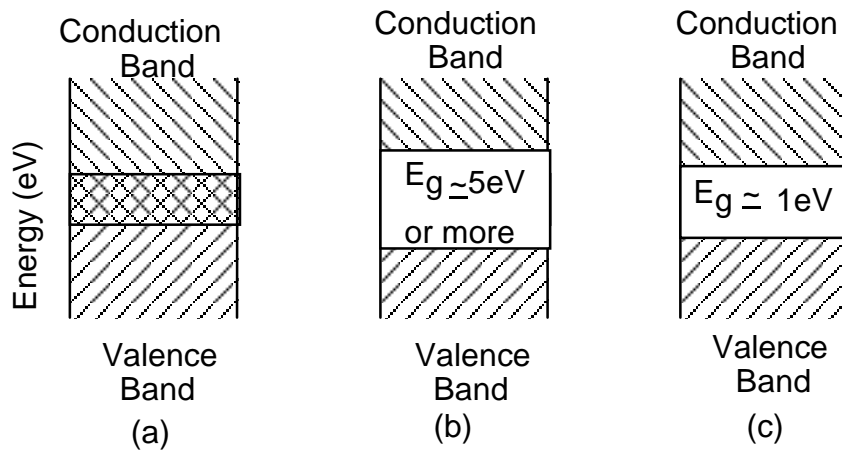$E_g \simeq 1eV$

Energy (eV)

Valence
Band

(a)
(b)
(c)

Fig. 2. Energy – band diagram for (a) metals (b) insulator (c) semiconductors

When an electric field is applied, electrons may flow through a material if there are empty states in the outer (valence) shells of the atoms that make up the material. An electron will not easily transfer between atoms if there is not a vacant state of similar energy in the receiving atom for it to occupy. We model the empty and filled states (electron energy levels) using quantum theory. A single atom has electrons localized about itself. An atomic orbital of one atom may overlap with an atomic orbital of another atom forming two molecular orbitals. One, called the bonding molecular orbital, is of low energy and the other with higher energy is called the anti-bonding molecular orbital. As more and more atoms assemble to form a solid, the number of bonding and anti-bonding orbitals of about the same energy increases, and they begin to take on the characteristics of an energy band. (See Figure 3). The energy differences between orbitals within a band is slight. Electrons can move freely among these orbitals within an energy band as long as the orbitals are not completely occupied. The highest occupied energy band is called the valence band. But, there is a region that separates the valence band from the conduction band where there are no orbitals. Electrons are not allowed to have these energies. In insulators, this energy gap is relatively large and in semiconductors, the energy gap is intermediate.

8.4.1 Conductors:
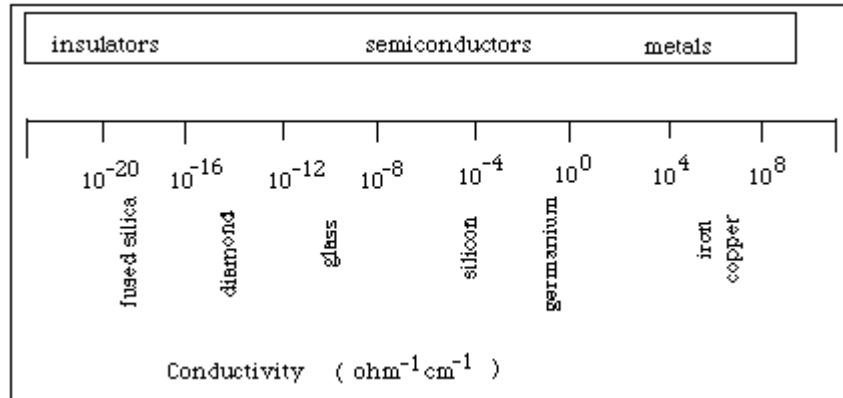
Figure 2: Electrical conductivities of some common materials

In a metal, the valence and conduction bands overlap and hence there is no forbidden energy gap. Therefore, metals are excellent conductors. At absolute zero all electrons fill up the lowest levels, the highest filled level is called the Fermi level. At normal temperatures, some electrons from highest energy levels are thermally excited to empty level above. Then the Fermi level represents the energy at which the levels are half filled and half empty (Fig 2(a)).

Name	# electrons	Configuration
neon:	10	**1**s2, **2**s2, **2**p6
sodium:	11	**1**s2, **2**s2, **2**p6 **3**s1
		or [neon] **3**s1

Whether or not a material is a conductor or an insulator depends on the separation of bands and whether the band is full or not. With *N* atoms making up the solid, each band may hold 2*N* electrons, related to filling the electronic orbitals. Let us consider an example consisting of two elements neon and sodium. Since the number of electrons in sodium is odd, the last band up is only half-filled. The even number of electrons in neon fills the final band. To have an electrical current in a solid, conduction electrons must be able to move through the solid by addition of some energy from an applied voltage. The energy level of conduction electrons can be approximated by the thermal energy, 0.025 eV at room temperature, smaller for lower temperature. The relative separation of bands must be considered and we should also consider how far away is the next unfilled band. Thus in this example, we have

- In **neon**,
  - The energy separation between the nearest empty band and the closest filled band is around 20 eV.
  - For conduction to take place in neon, the electrons in the upper most band, completely filled, would have to "jump" across the band gap of 20 eV, very unlikely with only 25 meV of energy kT (thermal energy)!

- In **sodium**,
  - The band is partially filled, thus a "little bit" of energy can be added to the electrons -- no quantum jump is involved.
  - The final electrons "added" to make sodium, the **3**s1 electrons, are very easy to strip from the "neon" ion core. They become the conduction electrons, often known as the **free electrons** in the metal.

Note the orbital configuration of the following elements that happen to be excellent conductors as solids:

Name	# electrons	Configuration
aluminum:	13	[neon], **3**s2, **3**p1
copper:	29	[argon], **3**d10, **4**s1
silver:	47	[krypton], **4**d10, **5**s1
gold:	79	[xenon], **4**f14, **5**d10, **6**s1

This is not to say that all conductors have one electron in an unfilled band -- but the best conductors do!

8.4.2 Insulators:

An insulator has a wide forbidden energy gap with the valance band being completely filled and the conduction band completely empty. Since there are no free electrons present, an insulator cannot conduct electricity (Fig. 2(b)). An electrical insulator resists the flow of electricity. Application of a voltage difference across a good insulator results in negligible electrical current. In comparison, a conductor allows current to flow readily. Controlling the flow of current in electrical wiring and electronic circuits requires both insulators and conductors. For example, wires typically consist of a current-carrying metallic core sheathed in an insulating coating.

Resistivity is the measure of a material's effectiveness in resisting current flow. Materials with resistivities higher than 10^8 ohm-m are usually considered to be good insulators; these include glass, rubber, and many plastics. Resistivities as high as 10^{16} ohm-m can be achieved in exceptional insulating materials. Normal conductors may have resistivities as low as 10^{-8} ohm-m. The enormous variation in room-temperature resistivity is one of the largest for any physical attribute of matter.

The charge carriers responsible for current in most conductors are electrons, moving relatively freely in a metal. In insulators, electrons cannot move freely. When atoms of simple metals combine to form a solid, the outer valence electrons become free for conduction. In an ideal insulator, all electrons stay tightly bound to the atoms, so there are no electrons that can be readily moved through the material for conduction.

A more complete understanding of insulators and conductors requires consideration of electronic band structure. The electrons in an isolated atom possess discrete energies, a consequence of quantum mechanics. These discrete levels evolve into bands of allowed energies when the atoms condense into a solid. Forbidden regions separate the allowed bands, as shown schematically in the figure. The electrons in the solid fill in the bands, from lower to higher energy.

The distinction between an insulator and a conductor lies in how the electrons fill in the allowed bands. For a simple metal, the highest band containing electrons will be only half full. The thermal energy (at ordinary temperatures) will be sufficient to generate conduction electrons -- electron states of slightly higher energy are available in the incompletely filled band.

In comparison, the highest energy band containing electrons is completely full in a good insulator. The thermal energy of the electrons is not sufficient for promotion from this band, known as the **valence band**, to the next band with available energy states, known as the **conduction band**. The gap between the valence and conduction band, known as the band gap, is at least several electron-volts (eV) wide in an insulator -- thermal electron energies are 100 times smaller.

8.4.3 Semiconductors:

The energy band model of a semi-conductor is similar to that of an insulator except that the forbidden energy gap is comparatively narrow. At very low temperatures, a semi-conductor behaves as an insulator. However, at higher temperatures, a few electrons are raised from the valence band to the conduction band by thermal

excitation. Electrons promoted to the conduction band can now conduct electricity in presence of an electrical field. The corresponding electron vacancies, or holes, created in the valence band can contribute to conductivity as well. Two commonly used semi-conductor crystals are Silicon(band gap-1.1 ev) and germanium (bandgap-0.7 ev). (Fig 2(c))

TABLE: Common Semiconductor Materials

Material	Bandgap (eV)	Bandgap Type
InSb	0.230	Direct
InAs	0.354	Direct
Ge	0.664	Indirect
Si	1.124	Indirect
InP	1.344	Direct
GaAs	1.424	Direct
CdTe	1.475	Direct
AlAs	2.153	Indirect
GaP	2.272	Indirect
ZnTe	2.394	Direct
SiC	2.416	Indirect
GaN	3.503	Direct
C	5.5	Indirect

Semiconductors constitute an enormous topic that can be surveyed here only briefly, however critical it is to the future development of information technology. Since the invention of the transistor some 40 or more years ago, 3 single-component and at least 10 binary semiconductor materials, as well as a number of tertiary materials (e.g., mercury cadmium telluride [HgCdTe] and aluminum gallium arsenide [AlGaAs]), have been exploited for the implementation of a variety of electronic devices and applications. These single and binary semiconductors, ordered by the magnitude of their bandgap, are listed in the above table. Others not listed here may someday be exploited, including mercury telluride (HgTe), manganese selenide (MnSe), gallium antimonide

(GaSb), indium nitride (InN), scandium nitride (ScN), aluminum nitride (AlN), zinc selenide (ZnSe), and boron nitride (BN). Also indicated in the Table is the nature of the bandgap, that is, whether it is direct or indirect gap material, as this determines to a large extent just what kinds of applications the semiconductor may be suited for.

8.4.3.1 Intrinsic semiconductor: Group IV elements (Si & Ge)

An instrinic semiconductor (ideal) has no chemical impurities and no atoms are displaced from their proper sites. Such a case is not possible to achieve. At absolute zero, the valence band is completely filled and the conduction band is completely empty. At T>O, two processes occur:

Due to thermal vibration of the lattice, electron-hole pairs (EHP) are generated due to break up of some covalent bonds. Recombination of EHP's to produce covalent bonds also occurs in thermal equilibrium. The number of electrons per unit volume (n_i) in CB is equal to the number of holes per unit volume (P_i) in VB. This means that the fermi level, E_F, is located in the middle of the forbidden energy gap. Hence, at T>O charge carries are obtained by breakdown of some covalent bonds.

8.4.3.2 Extrinsic Semiconductors

The electrical properties of a semiconductor are drastically altered when it is doped by some impurity atoms. Such a solid is called an extrinsic semiconductor. There are two type of extrinsic semiconductors:
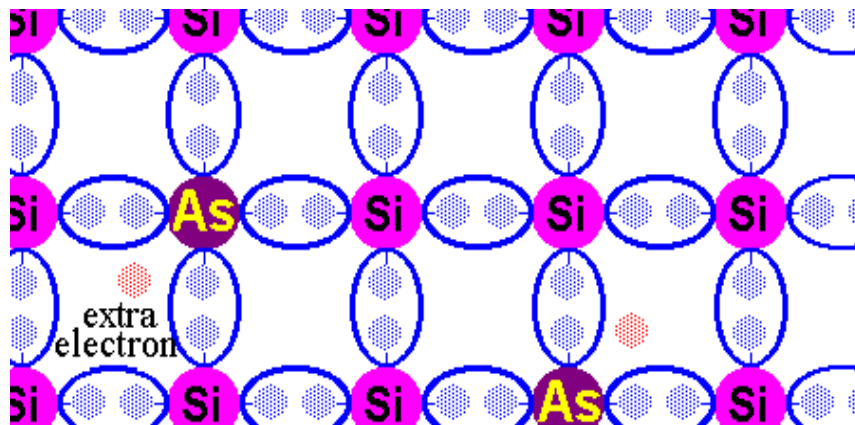
8.4.3.2.1 n-type semiconductors:

Figure : n-type substitutional doping with Arsenic atoms in a silicon lattice. Four of the valence electrons of As bind to neighboring Si atoms, the one left over becomes free for conduction.

When a group IV element (Si/Ge) is doped with a group V element (P/As/Sb), an N-type semiconductor is formed. At temperatures above absolute zero, four of the impurity atom electron play the same role as the four valence electrons of the VB. The fifth valence electron is, however, not involved in bonding and is free to move around. Thus, addition of donor atoms adds allowed energy states to the crystal.(fig. 3)

$$
\begin{array}{ll}
\text{———————} & \text{CB} \\
\text{———————} & E_C \\
\text{—— —— ——} & E_d \\
\text{— — — — — —} & E_{Fi} \\
\text{////////////} & E_V \\
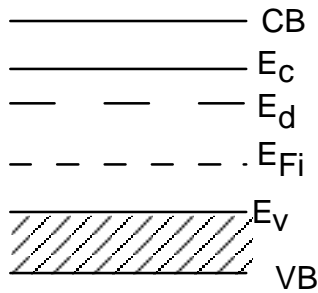\text{////////////} & \text{VB}
\end{array}
$$

Fig. 3. Energy level diagram of a typical n-type semiconductor. Here E_{Fi} is the fermi level of an intrinsic semiconductor.

At very low temperatures, T<100K, electrons are attached to the donor atoms i.e. they occupy the E_d state (see Fig. 3). At around 100K, the thermal energy enables the extra impurity electron to shift into one of the many empty states of the nearby conduction band, where it has effective mass m_e^*, mobility μ_e and can carry current. Note that in an n-type material, there are two types of charge carries from three processes:

Doping- produces electron as charge carries (majorities carries)

Thermal vibration- produces electrons & holes

Recombination- takes away electron and holes.

$$n \equiv \text{defined as the electron density}$$

$$p \equiv \text{defined as the hole density}$$

in an extrinsic semiconductor in thermal equilibrium. N_d is the donor concentration.

The product of concentrations of majority and minority carries in thermal equilibrium is independent of the doping impurity concentration and is a function of only of the temperature and the semiconductor material i.e. $n_p = n_i^2$ (constant) for every T.

Here, $n \gg n_i \gg p$.

Arsenic or phosphorous has one more valence electron than silicon -when it is placed substitutionally in the lattice for a Si atom four of the valence electrons bind to neighboring Si atoms, the one left over becomes free for conduction. In the band structure picture, impurity states are created much closer to the conduction band. These states are known as donors, since they "donate" electrons to the conduction band. It is much easier to "liberate" the electron for conduction at lower thermal energy. A semiconductor doped with donors is known as an "n-type" semiconductor (n for negative charge carrier).

8.4.3.2.2 P-type semiconductor

When a group IV element (Si/Ge) is doped with a group III element (In/Ga), a P-type semiconductor is formed. In this case, there is a vacancy in the covalent bond structure.
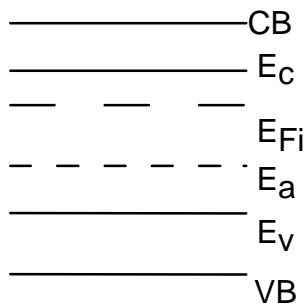
$$
\begin{array}{ll}
\text{————————} & \text{CB} \\
\text{————————} & E_C \\
\text{—— —— ——} & \\
& E_{Fi} \\
\text{— — — — — —} & E_a \\
\text{————————} & E_V \\
\text{————————} & \text{VB}
\end{array}
$$

Fig. 4. Energy level diagram of a typical p-type semiconductor. Here E_{Fi} is the fermi level of an intrinsic semiconductor.

Addition of the impurity adds allowed energy states (E_a) which are empty at absolute zero. At higher temperature (T>100 K) from VB can jump to E_a and leave a vacancy behind. In a P type material, following processes occurs:

Doping- produces holes as charge carries (majority carries).

Thermal vibration- produces electrons and holes.

Recombination- takes away electrons and holes.
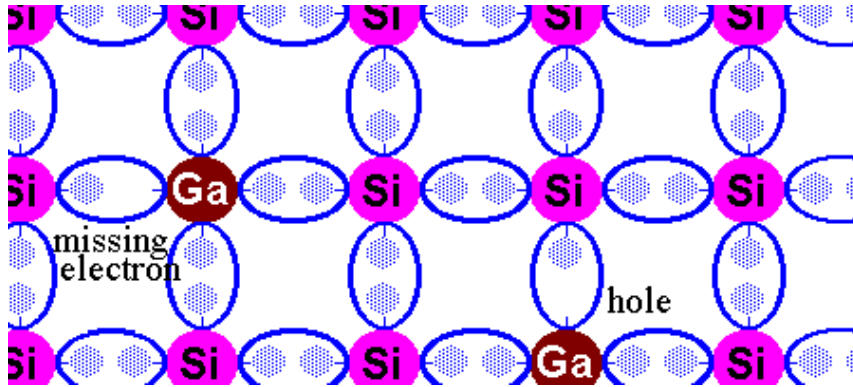
Here, again $n_p = n_i^2$.

Here, $p \gg n_i \gg n$.

Figure : n-type substitutional doping with Arsenic atoms in a silicon lattice. Four of the valence electrons of As bind to neighboring Si atoms, the one left over becomes free for conduction.

Gallium or boron has one fewer valence electron than silicon- when it is placed substitutionally in the lattice for a Si atom only three of the neighboring Si atoms are successfully bound, a hole remains, which also aids conduction since electrons may now move more freely through the lattice, "jumping" into a hole and leaving a hole behind to be filled.

In the band structure picture, impurity states are created much closer to the valence band. These states are known as acceptors, since they can accept electrons from the valence band. Again, it is much easier to "liberate" the electron for conduction at lower thermal energy. A semiconductor doped with acceptors is known as a "**p-type**" semiconductor (p for positive charge carrier).

Doping changes the resistivity of semiconductors drastically. A typical example of antimony doped germanium with different antimony concentrations and its relative resistivity is shown in the table below.

Donor Concentration (micropercent)	Resistivity (ohm-cm)
5	10^9
50	10^5
150	10
300	0.1

8.4.4 Agencies affecting mobility of charge carries

The driving agencies which affects mobility are:

Electric field

Concentration gradient

8.4.4.1 Electric field

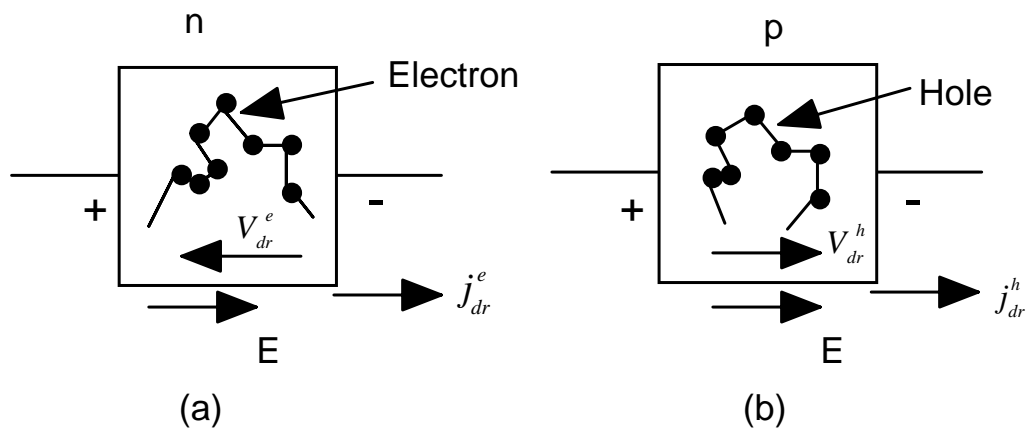(a)   (b)

Figure: Response of majority carriers in an applied electric field.

The motion of charge carries in response to an electrical field is described as drift. In semi conductors, carrier motion is impeded by lattice vibrations, impurities and crystal defects. When an electrical field is applied, electrons and holes are accelerated in opposite directions (Fig. 5) till they are scattered. The velocity of the carriers after each encounter becomes random once again, and their acceleration in the field direction starts afresh. This leads to an overall motion at constant velocity (drift velocity) the charge carries.

Holes : $V_{dr}^h = \mu_h E$

Electron: $V_{dr}^e = -\mu_e E$ (1)

Drift current density, J= neV

Holes: $J_{dr}^h = qp V_{dr}^h = qp\mu_h E = \sigma_h E$ ------------(2)

Electrons: $J_{dr}^e = qn V_{dr}^e = qn\mu_e E = \sigma_e E$ ------------(3)

Here, q stands for the magnitude of charge, p and n stands for hole & electron concentrations respectively, V_{dr}^h and V_{dr}^e are the drift velocity of holes & electrons

respectively while μ_h & μ_e the mobility and σ_h and σ_e the conductivity holes & electrons respectively.

8.5 Abrupt junction of n & p material :-

The p-n junction is a specimen made of a single crystal semiconductor in which there are two adjacent regions, an n-type and a p-type.
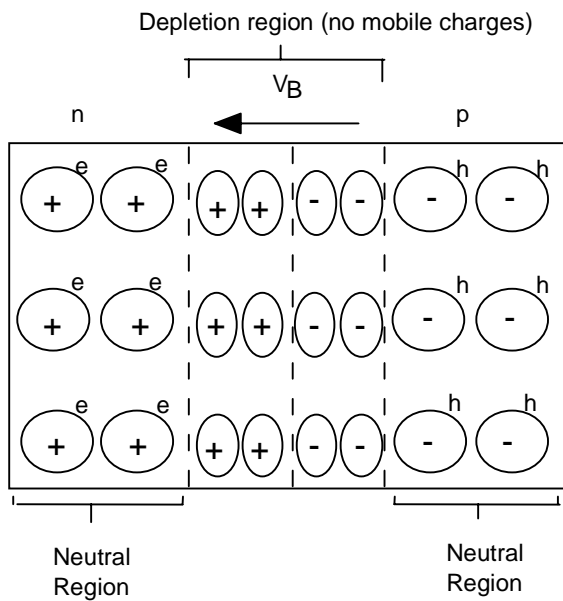

Figure: Abrupt p-n junction

Because of the concentration gradient, electrons diffuse from n to p and holes from p to n. Hence a potential barrier V_B builds up across the junction. V_B causes drift currents which exactly balance the diffusion currents (in equilibrium) i.e. there is no net flow of electrons or holes across the junction.

Barrier height V_B in absence of external bias

Consider fig. 6

(a) Fermi level is shifted due to doping

In general, $\quad E_F = E_{Fi} + \dfrac{KT}{2}\ln\dfrac{\bar{n}}{\bar{p}}$ ......(7)

E_{Fi} - Fermi level in intrinsic semiconductor.

$\left.\begin{array}{l}\bar{n}\text{: electron concentration}\\ \bar{p}\text{: hole concentration}\end{array}\right\}$ at temperature T in thermal equilibrium

N- type:

$$\frac{\bar{n}}{p} \simeq N_D$$

$$\bar{p} = \frac{n_i^2}{N_D}$$

N_D – donor concentration

Substituting (8) in (7)

$$E_F = E_{Fi} + KT \ln \frac{N_D}{n_i}$$

$$i.e. E_F > E_{Fi}$$

$$E_F - E_{Fi} = q^V{}_N = KT \ln \frac{N_D}{n_i}$$

ii) P-Type:

$$\bar{p} \simeq N_A$$

$$\bar{n} = \frac{n_i^2}{N_A}$$

N_A – acceptor concentration
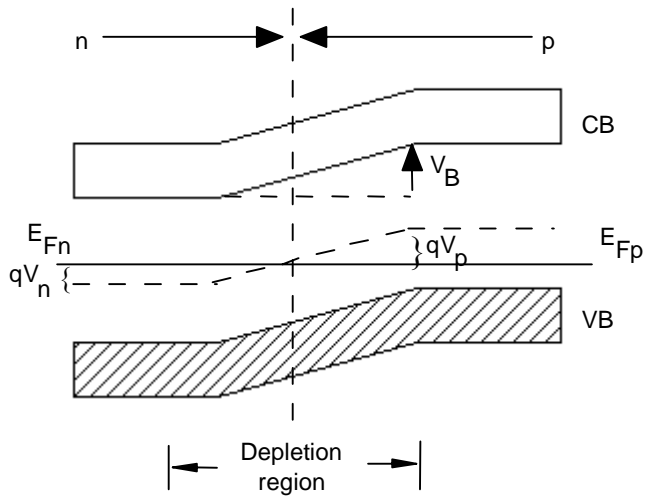
$$\therefore E_F = E_{F_i} - KT \ln \frac{N_A}{n_i}$$

$$i.e. E_F < E_{F_i}$$

$$E_F - E_{F_i} = qVp = -KT \ln \frac{N_A}{n_i}$$

From (9) & (11) we see that fermi level in N-type is shifted up as compared to intrinsic fermi level and is shifted down in P-type due to doping.
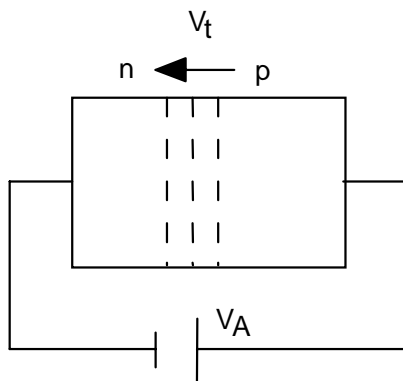
(b) At the junction, fermi level must be the same on both sides. Thus, the electron energy levels are higher on the p-side as compared to the N-side (Fig. 7).

$$V_B = V_N + |V_P|$$

$$= \frac{KT}{q} \ln\left(\frac{N_D N_A}{ni^2}\right)$$
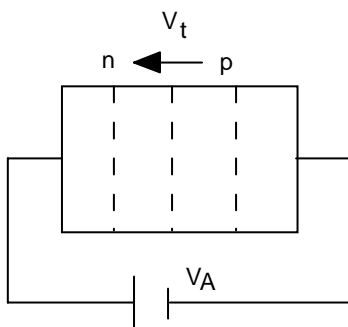
Forward bias

V_A is the applied voltage and V_t is the total voltage.

$$V_t = V_B - |V_A|$$

As V_A is increased, V_t and barrier width both decrease.

Reverse bias

$$V_t = V_B + |V_A|$$

As V_A increases, V_t decreases.

Poisson equation in one dimension is given by,

$$\frac{d^2V(x)}{dx^2} = -\frac{dE(x)}{dx} = -\frac{Q}{\varepsilon_r\varepsilon_o}$$

where ϵ_0 is the permittivity of vacuum, ε_r is the dielectric constant of the material, Q the charge density, E the electric field and V the potential.

Solving under the abrupt junction approximately, we get

$$V_t = V(-d_n) - V(d_p)$$
$$= \frac{q}{2\varepsilon_r\varepsilon_o}\left(N_D d_n^2 + N_A d_p^2\right) \quad\dots\dots\dots\dots\dots(14)$$

where Q = qN_D on N side, and Q = -qN_A on P side.

$\quad\quad d_n$ = barrier width on N side

$\quad\quad d_P$ = barrier width on P side

Now, $N_D d_N = N_A d_p$------------(15)

$$\therefore d_n^2 = \frac{2\varepsilon_r\varepsilon_o}{q}\frac{N_A}{N_D(N_A+N_D)}V_t\dots\dots(16)$$

Similarly, $d_p^2 = \frac{2\varepsilon_r\varepsilon_o}{q}\frac{N_A}{N_D(N_A+N_D)}V_t\dots(17)$

$\therefore$ Total barrier width, $d = d_n + d_p$

$$= \left[\frac{2\varepsilon_r\varepsilon_o}{q}V_t\frac{(N_A+N_D)}{N_AN_D}\right]^{1/2}\dots(18)$$

8.5.1   I-V Characteristics :-

Current through the P-N junction is given by

$$I = I_o \left[\exp\left(\frac{qV}{KT}\right) - 1 \right] \dots (19)$$

Where V is the applied voltage,

K is the Boltzman constant,

T is the absolute temperature

(1) When the junction is forward biased, V is positive

If $V \gg \dfrac{4KT}{q} i.e. V \gg 100 mV$

then $\exp\left(\dfrac{qV}{KT}\right) \gg 1$

then $I = I_o \exp\left(\dfrac{qV}{KT}\right)$

(2) When the junction is reverse biased, V is negative

Then, if $\exp\left(\dfrac{qV}{KT}\right) \ll 1, I = -I_o$

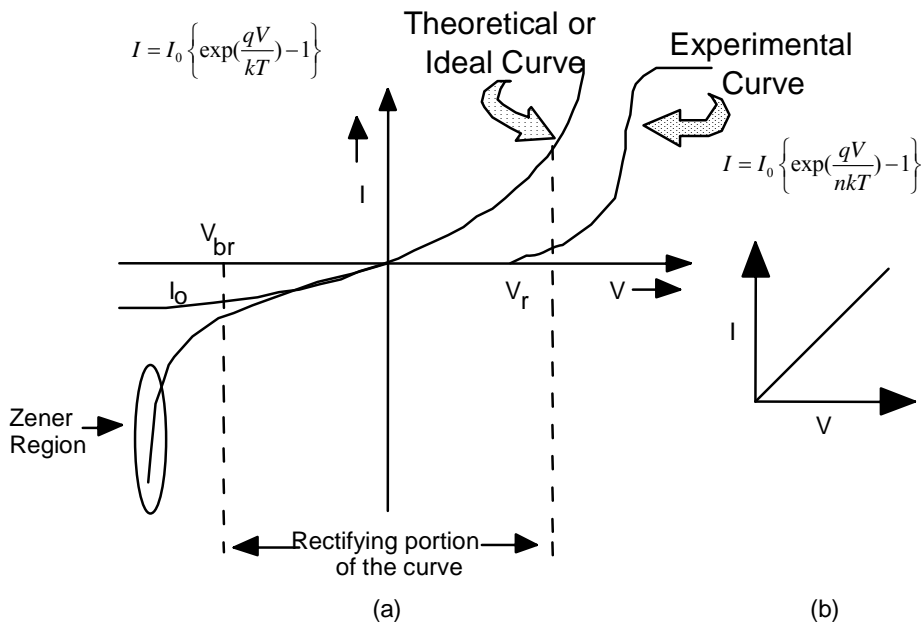I_o is thus called the saturation value for reverse bias condition

Figure: (a) Plot of the I-V characteristics of a diode (V_r is the cut-in voltage, V_{br} the breakdown voltage; (b) IV characteristics of a pure conductor

8.5.2   **Transistors**

The transistor is a three-layer semiconductor devices consisting of either two n-type and one p-type layers of material (referred to as npn transistor) or two p-type and n-type layers (referred to as pnp transistors) (Fig. 9). The middle range is called the base and the two outer regions are called the emitter and the collector. In most transistors, the collector region is made larger than emitter region since it is required to dissipate more heat. The emitter is heavily doped, the base is lightly doped and is thin, while the doping of collector is in between the other two. The emitter is so called since it emits electrons (holes in case of a pnp transistor) into the base. The base passes most of these electrons (hole for pnp) onto the collector. The collector gathers these electrons (holes for pnp) from the base.
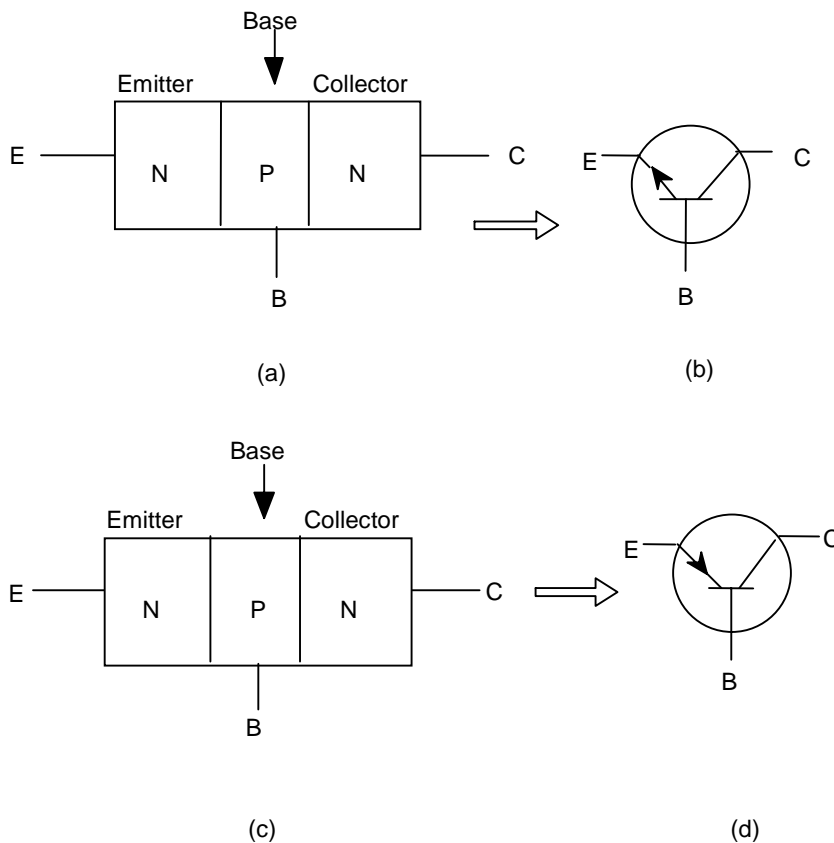
Fig 9. (a) NPN – type   (b) NPN-transistor symbol

(b) PNP – type   (d) PNP – transistor symbol

A transistor has two P-N junctions, the one between emitter and base is called emitter junction while the one between base & collectors is called collection junction. There are four possible ways of biasing these two junctions (Table 1).

Table 1.

Condition	Emitter junction	Collector junction	Region of operation
FR	Forward-Biased	Reverse-biased	Active
FF	Forward-biased	Forward-biased	Saturation
RR	Reverse-biased	Reverse-biased	Cut-off
RF	Reverse-biased	Forward-biased	Inverted

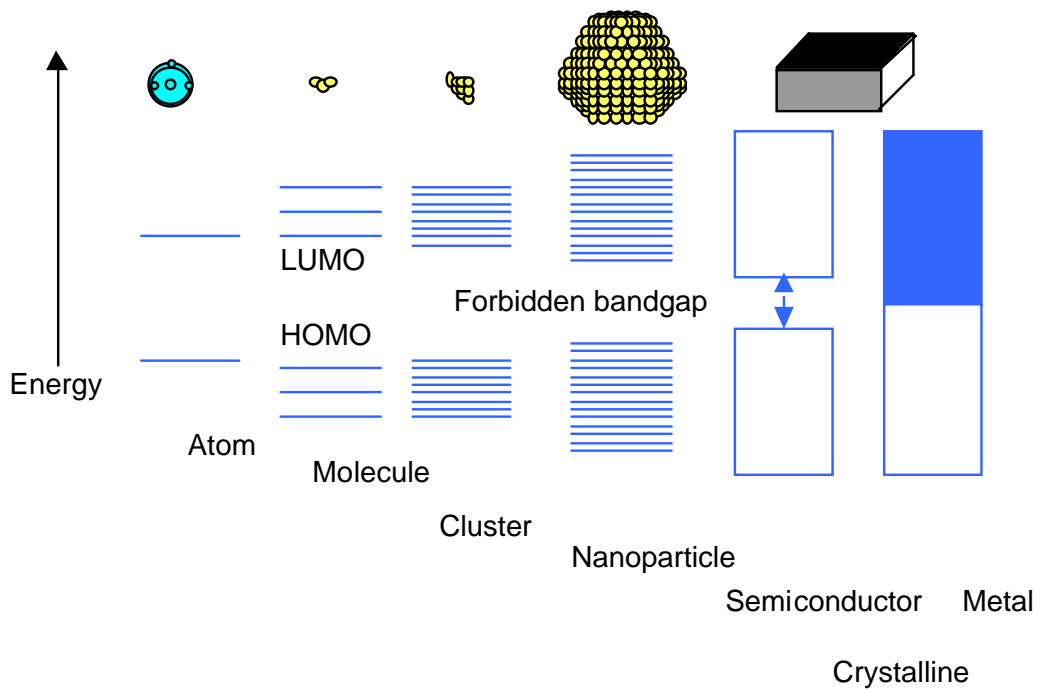# 8.6 Quantum size effect in metal or semiconductor nanoparticles

Figure 2.1 Size quantization effect. Electronic state transition from bulk metal/semiconductor to small cluster.

Nanocrystalline particles represent a state of matter in the transition region between bulk solid and single molecule. As a consequence, their physical and chemical properties gradually change from solid state to molecular behaviour with decreasing particle size. The reasons for this behaviour can be summarised as two basic phenomena.

First, as we have already discussed, owing to their small dimensions, the surface-to-volume ratio increases, and the number of surface atoms may be similar to or higher than those located in the crystalline lattice core, and the surface properties are no longer negligible. When no other molecules are adsorbed onto the nanocrystallites, the surface atoms are highly unsaturated and their electronic contribution to the behaviour of the particles is totally different from that of the inner atoms. These effects may be even more marked when the surface atoms are ligated.[193] This leads to different mechanical and electronic transport properties, which account for the catalytic properties of the nanocrystalline particles.[194]

The second phenomenon, which only occurs in metal and semiconductor nanoparticles, is totally an electronic effect. The band structure gradually evolves with increasing particle size, i. e., molecular orbital convert into delocalised band states. Figure above, shows the *size quantization effect* responsible for the transition between a bulk metal or semiconductor, and cluster species. In a metal, the quasi-continuous density of states in the valence and the conduction bands splits into discrete electronic levels, the spacing between these levels and the band gap increasing with decreasing particle size.[195,196]

In the case of semiconductors, the phenomenon is slightly different, since a band gap already exists in the bulk state. However, this band gap also increases when the particle size is decreased and the energy bands gradually convert into discrete molecular electronic levels.[197] If the particle size is less than the De Broglie wavelength of the electrons, the charge carriers may be treated quantum mechanically as "particles in a box", where the size of the box is given by the dimensions of the crystallites.[198] In semiconductors, the quantization effect that enhances the optical gap is routinely observed for clusters ranging from 1 nm to almost 10 nm. Metal particles consisting of 50 to 100 atoms with a diameter between 1 and 2 nm start to loose their metallic behaviour and tend to become semiconductors.[199] Particles that show this *size quantization effect* are sometimes called *Q-particles* or *quantum dots* that we will discuss later in this chapter.

Certain particle sizes, determined by the so-called *magic numbers,* are more frequently observed than others. This is not only due to the thermodynamic stability of

certain structures but is also related to the kinetics of particle growth. In semiconductor nanoparticles such as CdS, the growth of the initially formed smallest particles with an agglomeration number *k* occurs by combination of the particles. Thus, particles so formed would have the agglomeration number of 2*k*, 3*k* and so on.[200] Metals have a cubic or hexagonal close-packed structure consisting of one central atom, which is surrounded in the first shell by 12 atoms, in the second shell by 42 atoms, or in principle by $10n^2+2$ atoms in the *n*th shell.[201] For example, one of the most famous ligand stabilized metal clusters is a gold particle with 55 atoms (Au_{55}) first reported by G. Schmid in 1981.[202]

8.7   Increase in optical gap with decreasing particle size

The initial interest in nanoparticles were essentially focused on their application in catalysis for a wide range of chemical reactions such as free radical reactions initiated by light or ionising radiation, reduction of multiple bonds or selective hydrogenation of internal alkynes to *trans*-alkenes.[203,204] The *size quantization effect* that has been looked into at great lengths only recently leads to an important change in the electronic properties so that conductivity, magnetization, etc, start to change (diminish because of the increase in energy gap). In this state of matter, quantum effects (tunnelling, hopping of electrons) govern the propagation of the electrons and give rise to non-linear electrical and optical properties.[205,206]

For instance, the transition between bulk materials and nanoparticles can be simply observed by optical absorption spectroscopy. In the case of gold or CdS, nanoparticles studied here, there exists a strong dependence of particle size on UV/Vis absorbance (Figure 2.2) .[207] Charge carriers generated by absorption of light, which are free to move in a macrocrystalline material, "feel" the confinement in nanometer size particles. The band gap energy increases significantly so that the onset of absorption of light and the position of the fluorescence bands are shifted to shorter wavelengths.[208,209]

As we have already discussed, in metal particles, absorption in the UV-Vis spectra (with a peak at 520 nm for 10 nm gold particles, for instance) is due to the excitation of a plasmon resonance which corresponds to a collective oscillation frequency of conduction electrons.[210] These absorption spectra can be calculated using classical Mie theory,[211,212] in which the theoretical absorption spectrum of dilute

spherical particles (*'**surface plasmon resonance'**)* is related to their size, and their frequency- dependant dielectric constant, compared to the surrounding medium.[213]

In semiconductor nanoclusters, an electron can be excited from the valence band into the conduction band by an absorption of a quantum of light. A positive charge (a hole) remains in the valence band. The electron and hole can move independent of one another in the crystal, which results in electrical conductivity. The electrons and hole also experience coulombic forces and can form an '**exciton**', a state which is very similar to a hydrogen atom. In molecular terminology an exciton would be called the first excited state. Many models account for the increase of the band gap with decreasing particle size on the basis of a particle-in-a-box assumption.[214,215,216] UV absorption spectra may then be deduced from the calculated energies of the first exitonic transition.
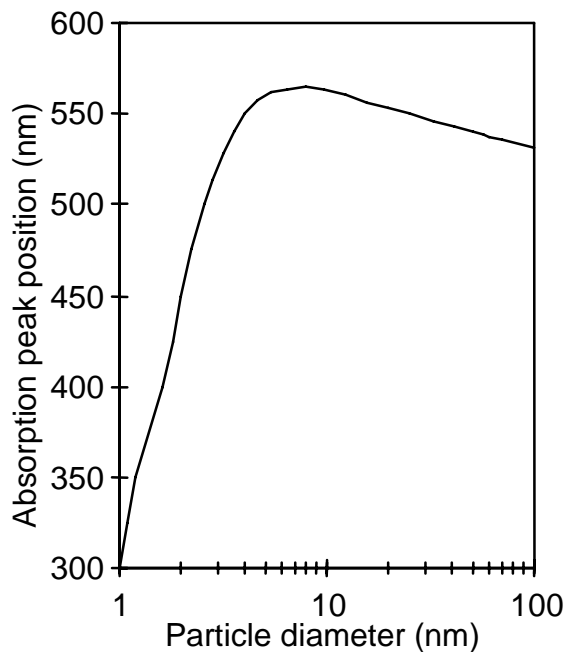

Figure 4.1.2: Absorption spectra of CdS particles with Increasing size.[217]

8.8 Quantum Wells, Wires and Dots

Quantum wells--ultrathin, quasi-two-dimensional planes--are just one of the three basic components of quantum devices. A narrow strip sliced from one of the planes is a one-dimensional quantum wire. Dicing up a one-dimensional wire yields zero-dimensional quantum dots. Reducing the number of dimensions in this manner forces electrons to behave in a more atomlike manner. By controlling the physical size and composition of the different semiconductors in a device, researchers can induce predictable changes in electron energy. In this way, scientists can literally pick, or tune,

the electronic properties they want. In theory, the fewer the dimensions, the finer the tuning. Creating a zero-dimensional, or quantum, dot is analogous to custom-designing an atom. Like an atom, a quantum dot contains a certain amount of electrons. But whereas the electrons are held in an atom by their attraction to the nucleus, electrons in a quantum dot are physically trapped within barriers between semiconductor materials.

The theme of dimensional reduction is strictly related to the wave nature of electron in microdomain. If an AlGaAs semiconductor layer (n- type) is grown on undoped gallium arsenide to form a heterojunction, electrons are trapped in the well formed on the GaAs side of the AlGaAs/GaAs heterojunction. This type of trapping leads to high electron mobility and energy quantization. The important feature of this well is that the electrons inside have only two degrees of freedom with restricted lateral movement by the side of the well. Now further dimensional reduction leads to quantum wire with electron in one degree of freedom. Finally if we take away the only degrees of freedom we are left with a quantum dot.

The only significant difference between an ordinary semiconductor laser and a quantum-well laser is in the relative size of each device's active region, where electrons and holes (electron deficiencies) recombine, neutralizing one another and causing a photon to be emitted. The quantum-well laser's active region is small enough for the energy levels of the electrons in the well to become quantized--that is, constricted to discrete values. This single difference, however, brings a major advantage:

- a quantum-well laser radiates light very efficiently, powered by much less current than a conventional semiconductor laser.

As a result, semiconductor lasers that operate on the principle of quantum confinement dissipate far less excess heat. This feature, combined with the small physical size of the lasers, means that the devices can be packed tightly together to form arrays, are more reliable and can operate at higher temperatures.

What is true for quantum wells is even more so for quantum wires and dots--at least in theory. In practice, it has turned out to be quite a bit more difficult to exploit the advantages of the wires and dots than was expected a decade ago when the first such low-dimensional devices were built. Over the past few years, quantum-well semiconductor lasers have become commonplace. In fact, anyone who recently

purchased a compact-disc player owns one. In contrast, quantum wires and dots are still in the laboratory.

The difficulty of building useful quantum wires and dots has been sobering, after the intoxicating rush of advances in quantum devices in the 1980s and early 1990s. Researchers in those days envisioned two different classes of quantum devices: quantum optical devices, such as lasers and light detectors, and quantum electron devices, such as diodes and transistors.

They even spoke enthusiastically of fundamentally different electron devices that, unlike today's binary "on-off" switches, would have three or more logic states. Functioning in parallel, these devices, it was hoped, would lead to more powerful forms of computer logic and become the building blocks of dramatically smaller and faster integrated circuits. There were also high hopes for so-called single-electron devices. These would include, for example, quantum dots that could contain so few electrons that the addition or removal of even a single electron would result in observable--and exploitable--effects. Using so few electrons, the devices could be switched on and off at blistering speeds and with very little power, investigators reasoned.

Yet even as work on these devices has stalled, enthusiasm is high for quantum optical devices, thanks to the quantum-well lasers, the quantum-cascade laser and a few other encouraging developments. Lucent, Philips, Thomson-CSF and Siemens have active research efforts. Many of those groups, including the one at Lucent's Bell Labs, hope to use such highly efficient, tiny quantum-well lasers to transmit data more efficiently and at higher rates through optical-fiber networks. One promising project at Lucent centers on a quantum-wire laser that promises lower-current operation. This laser would be desirable in a variety of applications, such as optical communications, because its low-current operation would enable the use of a smaller, less costly power supply.

8.9 Quantum Dot

Quantum dots are one of the most familiar features of nanostucturized material with numerous practical applications. It is again related to the general concept of nanostructure where the intrinsic quantum properties of a material comes out to be size

dependent. The journey to achieve quantum dot started in the late 1960's when Leo Esaki, Leroy L. Chang & Raphel Tsu at the IBM, Thomas J Watson Research Centre. (Yorktown height, NY) began to build structures that would trap electrons in dimensionally limited environments. Progress continued with experimental improvement (Molecular beam epitaxy) which leads to the construction of quantum wells (1974) then lines and ultimately the dots were obtained in 1980.
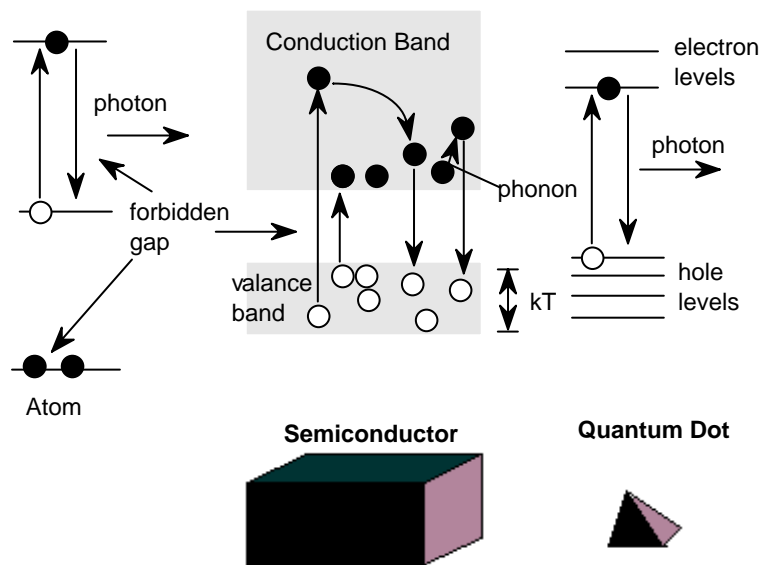
8.9.1 Semiconductor quantum dots (Detailed feature)

Figure: Schematic representation of energy diagrams in case of a single atoms (left), a bulk crystal (center) and a quantum dot (right).

8.9.1.1 Excitons in semiconductor QD:

The part consists of the process of optical absorption, the formation of excitons or electron hole pair & e-h recombination leading to photo luminescence (PL). The excitons in QD nanocrystals can be treated as bosons and in case of optical transitions involving exciton formation exciton photon interaction is relevant. Before going to regorous theoretical model let us cite exciton related cases. If the dot radius R $\leq a_B$ (= bulk exciton Bohr radius) which is known as strong confinement condition we mostly speak of energy levels than bands the optical transitions near the band edge as shown in fig. 1 should only involve the S conduction band level while the valance band the top P levels could be involved. For CdSe QDS some of observed transitions $IS_{3/2} - IS_e$, $2S_{3/2}$ - IS_e $IS_{1/2} - IS_e$ $IP_{3/2}$ - IP_c etc.[218] If we take spin orbit coupling into account the situation is rather more involved.

8.9.1.2 Model for strong confinement condition

The proposed model of Efros et. al. (1996)[219] concerning tocubic zinc blende structure treats the QDs in strong confinement condition. An emitting state following excitation of light. When an electron is placed in the conduction level and a hole in the valance level leading to an e-h pair (exciton). Following is the experimental result relating to the PL of a QD.

PL spectra for Qd is found to be redshifted unlike that for band edge emission. Even the radiative life time is longer (MS) than that for band edge emission (ins).

PL greatly depends upon surface effect i.e. it could be due to the recombination of weakly overlapping carriers localized at the surface. In band edge emission it's the internal states that is involved in PL.

An alternative explanation to the two items just given is that the formation of the ground state exciton or e-h pair is an optically forbidden transition separated from the first optically active state by the e-h exchange interaction. In this situation the lowest excited state level is not strongly coupled to the ground state. The forbidden transitions has also been said to form passive or dark excitons. Dark excitons varies with magnetic field.[220]

8.9.1.3 Magnetic field on dark exciton recombination

Application of an external magnetic field H on dark excitons in hexagonal QDs leads to an allowed transition for e-h pairs, provided the field is not directly along the hexagonal axis. Under this condition F is not a good quantum number and this results in a mixing of the $\pm$ 2 dark excitons states with the optically active and bright $\pm$ 1 exciton states and the outcome is to develop an allowed & direct optical recombination of I2 excitons to ground state.

8.9.1.4 Effect of internal electric field on dark exciton:

By the formation of an internal electric field we can allow a parity forbidden transition (e.g. Wurtzite CdSe). For 'good' small platelets of such materials it has been known for time that the top and bottom faces of the platelets consists of ions having opposite charges i.e. $Cd^{++} Se^{--}$ which results in the existence of an electric field whose value depends on the platelet-thickness. Under this condition from the measurement of dielectric dispersion the estimated diameter of CdSe QDs is equal to 34 to 46 Å & there

was a potential drop of ~0.25 ev across the dot. The permanent dipolement of the dots are found to be 25 to 47 Debye. From the existence of such polarity we conclude that a centrosymmetric confinement potential for the uppermost hole states no longer holds.

8.9.1.5 Phonon bottleneck & photoluminescence:

After laser excitation of quantum dots higher excited states are generated & for e-h recombination & PL to occur, it is advantageous to have the electrons now in the discrete higher excited states to lose energy by LO phonon emission & to trickle down to the lowest excited states from where emitted luminescence is allowed. It rarely happens however that the spacing in the discrete conduction or valance energy levels for the excited states is equal to an integer number of LO photons in order that the electrons become able to reach the lowest of the excited states such as E_1 in fig above. For recombination & intense PL to occur, it is the LO phonon that is the most effective. This problem has been referred to as the phonon bottleneck. Energy can also be lost by acoustic phonon emission, since these phonon energies are small & there exists almost a continuum of energy levels for such phonons. PL involving these phonon is however not an effective way to obtain strong luminescence peaks. A number of mechanisms have been proposed to avoid this phonon bottleneck problem. For example,

Sercel (1995)[221] in his studies on the $In_xGa_{1-x}As$ QD system embedded in a GaAs martix, argues that the matrix contains a deep level trap close to the dot & that electron in the excited state level of the dot then couple of the traps or interfacial defects, so that the defect can be relax by multiphonon emission, so allowing the electron to make a second transition to a lower level of the dot.

As a concluding remark we just say that PL spectra depend not only on the ground state transition for the lowest energy confined electron states of the QD as well as the 2-D valance band hole continuum that is associated with the quantum well wetting layer. Support of this view comes from the large increase of PL intensity as well as the oscillator strengths of the observed experimental peaks.

8.9.1.6 Exiton – phonon – interaction:

Experimental evidence in late sixties, for example for ZnO, when the excitons spectra in this platelets at 4k was shown to have bands associated with the n = 1 & higher excitons peaks at clearly separated nearly phonon energy intervals (Liang & Yoffe' 68)[222]. The reason of this was proposed to be due to polaron formation as a result of exciton-phonon coupling. The fine structure found in main PL spectra, where the

separation between IP & the IS states of the exciton is close to an integer number of optical phonons is then attributed to the exciton-phonon complex quasi particles. Experiments with QDs like Pbs shows that exciton-phonon coupling strength depends upon the dot size. For CDs the situation is more complicated as the exciton-phonon interaction as well as the presence of charge point depeets are present there.

8.9.2 Coupled Quantum Dots:

8.9.2.1 General features:

QDs can be arranged in a vertical array or 2-D layer to form a coupled Q-D system. While studying coupled QD system. While studying coupled QD system the following basic ideas are useful.

Energy spectrum of the charge carries in the QD can be treated by considering a discrete set of energy levels.

Their size should be chosen suitable. For example in laser, the quantized energy levels should be separated by several KT at room temperature to avoid thermally activated population of higher levels from the ground state.

A desirable aim to attempt to reduce to a minimum defect & other non-radiative recombination centers at the boundaries between the dots & the matrix.

In order to attain sufficient gain to be of use in application such as injection heterolasers, it is necessary to have a dense ordered array of QDs along the substrate plane, or vertical to it particularly for cascade-type lasers or for applications such as photodetectors or single electron transistors.

Photoluminescence (PL) spectra of InAs (at 77k) shows of peaks from the QDs to longer wave length. This is due to coupling between electron & holes and this results in a reduction of the dimensional energy quantization for the electron & hole ground state. Another important point is that there is also a decrease in the exciton (e-h) radiative recombination lifetime with coupled system.

Experiment with QDs embedded in MISFET shows some properties in spectroscopic context. From capacitance spectra discrete density of states for QDs were obtain. From infrared measurement, dipole allows transition between the levels were studied.

QDs are usually capped with organic molecules mainly in order to reduce surface states but also to keep the dots apart at fixed distances. The observed spectra of these

cluster of dots shows some different behaviors with respect to a single dot. There is a quenching of the luminescence lifetime with the small dots & a concurrent enhancement of the luminescence lifetime with the larger dots. These results are consistent with the long range transfer of electron excitations from the confined states of the smaller dots to the higher excited states of the larger dots. The smaller dots can it seems be considered as donors & the larger dots as acceptors resulting in the long range resonance transfer of electronic excitation.

8.9.2.2 Models for coupling between dots:

We shall start with well & then reduce the dimension on an adhoc basis. If two wells are separated by a thin barrier where the tails of the wave functions overlap. The well depth in V_o & for large separation between the wells each of the quantified energy levels is doubly degenerate & have values e_1, e_2, e_3 etc. When overlap is introduced in the valance band each degenerate level splits into two becoming doublets having energies $e_1 \pm \Delta V$, where ΔV (the interaction energy due to overlap) is given by $\Delta V = <|\Psi_1|V_o|\Psi_2>$, where $|\Psi_1>$ & $|\Psi_2>$ are the upperturbed wave function for the single QW.

The spectra of such system shows the peak developing into doublets when the separation between the wells we would, of course, get triplet for the energy levels etc. and these can be doubled again if spin is included. For multiple well super lattices there can also be Brillouin zone folding leading mini band formation.

8.9.3 QDs as artificial atoms and molecules:

QDs can be viewed as an artificial atoms or molecules. The single electron dot is assumed to have a cell type electronic structure characterized by radial & angular momentum (Q number). These numbers are then used to identify different excited states. With the application of magnetic field transition between ground & excited states can then be induced and the magnetic field dependence of the level used to give the angular momentum of the states as for atomic systems. When the thickness of the circular disk is small only the confinement within the plane of the disc needs to considered. When only one electron is present in the high symmetry dot it is then comparable with H-atom and for a two-electron confinement it's like He-atom. In presence of Coulomb interaction there occurs the splitting between singlet & triplet states. It's relevant to mark that Heind's rule is applicable here too.

On the other hand a coupled system of QDs are treated as molecules. As the dot-separation is reduced coupling strength increases. The sharp excitonic resonance's from the ground state seen with single dots or when the separation between the dots was high is seen to split into a pair of lines and thus the excitons bound to two quantum mechanically coupled QDs develop. Such a system could then be compared to a positively charged H_2+ molecule. Optical spectrum then reveals the bonding & anti bonding states & the strength of bonding is described the distance between the two dots. We can work out the energy difference of bonding & anti bonding states and predict the shifting of PL peaks etc.

8.9.4 Cluster systems:

QD clusters are a bit different from the molecular view of QDs. For example Si cluster and a Si QD concerns the geometry and structure. In Si cluster number of Si atoms $\leq$ 13 & are most compact than Si QDs with higher coordination number. The bonding of Si atoms deviates from the simple sp^3 hybrid type. The optical absorption spectra for QD cluster shows very sharp absorption feature. Theoretical & experimental investigation shows that the cluster dimension should be ~ 49 Å. When QDs form a cluster covalent type bonding is relevant unlike binary system where electronagitivity is the main factor in bond formation.

8.9.5 QD – Qw system:

A spherically shaped QDs, if coated with a thin layer of a different semiconductor (that has a large energy gap) is called a QD – QW system. CDs QDs coated a layer of β- HgS that acts as a QW and further coated with thin CDs outer coating is one of the examples of QD – QW system. This system if refereed to as 'nano-opinions' by Weller (1996)[223]. Typical dimensions are R $\leq$ 2 nm for th CDs Qd L_{well} ~lnm for the HgS QW layer and L_{clad} $\leq$ 1.5 nm for CDs outer shell. In this system HgS acts as a QW where both the electrons and holes a thought to be localized.

8.9.5.1 Some characteristics of QD – QW system:

In general e-h pair in QDs of CDs are strongly correlated. After the addition of a HgS QW layer at the dot surface, the e-h pairs appear to act as more as independent electrons and holes.

The e-h pair binding energy and pay a correlation for dot – QW combination is reduced relative to the corresponding values for the dot without well. This is due to the increase in the e-h pair separation as a result of decrease in the binding energy.

The exciton of oscillator strength is also increased in the QD – QW system.

The precise behavior of the various QD – QW systems depends to a great extend on the values of the effective masses m_e^* and m_h^* as well as on the interaction strengths and band of set.

8.9.6 Core shell QD systems or Q – D film composites:

If unlike the above constructions QD – QW systems, CdSe is coated with a thin layer of a second semiconductor with a layer band gap such as CDs or ZnSe we obtain Q-D film composites. The holes are confined in the core Cdfe QD, since the holes are not trapped at the QD surfaces due to the passivation of the surface by the CDs layer, but the electron wave function extends into the CDs shell and this time the Q – D layer combination is passivated by an absorbed capping monolayer of TOPO (tri – n – octyl – phosphere oxide) to eliminate electron surface traps. The extent of the penetration of electronic wave function into CDs shell depends on the band offset, nature of the semiconductor & the shell dielectric constants.

8.9.7 QD – Conjugated Polymer Composites:

A promising development for the application of QDs came from the observation of EL from devices made using Q – D conjugated organic polymer complexes, under the action of an applied electric field. The aim was to construct LEDs for which the wave length of the limited light could be varied by the use of different size QDs. The electron & hole transport behavior are different for these two entities & are such that with a dot polymer composite, the device specification can be made so that e – h recombination takes place near the interface between the dot & the polymer. Colvin et al (1994)[224] used a CdSe QD – PPV (p- paraphenylene vinylene) combination PPV being a well-known electroluminescent polymer. Rigorous experimentation reveals that EL comes mainly from 2D layer for lower voltage & for higher voltages it comes predominantly from PPV layer. Experiments was also done with MEHPPV (poly (2-methoxy s-(2 ethy 1) hexyloxy – ppv) with a view to the possible development of optoelectronic devices such as thin films hetero junction diodes & photo voltaic cells.

One important phenomenon that we have not dealt with is the possible formation of 'hybrid excitons' between Frankel & tightly bound excitons created in the organic constituent & the move loosely bound Mott-Wannier excitons formed in the semiconductors QD, with the Q – D polymer systems. Calculations by Arganovich et al (1994) [225] were for QW system consisting of organic – inorganic layers where such hybrid excitons might form at the layer interfaces as a results of dipole, dipole interactions for combination of inorganic semiconductor quantum wires with polymer layers. This type of system like inorganic spherical QD wated with organic thin layer has a connection with the nonlinear optical properties (NLO).

8.9.8 Dielectric constants & QD size effects:

The dielectric constants determine the size effect in QDs. Changes of ε as R is reduced will alter the screening effects and may lead to a reduction in the Coulomb term for the exciton (e – h) interaction. For theoretical model the dependence of ε on R is given by

$$\varepsilon_s(R) = 1 + \frac{\varepsilon_b - 1}{1 + \left(\alpha/R\right)^2} \text{ for Si QD}$$

8.9.9 Transport tunneling & Coulomb blockade behavior, in single & coupled QDS:

If a semiconductor QD is placed between two metallic electrodes that acts as electron reservoirs and a voltage is applied between the electrodes which acts as the source or drain. There will of course, be barriers present at the interfaces between the dots & the electrodes & these act as tunneling barriers. For small dots and in a simple treatment the capacitance C involved is very small so that the energy required to introduced an extra electron into the dots in such a way that the single electron charging energy $\Delta = e^2/2c = e^2/4\pi\varepsilon R$ KT ($e^2/2c > KT$). This means that single electron tunneling in & out of the dot structure, or charge transfer can be minimized due to charging energy, if the measurements are made at low temperatures & with relatively low applied voltages. Such a phenomenon is known as Coulomb blockade.

With metal QDs where the electron density is very high the CB behavior can be simply described as a charging phenomenon. With semiconductor dots, the situation as we have seen is different due to the large separation in quantum states due to

confinement effects, and it is the discrete nature of the energy leels that is the dominating factor in the transport behavior.

Pepper & his colleagues have worked to describe the CB phenomenon for a semiconductor QD for a double barrier tunnel structure of the type illustrated in figure before, with dots represented as having a discrete set of energy levels. The potential is assumed to be approximately spherical in the region bordering the dots and εI is the energy of the ith level & is taken to be an averaged value of the vicinity of εi. the mean energy separation between the levels at ε_j and ε_{j+1} is Δ so that for CB $\Delta = \varepsilon_{j+1} - \varepsilon_j$. where each level is separated from the next level by the single electron charging energy $e^2/_{c\Sigma}$ when an extra electron is added to the dot.

CB oscillation is observed in the low temperature linear conductance results for a QD, have peaks in the conductance G which can be periodic as the gate voltage that controls the equilibrium charge is varied. Each oscillation period correspond to the addition of a single electron to the dot & the conductance peak are then periodic with the gate voltage, the period being $\Delta = e/_{C_o}$, C_o being the capacitance between the gate and the dot.

8.9.10 I – V Characteristics – for CdSe QD:

In a 2D electron gas in semiconducting material it is possible to form a lateral QD by the technique of electrostatic squeezing. This QD can weakly couple to electrical leads via tunnel barriers. The conductance for such a QD structure has been shown to oscillate as the really get potential is altered, where each oscillation corresponds to the passage of a single electron into a dot. Such a oscillation can also be reffered to as CB oscillation.

8.10 Coulomb staircase:

Using the surface oxidized (SiO_2) Si QDs Otobe et al (1998)[226] followed the single electron tunneling and charging effect and also observed both the CB and Coulomb staircase phenomena in the experimental I – V data. As is expected for single electron charging effects the period of the staircase increases with the decreasing dot size, but it is clear that their experiments need to be extended to lower temperatures.

8.10.1 CB for coupled dots:

In case of coupled dots there prevail the interaction between two adjacent dots, new effects were found in the spectra relating to the CB as the inter dot tunnel conductance is varied. When the right conditions are met for finite inter dot tunnel conductance, the data provided evidence of quantum fluctuations of charge between two dots. However, when two well isolated dots are involved corresponding to weak tunneling the classical capacitance model seem to reproduce the features found in CB data. The addition of an electron to an non-conducting dot can be seen to strongly influence the conductance measured through the neighboring conducting dot. As the dot – dot separation is reduced to increase the inter dot coupling beyond the quantum charge fluctuation regime and the inter dot conductance approaches the expected $2c^2/_h$ value, the coupled dot then behave as a single large dot. When the dots are not identical and the condition of charge degeneracy is not satisfied simultaneously for both dots, then the treatment of Ruzin et al. (1992)[227] shows that the conductance spectra becomes much more complex & a quasi randomness in the structure of the conductance vs. gate voltage spectra develops even at low temperatures.

8.11 Building to Smaller Dimensions

How small can electronic devices be made before the classical laws of physics prohibit them from operating? This question brings together several scientific disciplines in the nanoscience field: condensed-matter physics, solid-state electronics, chemistry, materials science, and electrical engineering. Some observers have described the various approaches to nanotechnology as top-down by the engineering disciplines and bottom-up by the physical disciplines. That is, people working from the bottom up are attempting to create a new understanding and structure from the dynamics of the basic materials and their molecules. Those working from the top down seek to improve existing devices, such as transistors, and to make them smaller.

Specifically, condensed-matter physics addresses the various properties that describe solid and liquid substances, including their thermal, elastic, electrical, chemical, magnetic, and optical characteristics. In terms of solid matter, theoretical advances have been made in recent years to study crystalline materials whose simple repetitive geometric arrays of atoms are multiparticle systems. These systems are

described in terms of quantum mechanics. However, because atoms in solids are coordinated over large distances, the theory must extend beyond the atomic and molecular levels. In addition, conductors such as metals contain free electrons that govern the electrical conductivity of the whole material, which is a property of the entire solid rather than its individual atoms. Crystalline and amorphous semiconductors and insulators, as well as properties of the liquid state of matter (liquid crystals and quantum liquids, for example) are also studied in condensed-matter physics. The macroscopic quantum phenomena observed in quantum liquids, such as superfluidity, is also seen in certain metallic and ceramic materials as superconductivity.

A classic example of a nanostructure is the single-electron transistor (SET). It consists of a metal island, a few hundred nanometers across, coupled to two metal leads via tunnel barriers. At temperatures below 1 K, no current can pass through the island for low-voltage biases. This effect is known as the Coulomb blockade, which is the result of the repulsive electron-electron interactions on the island. Most importantly, the current through the island can be accurately controlled down to a single electron. SETs are also realized in semiconductor devices, where their behavior is characterized as a quantum dot. (For a more in-depth description of SETs, see article above.) Quantum dots are nanometer-sized human-made boxes that control the flow of atoms by selectively holding or releasing them.

8.12 What is Single Electronics?

We talk about single-electronics whenever it is possible to control the movement and position of a single or small number of electrons. To understand how a single electron can be controlled, one must understand the movement of electric charge through a conductor. An electric current can flow through the conductor because some electrons are free to move through the lattice of atomic nuclei. The current is determined by the charge transferred through the conductor. Surprisingly this transferred charge can have practically any value, in particular, a fraction of the charge of a single electron. Hence, it is not quantized.

This, at first glance counterintuitive fact, is a consequence of the displacement of the electron cloud against the lattice of atoms. This shift can be changed continuously and thus the transferred charge is a continuous quantity (see left side of Fig. 1.1).
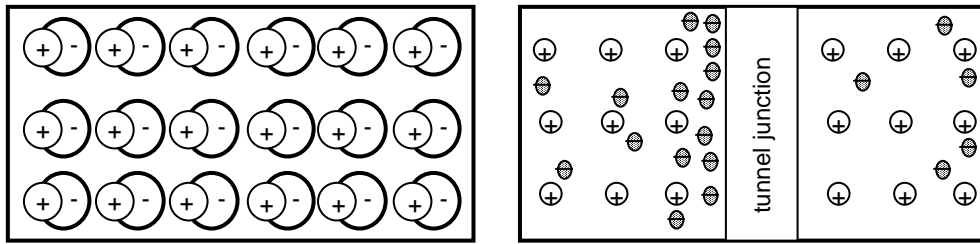
Figure 1.1: The left side shows, that the electron cloud shift against the lattice of atoms is not quantized. The right side shows an accumulation of electrons at a tunnel junction.

If a tunnel junction interrupts an ordinary conductor, electric charge will move through the system by both a continuous and discrete process. Since only discrete electrons can tunnel through junctions, charge will accumulate at the surface of the electrode against the isolating layer, until a high enough bias has built up across the tunnel junction (see right side of Fig. 1.1). Then one electron will be transferred. Likharev [79] has coined the term `dripping tap' as an analogy of this process. In other words, if a single tunnel junction is biased with a constant current I, the so called Coulomb oscillations will appear with frequency $f = I/e$, where e is the charge of an electron (see Fig. 1.2).
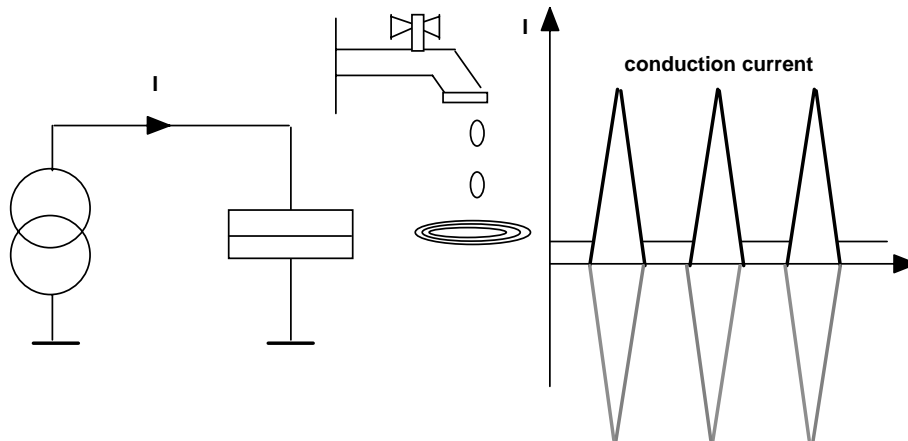
Figure 1.2: Current biased tunnel junction showing Coulomb oscillations.

Charge continuously accumulates on the tunnel junction until it is energetically favorable for an electron to tunnel. This discharges the tunnel junction by an elementary charge e. Similar effects are observed in superconductors. There, charge carriers are Cooper pairs, and the characteristic frequency becomes $f = I/2e$, related to the so called Bloch oscillations.
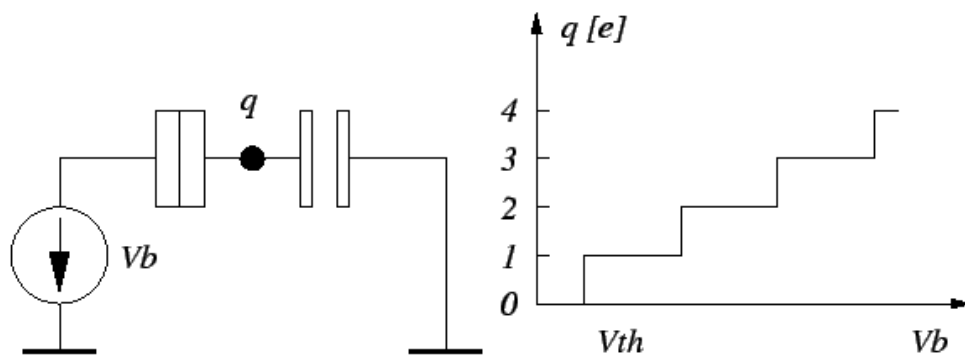
Figure 1.3: The electron-box can be filled with a precise number of electrons.

The current biased tunnel junction is one very simple circuit, that shows the controlled transfer of electrons. Another one is the electron-box (see Fig. 1.3). A particle is only on one side connected by a tunnel junction. On this side electrons can tunnel in and out. Imagine for instance a metal particle embedded in oxide, as shown in Fig. 1.4.
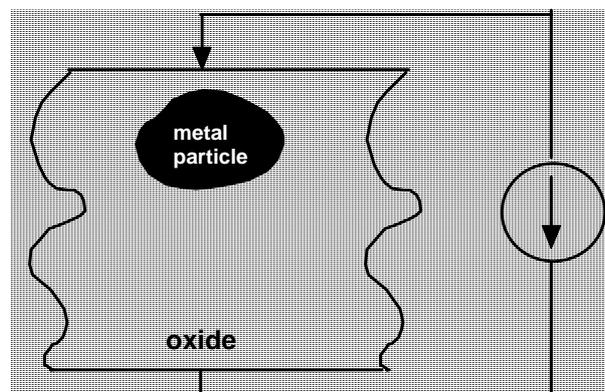
Figure 1.4: Metal particle embedded in oxide. Tunneling is only possible through the thin top layer of oxide.

The top oxide layer is thin enough for electrons to tunnel through. To transfer one electron onto the particle, the Coulomb energy $E_C = e^2/2C$, where C is the particles capacitance, is required. Neglecting thermal and other forms of energy, the only energy source available is the bias voltage V_b. As long as the bias voltage is small enough, smaller than a threshold $V_{th} = e/C$, no electron can tunnel, because not enough energy is available to charge the island. **This behavior is called the Coulomb blockade** . Raising the bias voltage will populate the particle with one, then two and so on electrons, leading to a staircase-like characteristic.

It is easily understandable, that these single-electron phenomena, such **as Coulomb oscillations and Coulomb blockade**, only matter, if the Coulomb energy is bigger than the thermal energy. Otherwise thermal fluctuations will disturb the motion of electrons and will wash out the quantization effects. The necessary condition is,

$$E_c = \frac{e^2}{2C} > k_B T$$

where k_B is Boltzmann's constant and T is the absolute temperature. This means that the capacitance C has to be smaller than 12 nF for the observation of charging effects at the temperature of liquid nitrogen and smaller than 3 nF for charging effects to appear at room temperature. A second condition for the observation of charging effects is, that quantum fluctuations of the number of electrons on an island must be negligible. Electrons need to be well localized on the islands. If electrons would not be localized on islands one would not observe charging effects, since islands would not be separate particles but rather one big uniform space. The charging of one island with an integer number of the elementary charge would be impossible, because one electron is shared by more than one island. The Coulomb blockade would vanish, since no longer would a lower limit of the charge, an island could be charged with, exist. This leads to the requirement that all tunnel junctions must be opaque enough for electrons in order to confine them on islands. The `transparency' of a tunnel junction is given by its tunnel resistance R_T which must fulfill the following condition for observing discrete charging effects, where h is Planck's constant. This should be understood as an order-of-magnitude measure, rather than an exact threshold.

$$R_T > \frac{h}{e^2} = 25813\Omega$$

Therefore, these effects are experimentally verifiable only for very small high-resistance tunnel junctions, meaning small particles with small capacitances and/or very low temperatures. Advanced fabrication techniques, such as the production of granular films with particle sizes down to 1 nm, and deeper physical understanding allow today the study of many charging effects at room temperature.

Based on the Coulomb blockade many interesting devices are possible, such **as precise current standard,**[228] **very sensitive electrometers**,[229] **logic gates**[230] and **memories**[231] with ultra low power consumption, down-scalability to atomic dimensions, and high speed of operation. Altogether, single-electronics will bring new and novel devices and is a very promising candidate to partly replace MOS technology in the near future.

2.1 Characteristic Energies

Charging an island with a small number of electrons is associated with two kinds of energies. One kind arises from electron-electron interaction and the other is linked to the spatial confinement of electrons. These energies are only significant for very small structures in the nanometer regime. Otherwise they are masked by thermal fluctuations. *We discuss two other important characteristic energies, the work done by the voltage sources and Helmholtz's free energy, and the role they play in single-electron device behavior.*

2.1.1 Electron Electron Interaction

An entirely classical model for electron-electron interaction is based on the electrostatic capacitive charging energy. The interaction arises from the fact, that for every additional charge *dq* which is transported to a conductor, work has to be done against the field of already present charges residing on the conductor. Charging a capacitor with a charge *q* requires energy, where *C* is the total capacitance of the capacitor. A first simple model for an island is a conducting sphere which has a self-capacitance of (see the next table)

$$E_c = \frac{q^2}{4\pi\varepsilon d}$$

where ε is the permittivity of the surrounding dielectric material and *d* is the diameter of the sphere. Inserting (2.2) in (2.1) yields

$$C = 2\pi\varepsilon d$$

an indirect proportionality to the size of the particle. Fig. 2.1 to Fig. 2.3 compare this electrostatic energy to the other characteristic energies involved in charging an island with a small number of electrons.
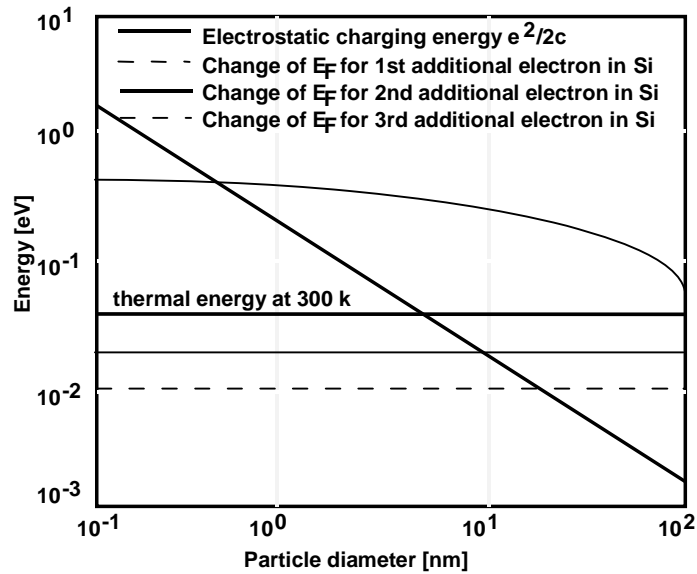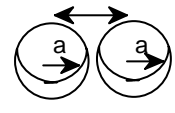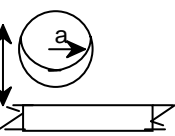
Figure 2.1: Comparison of the change in Fermi energy for the addition of one, two, and three electrons in Si to the electrostatic charging energy.
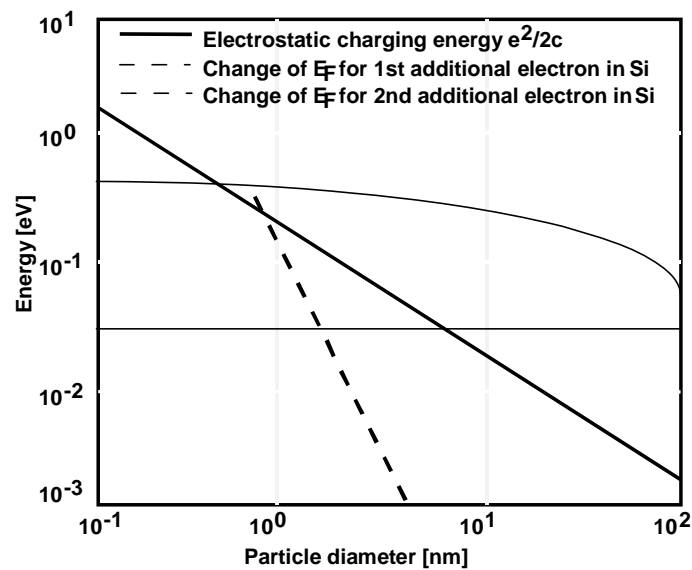
Figure 2.2: Comparison of the change in Fermi energy for the addition of one electron in Si and Al. The values below 1 nm particle diameter are questionable, because the derivations of ([2.6](#)) and ([2.7](#)) cease to be valid.

For the sake of simplicity, the relative permittivity, ε was assumed to be 10. A more accurate model for the capacitance of an island is the capacitance of two or more spheres in a line. A calculation for characteristic spatial dimensions shows an increase of about 15% of the total capacitance. A collection of practical analytical capacitance formulas is given in Table below:
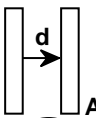
paralel plates	$C = \dfrac{\varepsilon\,A}{d}$	
sphere	$C = 4\pi\varepsilon a$	
sphere with dielectric shell	$C = 4\,\pi\varepsilon\ \dfrac{ab}{ba-(1)\ \varepsilon_r}$	
disc	$C = 8\pi a$	
two spheres	$C = \pi\varepsilon\sqrt{d^2-4a^2}\displaystyle\sum_{j=0}^{\infty}\left(\coth\left[(j+\tfrac{1}{2})ar\cosh(\tfrac{d}{2a})\right]-1\right)$	
sphere and plane	$C = 2\pi\varepsilon\sqrt{d^2-4a^2}\displaystyle\sum_{j=0}^{\infty}\left(\coth\left[(j+\tfrac{1}{2})ar\cosh(\tfrac{d}{2a})\right]-1\right)$	

Table: A collection of practical capacitance formulas. The expressions for two spheres and sphere above plane are taken from S. A. Roy, *Simulation Tools for the Analysis of Single Electronic Systems.* PhD thesis, University of Glasgow, June 1994.

For a system of *N* conductors the charge on one conductor may be written as

$$q_i = \sum_{j=1}^{N} C_{ij}\varphi_j \qquad (i=1,2,3,......)$$

where the C_{ij} denote the elements of the capacitance matrix. The diagonal elements of the capacitance matrix C_{ij} are the total capacitances of the conductors *i* and the off-diagonal elements C_{ij} are the negative capacitances between conductor *i* and *j*. The electrostatic charging energy is in analogy to (2.1)

$$E_c = \frac{1}{2}\sum_{i=1}^{N} q_i\varphi_i = \frac{1}{2}\sum_{i=1}^{N}\sum_{j=1}^{N}\left(C^{-1}\right)_{ij} q_i q_j$$

where **C**⁻¹ is the inverse of the capacitance matrix.

Systems with sufficiently small islands are not adequately described with this model. They exhibit a second electron-electron interaction energy, namely the change in Fermi energy, when charged with a single electron. One must distinguish between metals and semiconductors, because of their greatly different free carrier concentrations and the presence of a band gap in the case of semiconductors. Metals have typically a

carrier concentration of several 10^{22} /cm^3 and undoped Si about 10^{10} /cm^3 at room temperature. The low intrinsic carrier concentration for semiconductors is in reality not achievable, because of the ubiquitous impurities which are ionized at room temperature. These impurities supply free charge carriers and may lift the concentration, in the case of Si, to around 10^{14}/cm^3, still many orders of magnitude smaller than for metals. Clearly, doping increases the carrier concentration considerably, and can lead in the case of degenerated semiconductors to metal like behavior. We are considering only undoped semiconductors to emphasize the difference to metals.

The dependence of the Fermi energy E_F on carrier concentration n can be expressed as below (N. W. Ashcroft and N. D. Mermin, *Solid State Physics*, W. B. Saunders Company, international edition, 1976). For metals it is given by

$$E_F = \frac{\hbar^2}{2m^*}\left(3\pi^2 n\right)^{2/3}$$

and for semiconductors it is

$$\frac{n_{net}}{n_i} = 2\sinh\frac{E_F - E_{F,i}}{k_B T}$$

where **n$_{net}$** is the net carrier concentration defined as **n$_{net}$= n-p**. Fig. 2.1 compares the change in the Fermi energy for the addition of one, two, and three electrons in Si to the electrostatic charging energy.

The first electron causes the biggest change in Fermi energy. The second and third electron contribute a change smaller than the thermal energy for room temperature. ***Hence, for single-electron devices one will try to build structures with few free carriers, to achieve a high change in energy when charging an island.***

Fig. 2.2 compares Si with Al. It is clearly visible that the change is much bigger in Si. This is caused by two reasons. First, the difference in free carrier concentration. In metals much more carriers are available and therefore the addition of one electron has not such a big impact anymore. Second in metals an additional electron finds a place slightly above the Fermi level. In semiconductors due to the energy gap the electron needs to be inserted considerably above the Fermi level.

2.1.2 Quantum Confinement Energies

With decreasing island size the energy level spacing of electron states increases indirectly proportional to the square of the dot size. Taking an infinite potential well as a simple model for a quantum dot, one calculates by solving Schrödinger's equation the energy levels to

$$E_N = \frac{1}{2m^*} \left(\frac{\hbar \pi N}{d} \right)^2$$

Because of the lower effective mass in Si compared to Al, the quantum confinement energy is bigger in Si (see Fig. 2.3).
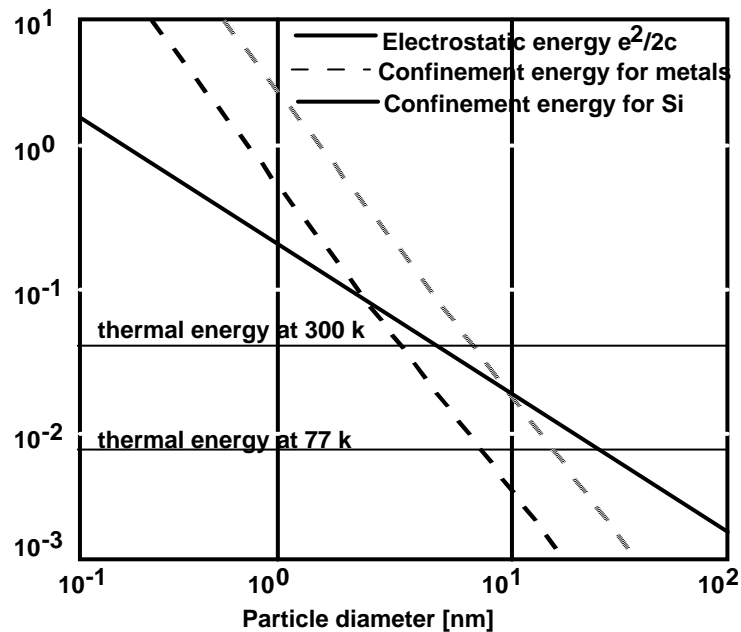
Figure 2.3: Comparison of the quantum confinement energy in Si and Al.

For very small particle diameters (around 1 nm) the formulas (2.6), (2.7), and (2.8) cease to be valid. The concept of the effective mass is based on a periodic lattice and starts to break down for small islands. One would have to apply cluster theory to calculate the energy levels more precisely. In reality slightly smaller confinement energies than predicted in (2.8) are observed, which may partly be attributed to the model of an infinite well. The energy levels slightly decrease in the case of a finite well (see Appendix C.2). Furthermore, the lattice constant for metals is about 0.4 nm whereas for semiconductors it is almost 0.6 nm. Thus the concept of carrier densities is not valid anymore.

Room temperature operation is achievable with structures smaller than 10 nm. Cooling single-electron devices with liquid nitrogen reduces thermal fluctuations to some extent, but relaxes the size constrains only by a factor of two.

2.4 Tunneling

In 1923 de Broglie introduced a new fundamental hypothesis that particles may also have the characteristics of waves. Schrödinger expressed this hypothesis 1926 in a definite form which is now known as the Schrödinger wave equation. The continuous nonzero nature of its solution, the wave function which represents an electron or particle, implies an ability to penetrate classically forbidden regions and a probability of tunneling from one classically allowed region to another. Fowler and Nordheim explained in 1928 the main features of electron emission from cold metals by high external electric fields on the basis of tunneling through a triangular potential barrier. Conclusive experimental evidence for tunneling was found by L. Esaki in 1957 and by I. Giaever in 1960. Esaki's tunnel diode had a large impact on the physics of semiconductors, leading to important developments such as the tunneling spectroscopy, and to increased understanding of tunneling phenomena in solids. L. Esaki , I. Giaever and B. Josephson received 1973 the Nobel prize for their work about tunneling in semiconductors, superconductors and theoretical predictions of the properties of a supercurrent through a tunnel barrier, respectively. The concept of resonant tunneling in double barriers was first introduced by R. Davis and H. Hosack. At about the same time C. Neugebauer and M. Webb and some years later H. Zeller and I. Giaever and J. Lambe and R. Jaklevic studied granular films. They observed a current suppression at low bias voltage, which is today known as the Coulomb blockade. It took almost two decades until in 1985 D. Averin and K. Likharev formulated the `orthodox' theory of single-electron tunneling or short SET, which quantitatively describes important charging effects such as Coulomb blockade and Coulomb oscillations. The orthodox theory makes the following assumptions: It neglects dimensions and shapes of islands. Thus it is a zero-dimensional model. The tunnel process is assumed to be instantaneous. Actually the tunnel time, the duration an electron spends below a barrier, is of the magnitude of 10^{-14} s. Charge redistributions after a tunnel event are also assumed to be instantaneous. In addition energy spectra in leads and islands are taken to be continuous. The main result of the orthodox theory is that the rate of a tunnel event strongly depends on the change in free energy the event causes.

2.5 Minimum Tunnel Resistance for Single Electron Charging

The formulation of the Coulomb blockade model is only valid, if electron states are localized on islands. In a classical picture it is clear, that an electron is either on an island or not. That is the localization is implicit assumed in a classical treatment. However a preciser quantum mechanical analyses describes the number of electrons localized on an island **N** in terms of an average value **<N>** which is not necessarily an integer. The Coulomb blockade model requires

$$\left| N - \langle N \rangle \right|^2 \langle\langle 1$$

Clearly, if the tunnel barriers are not present, or are insufficiently opaque, one can not speak of charging an island or localizing electrons on a quantum dot, because nothing will constrain an electron to be confined within a certain volume.

A qualitative argument is to consider the energy uncertainty of an electron

$$\Delta E \Delta t > h$$

The characteristic time for charge fluctuations is

$$\Delta t \cong R_T C$$

the time constant for charging capacitance **C** through tunnel resistor **R_T,** and the energy gap associated with a single electron is

$$\Delta E = \frac{e^2}{C}$$

Combining ([2.26](2.26)) and ([2.27](2.27)) gives the condition for the tunnel resistance

$$R_T > \frac{h}{e^2} = R_Q = 25813\Omega$$

Another line of thought proceeds as follows. The condition

$$\left| N - \langle N \rangle \right|^2 \langle\langle 1$$

requires that the time **t** which an electron resides on the island be much greater than Δt, the quantum uncertainty in this time.

$$t >> \Delta t \geq \frac{h}{\Delta E}$$

The current **I** cannot exceed *e/t* since for moderate bias and temperature at most one extra electron resides on the island at any time. The energy uncertainty of the electron Δ **E** is no larger than the applied voltage *V_b.*

$$\Delta E < eV_b$$

Inserting **t=e/I** and ([2.30](#)) into ([2.29](#)) results in

$$R_T = \frac{V_b}{I} >> \frac{h}{e^2}$$

In fact, more rigorous theoretical studies of this issue have supported this conclusion. Experimental tests have also shown this to be a necessary condition for observing single-electron charging effects.[232]

2.7 The Double Tunnel Junction

Consider two tunnel junctions in series biased with an ideal voltage source as shown in Fig. [2.7](#). The charges on junction one, junction two, and on the whole island can be written as

$$q_1 = C_1 V_1, q_2 = C_2 V_2, and$$
$$q = q_2 - q_1 + q_0 = -ne + q_0$$

respectively, with n_1 the number of electrons that tunneled through the first junction entering the island, n_2 the number of electrons that tunneled through the second junction exiting the island, and $n=n_1-n_2$ the net number of electrons on the island.

A background charge q_0 produces generally a non-integer charge offset. The background charge is induced by stray capacitances that are not shown in the circuit diagram Fig. [2.7](#) and impurities located near the island, which are practically always present. Using ([2.32](#)) and $V_b=V_1+V_2$ gives

$$V_1 = \frac{C_2 V_b + ne - q_0}{C_\Sigma}, V_2 = \frac{C_1 V_b - ne + q_0}{C_\Sigma}$$

$$where, C_\Sigma = C_1 + C_2$$
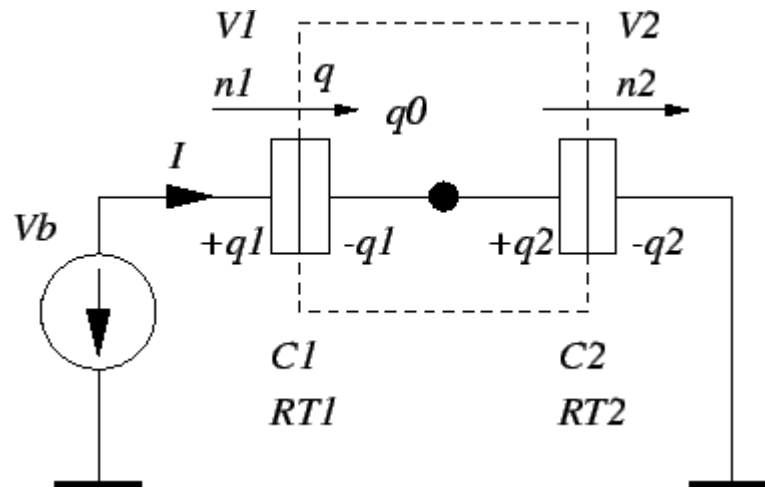
Figure 2.7: Two tunnel junctions in series biased with an ideal voltage source. The background charge q_0 is non-integer, and n_1 and n_2 denote the number of tunneled electrons through junction one and junction two, respectively.

With (2.33) the electrostatic energy stored in the double junction is

$$E_C = \frac{q_1^2}{2C_1} + \frac{q_2^2}{2C_2} = \frac{C_1 C_2 V_b^2 + (ne - q_0)^2}{2C_\Sigma}$$

In addition, to get the free energy one must consider, as in (2.11), the work done by the voltage source. If one electron tunnels through the first junction the voltage source has to replace this electron *-e,* plus the change in polarization charge caused by the tunneling electron. **V$_1$** changes according to (2.33) by

$$-e/C_\Sigma$$

and hence the polarization charge is

$$-eC_1/C_\Sigma$$

The charge q_1 gets smaller, which means that the voltage source `receives' polarization charge. The total charge that has to be replaced by the voltage source is therefore

$$-eC_2/C_\Sigma$$

and the work done by the voltage source in case electrons tunnel through junction one and junction two is accordingly

$$W_1 = -\frac{n_1 e V_b C_2}{C_\Sigma}$$

and

$$W_2 = -\frac{n_2 e V_b C_1}{C_\Sigma}$$

The free energy of the complete circuit is

$$F(n_1, n_2) = E_c - W = \frac{1}{C_\Sigma}\left[\frac{1}{2}\left\{C_1 C_2 V_b^2 + (ne - q_0)^2 + e V_b (C_1 n_2 + C_2 n_1)\right\}\right]$$

At zero temperature, the system has to evolve from a state of higher energy to one of lower energy. At non-zero temperatures transitions to higher energy states are possible, but have exponentially reduced probability (see 2.23). The change in free energy for an electron tunneling through junction one and two is given by

$$\Delta F_1^\pm = F(n_1 \pm 1, n_2) - F(n_1, n_2) = \frac{e}{C_\Sigma}\left[\frac{e}{2} \pm (V_b C_2 + ne - q_0)\right]$$

$$\Delta F_2^\pm = F(n_1, n_2 \pm 1) - F(n_1, n_2) = \frac{e}{C_\Sigma}\left[\frac{e}{2} \pm (V_b C_1 - ne + q_0)\right]$$

The probability of a tunnel event will only be high, if the change in free energy is negative - a transition to a lower energy state. This is a direct consequence of (2.23). The leading term in (2.37) and (2.38) causes **F** to be positive until the magnitude of the bias voltage V_b exceeds a threshold which depends on the smaller of the two capacitances. This is the case for all possible transitions starting from an uncharged island, $n=0$ and $q_0=0$. For symmetric junctions ($C_1 = C_2$) the condition becomes

$$|V_b| > e/C_\Sigma$$

This suppression of tunneling for low bias is the Coulomb blockade. The Coulomb blockade can be visualized with an energy diagram Fig. 2.8.

filled energy

emptyenergy
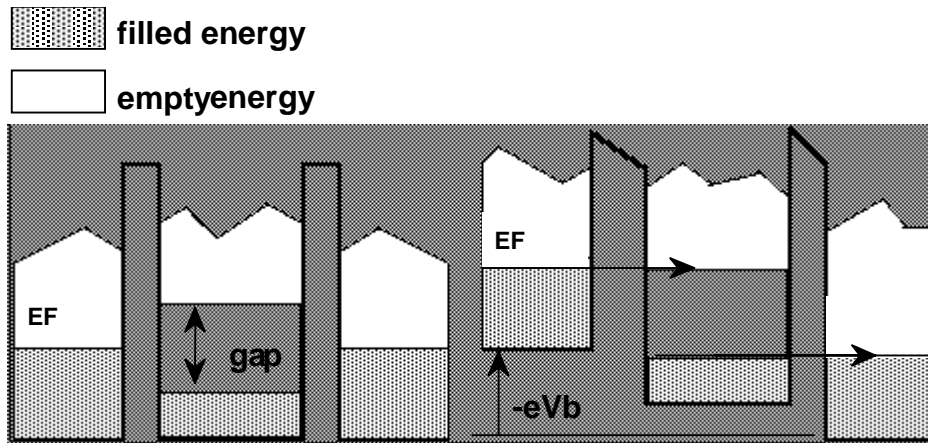
Figure 2.8: Energy diagram of a double tunnel junction without and with applied bias. The Coulomb blockade causes an energy gap where no electrons can tunnel through either junction. A bias larger than e/C overcomes the energy gap.

Due to the charging energy of the island, a Coulomb gap has opened, half of which appears above and half below the original Fermi energy. No electrons can tunnel into the island from the left or right electrode, or out of the island. Only if the bias voltage is raised above a threshold can electrons tunnel in and out, and current will flow.

The same fact, the existence of a Coulomb blockade, is clearly visible in the *IV*-characteristic, Fig. .
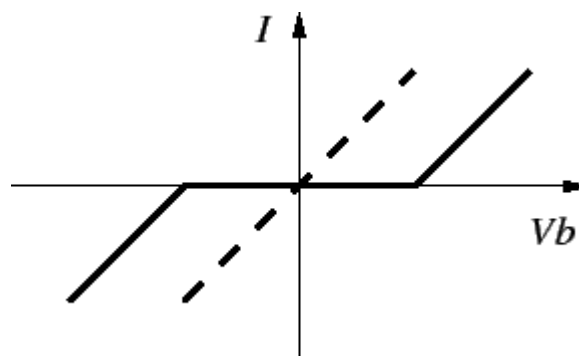
Figure 2.9: *IV*-characteristic of a double tunnel junction. The solid line gives the characteristic for q_0=0 and the dashed line for q_0=0.5e. The Coulomb blockade is a direct result of the additional Coulomb energy, $e^2/2C$, which must be expended by an electron in order to tunnel into or out of the island.

For low bias no current flows. As soon as V_b exceeds the threshold the junction behaves like a resistor.

However, the background charge q_0 can reduce, or for

$$q_0 = \pm(0.5 + m)e$$

even eliminate the Coulomb blockade. This suppression of the Coulomb blockade due to virtually uncontrollable background charges is one of the major problems of single-electron devices. It will be addressed in more detail in Section 5.2.3.

If an electron enters the island via junction one, it is energetically highly favorable for another electron to tunnel through junction two out of the island. Thus an electron will almost immediately exit the island after the first electron entered the island. This is a space-correlated tunneling of electrons (see Fig. 2.10). After a varying duration another electron might first exit the island via junction two and again, immediately a new electron will tunnel through junction one, entering the island and establishing charge neutrality on the island. If the transparency of the tunnel junctions is strongly different, for example

$$R_{T1} << R_{T2} = R_T$$

a staircase like *IV*-characteristic appears, as shown in Fig. 2.11.
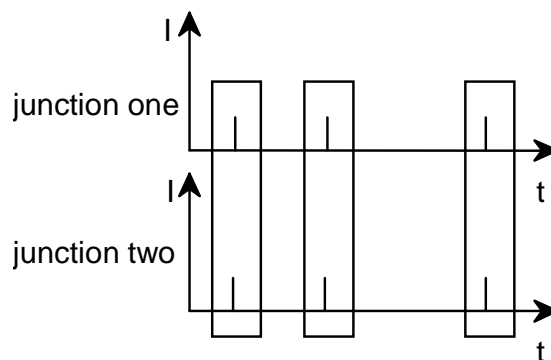
Figure 2.10: Space-correlation of tunneling in a double tunnel junction. A tunnel event in junction one is immediately followed by an event in junction two and vice versa. The duration between those tunnel pairs is varying.
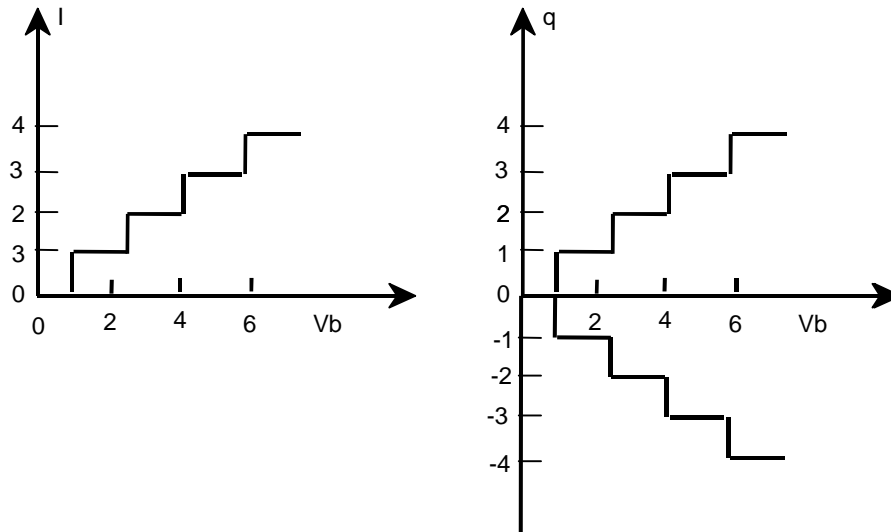
Figure 2.11: For strongly differing tunnel junctions a staircase like *IV*-characteristic appears. Depending on which tunnel junction is more transparent, and the direction in which the charge carriers flow, the island will be populated or depleted by an integer number of carriers with increasing bias voltage. If carriers enter the island through the more transparent junction and leave through the opaque one the island will be populated with excess carriers. If they have to enter through the opaque junction and leave through the transparent one, the island is depleted of carriers.

Carriers enter the island through the first tunnel junction and are kept from the high resistance of the second junction from immediately leaving it. Finally the carrier will, due to the high bias, tunnel out of the island, which quickly triggers another electron to enter through junction one. For most of the time the island is charged with one excess elementary charge. If the bias is increased more electrons will most of the time populate the island. The charge characteristic is shown on the right side of Fig. 2.11. If the asymmetry is turned around and the second junction is more transparent then the first one,

$$R_{T2} << R_{T1} = R_T$$

the island will be de-populated and the charge on the island shows a descending staircase characteristic. Carriers are sucked away from the island through the transparent junction and can not be replenished quickly enough through the opaque one. However, the *IV*-characteristic does not change.

2.8 Single Electron Transistor

Adding to the double tunnel junction a gate electrode V_g which is capacitively coupled to the island, and with which the current flow can be controlled, a so-called SET transistor is obtained (see Fig. 2.12).
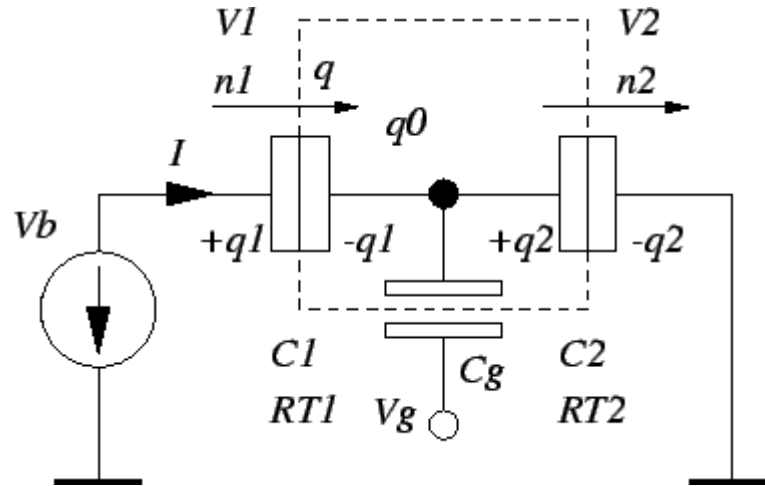
Figure 2.12: SET transistor.

The first experimental SET transistors were fabricated by Fulton and Dolan,[233] and Kuzmin and Likharev[234] already in 1987. The effect of the gate electrode is that the background charge q_0 can be changed at will, because the gate additionally polarizes the island, so that the island charge becomes

$$q = -ne + q_0 + C_g \left(V_g - V_2 \right)$$

The formulas derived in Section 2.7 for the double junction can be modified to describe the SET transistor. Substituting

$$q_0 \rightarrow q_0 + C_g \left(V_g - V_2 \right)$$

in (2.33), the new voltages across the junctions are

$$V_1 = \frac{\left(C_2 + C_g \right) V_b - C_g V_g + ne - q_o}{C_\Sigma},$$

$$V_2 = \frac{C_1 V_b + C_g V_g - ne + q_o}{C_\Sigma}$$

with $C_\Sigma = C_1 + C_2 + C_g$

The electrostatic energy has to include also the energy stored in the gate capacitor, and the work done by the gate voltage has to be accounted for in the free energy. The change in free energy after a tunnel event in junctions one and two becomes

$$\Delta F_1^{\pm} = \frac{e}{C_\Sigma}\left[\frac{e}{2} \pm \left\{\left(C_2 + C_g\right)V_b - C_g V_g + ne - q_0\right\}\right]$$

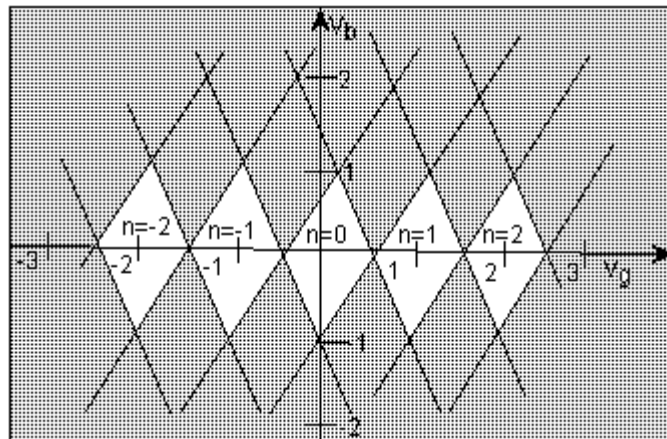$$\Delta F_1^{\pm} = \frac{e}{C_\Sigma}\left\{V_b C_1 + V_g C_g - ne + q_0\right\}$$

At zero temperature only transitions with a negative change in free energy,

$$\Delta F_1 < 0$$

Or,

$$\Delta F_2 < 0$$

are allowed. These conditions may be used to generate a stability plot in the V_b-V_g plane, as shown in Fig. 2.13.

Figure 2.13: Stability plot for the SET transistor. The shaded regions are stable regions.

The shaded regions correspond to stable regions with an integer number of excess electrons on the island, neglecting any non-zero background charge. If the gate voltage is increased, and the bias voltage is kept constant below the Coulomb blockade,

$$V_b < e/C_\Sigma$$

which is equivalent to a cut through the stable regions in the stability plot, parallel to the x-axis, the current will oscillate with a period of **e/C$_g$**. As opposed to the Coulomb oscillations in a single junction, which were explained in the introduction, where the periodicity in time of discrete tunnel events is observed, these are Coulomb oscillations

which have a periodicity in an applied voltage, where regions of suppressed tunneling and space correlated tunneling alternate. Fig. 2.14 shows the qualitative shape of the current oscillations
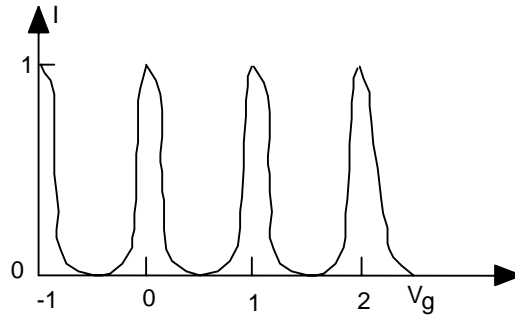
Figure 2.14: Coulomb oscillations in a SET transistor.

Increasing the bias voltage will increase the line-width of the oscillations, because the regions where current is allowed to flow grow at the expense of the remaining Coulomb blockade region. Thermal broadening at higher temperatures or a discrete energy spectrum change the form of the oscillations considerably.

8.12.1 Coulomb Blockade in a Quantum Dot: Phenomenological Explanation
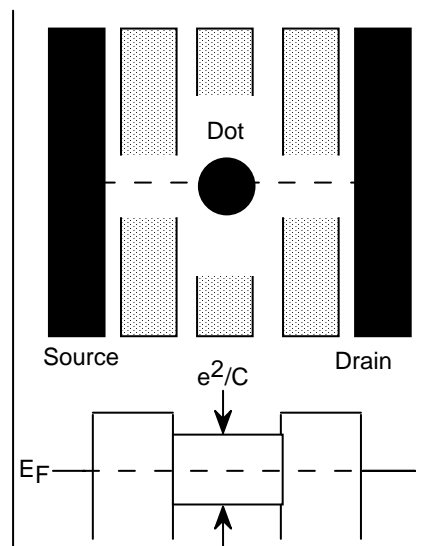
Figure: Quantum dot for Coulomb blockade demonstration.

By using the split-gate techniques, one can form tunnel barriers which isolate a puddle of electrons, often called a "**dot**", from the leads. To add one electron to the dot

costs a "**charging energy**" e^2/C. The total capacitance of a sub-micron-sized dot to the surrounding gates and leads can be very small, less than 1 fF (10^{-15} F), so this energy is greater than the thermal energy for temperatures of a few Kelvin or less. Thus at such temperatures, transport through the dot is determined by Coulomb charging. Smaller dots can give even higher temperatures of operation.

For an electron to tunnel onto the dot, when the applied bias is small, there must be no net energy cost of adding an electron. Thus tunneling can only occur when the size of the dot is such that it would be neutral if it contained an integer N plus a half electrons. Since it can only contain an integer number, the net charge on the dot will be $\pm e/2$, depending on whether there are N or $N+1$ electrons in the dot. The charging energy is then $(\pm e/2)^2/C$, which is the same in both cases. Hence changing the number of electrons in the dot between N and $N+1$ costs no energy, so electrons can flow on and off the dot with ease, and a current can flow. If the size of the dot is changed slightly, the charging energy in the two cases is no longer the same, and so the current falls to zero, only rising again when the size of the dot has changed by one electron. This is called the **Coulomb Blockade** (CB) **of tunnelling**. Sweeping a gate (shown shaded in the figure) changes the size of the dot and thus the conductance between the leads (source and drain) has periodic peaks rising from zero to a value which may be as high as $2e^2/h$.

This effect can be seen in metal and semiconductor dots. In the latter, the quantum-mechanical energy levels of the electrons are also important, as their wavelength is comparable to the size of the dot, thus the term "**quantum dot**" is used. The number of electrons in a semiconductor dot can also sometimes be reduced all the way to zero, close to which the spacing of CB peaks becomes less regular as the energy spacing of the electronic states, and the mutual Coulomb interactions of the electrons in the dot, cannot be ignored.

8.12.1.1 Quantized charge transport

The S.I. definition of the ampere is still "That current which, when flowing through two parallel infinite wires held one meter apart will induce between the wires a force of $2*10^{-7}$ N/m of length". A much better definition would be one based on the flow of a known number of electrons through a system.

Several results have been published on devices which "pump" one electron at a time through the circuit, giving a current equal to ef, where e is the charge on an

electron and *f* is the pumping frequency. All of these devices have relied on the same principle, that of Coulomb Blockade by an isolated region of electrons (known as a quantum dot). These are generally defined electrostatically using surface gates, with electrons able to move in and out of the quantum dot across tunnel barriers. Lowering the entrance barrier allows a single electron to tunnel onto the dot. The entrance barrier is then raised, and the exit lowered so an electron may move off the dot on the other side of the device. The reliance on quantum-mechanical tunneling limits the frequency of operation of these "electron turnstiles" to about 10MHz. This corresponds to a current of a few picoamps, which is too small to be measured to the required level of accuracy (parts per billion) at the moment. However researchers have demonstrated that the devices are stable to this level, and attempts are being made to improve the accuracy of the measurements.

8.12.1.2   Harnessing the Energy of a Single Electron
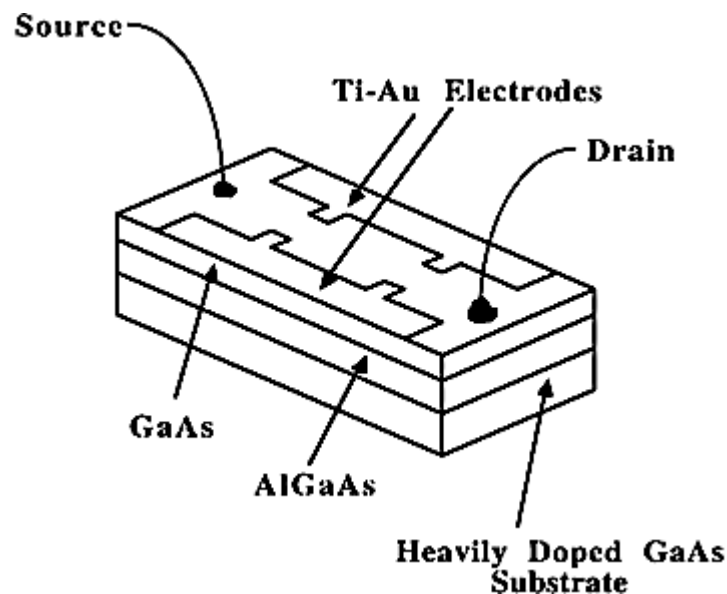
Figure: A schematic of the device structure of the artificial atom consisting of an inverted heterostructure of a degenerately doped substrate upon which is grown a layer of aluminum gallium arsenide and a layer of undoped gallium arsenide. (from *The Foundations of Next-Generation Electronics: Condensed-Matter Physics at RLE,* RLE Currents *Vol. 10, No. 2: Fall 1998; MIT, USA)*

As the physical laws related to today's computer memory and processor fabrication reach their limits, new approaches such as single-electron technology are

being explored. Single-electron devices are the potential successors to the conventional technology employed to make metal-oxide semiconductor field-effect transistors (MOSFETs). This is because they make use of the electron—the smallest unit of electrical charge—to represent bits of information. While electron tunneling in MOSFETs limits their smallest integration scale, this same behavior in single-electron devices may prove to be the ultimate solution.

When electrons are confined to a small particle of metal or a small region of a semiconductor, both the energy and charge of the system are quantized. In this way, such nanometer-sized systems behave like artificial atoms. While artificial atoms can be constructed using metals and semiconductors in various geometries, the physics of these devices remains the same.

Considered one of the simplest types of artificial atoms, the metallic single-electron transistor (SET) is a nanoscale device that was developed in 1987. A metallic SET consists of a metal particle isolated from its leads by two tunnel junctions (which are similar to diodes) and capacitively coupled to a common gate electrode. The tunnel junctions create what is known as a Coulomb island, which the electrons can enter only by tunneling through one of the insulators. Coulomb repulsion prohibits more than one extra electron at a time on the island (near the gate). Thus, electronic circuits can be made to pump or count electrons one at a time. Because an SET's electrical resistance is highly sensitive to the electrical fields from nearby charges, it can easily detect not only single electrons, but also charges as small as 1 percent of an electron's electrical field. The current as a function of bias across the tunnel barriers can also be measured in order to observe the so-called Coulomb staircase, a stepwise increase of current as electrons are added to the metal particle.

Because SETs exhibit extremely low power consumption, reduced device dimensions, excellent current control, and low noise, they promise to reveal new physics and innovative electronic devices. These features hold the potential for using SETs in specialized metric-scale applications, such as in current standards and precision electrometers. Also, possible design applications that exploit the SET's reduced dimensions and use a minimum number of devices may result in the creation of high-density neural networks. However, their use in high-density computer memory and data-

processing systems must overcome problems associated with quantum charge fluctuations and the SET's sensitivity to microwave radiation.

9 SPECIAL NANOSTRUCTURED MATERIALS

9.1 Fullerenes, nanotubes, onions

9.2 Some recently synthesized nanocrystalline carbon-structure:

Diamond & Graphite are well known carbon allotropes found in nature with different hybridization state of carbon (Sp^3 for diamond & Sp^2 for Graphite) in them. In late 60's several closed cage carbon molecules were proposed and prepared in subsequent time. To name one of them it is the fullerenes, an allotrope with 60-carbon atom arranged to form a soccer ball shaped structure. This material is famous for its novel super-conducting and magnetic properties. Early of 90's fullerenes are proposed to have been observed in the soot produced by arcking graphite electrode. Under the some excitement condition, helical nanotubes of graphite were also observed (1991). These nanotubes are concentric graphitic cylinders closed at either end due to the presence of five-membered rings. In 1992 concentric spherical shells of graphite forming onion like structure was observed (Ugarte) and known as nano onions.

9.2.1 Fullerenes:

Fullerenes are usually prepared by laser ablation of rotating graphite disc, or arc-evaporation technique. Spectroscopic results speaks largely in support of cage like structure of fullerenes. Some properties and applications of fullerenes are given below.

As superconducting material: the fee structure of fullerenes has octahedral & tetra hedral voids that can easily accommodate dopant atoms. In addition to this, Vander-Waals nature of C_{60} - C_{60} cohesion makes C_{60} a good host for the intercalation of alkali metal atoms. Ref. (162 – 164 &183). Fullerenes with metallic combination (K_xC_{60}) is much useful as a superconductor due to stronger phononic state. Besides, metal mercury & thallium alloys with fullerenes structure shows efficient superconducting properties. Various metallic combination of fullerenes are found showing metallic behaviors is resistivity vs. temperature curve. This is also a favourable sign of using fullerenes as superconductors.

9.2.1.1 Magnetism & tunneling:

The critical field of coherence length of fullerenes are found showing an extreme dirty limit superconductor. Tunneling studies shows a fairly large deviation in K-shape gap then that from usual BCS estimates. A high quality ferromagnet is obtained when a benzene solution of C_{60} is mixed with tetrakis – dimethylamino ethylene. (a strong electron donor)

9.2.1.2 Fullerenes films:

C_{60} & C_{70} both have low vapour pressure. Hence an easy deposition of fullerenes on metal is a thin film system. It can be used as surface capping system in nanoscale device. Tribology is an area where fullerenes can make a possible impact. Here ion – beam modified fullerenes can be used.

9.2.1.3 Other applications:

Many alkaline earth metal derivatives of fullerenes have been produced to obtain high quality superconductor. Some organic derivatives are also used. Recently, some higher fullerenes (C_{76}, C_{78}, C_{82}, C_{84}) have been prepared under same experimental condition.

9.2.2 Carbon nanotubes

Some tube like graphite structures have also been observed in time of fullerenes preperation. These concentric nanotubes of graphite is widely used for different purposes. Nanotubes shows a higher extent of conductivity, quite comparable to copper. On the other hand it has also a diamagnetic property with much involved temperature dependence.

Another important field is the stuffing of nanotube with metals. Heating of nanotubes with Pb_3O_4 results to lead stuffing and is believed to occur due to nano – capillarity. A lead filled carbon nanotubes might be an ideal nanowire, which might have favourable electronic property including superconductivity. Metal mixes with nanotubes has also the catalytic effects. It is proposed to be as heterogeneous catalyst in the catalytic hydrogenation process.

9.2.3 Carbon onions:

Onion consists of polyhedral graphite particles & appears to be like the form of concentric graphite sphere. Recently it has been observed that the thermal annealing of dispersed nanodiamonds also results in the formation of carbon onions.

9.3 Porous Silicon

Ever since the discovery of photoluminescence in an indirect band gap material like Si upon electrochemically etching a Si wafer as reported by Leigh Canham in 1990,[235] there has been a tremendous interest in the study of these electrochemically etched crystalline Si materials, called porous Silicon. These materials have been synthesized generally by treating the Si wafers in hydrochloric acid solutions as early as the fifties. Today porous Si is considered suitable for electronic applications as well as for opto-electronic applications. Inspite of all the advancements made to date, there is still ample controversy regarding the special properties that these materials render making this a challenging material for the scientists and engineers alike. These special properties are achieved due to the nanocrystalline structure produced by electrochemical etching process. The blue shift of the optical edge i.e. the enhancement of the band gap in these materials has been reported by various groups.

9.3.1 Preparation methods
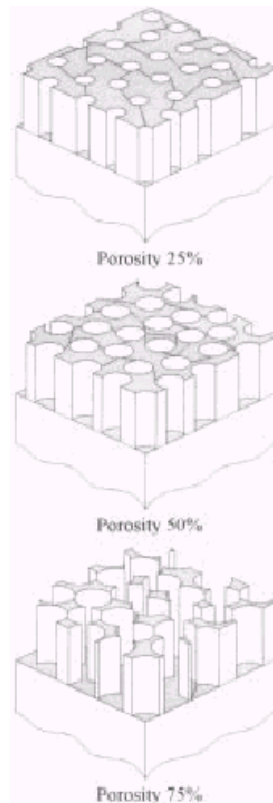
Figure: Ideal model of porous silicon structure with different porosity.

As already mentioned porous Si materials can be prepared by the electrochemical etching of crystalline Si wafers in the presence of hydrochloric acid.. The formation of porous Si materials is mainly done by means of electrochemical anodic treatment of Si wafers in aqueous or alcoholic electrolytes on the base of hydrofluoric acid of typical concentrations from 20 to 50.[236] In this case the Si is an anode and the current density passing through it (typically varies between 1-100mA/cm^2 for 1 to 60 minutes) should be less than certain critical value. This critical value is determined by concentration and viscosity of the electrolyte, geometry of anode as well as the physical properties of the Si electrolyte interphase. Dimensions and type of conductivity (n or p type) of the original Si substrate influences the characteristic crystallite dimensions and microstructure, thickness of the porous layer and some other parameters of the final material.

9.3.2 Electrical and optical properties of porous Silicon

9.3.2.1 Conductivity

The d.c. conductivity of 'ps' is proposed to be due to the following facts

- Excitation of charge carrier from deep traps associated with the defects of Si nanoparticles.
- The absorbed chemical species by ps may have influences on d.c. conductivity.
- Tunneling through the surface barrier layer.
- Space-charged limited current was also proposed

In contrast, the A.C. conductivity of ps stays almost constant for low frequency, faces a kink at higher frequency and finally become linear for the higher frequency

9.3.3 Photo Luminescence:

Existence of PL is explained on the basis of following models

- Those based on quantum confinement
- Nano-crystal surface states.
- Specific defects and molecules.
- Structurally disordered phases.

Some experimental evidences speak in favour of Si crystal phonons into the luminescence mechanism. On the other hand there is a variety of models where the surface center of Si nanocluster are suggested as luminescent sites.

9.3.4 Applications of porous Si

Applications of porous Si includes the following fields

- Opto electronic applications.
- Micro electronic applications.
- Sensors and actuators.
- Chemical sensors.
- Biological applications.

9.3.4.1 Optoelectronic applications

9.3.4.1.1 Light emitting diodes (LED):

The formation of electroluminiscent devices by ps was first proposed by Richter et.al.[237]. And later by Koyama and Kashida, using Au/ps/c-Si Schottky dyodes with rather low quantum efficency $10^{-5} – 10^{-4}$%. Subsequently, LEDs with porous p-n contact was introduced by Stiener et.al.[238]. Works in these field were motivated to obtain higher quantum efficiency as well as environmental stability. The environmental stability was improved using Au/(p^{+1}–n) PS/n^{-1} Si/Al. Lazarunk et.al.[239] reported the formation of very stable Al/ps LEDs using 'CVD' deposition of Si onto sapphire subtrates, formation of porous Si layer and Al-contacting pattern. Under reverse-biasing condition the diode emit white light, presumably due to the surface plasmons in oxide (Al_2o_3 or SiO_2) near the edges of Al metallization stripes where the maximum local electric field is concentrated. Tsybeskov et.al.[240] have performed a partial oxidation of ps material to stabilize the structure. The device has shown tunable EL yield in the visible spectra, high quantum efficiency (0.1%) at a working voltage 2V.

9.3.4.2 Photo detectors :

Photodetectors were formed of 3μm thick porous ilicon layer on p-Si (7-10 Ωcm) by depositing Al-film on top of ps and oxidizing the structure. When light reflected from rough PS surface its reflecting gets reduced. So PS is used as anti-reflecting coating for coating for p-n photocells. PS structure working as selectively absorptive filters is used to modify the sensitivity of photo-detectors. The photo-detector with integrated Febry-Perot filter was selectively sensitive to predetermined wave lengths while without it the special response was rather wide in the visible range of spectrum.

9.3.4.3 Photonic Crystal :

Photons propagates through periodic dielectrics in a like fashion as electron does in a periodic lattice structure and hence show eqivalent band structure. Such medium is known to be photonic crystal. Microporous Silicon is much suitable to construct 2-D photonic crystals with band gap in IR range. Perfect arrangement of micropores is achieved by a photolithographic masking of anodized n-Si.,

formation of regular pattern of Pyramidal grooves on top of Si and anodization by black-light illumination.

9.3.4.4 Wave Guides :

The refractive index of PS depends on the porosity. So it can be used to form planer optical waveguides integrated into Si crystal. The motive to construct the WG is to achieve low optical losses and has higher refractive index than the cladding region. The most popular mechanism of constructing such WG was that suggested by Bonderenko et. al.[241] The scheme involves the local anodization of p-Si regions and their conversion into oxide in multistage oxidation process. Loni et. al.[242,243] have developed WGs by forming a PS layer of varying porosity.

9.3.4.4.1 Optical Logic Gates :

PS has non-linear optical properties. Using free –standing PS films as active elements of all-optical integrated circuits optical logic gate can be constructed. A non-linear optical absorption allows to achieve 50% modulation of the intensity of secondary by subjecting the PS substance to irradiation by primary light beam. It is used to build logic inverters and NOR commutators. PS shows a saturation of absorption of monochromatic light by free standing PS films.Transperency of Laser light increases with time as a result of time dependent decrease of light absorption. This state of improved transparency is remembered by the sample for as long as one day in dark. The memory can be partially erased by illumination of transparent PS by a light with shorter wavelength. Reflectivity of freestanding porous silicon films was also found to experience certain memory effects.

9.3.4.4.2 Microelectronic Application :

9.3.4.4.2.1 Cold Cathodes :

The principal of cold cathode is based on the emission of electron from metallic or semiconducting surface. Si micro cathode is prepared by photolithography or by chemical etching and PS just enhance the stability and performance of this cathode. Use of PS also improves the uniformity of emission.

9.3.4.4.2.2 Isolation of IC. :

PS undergoes fast oxidation which is useful in dielectric isolation of transistors in Ics. The IPOS process includes basically two stages : a transformation of local regions of epitaxial Si film in PS and a treatment of substrate in oxidizing atmosphere.

9.3.4.4.3 Sensor and Actuators :

PS has highly developed surface with sensitivity in electrical, chemical and mechanical processes. These processes are useful to prepare sensors and actuator devices.

9.3.4.4.3.1 Micromachining :

Microelectromechanical systems (MEMs) are presently considered as the basis of further progress in many spheres of technology. The reason behind this wide application of PS is

i) Sensitivity or activity of PS depends on doping level of Si wafer. Activity of PS isthus controlled by local doping and subsequent anodization.

ii) PS is easily soluble in alkaline solution while monocrystalline Si remains stable.

iii) PS is much prone to be oxidized in oxygen containing atmosphere.

9.3.4.4.4 Chemical sensor :

Absorption of chemical species affects the A.C. or D.C. electrical conductivity of PS. Fabrication of sub-ppm- sensor for benzene using porous Silicon membrane permeated with Sn-V oxide has already been done.

9.3.4.4.5 Sensors involving photoluminescence quenching :

PL of Por Si in contact with various vapour phases and gases may change significantly thus opening the possibilities of optical sensing of chemical substances. It was found that if a freshly formed of PS film is exposed to humid atmosphere at room temperature, the PL effect increases. PS soaked with chemical reagents strongly alters its PL features. A very strong irreversible quenching effect is produced by absorption of organomines (C_1HgNH_2) at the surface of p-type porous silicon.

9.3.4.4.6 Biological Application:

PS in much more biologically active than ordinary Si. PS simulates a deposition of hyappatite (main bone tissue) at the surface of microporous layers. Nanocrystalline &

porous silicon is quite useful in cell cultures. It is observed experimentally that live cells are adherent & viable at the surface of PS without depositing special bio-compatiable coating (poly-lyrine) at the surfaces. A beautiful interferometric technique is recently being applied to test DNA, antibody & biotin/avidin system.

9.3.4.4.7 PS in Solar cell structures:

For the photovoltaic application, the most common interest of study is the resistivity & photo conductivity of PS. PS layers have abnormal high value of resistivity (10^6-10^7 rcm). While p-type Si wafers has significant photo-conductivity in visible range of spectrum, despite their high dark resistance. Por Si/Si structure has rectifying properties.
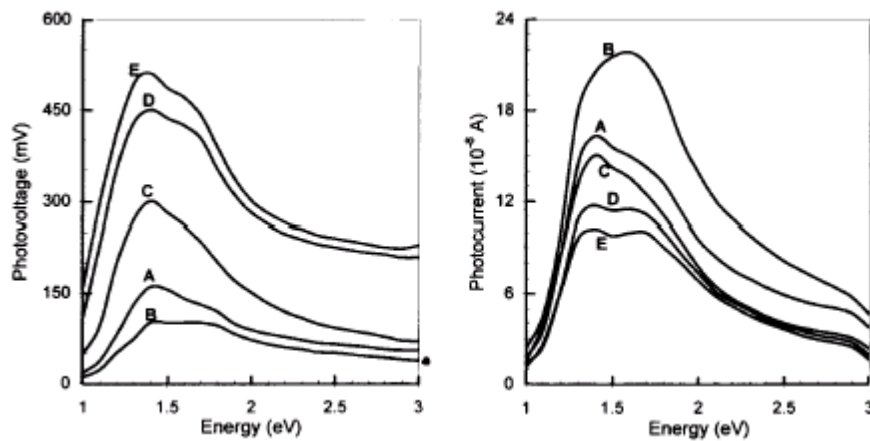
Fig. 14. Photovoltage and photocurrent spectra of different por-Si films. Film thickness (µm): **A**—5.6; **B**—9.1; **C**—16.3; **D**—24.7; **E**—30.0 (from Ref. [40]).

Figure. Photovoltage and photocurrent spectra of different por-Si films. Film thickness (m): A- 5.6, B- 9.1, C- 16.3, D- 24.7, and E- 30.0.[244]

Photovoltaic applications: PS is favoured for PV application for its certain properties.

i)   Highly texturized surface of PS enhances light trapping & reduces reflection losses.

ii)   Its wide bandgap may make it a candicate for window layer in a heterojunction cell.

iii)   PS can fairly be used for solar transformation fromUV to long wavelength range.

iv)   It surface properties & chemical activity can serve for effective impurity getting in silicon SC substrates,

v)   It is appealing for its easier technological formation & its electrochemical growth technology is largely adaptable for SC chip fabrication.

Use of por-Si in SC structure is made due to the following reasons:

i) Due to its high sp. Resistance there is always a limitation of effective carrier transport in a material volume.

ii) In SC high porosity PS layer is used, which has low mechanical strength, insufficient thermal conductivity, & high sensitivity to high temperature processing which in turn is related to the stability.
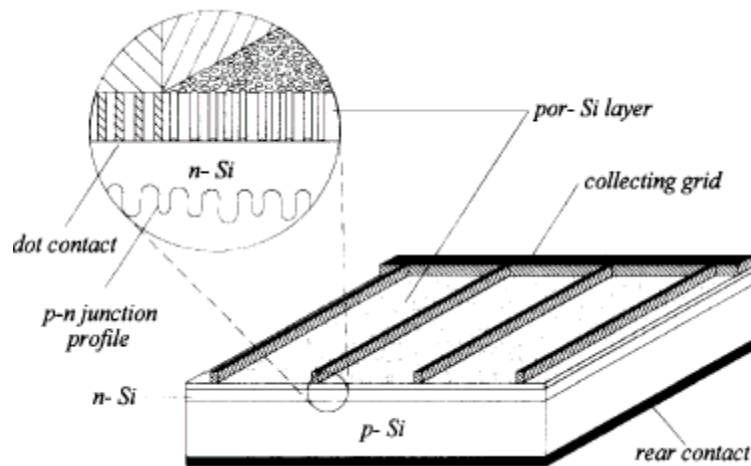

Figure: Typical solar cell structure with frontal porous silicon layer.

9.3.4.4.8 Por-Si/Si Hetero junction:

The expansion of por-Si bandgap due to quantum size efect, is interesting & from the point of view of hetero-junction Si-based SC creation. At that point can be used a simple electrochemical etching of a Si wafer. The whole idea can be divided into 3 parts :-

i) Use of a por-Si layer as the Si SC emitter.

ii) Creation of a tandem design SC with por-Si/n-Si/p-Si type structure.

iii) Por Si layer formation through diffusion p-n junction created in a substrate.

9.4 BIOLOGY & NANOMATERIALS

9.5 Biomimetics:

The use of biological principles in materials formation is an emerging field called biomimetics. Many multicellular organism produce hard tissues such as bones, teeth, shells etc.[245] which are biocomposites and include both structural macromolecules (lipids, proteins, and polysaccharides) and minerals (including hydronyapatite, calcium

carbonate and slica). Some single celled organisms also produce inorganic materials either intracellularly or extracellularly.[246]

Many species of bacteria and algae can produce small inorganic particles which may be oxides, sulphides, carbonates, or phosphates. These particle are ordered during assembly and have intricate architectures.[245,246] The particles may have a well defined shape formed within a certain size range and have orientational (if crystalline) and geometrical (even if non crystalline) symmetry. These structural features depend on the species concerned, and are though to originate in the macromolecules that control particle synthesis. For example, in Aquaspirillum magnetotacticum, a magnetotactic bacterium, small magnetite particles are formal within cytoplasmic vesicular compartments (magnetosomes) in ordered geometries,[247] and these particles are perfectly crystalline. These particles act as magnetic sensing devices that direct bacteria towards anaerobic sediments. Such observations make bacteria useful for manufacturing nanostructured thin films or particulate materials to support technological applications.

Materials produced by organisms have properties that are superior to those analogously synthetically manufactured materials with similar phase compositions. Organic macromolecules both collect and transfer raw materials and at the same time self-assemble uniformly and co-assemble subunits into short and long range ordered nuclei and substrates. The structures so formed are highly organized having intricate nanoarchitectures that ultimately make up a whole lot of different tissues.[248] They have unique properties in that they are simultaneously dynamic, self-healing and multifunctional, characteristics which are difficult to achieve in purely synthetic systems.[249] Therefore, biomimetics may be a possible path for realizing nanotechnology in the days to come.
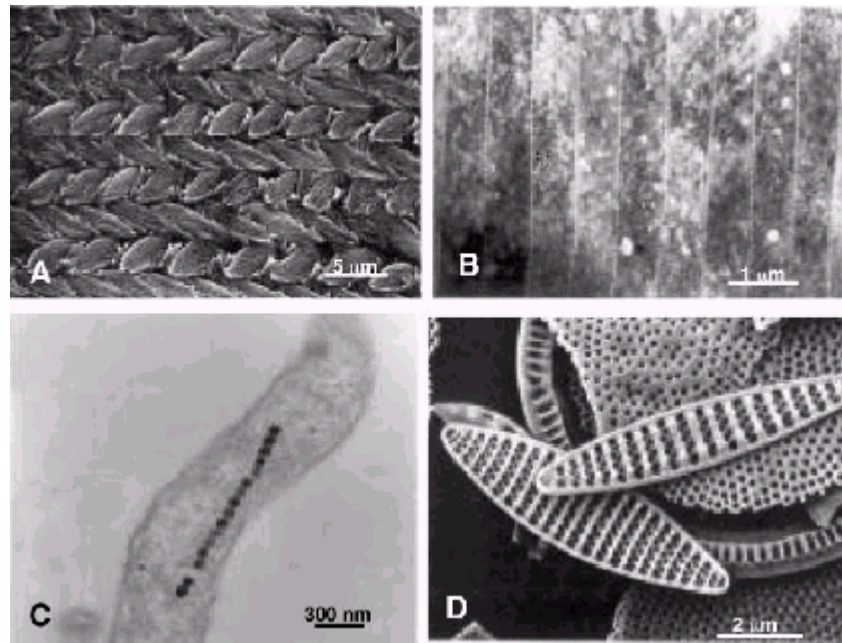
Figure: *(A)* This intricately architectured mouse incisor tooth has enamel rods. *(B)* Layered composite structure of nacre (mother-of-pearl) from *Nautilus pompelius* shell. *(C)* Magnetite particles *in Aquaspirillum magnetotacticu*m.(D) Siliceous skeletal structures in diatomaceous earth. Images in *A* and *D* were recorded by scanning electron microscopy, and *B* and *C* were recorded by transmission electron microscopy.[250]

9.6 Drug Delivery

A whole lot of work has been done to study the benefits of administering polymeric nano and microparticles for the purpose of drug delivery in the gastrointestinal tract (GIT). It has been found that the critical factors affecting particle uptake are the size and nature of the polymer concerned, zeta potential, vehicle, coating with lectins or other adhesion factors and presence of nutrients.[251,252,253,254,255,256] However no clearly defined parameters have yet been found to design the best carrier for oral administration of nanoparticles.

The part of the work on intestinal absorption of particulates has been done with polystyrene latex (PS) particles (sizes vary from 10 nm to > 20 nm). Since they are charged particles, they can be created easily with protein or adhesion factors.[253,254,255,257,258,259] Also, the presence of covalently bound fluorescent probes make PS particles a valuable tool to follow the fate of ingested particles. However, being non-biodegradable it cannot be used as an invivo drug carrier. Fluorescent nano

and microspheres are the most widely used tools to assess intestinal uptake. Since fluorescence allows better visualization of particles in tissue.

9.7 Utilization of DNA as construction material in nanotechnology:

Biological macromolecules, such as proteins and nuclei acids, may be used as building blocks for nano-structural systems. DNA is particularly suitable because of its unique properties:

1)   It has a large structural variety and carries a whole lot of information,[260]
2)   It shows a high degree of mechanical rigidity,[261]
3)   It is physicochemically stable.

Due to its above mentioned properties, DNA might be used in chip construction for circuits with sizes below 100 nm. The advantage of DNA technology in based on the precision of DNA biosynthesis and hybridization in matrix generation. The concept of DNA hybridization based self assembly of DNA derived gold colloids.[262,263,264] Efforts are on to understand such well defined arrangements of nanocrystal metal clusters (quantum dote) for new material properties as they may have actual applications in the field of laser technology in the near future.[265,266,267,268]

9.8 Medical applications

9.8.1 Hyperthermia:

There are several reports regarding the efficacy of hyperthermia for the treatment of musculoskeletal tumors.[269,270,271,272] Currently, the principal methods of hyperthermia for clinical use are microwaves or radiofrequency waves to generate heat in the tumor. Using these methods, however, it is difficult to heat deeply seated tumors effectively and selectively.[273] New types of ferromagnetic thermoseeds are being developed experimentally to solve this problem, but they have never been used clinically because of their unreliable rise in temperature. Application of magnetic materials for hyperthermia of biological tissue with the goal of tumour therapy is known in principle for more than four decades. Many empirical work was done in order to manifest a

therapeutic effect on several types of tumours by performing experiments with animals or using cancerous cell cultures. However, routine medical applications are not known till now and there is demand for more profound understanding of the related materials properties to render that method reliably for tumour therapy of human beings. The heating of oxide magnetic materials with low electrical conductivity in an external alternating magnetic field is due to loss processes during the reorientation of the magnetization. If thermal energy k_BT is too low to facilitate reorientation, hysteresis losses dominate which depend on the type of remagnetization process (wall displacement or several types of rotational processes). With decreasing particle size thermal activation of reorientation processes lead in dependence on temperature and measurement frequency to superparamagnetic behaviour of the particle ensemble and the occurrence of the so- called Néel-losses.[274] In the case of ferrofluids losses related to the rotational Brownian motion of magnetic particles may arise, too, and hence care should be taken to analyse the results, depending on the temperature and measurement frequency.
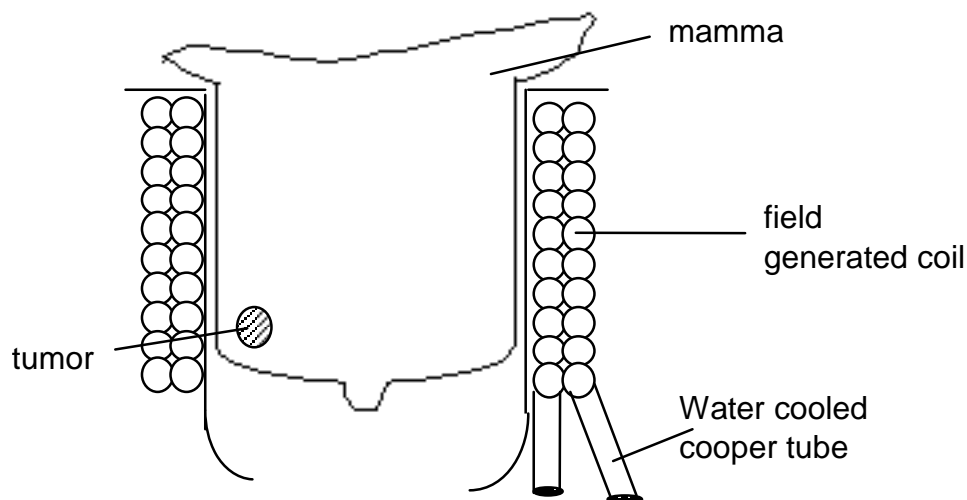
Fig: Scheme of localized magnetic hyperthermia applied a breast carcinoma. The tumor region contains injected magnetic particles.
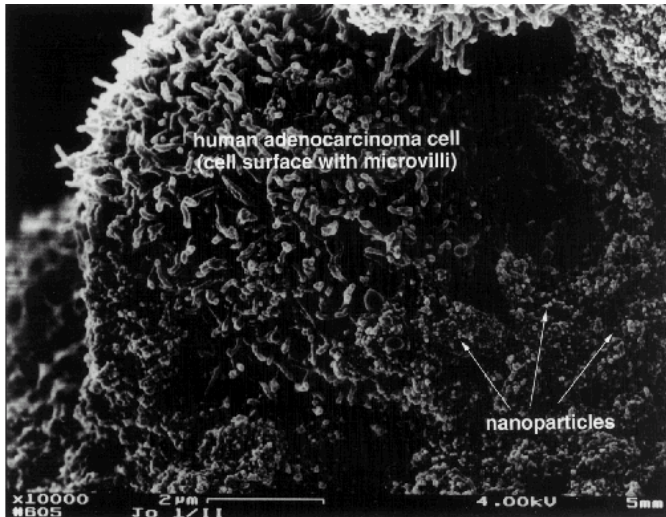
Fig. Scanning electron micrograph of a colon adenocarcinoma cell, which has been grown in a ferrofluid containing growth medium (modified aminosilane shell magnetite, core diameter around 10 nm, 0.6 mg/ml) for 72 h. Note, that the particles are highly adhesive to the surface of the cell, which was not or far less observed with normal cells.[275]

9.8.2 Ocular:

The inter segment of eye is bounded by cornea and lens – iris diaphragm, and contains the aqueous humor. The position segment begins behind the lens – iris diaphragm and includes, from inside outwards the vitreous (gel / fluid), retina (neurosensory tissue), and choroid (heavily muscular). The retinal photoreceptors are supported by the choroid. The retina and the choroid stay attached to each other with a suction pump, which keeps the sub retina space dry.
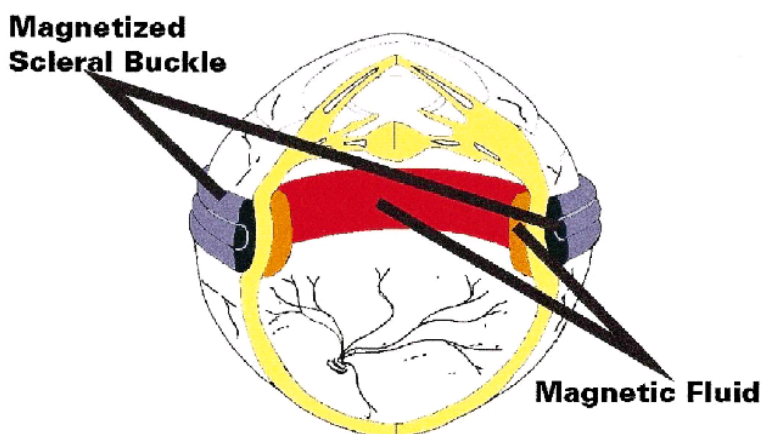
Fig: Internal tamponade using silicone magnetic fluids- magnetic fluid for use in eye surgery.[276]

Retinal detachment is a major cause of vision loss in adults. It occurs when the retina separates from the choroid, resulting in eventual death of the retina and subsequent loss of vision. As one ages, the vitreous gel normally undergoes liquefaction, collapse and separation from the retina. Separation of the vitreous gel may result in the formation of a tear in the retina at a site of vitreoretinal adhesion. The tear provides a pathway for vitreous fluid to pass through and underneath the retina, overcoming the suction attraction of the retina to the choroid, thus detaching the retina from the under lying choroid.

The goal of surgery is to close the holes in the retina, preventing further fluid flow into the subretinal space, allowing for reattachment of the retina. Efforts are going on to develop an internal tamponade from modified silicon fluid containing spherically stabilized 4 – 10 nm sized metal particles, which will be held in place with an external magnetized scleral buckle. With an appropriate magnetic fluid inside the vitreous cavity, a stable, 360° internal tamponade might be achieved. The enriching magnetized spherical buckle and magnetic fluid would produce a ring of silicon oil in opposition to the retinal periphery. The central vitreous cavity would be free of the magnetic fluid and the lens, anterior dumber structures, or macula, thus avoiding the complications of currently available treatment modalities.

9.9 Health hazards of nano-particles

Due to the fine structure of nanoparticles care need to be taken in handling because unwanted absorption through nasal tracks on to the mucous membrane may cause medical anomalies. On top of this, it has been found that nanoparticles can be more toxic compared to their bulk counterparts. For example, carbon or TiO_2 which are biologically inert and considered nontoxic develop toxicity as the particle sizes decrease to less than 50nm. Due to their fine sizes successful clearance of particles absorbed in the lung is difficult, since the macrophages that are present in the lung engulf them, minimizing the probability of their extraction through the epithelial tissue. In the process, the macrophages release minimum amount of inflammatory mediators and move to the mucociliary escalator leaving the lung with their particle burden. If anything disturbs these chain of events, interstitialization occurs. Interstitialization is an adverse outcome since the interstitial particles cannot now be cleared via the normal pathways and thus either remain in the interstitium where they can chronologically stimulate cells or move on to the lymph nodes. The events, which may lead to failed clearance, are:

particle mediated macrophage toxicity,

Overload.

Overload occurs when large numbers of respirable particles (nanometre particles) owing to their small size and hence large surface area deposit in the lungs following exposure to high airborne mass concentrations. What happens is that macrophages engulf large volumes of particles which interfere with their clearance functions and ultimately are unable to adequately phagocytose or transport the large number of particles which have deposited on the surface on the surface of the peripheral lung. These exposed particles interact with epithelial cells and eventually move through the epithelium and deposit in the interstitium. The interstitium includes a portion of the connective tissue of the blood vessels and air sacs and forms the membrane where gas exchange occurs. Besides this, many pathogenic particles appear to have the ability to cause direct oxidative stress and injury, e.g. asbestos, quartz and coal mine dust, on the macrophages that phagocytose the nanometre particles and on the epithelial cells in contact with non-phagocytosed particles. If this kind of continued exposure to nanometre particles occurs then it may result in inflammation, increased epithelial permeability, proliferation and retardation of clearance, and hence lead to fibrosis and cancer in the long term.
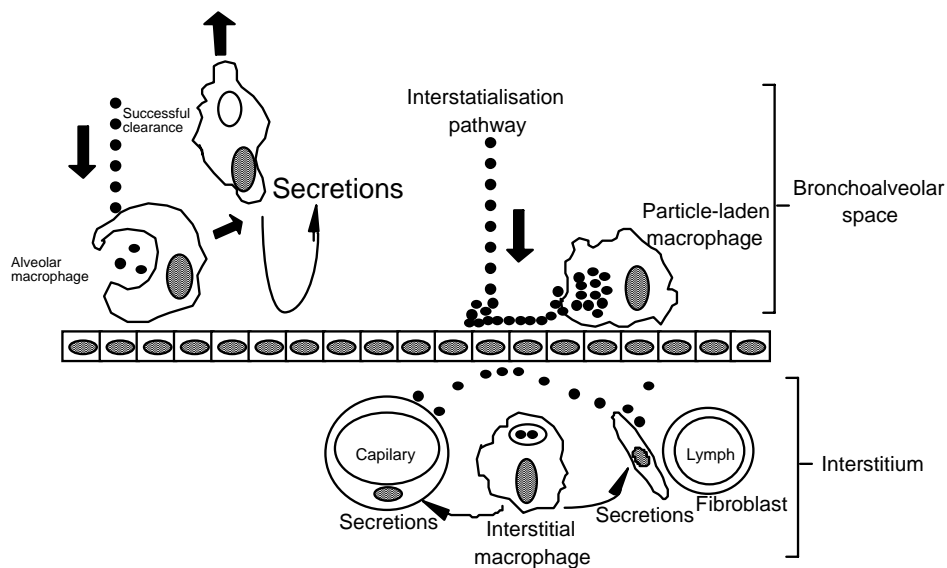
Figure: Comparison of the fate of particles that are cleared by the normal pathway (left) and those that enter the intestinal compartment of the lung (right).

[1] N. Taniguchi, 1974, "On the basic concept of nanotechnology", Proc. Int. Conf. Prod. Eng., Tokyo, Part 2 (Tokyo: JSPE) pp. 18-23.

[2] M. Faraday, Philos. Trans. Roy. Soc. (London) **147** (1857) 145.

[3] M.N. Rittner, T. Abraham, Am. Cer. Soc. Bull. **76** (1997) 51.

[4] R. Kubo, J. Phys. Soc. Jpn. **17** (1962) 975.

[5] C.G. Granqvist, R.A. Buhrman, J. Appl. Phys. **47** (1976) 2200.

[6] M. Jose-Yacaman, L. Rendon, J. Arenas, M.C.S. Puche, Science **273** (1996) 223.

[7] Siegel, R.W. 1994. Nanophase materials. In Encyclopedia of applied physics, Vol. 11, G.L. Trigg, ed. Weinheim: VCH, pp. 1-27.

[8] J. Dutta, I.M. Reaney, P.R.I. Cabarrocas and H. Hofmann, Nanostructured Mater. 6 (1995) 843.

[9] H. Konrad, J. Weissmüller, J. Hempelmann, Birringer, R., Karmonik, C. and Gleiter, H., Phys. Rev. B58 (1998) 2142.

[10] H. Gleiter Acta mater. 48 (2000) 1-29.

[11] H. Gleiter, Nanostructured Mater. 6 (1995) 3.

[12] adapted from WTEC Panel on 'nanostructure science & technology- a worldwide study',1999, http://itri.loyola.edu/, pg. XX

[13] www.cabot-corp.com

[14] www.degussa.com

[15] www2.powercom.net

[16] www.amcol.com

[17] www.laporteplc.com

[18] www.rtpcompany.com

[19] www.dow.com

[20] www.ube-ind.co.jp

[21] www.unitika.co.jp

[22] www.principiaconsulting.com

[23] www.mercorp.com

[24] www.elan.ie

[25] www.qdots.com

[26] http://www.solaronix.ch/

[27] www.ferx.com

[28] www.nanophase.com

[29] www.basf-ag.de

[30] www.schering-plough.com

[31] www.altairtechnologies.com

[32] www.nanopowderenterprises.com

[33] www.shonstromresearch.com

[34] W. Oswald, The World of Negected Dimensions; Dresden, 1915.

[35] G. Schmid, Endeavour New Series 14 (1990) 172.

[36] G. Jimbo, Proc. 2nd. World Congress on Particle Technology, (1990)19-22, September 1990, Kyoto, Japan.

[37] O. Preining, Pure & Appl. Chem. 64 (1992) 1679.

[38] K. Kamiya & S. Sakka, Gypsum Lime, 163 (1979)23.

[39] V. Paillard, P. Melinon, J. P. Perez, V. Dupuis, A. Perez and B. Champagnon 1993 Phys. Rev. Lett. 71 4170

[40] P. Melinon, V. Paillard, V. Dupuis, A. Perez, P. Jensen, A. Hoareau, M. Broyer, J.-L. Vialle, M. Pellarin, B. Baguenard and J. Lerme, Int. J. Mod. Phys. **B 9** (1995) 339

[41] H. Haberland, M. Moseler, Y. Qiang, O. Rattunde, T. Reiners and Y. Thurner, Surf. Rev. Lett. **3** (1993) 887

[42] J .-L. Rousset, A.M. Cadrot, F. J. Cadette Santos Aires, A. Renouprez, P. Melinon, A. Perez, M. Pellarin, J.-L. Vialle and M. Broyer, J. Chem. Phys. **102** (1995) 8574

[43] P. Pawlow, Z. Phys. Chem. 65, 1 (1909).

[44] P. R. Couchman and W. A. Jesser, Nature (London) 269 481 (1977); K. Hoshino and S. A. Shimamura, Philos. Mag. A 40, 137 (1979); J. Ross and R. P. Andres, Surf. Sci. 106, 11 (1981).

[45] T. L. Beck, J. Jellinek, and R. S. Berry, J. Chem. Phys. 87,545 (1987); D. J. Wales and R. S. Berry, J. Chem. Phys. 92, 4473(1990); P. Labastie and R. L. Whetten, Phys. Rev. Lett. 65, 1567(1990).

[46] A. Maiti and L. M. Falicov, Phys. Rev. A 45, 6918 (1992).

[47] S. Valkealahti and M. Manninen, Z. Phys. **D 26**, (1993) 255.

[48] F. Ercolessi, W. Andreoni, and E. Tosatti, Phys. Rev. Lett. **66**, (1991) 911; I. L. Garzon and J. Jellinek, Z. Phys. **D 20** (1991) 235.

[49] Z. X. Cai, S. D. Mahanti, A. Antonelli, S. N. Khanna, and P. Jena, Phys. Rev. **B 46** (1992)7841

[50] H. S. Lim, C. K. Ong, and F. Ercolessi, Z. Phys. **D 26** (1993) S45.

[51] M. Zhang, M. Yu Efrenov, F. Schiettekatte, E.A. Olson, A.T. Kwan. S.L. Lai, T. Wisleder, J.E. Greene and L.H. Allen, Phys. Rev. **B62** (2000)10548.

[52] Z. B. Güvenç and J. Jellinek, Z. Phys. **D 26** (1993) 304

[53] H. Reiss, P. Mirabel, and R. L. Whetten, J. Phys. Chem. **9**2, 7241 (1988); P. R. Couchman and W. A. Jesser, Nature (London) **26**9, 481 (1977); V. P. Skripov, V. P. Koverda, and V. N. Skokov, Phys. Status Solidi A **6**6, 109 (1981); R. R. Vanfleet and J. M. Mochel, Surf. Sci. **34**1,40 (1995)

[54] R. Defay and I. Prigogine, *Surface Tension and Adsorption,* Wiley, New York, (1951), English translation, 1966.

[55] K. F. Peters, J. B. Cohen, and Y.-W. Chung, Phys. Rev. B **57**,13 430 (1998)

[56] Ph. Buffat and J.-P. Borel, Phys. Rev. **A 13** (1976) 2287.

[57] A.N. Goldstein, C.M. Echer and A.P. Alivisatos, Science 256 (1992) 1425.

[58] A.A. Shvartsburg and M.F. Jarrold, Phys. Rev. Lett, 85 (200) 2530.

[59] Z. Y. Lu, C. Z. Wang, and K. M. Ho, Phys. Rev. B 61, 2329 (2000).

[60] J.R. Shambles, L.M. Skinner and N.D. Lisgarten, Proc. R. Soc. Lond A 318 (1970) 507.

[61] V.A. Spitsyn, R.A. Isakova and S.M. Kozhakhmetov, J. Appl. Chem. USSR (engl. Trans.) 49 (1976) 1093.

[62] C. Solliard and M. Flueli, Surf. Sci. 156 (1985) 487.

[63] J.A. Stroscio, D.M. Eigler, Science 254 (1991) 1319; D.M. Eigler, C.P. Lutz, W.E. Rudge, Nature 352 (1991) 600; S. Hosoki, S. Hosaka, T. Hasegawa, Sppl. Surf. Sci. 60:61 (1992); 643; A. Kobayashi, F. Grey, R.S. Williams, M. Aono, Science 259(1993) 1724; T.T. Tsong, C.S. Chang, Jpn. J. Appl. Phys. 34 (1995) 3309.

[64] A detailed review of milling processes can be found in: C. Suryanarayana, Progress in Materials Science, **46** (2001) 1.

[65] R.M. Mehra; V. Agarwal; P.C. Mathur, Solid State Phenomena, **55** (1997) 71

[66] eg. C.B. Murray, C.R. Kagan & M. G. Bawendi, Annu. Rev. Mater. Sci.. 30 (2000) 545

[67] C.J. Brinker and G.W. Scherer, 'Sol-gel Science' (Academic Press, San Diego 1990), pg. 21.

[68] B.I. Lee and E.J.A. Pope, 'Chemical Processing of Ceramics', (Marcel Dekker Inc., 1994) pg. 3

[69] H. Itoh, S. Utamapanya, J. V. Stark, K. J. Klaubunde, J. R. Schlup, Chem. Mater. 5 (1993), 71.

[70] A. Celikkaya and M. Akinc, J. Am. Ceram. Soc. 73 (1990) 2360.

[71] A. Celikkaya and M. Akinc, J. Am. Ceram. Soc. 73 (1990) 245.

[72] R. Vacassy, S. M. Scholz, J. Dutta, J. Lemaitre, C. Plummer, and H. Hofmann, J AM CERAM SOC 81: (1998) 2699.

[73] Courtesy, Herbert Hofmeister (Max-Planck Institute)

[74] I. Schoonman, Solid State Ionics, 135 (2000) 5.

[75]   www.besoptics.com/html/corning_fused_silica.html; www.corning.com/semiconductormaterials/hpfs_main.html

[76] www.schottglasstech.com/silica.htm

[77] F. L. Yuan, C.H. Chen, E.M. Kelder, J. Schoonman, Solid State Ionics 109 (1988) 119.

[78] mesun4.wustl.edu/ME/lacer/nano.html

[79] R. Birringer, H. Gleiter, H.P. Klein and P. Marquart, Phys. Lett. 102A (1984) 365.

[80] www.nanophase.com

[81] C. Hollenstein, J.-L. Dorier, J. Dutta, L. Sansonnes, A.A. Howling, Plasma Sources Sci. Technol. **3** (1994) 278.

[82] H. Hahn and A.S. Averback, J. Mater. Res. **67** (1990) 113

[83] V. Hans and R. Birringer, Nanostructured Mater. **1** (1992) 491.

[84] D. Vollath and K.E. Sickafus, Nanostructured Mater. **1** (1992) 427.

[85] Following, J. Dutta, H. Hofmann, R. Houriet, H. Hofmeister and Ch. Hollenstein, Colloid Surface **A 127** (1997) 263.

[86] T. Venkatesan and S. Green, Industrial Physicist **2** (1996) 22.

[87] T. Yamamoto and J. Mazumdar, Nanostrucred Mater. **7** (1996) 305.

[88] R. Houriet, R. Vacassy, H. Hofmann, Nanostr. Mater. **11**, 1155 (1999); R. Houriet, R. Vacassy, H. Hofmann, W. Vogel, Mater. Res. Soc. Symp. Proc., **526**, (1998) 117.

[89] Laser Ablation and Desorption, edited by J.C. Millerand R.F. Haglund, Jr., Academic Press, New York (1998).

[90] S. Li, S.J. Silvers, M.S. El-Shall, J. Phys. B, **101**, (1997) 1794

[91] R. Houriet, R. Vacassy, H. Hofmann, W. Vogel, Mater. Res. Soc. Symp. Proc., **526**, 117 (1998).

[92] R. Houriet, R. Vacassy, H. Hofmann, Nanostr. Mater. **11**, 1155-1163 (1999)

[93] R. Vacassy, R. Houriet, C.J.G. Plummer, J. Dutta, H. Hofmann, Mat. Res. Soc. Symp. Proc., **501** (1998) 41

[94] J. Dutta, J. Perrin, T. Emeraud, J-M. Laurent and A. Smith, J. Mater. Sci. **30** (1995) 53.

[95] H.-L. Tasi; J.-L. Schindler; C. R. Kannewurf; M. G. Kanatzidis, Chem. Mater. **9** (1997) 875.

[96] L. F. Nazar, Z. Zhang, D. J. Zinkweg, Am. Chem. Soc., **114** (1992) 6239.

[97] J. K. Vassilion; R.P. Ziebarth, F. Disalvo, J. Chem. Mater. **2** (1990) 738.

[98] L. L. Beecroft, C.K. Ober, Chem. Mater. **9** (1999) 1302

[99] G. Cao, M.E. Garcia, M. Aleala, L.F. Burgess, T.E. Mallouk, J. Am. Chem. Soc. **114** (1992) 7574.

[100] R.H. Brill, D. Whitehouse, The Thomas Panel, J. Glass Studies, **30** (1988) 34.

[101] M. Copel, M.C. Reuter, E. Kaxiras, R.M. Tromp, Phys. Rev.Lett. 63 (1989) 632.

[102] I-S Hwang, T-C Chang, T.T. Tsong, Phys. Rev. Lett. 80 (1998) 4229.

[103] D. H. Napper, Polymeric stabilization of colloidal dispersions; Academic Press; London, 1983.

[104] C.S. Hirtzel, R. Rajagopalan, Colloidal Phemonena: Advanced Topics, 1985, pp. 27.

[105] J.D. Aiken III, Y. Lin, R.G. Finke, J. Mol. Catal. A: Chem. 114 1996 29–51.

[106] J. T. G. Overbeek, Colloidal dispersions; Royal Society of Chemistry; London, 1981.

[107] R.J. Hunter, Foundations of Colloid Science, Vol. 1, Oxford Univ. Press, New York, 1987.

[108] P. C. Hiemenz, Principles of Colloid and Surface Chemistry; Marcel Dekker Inc.; New York, 1986.

[109] D. Myers, Surfaces, Interfaces and Colloids; VCH publishers, Inc.; Weinheim, 1991.

[110] F.T Hesselink, A.Vrij, J.T.G. Overbeek, J. Phys. Chem. **75** (1971) 2094.

[111] D.J. Meier, J. Phys. Chem. **71** (1967) 1861.

[112] P.J. Flory, W.R. Krigbaum, J. Chem. Phys. **18** (1950)1086.

[113] P.-G. De Gennes, Rep. Prog. Phys. **32** (1969) 187

[114] F. R. Eirich, J. Coll. Int. Sci. **58** (1977) 423.

[115] A. J. Silberberg, J. Chem. Phys. **46** (1967) 1105.

[116] G. Steinberg, J. Phys. Chem. **71** (1967) 292.

[117] T. F. Tadros, Polymer J. **23** (1991) 683.

[118] G. J. Fleer, M. A. Cohen-Stuart, J. M. H. Scheutjens, T. Cosgrove and B. Vincent, Polymers at interface; Chapman & Hall; London, 1993.

[119] D. A. Guzonas, D. Boils, C. P. Tripp, M. L. Hair, Macromolecules **25** (1992) 2434.

[120] J. R. Dorgan, M. Stamm, C. Toprakcioglu, R. Jérôme, L. Fetters, Macromolecules **26** (1993) 5321.

[121] J.-F. Argillier and M. Tirrell, Theor. Chim. Acta, **82** (1992) 343.

[122] P. E. Laibinis, D. L. Allara, Y.-T. Tao, G. M. Whitesides, A. N. Parikh, R. G. Nuzzo, J. Am. Chem. Soc. **113** (1991) 7152.

[123] L. Bertilsson and B. Liedberg, Langmuir, **9** (1993) 141.

[124] D. E. Weisshaar, B. D. Lamp and M. D. Porter, J. Am. Chem. Soc. **114** (1992) 5860.

[125] J. B. Schlenoff, J. R. Dhaia, H. Xu, L. Q. Wen and L. Ming, Macromolecules, **28** (1995) 4290.

[126] J. M. Stouffer and T. J. McCarthy, Macromolecules, **21** (1988)1204.

[127] E. Killman, J. Eisenlauer and M. Korn, J. Polym. Sci., Polym. Symp. **61** (1977) 413.

[128] P.-G. de Gennes, Macromolecules, **13** (1980) 1069.

[129] H. Hirai, Y. Nasako and N. Toshima, J. Macromol. Sci.-Chem., **A13** (1979) 727.

[130] Y. Wang, H. Liu, Polym. Bull. **25** (1991) 139.

[131] A. M. Lyons, M. J. Vasile, E. M. Pearce and J. V. Waszczak, Macromolecules **21** (1988) 3125.

[132] P.-A. Brugger, P. Cuendet and M.Grätzel, J. Am. Chem. Soc. **103** (1981) 2923.

[133] L. Longenberger, S. Thornton and G. Mills, Polym. Mater. Sci. Eng. **73** (1995) 164.

[134] M. S. Kunz, K. R. Shull and A. J. Kellogh, J. Colloid Int. Sci. **156** (1993) 240.

[135] M. S. Kunz, K. R. Shull and A. J. Kellogh, J. Polym. Sci. Polym. Phys. **33** (1995) 1417.

[136] Y. Yuan, I Cabano and J. K. Fendler, Macromolecules **23** (1990) 3198.

[137] M. E. Wozniak and A. Sen, Chem. Mater. **4** (1992) 753.

[138] J. J. Watkins and T. J. Mc Carthy, Chem. Mater. **7** (1995) 1991.

[139] R. Gangopadhyay and A. De, Chem. Mater. **2000,** *12,* 608

[140] J. Zhao, L.C. Stearns, M.P. Harmer, H.M. Chan, G.A. Miller, and R.E. Cook, J. Am. Ceram. Soc. **76** (1993) 503

[141] K. Niihara, J. Ceram. Soc. Jpn*.,* **99** (1991) 974

[142] K. Niihara and A. Nakahira, In *Proc. 3rd, Int. Symp. on Ceramic materials and Components for Engines,* ed. V. J. Tennery. Westerville Ohilo, 1998, pg. 919

[143] K. Niihara, A. Nakahira, G. Sasaki, and M. Hirabayashi, MRS Int. Mtg on Adv. Mater, **4** (1989) 129

[144] K. Niihara, A. Nakahira, and M. Inoue, *Mater. Res. Soc. Symp. Proc.,* **271** (1992) 589

[145] K. Niihara and A. Nakahira, *Ann. Chim. Fr.,***16** (1991) 479

[146] K. Niihara and A. Nakahira, In *Advanced Structural Inorganic Composites,* ed. P. Vincenzini. Elsevier Applied Science, 1991, pg. 637

[147] K. Niihara and A. Nakahira, *SiC-Al2O3 composite sintered bodies and method of producing the same.* European Patent, EP 0 311 289 Bl, 27 Jan, 1993

[148] A. Niihara and K. Nakahira, *J. Ceram. Soc. Jpn,* **100** (1992) 448

[149] C.E. Borsa, S. Jiao, R.I. Todd and R.J. Brook, J. Microscopy **177** (1994) 305

[150] R. W. Davidge, R.J. Brooks, F. Cambier, M. Poorteman, A. Leriche, D. O'Sullivan, S. Hampshire and T. Kennedy, J. Eur. Ceram. Soc. **16** (1996) 799

[151] C. S. Smith, Trans Metall. Soc*., AIME,* **175** (1949) 15

[152] L. Carroll, M. Sternitzke and B. Derby, Acta Metall. Mater. **44** (1996) 4543

[153] J. Fang, H. M. Chan, and M. P. Harmer, Mater. Sci. Engng, **A195** (1995) 163

[154] B. Lawn, *Fracture of Brittle Solids.* Cambridge University Press, Cambridge, 1993.

[155] R. W. Davidge and T. J. Green, J. Mater. Sci., **3** (1968) 629

[156] K. T. Faber and A. G. Evans, Acta Metall., **31** (1983) 565.

[157] S. Jiao, M.L. Jenkins, and R. W. Davidge, Acta Metall. Mater., **45** (1997)149

[158] C.N. Walker, C.E. Borsa, R. I. Todd, R.W. Davidge and R. J. Brook, Br. Ceram. Proc., **53** (1994) 249

[159] J. Selsing, J. Am. Ceram. Soc., **44** (1961) 419

[160] M. Taya, S. Hayashi, A. S. Kobayashi and H. S. Yoon, J. Am. Ceram. Soc., **73** (1990) 1382

[161] I. Levin, W. D. Kaplan, D. G. Brandon and A.A. Layyous, J. Am. Ceram. Soc., **78** (1995) 254

[162] C. Kittel, Introduction to Solid State Physics, Edition Wiley, 1986.

[163] G. Mie, Ann. Physics, **25** (1908) 377

[164] D. Stroud, Phys. Rev. **B 12** (1975) 3368.

[165] P. B. Johnson and R.W. Christy, Phys. Rev. **B 11** (1975) 1315

[166] H. Rawson, Phys. and Chem. of Glasses, **6** (1965) 81.

[167] Dr. Lionel Lemaire, Thesis entitled: 'Coloration d'une zircone yttriée par des nanoparticules de cuivre métallique', Ecole Polytechnique Fédérale de Lausanne Thesis no. **1843** (1998).

[168] M. P. Andrews, M. G. Kuzyk, Polym. Prep. **32** (1991) 105.

[169] D. F. Eaton, G. R. Meredith and J. S. Miller, Adv. Mater. **24** (1991) 133.

[170] A. Henglein and Ber. Bunsenges. Phys. Chem. **99** (1995) 903.

[171] D. Richard, Ph. Roussignol and Chr. Flytzanis, Optics letters **10** (1985) 511

[172] H. Cao, J. Y. Xu, E. W. Seelig and R.P.H. Chang, Appl. Phys. Letts. **76** (2000) 2997

[173] W. A. de Heer, Rev. Mod. Phys. **65**, 611 (1993).

[174] V. Dupuis, J. P. Perez, J. Tuaillon, V. Pillard, P. Melinon, G. Guiraud, J. P. Dupin, A. Perez, L. Thomas, B. Barbara, B. Bouchet, Scripta Metallurgica et Materialia **33**, 1563 (1995).

[175] W. D. Knight, R. Monot, E. R. Dietz and A. R. George, Phys. Rev. Lett. **40**, 1324 (1978).

[176] I. Billas, Thesis No. 1415, Ecole Polytechnique Fédérale de Lausanne, Switzerland (1995).

[177] W. A. de Heer et. Al. Phys. Rev. Lett. **71** (1993) 4067.

[178] D. C. Douglass, A. J. Cox, J. P. Bucher, and L. A. Bloomfield, Phys. Rev. **B47**, 12874 (1993).

[179] W. A. de Heer et al. Science **265** (1994)1682.

[180] M. Pellarin, B. Baguenard, J. L. Vialle, J. Lermé, M. Boyer, J. Millar and A. Perez, Chem. Phys. Lett. **217**, 349 (1994).

[181] A. J. Cox, J. G. Louderback, S. E. Apsel, L. A. Bloomfield, Phys. Rev. **B49**, 12295 (1994).

[182] Z. Jibin and L. Yongping, IEEE Trans. Magn. **28** (1992) 3367.

[183] G. Binasch, P. Grünberg, F. Saurenbach & W. Zinn, Phys. Rev. **B 39** (1989) 4828.

[184] W. Folkerts, J. C. S. Kods, T. G. S. M. Rijks, R. Coehoorn, M. C. de Nooijer, G. J. H. Somers, J. J. M. Ruigrok & L. Postma, IEEE Trans. Magn. **30** (1994) 3813

[185] B. Dieny, V. S. Speriosu, B. A. Gurney, S. S. P. Parkin, D. R. Wilhoit, K. P. Roche, S. Metin, D. T. Peterson & S. Nadimi, J. Magn. Magn. Mater, **93** (1991) 101

[186] B. Dieny, V. S. Speriosu, S. S. P Parkin, B. A. Gurney, D. R. Wilhoit & D. Mauri, Phys. Rev **B 43** (1991) 1297.

[187] N. Mott. Proc. R. Soc, **156** (1936) 368.

[188] Th. G. S. M. Rijks, Layered thin film for sensor applications: magnetoresistance & magnetic interactions, PhD thesis, Eindhoven University of Technology (1996).

[189] Th. G. S. M. Rijks, R. Coehoorn & W. J. M. de Jonge, In magnetic Ultrathin films, eds. B. T. Jonker et al., MRS Symposia Proceedings No.313 (1993) MRS, Pittsburg, pg. 283.

[190] J.C.S. Kools, Th. G. S. M. Rijks, A. E. M. de Veirman & R. Coehoorn, IEEE Trans. Magn. **31** (1995) 3918.

[191] Grabert, H., and M.H. Devoret. 1992. Single Charge Tunneling, Plenum Press, New York and London

[192] Jasprit Singh, 1994, Semiconductor Devices: An Introduction, McGraw-Hill, New York

[193] Marquardt, P.;Börngen, L.;Nimtz, G.;Gleiter, R.;Sonneberger, R., Zhu, J., Phys. Lett. 1986, 114 , 39.

[194] Henglein, A., Chem. Rev. 1989, 89 , 1861.

[195] G. Schön, G., Simon, U., Colloid Polym. Sci. 1995, 273 , 101.

[196] Weller, H., Eychmüller, A. Semiconductor Nanoclusters; Elsevier Science; Amsterdam, 1996.

[197] Weller, H., Adv. Mater. 1993, 5 , 2, 88.

[198] G. Schön, G., Simon, U., Colloid Polym. Sci. 1995, 273 , 202.

[199] U. Simon, U.;Schön, G., Schmid, G., Angew. Chem. Int. Ed. Engl. 1993, 232 , 250.

[200] Weller, H., Angew. Chem. Int. Ed. Engl. 1993, 32 , 41.

[201] Schmid, G., Chem. Rev. 1992, 92 , 1709.

[202] Schmid, G.;Pfeil, R.;Boese, R.;Bandermann, F.;Mayer, S.;Calis, G. H. M., Van der Velden, J. W. A., Chem. Ber. 1981, 114 , 3634.

[203] Henglein, A., Top. Curr. Chem. 1988, 143 , 113.

[204] Lewis, L. N., Chem. Rev. 1993, 93 , 2693.

[205] Alivisatos, A. P., J. Phys. Chem. 1996, 100 , 13226.

[206] Alivisatos, A. P., M.R.S. Bull. 1998, 23 , 2, 18.

[207] Creighton, J. A., J. Chem. Soc. Faraday. Trans. 1991, 32 , 2, 250.

[208] Kreibig, U., Vollmer, M. Optical properties of metal clusters; 1995.

[209] Brus, L., Phys. Chem. 1986, 90 , 2555.

[210] Schmid, G. Clusters and colloids; VCH Publishers; Weinheim, 1994.

[211] Kerker, M. The Scattering of Light and Other Electromagnetic Radiation; Academic Press; New York, 1969.

[212] Kreibig, U., Zacharias, P., Z. Phys. 1970, 231 , 128.

[213] Doremus, R. H., Rao, P., J. Mater. Res. 1996, 11 , 2834.

[214] Brus, L. E., J. Chem. Phys. 1984, 80 , 4403.

[215] Weller, H.;Schmidt, H. M.;Koch, U.;Fojtik, A.;Baral, S., Henglein, A., Chem. Phys. Lett. 1986, 124 , 557.

[216] Nosaka, Y., J. Phys. Chem. 1991, 95 , 5054.

[217] Voßmeyer, T.;Katsikas, L.;Giersig, M.;Popovic, I. G.;Diesner, K.;Chemseddine, A.;Eychmüller, A., Weller, H., J. Phys. Chem. 1994, 98 , 7665.

[218] U. Banin, G. Cerullo, A. A. Guzelian, A. P. Alivistors and C. V. Shank Phys. Rev. B, 55 (1997), 7059.

[219] A. L. Efros, M. Rosen, M. Kuno, M. Nirmal, D. J. Norris and M. Bawendi Phys Rev. B. 54 (1996), 4843.

[220] M. Nirmal, B. O. Dabbousi, M. G. Bawendi, J. J. Macklin, J. K. Trautman, T. D. Harris and L. E. Brus, Nature, 383 (1996), 802.

[221] P. C. Sercel, Phys. Rev. B, 51 (1995), 14532.

[222] W. Y. Liang and A. D. Yoffe, Phys. Rev. Lett., 20 (1968), 69.

[223] A. Weller, Phil. Trans. Roy. Soc. (London) A, 354 (1996), 757.

[224] V. L. Colvin, M. C. Schlamp and A. P. Alivistors, Nature, 370 (1994), 354

[225] V. Agranovich, R. Atanasov and F. Bassani, Solid-State Common, 92, (1994), 295

[226] M. Otobe, H. Yajime, and S. Oda, Appl. Phys. Lett. 72 (1998), 1089

[227] I. M. Ruzin, V. Chandrasekhar, E. I. Levin, and L. I. Glazman, Phys. Rev. B,45 (1992), 13469.

[228] *J. M. Martinis, M. Nahum, and H. D. Jensen,* Physical Review Letters*, 72, (1994) 904.*

[229] *A. N. Korotkov, D. V. Averin, K. K. Likharev, and S. A. Vasenko, In H. Koch and H. Lübbig, editors,* Single-Electron Tunneling and Mesoscopic Devices*, pages 45-59. Springer-Verlag, Berlin Heidelberg New York, 1992.*

[230] P. D. Tougaw and C. S. Lent, Journal of Applied Physics*,* **75** (1994)1818; J. R. Tucker, J. Appl. Phys., **72** (1992) 4399.

[231] K. Nakazato, R. J. Blaikie, and H. Ahmed*,* J. Appl. Phys., 75 (1994) 5123; K. Yano, T. Ishii, T. Sano, T. Mine, F. Murai, and K. Seki, *IEEE International Solid-State Circuits Conference*, pages 266-267, 1996.

[232] L. J. Geerligs, V. F. Anderegg, C. A. van der Jeugd, J. Romijn, and J. E. Mooij, Europhysics Letters, **10** (1989) 79.

[233] T. A. Fulton and G. J. Dolan, Phys. Rev. Letts. **59** (1987)109.

[234] L. S. Kuzmin and K. K. Likharev, JETP Letters **45** (1987) 495

[235] L. Canham, Appl. Phys. Lett. **57** (1990), 1046.

[236] K H Jung, S Shih, D L Knong, J.Electrochem Soc, **140** (1993) 3046.

[237] A. Tichter, P. Steiner, F. Kozlowski,W, Lang, IEEE Electron Device Lett. 12 (1991), 691.

[238] P. Steiner, F. Kozlowski, W. Lang, Appl. Phys. Lett. 62 (1993), 2700.

[239] S. Lazarouk, I. Baranor, G.Maiello, E. Proverbio, G.de Cesare, A.J. Ferrari, Electrochem Soc., **141** (1994), 2556.

[240] L. Tsybeskov, S. Duttagupta,K. Kirshmann, P. Fauchet, Appl. Phys. Lett.   **68** (1996), 2059.

[241] V. Bondarenko, A. Dorofeen, M. Kazutehiz, Microelectr. Engineer **28** (1995), 447

[242] A. Loni, L. T. Canham. M. G. Berger, Thin solid Films, **276**(1996), 143

[243] L. T. Canham, T. I. Cox, A. Loni, A. J. Simons, Applied surface Science,**102**(1996), 436

[244] C. Palsule, S. Liu, S. Gangopadhyay, M. Holtz, D. Lamp and M. Kristiansen, Solar Energy Materials and Solar Cells **46** (1997):261.

[245] H.A. Lowenstan, Science, 211 (1981), 1126.

[246] K. Simkiss, K.M. Wilbur, Biomineralization (1989), Academic, New York.

[247] R.B. Frankel, R.P. Blakemoire, eds. Jron Biominerals (1991), Plenum, New York.

[248] D.A. Tirrel, Mierarchial Structures in Biology as a Guide for New Materials Technology (1994), Natd. Acad. Press, Washington, DC.

[249] I.A. Aksay, E. Baer, M. Sarikaya, D.A. Tirrell, Hierarchically Structural Materials, eds., Vol. 255 (1992), Mater. Res. Soc., Pittsburgh.

[250] M. Sarikaya and I. A. Aksay, eds. (1995) *Biomi-metics: Design and Processing of Material*s, (Am. Inst. Phys., New York).

[251] J.H. Eldridge, C.J. Hammond, J.A. Memlbrock, J.K. Staas, R.M. Gilley, T.R. Tice, J. Control Release 11 (1990), 205.

[252] J.P. Ebel, Pharm. Res. 7 (1990), 848.

[253] J. Pappo, T.H. Ermak, H.J. Steger, Immunology 73 (1991), 277.

[254] M.A. Jepson, N.L. Simmons, D.T. O'Hagan, B.H. Hirst, J.Drug Target 1 (1993), 245.

[255] A.T. Florence, A.M. Hillery, P.U. Jani, J. Drug Target 3 (1995), 65.

[256] J. Eyles, H.O. Alpar, W.N. Field, D.A. Lewis, M. Keswick, J. Pharm. Pharmacol. 45 (1995), 561.

[257] C. Diirrer, J.M. Irache, F. Puisieut, D. Duchine, G. Pouchel, Pharm. Res. 11 (1994), 674.

[258] M.W. Smith, N.W. Thomas, P.G. Jenkins, N.G.A. Miller, D.Cremashi, C. Porta, Exp. Physiol, 80 (1995), 735.

[259] A. Frey, K.T. Giannasca, R. Wellzin, P.J. Giannesca, H. Reggis, W.I. Lencer, M. Neutra, J.Exp. Med. 184 (1996), 1045.

[260] L. Stryer, Biochemistry, 3rd Edn. (1988) W.H. Freeman, New York, Pg. 677.

[261] P.J. Hagerman, Annu. Rev. Biophys. Chem., 17 (1988), 265

[262] C.A. Mirkin, R.L. Letsinger, R.C. Mucic, J.J. Stoqhoff, Nature, 382 (1996), 607.

[263] A.P. Alivisatos, K.P. Johnsson, X. Peng, T.E. Wilson, C.J. Loweth, M.P. Bruchez Jr., P.G. Schultz, Nature, 382 (1996), 609.

[264] R. Elghanian, J.J. Stoqhoff, R.C. Mucic, R.L. Letsinger, C.A. Mirkin, Science, 277 (1977), 1078.

[265] H. Weller, Angew, Chem., 108 (1996), 1159.

[266] D. Bethell, D.J. Schiffrin, Nature, 382 (1996), 581

[267] A.P. Alivisatos, Science, 271 (1996), 933.

[268] R.F. Service, Science, **271** (1996), 920.

[269] R.K. Gilchrist et al., Ann. Surgery **146** (1957) 596.

[270] C. Stre!er, D. van Beuningen, in: J. Stre!er (Ed.), Hyperthermia and the Therapy of Malignant Tumors, Springer, Berlin, 1987.

[271] A. Jordan, R. Scholz, J. SchuKler et al., Int. J. Hyperthermia13 (1997) 83.

[272] P. Burgman, A. Nussenzweig, G.C. Li, in: M.H. Seegen-schmiedt, P. Fessenden, C.C. Vernon (Eds.), Ther moradiotherapy and Thermochemotherapy, vol. 1: Biology, Physiology, Physics, Springer, Berlin, 1995.

[273] D.C.F. Chan, D.B. Kirpotin, P.A. Bunn Jr., J. Magn. Magn.Mater. **122** (1993) 374.

[274] L. Néel, C.R. Ac, Sci. **228** (1949) 664

[275] A. Jordan et al. J. of Magnetism and Magnetic Materials **201** (1999) 413.

[276] J.P. Dailey et al. / J. of Magnetism and Magnetic Materials **194** (1999) 140.